Coupled Interactions between Charged Spacecraft: Relative Motion, Charging and Sensing

by

Julian Hammerl

B.S., Technische Universität Wien, 2020

M.S., University of Colorado Boulder, 2023

A thesis submitted to the

Faculty of the Graduate School of the

University of Colorado in partial fulfillment

of the requirements for the degree of

Doctor of Philosophy

Department of Aerospace Engineering Sciences

2025

Committee Members:

Prof. Hanspeter Schaub

Prof. Robert Marshall

Prof. Jay McMahon

Prof. Daniel Scheeres

Dr. Kieran Wilson

Hammerl, Julian (Ph.D., Aerospace Engineering Sciences)

Coupled Interactions between Charged Spacecraft: Relative Motion, Charging and Sensing

Thesis directed by Prof. Hanspeter Schaub

Interest in on-orbit servicing and active debris removal has increased in recent years due to the increasingly high population of active and retired satellites in Earth orbits. Spacecraft charging and the resulting inter-spacecraft electrostatic forces and torques have emerged as a promising field of study for on-orbit servicing and debris removal. While these forces and torques perturb the relative motion of two spacecraft during servicing operations, they may be utilized to touchlessly detumble and relocate space debris. Three related key technologies are advanced in this thesis: remote sensing of electric potentials, active charging control, and relative motion control.

A sensing method based on x-rays was recently proposed to estimate the electric potential of a nearby spacecraft using an electron beam. In contrast to prior work, in which homogeneously charged flat plates were used, experiments are conducted with complex shapes and multiple components charged to different potentials. An augmented estimation process is introduced that allows for the simultaneous estimation of multiple potentials.

Through analysis of the spacecraft charging dynamics, it is discovered that the electron beam introduces the existence of multiple co-existing equilibrium potentials. One of the equilibria types enables a promising open-loop charging control strategy that may be further advanced with a pulsed beam. Using a pulsed beam instead of a continuous beam is also investigated to create better sensing conditions for various remote potential estimation methods.

The relative motion control of the Electrostatic Tractor debris removal concept is investigated for complex-shaped debris objects. It is found that the debris orientation significantly affects the sensitivity of the control to electric potential estimation errors as well as general reorbit performance. Finally, an intuitive description of the relative motion as seen from the inertial frame is developed, with broad applicability beyond charged proximity operations.

für Mutti und Vati

Eine Entschuldigung schulde ich meinen Söhnen Stefan und Julian, die meine arbeitsbedingte Abwesenheit sicher am meisten geschmerzt hat. Ihnen, denen die Welt von Morgen gehört, möchte ich deshalb diese Arbeit widmen.

– Dr. Karl Hammerl, 1996

Vati, wie gern du heute noch hier sein wolltest.
Wie gern ich hätte, dass du heute hier wärst.

Ich danke euch für alles.

Acknowledgements

I would like to deeply thank my advisor, Dr. Hanspeter Schaub, for the invaluable guidance over the last few years. Thank you for encouraging me and pushing me to work at such a high level, and for being understanding and supportive whenever that was not possible.

Thank you, Dr. Kieran Wilson, for sharing so much of your knowledge during my first year here as a colleague, for your feedback as a committee member, and for all your advice as a friend. Thanks to the members of my committee, Dr. Robert Marshall, Dr. Jay McMahon and Dr. Daniel Scheeres, for the great feedback and support of this work. I would also like to acknowledge funding from NASA through the Future Investigators in NASA Earth and Space Science and Technology (FINESST) fellowship, and from the Air Force Office of Scientific Research (AFOSR).

A special thanks to the entire LASP EMA-GNC team, for such an amazing and incredibly rewarding time working on such a complex mission to the asteroid belt. To Dr. Álvaro Romero-Calvo, thank you for being such a remarkable teacher and for your unmatched sense of humor.

To the entire AVS Lab, past and present, thank you for playing such a central role during my time in Boulder, both inside and outside the lab. To the many skiing buddies, thank you for following me to the mountains when I needed a break. To each and everyone who has been part of my life during these years: thank you. I have grown so much because of you.

Finally, I owe the greatest thank you to my parents, for teaching me the importance of education and for always supporting my interests, even if that meant I would move across the Atlantic. Thank you for raising me to be the person that I am today. To Jackson (aka J-Baby, Boo-Boo): thank you for being the most wonderful dog.

Contents

Chapter

1 Introduction **1**

1.1 Motivation 1

1.2 Background and previous work 6

1.2.1 Spacecraft charging and electric potential sensing 6

1.2.2 Charged proximity operations 10

1.2.3 Inertial frame relative motion 12

1.3 Summary of contributions 14

1.4 Publications 17

1.4.1 Journal Papers 17

1.4.2 Conference Papers 18

2 Spacecraft charging and electrostatic force modeling **20**

2.1 Spacecraft charging model 21

2.1.1 Naturally occurring currents 22

2.1.2 Electron beam induced currents 26

2.1.3 Faceted charging model 27

2.1.4 Equilibrium potentials and charging dynamics 28

2.1.5 Justification of electron beam assumptions 30

2.2 Multi-sphere method for electrostatic force and torque approximation 32

2.3 Cislunar space study of natural electric potentials 35
2.4 Effect of differential charging on electrostatic force and torque 38
2.5 Conclusions 44

3 Electric potential sensing of complex shapes and differentially charged objects using x-rays 46
3.1 Fundamentals of x-ray based electric potential estimation 47
3.1.1 Theory of x-ray spectroscopic potential estimation 47
3.1.2 Theoretical x-ray models 48
3.1.3 Parametric study 52
3.2 ECLIPS space environment simulation facility 55
3.3 Differential charging 58
3.3.1 Experimental setup 58
3.3.2 Particle tracing simulation framework 60
3.3.3 Measuring each component individually 62
3.3.4 Target observability 65
3.3.5 Measuring multiple potentials simultaneously 67
3.3.6 Detectability of differential charging of a rotating object 75
3.4 Multiple materials 77
3.4.1 Experimental Setup 77
3.4.2 Beam steering 78
3.4.3 Simultaneous estimation 80
3.5 Sensing time 82
3.5.1 Chamber conditions 84
3.5.2 In-orbit conditions 86
3.5.3 Implications for active debris removal and on-orbit servicing 88
3.6 Conclusions 89

4 Spacecraft charging using a continuous electron beam **91**

4.1 Electron beam parameters: current and energy . . . 92

4.2 Multiple equilibria . . . 98

4.2.1 Overview . . . 98

4.2.2 Change of equilibrium . . . 101

4.2.3 Significance and potential applications . . . 106

4.3 Study of electron beam effects around Earth and Moon . . . 107

4.3.1 Geostationary Earth Orbit . . . 107

4.3.2 Cislunar space . . . 111

4.4 Conclusions . . . 113

5 Spacecraft charging using a pulsed electron beam **115**

5.1 Pulsing Parameters . . . 117

5.2 Open-loop pulsing . . . 118

5.2.1 On-Off pulsing . . . 118

5.2.2 Energy pulsing . . . 119

5.2.3 Open-loop potential control . . . 122

5.3 Closed-loop pulsing . . . 123

5.4 Conclusions . . . 126

6 Electrostatic tractor relative motion control **127**

6.1 Dynamics and control model . . . 128

6.1.1 Electrostatic Tractor relative motion dynamics . . . 128

6.1.2 Rotational dynamics . . . 131

6.1.3 Electrostatic Tractor relative motion control design . . . 131

6.2 Effects of electric potential uncertainty on relative motion equilibria . . . 133

6.2.1 Equilibria under standard conditions . . . 133

6.2.2 Change over distance . . . 138

6.2.3 Change over attitude . . . 140
6.2.4 Multi-Sphere model comparison . . . 145
6.2.5 Servicer electric potential uncertainty . . . 150
6.3 Debris attitude . . . 150
6.3.1 Prescribed attitude . . . 151
6.3.2 Freely rotating debris . . . 153
6.3.3 Debris attitude effects including electric potential error . . . 155
6.4 Control without feed-forward of electric potential . . . 156
6.5 Comparison of reduced order charging and force models . . . 158
6.6 Conclusions . . . 164

7 Spacecraft relative motion in the inertial frame **166**
7.1 Background . . . 169
7.1.1 Relevant coordinate frames . . . 169
7.1.2 Cartesian coordinate description . . . 171
7.1.3 Orbit element difference description . . . 173
7.2 Circular chief orbits . . . 174
7.2.1 Inertial frame relative orbit elements . . . 174
7.2.2 General chief orbit orientation . . . 179
7.2.3 Invariants of motion . . . 179
7.2.4 Closed relative orbits . . . 181
7.2.5 Drift Motion . . . 182
7.3 Elliptic chief orbits . . . 182
7.4 Control development . . . 186
7.4.1 Variational equations . . . 186
7.4.2 Continuous feedback control . . . 190
7.4.3 Control application . . . 191

7.5 Application to on-orbit servicing 193
7.6 Conclusions 196

8 Conclusions and future work **198**
8.1 Contributions of this work 198
8.2 Directions for future work 200

Bibliography **202**

Appendix

A Mappings between relative orbit element sets **215**
A.1 Cartesian Hill state to linearized relative orbit elements 215
A.2 Inertial frame relative orbit elements to linearized relative orbit elements 215
A.3 Inertial frame relative orbit elements to differential orbit elements 217
A.4 Cartesian perifocal state to inertial frame relative orbit elements 218

Tables

Table

2.1 Cislunar plasma parameters (taken from DSNE) 35

3.1 Theoretical x-ray model parameters 52

3.2 X-ray Observations. (a) $\Phi_B = -0.5$ kV, $\Phi_P = -1.5$ kV, (b) $\Phi_B = -1.5$ kV, $\Phi_P = -0.5$ kV 66

6.1 Parameters used in this analysis 135

6.2 MSM Model configurations 146

6.3 Computation time ratios with respect to Configuration A 149

6.4 Navigation Error Parameters 158

7.1 Initial and desired inertial frame relative orbit elements 191

Figures

Figure

1.1 Illustration of Active Debris Removal (Image Credit: ClearSpace) and On-Orbit Servicing (Image Credit: Starfish Space) 2

1.2 The three main topics of charged astrodynamics for OSAM and ADR: charging, sensing, and relative motion 5

1.3 Illustration of spacecraft charging and sensing processes 6

1.4 Illustration of charged proximity operations 10

1.5 Illustration of plasma wake 13

2.1 Faceted Spacecraft Model 27

2.2 SIMION Simulation 30

2.3 Percentage of electron beam that hits the servicer for a beam energy of 20 keV. Solid red line: $\phi_S = \phi_T + E_{EB}$. Dashed red line: $\phi_S = E_{EB}$ 32

2.4 Multi-Sphere Spacecraft Models. Target spacecraft on the left, servicing spacecraft on the right 34

2.5 Natural potentials in cislunar space for an eclipsed spacecraft, obtained using a faceted model of the target. The teal area indicates the range of equilibrium potentials, depending on the spacecraft orientation. The average equilibrium potential across all orientations is also indicated. 37

2.6 Electrostatic force as function of target orientation for differentially charged target . 40

2.7 Differential charging effects over various separation distances. The shaded regions represent the range of forces for all target orientations, while the lines themselves indicate the average force across all orientations. 41
2.8 Electrostatic torque on the target as function of target orientation for differentially charged target 42

3.1 Sample Theoretical spectrum for aluminum with incident electron energy $E_e = 10$ keV 49
3.2 Efficiency of Si-Pin x-ray detector from Amptek. The detector used in this work has a 1 mil beryllium frontal window (red curve). 51
3.3 ECLIPS vacuum chamber facility 56
3.4 Pressure evolution with time with and without bakeout 57
3.5 Experimental setup with a box-and-panel object representing a spacecraft 59
3.6 SIMION Model 61
3.7 Narrow Electron Beam for measuring each component individually 62
3.8 X-ray spectra for different target object angles. $\Phi_B = -0.5$ kV, $\Phi_P = -1.5$ kV . . . 63
3.9 Narrow Beam trajectories from SIMION simulation. $\Phi_B = -0.5$ kV, $\Phi_P = -1.5$ kV 64
3.10 Narrow Beam Results 65
3.11 Theoretical superposition of X-ray spectra 67
3.12 Wide Electron Beam for measuring multiple potentials simultaneously 69
3.13 Wide Beam trajectories from SIMION simulation. $\Phi_B = 0$ V, $\Phi_P = -3000$ V 70
3.14 Sample Spectrum for 80°. $\Phi_B = 0$ kV, $\Phi_P = -3$ kV 71
3.15 Sample Spectrum for 30°. $\Phi_B = 0$ kV, $\Phi_P = -3$ kV 72
3.16 Wide Beam Results. $\Phi_B = 0$ V, $\Phi_P = -3000$ V 73
3.17 Beam trajectories for dynamic experiment from SIMION simulation. $\Phi_B = -3$ kV, $\Phi_P = -1$ kV 74
3.18 Dynamic Experiment Results 76
3.19 Experimental setup with two panels 78

3.20 Estimated potentials for different beam deflections 79
3.21 Sample spectra for two-panel test object with multiple materials 81
3.22 Simultaneous estimation of potentials 82
3.23 Photon count at range start of estimation linear fit as function of accumulation time and beam current for chamber conditions 83
3.24 Sensing time and max. beam current to avoid detector saturation for chamber conditions 85
3.25 Photon count at range start of estimation linear fit as function of accumulation time and beam current for orbital conditions and landing energy of 10 keV 86
3.26 Sensing time and max. beam current to avoid detector saturation for orbital conditions 87

4.1 Currents vs. Potential of Target. $I_{EB} = 50$ µA, $E_{EB} = 20$ keV, resulting servicer equilibrium potential of about +4.5 keV 93
4.2 Current vs. Potential of Target for various beam parameters. $E_{EB} = 20$ keV 95
4.3 Charging as function of effective energy 96
4.4 Multiple Equilibria: Left and right equilibria are stable, center equilibrium is unstable. 98
4.5 Multiple Equilibria Transients for various initial servicer potentials $\phi_{S,0}$ 100
4.6 Change of Equilibria due to Electron Beam Energy Variation. $I_{EB} = 50$ µA 101
4.7 Change of Equilibria due to Sunlight Variation. $I_{EB} = 50$ µA 103
4.8 Current Sum for bivariate root-finding. $I_{EB} = 50$ µA, $E_{EB} = 20$ keV 105
4.9 Equilibrium Potential vs. Electron Beam Current in GEO. $E_{EB} = 20$ keV 108
4.10 Equilibrium Potential vs. GEO Local Time. $E_{EB} = 20$ keV 110
4.11 Maximum Allowed Current in GEO eclipse 111
4.12 Equilibrium Potential vs. Electron Beam Current in cislunar space. $E_{EB} = 20$ keV . 112

5.1 Types of Pulsing 117
5.2 Duty Cycle d and Pulsing Frequency f 118
5.3 Illustration for energy pulsing 120

5.4 Open Loop Energy Pulsing: color shading indicates which sensing method benefits from a better signal . . . 121
5.5 Open Loop Potential Control . . . 122
5.6 Closed Loop On-Off Pulsing . . . 124
5.7 Closed Loop Energy Pulsing . . . 125

6.1 Hill frame $\mathcal{H}$ and Spherical frame $\mathcal{K}$ . . . 129
6.2 Equilibrium locations L_{eq} of the closed-loop response for potential estimation error $\Delta\phi$ and $L_r = 20$ m: the solid lines correspond to stable equilibria, the dashed line represents unstable equilibria. . . . 136
6.3 Changes to the reference distance L_r without adjustment of the gain K_L, for $L_{r,KL} =$ 20 m . . . 139
6.4 Changes to the reference distance L_r with adjusted feedback gain K_L . . . 140
6.5 Attitude effects on the critical potential estimation error $\Delta\phi^*$ . . . 141
6.6 Attitude effects on the minimal distance between the debris and the servicer, for $\Delta\phi = \Delta\phi^*$ . . . 142
6.7 Attitude effects over distance, without adjustment of the gain K_L, for $L_{r,KL} = 20$ m 143
6.8 Attitude effects over distance, with adjusted feedback gain K_L . . . 144
6.9 MSM Models . . . 145
6.10 MSM model effects for standard scenario . . . 147
6.11 MSM model effects on critical estimation error of worst and best case scenario . . . 148
6.12 Reorbit Times for 300 km altitude raise with prescribed attitude . . . 152
6.13 Maximum angular velocity during 300 km altitude raise . . . 153
6.14 Histograms for 300 km altitude raise and randomized potential error . . . 155
6.15 Average separation distance and $\pm 3\sigma$ during one orbit revolution as function of feedback gain K_L . . . 157

6.16 Average separation distance and $\pm 3\sigma$ during one orbit revolution as function of feedback gain K_L, with navigation errors 159

6.17 Electric Potential of the target ϕ_T as function of target orientation 160

6.18 Electrostatic force and torque magnitude as function of target orientation, using different models 161

6.19 Electric potential ϕ of target and servicer and force magnitude F over time during the Electrostatic Tractor debris reorbit scenario 162

7.1 Plasma wake orientations in different orbital regimes 167

7.2 Illustration of Hill frame and Inertial frame: The Hill frame $\mathcal{H}$ is centered at the chief and rotates as the chief orbits the central body, with $\hat{\boldsymbol{h}}_r$ aligned with the orbit radial direction of the chief and $\hat{\boldsymbol{h}}_h$ aligned with the orbit normal direction. The inertial frame $\mathcal{N}_O$ is located at the central body with fixed directions of the frame axes. A moving frame $\mathcal{N}_C$ is used that is centered at the chief, but its axes remain aligned with the inertial frame. 169

7.3 Relative motion in Hill frame for a circular chief orbit: A_0 creates a 2-by-1 relative orbit ellipse that is offset in the y-direction by y_{off}. Drift motion is induced by x_{off}. The projections of the relative orbit on the three planes are shown in lighter color. . 173

7.4 Inertial frame relative orbit elements: The relative motion in the inertial frame traces an epitrochoid curve, in which a circle with radius r_i rolls without slip on a fixed circle with radius r_i, and the curve is generated by a point that is at a distance of d_i away from the center of the rolling circle. The formation is $3d_i$ away from the origin and rotated by α_i. 176

7.5 Relative motion in Inertial frame: The in-plane motion corresponds to an epitrochoid curve. The projections of the relative orbit on the three planes are shown in lighter color. 177

7.6 Effect of chief orbit orientation (Ω, i, ω) on inertial frame relative motion: the relative motion may be conveniently described in the perifocal frame, as the mapping from perifocal frame to inertial frame is a pure rotation. 179

7.7 Inertial frame relative orbits for circular chief orbits: The size of the relative orbit changes with r_i, while the shape changes with the ratio of r_i and d_i. 182

7.8 Drift motion in the inertial frame: An offset x_{off} causes the radius r_i to change over time. 183

7.9 Inertial frame relative orbits for elliptic chief orbits: The relative orbit is stretched for elliptic chief orbits. 185

7.10 Rotation of inertial frame relative orbit for elliptic chief orbits: a rotation by α_i also changes the relative orbit shape. 186

7.11 Control of inertial frame relative orbit element set $\boldsymbol{\alpha e}_{i,0}$ 192

7.12 Control of non-singular inertial frame relative orbit element set $\boldsymbol{\alpha e}_{i,0,ns}$ 194

7.13 Relative motion in Inertial frame subject to cylindrical keep-out zone 196

7.14 Relative motion in Inertial frame subject to cylindrical keep-out zone, YZ-plane projection 196

Chapter 1

Introduction

1.1 Motivation

Geostationary Earth Orbit (GEO) is becoming increasingly populated with both active and retired satellites due to the unique and valuable properties of geosynchronous orbits that allow spacecraft to maintain a fixed position above Earth. In contrast to Low Earth Orbit (LEO), there is no atmospheric drag that eventually deorbits retired satellites and debris. As studied in 1978 and commonly compared to a cascade effect, an increasing number of objects in orbit leads to an increased probability of collision [1]. A collision of two satellites in orbit, in turn, adds even more uncontrolled objects. The space debris mitigation guidelines of the Inter-Agency Space Debris Coordination Committee (IADC) recommend a minimum altitude increase of at least 235 km at the end-of-life of a geostationary satellite, depending on spacecraft characteristics such as solar radiation pressure coefficient, cross-sectional area, and mass [2]. The percentage of successful re-orbit attempts to such a graveyard orbit increased from about 20% in the year of 2000 to about 90% in 2024, according to the annual space environment report [3] of the European Space Agency (ESA). However, at a rate of about 20 new satellites delivered to GEO every year, the cumulative number of satellites with either no attempt or insufficient attempt of relocation leads to a high number of uncontrolled objects near geostationary orbit. Of the nearly 2000 geostationary objects, less than 600 were controlled as of 2024 [3].

Two related fields that deal with the mitigation of space debris in one way or another are Active Debris Removal (ADR) and On-orbit Servicing, Assembly and Manufacturing (OSAM). Active

(a) Active Debris Removal

(b) On-Orbit Servicing

Figure 1.1: Illustration of Active Debris Removal (Image Credit: ClearSpace) and On-Orbit Servicing (Image Credit: Starfish Space)

Debris Removal aims at either deorbiting retired and dysfunctional satellites or reorbiting them to a graveyard orbit where they do not pose a threat to active satellites. A number of ADR concepts have been investigated for large objects [4, 5], such as nets [6], harpoons [7], robotic arms [8] and the Ion Beam Shepherd [9]. However, most of these concepts involve physical contact between the servicing satellite and the debris object. Nets and harpoons might create new fragments when they impact the debris, and the required tether between the debris and the servicer adds complexity to the removal process [10]. The capture with robotic arms or tentacles requires complicated rendezvous and docking maneuvers. Retired satellites may tumble at rates of 10s of degrees per second [11, 12], exceeding the capabilities of certain grappling methods [13]. Thus, touchless ADR techniques provide a great benefit for space debris removal. Unlike ADR, where the goal is to remove retired satellites from their current orbit, part of OSAM aims at servicing retired (or active) satellites in order to extend the life of the satellite. Proposed methods include repairing or refueling the target satellite, or to dock with the target and provide orbit correction maneuvers using the propulsion system of the servicing satellite [14]. The first of such servicing operations happened in 1993, when astronauts onboard the space shuttle fixed a flaw in the primary mirror of the Hub-

ble Space Telescope during several space walks [15]. However, such a human-assisted mission is quite different than the autonomous missions discussed in this work. In 2020, the first servicing mission without astronaut assistance was accomplished, when Northrop Grumman's Mission Extension Vehicle-1 (MEV-1) docked with Intelsat 901 in a graveyard orbit to relocate it to GEO and extend the operational lifetime of Intelsat 901 by an expected five years [16]. This was followed by MEV-2 extending the life of Intelsat 10-02 in 2021. A similar mission is OSAM-1 [17] by the National Aeronautics and Space Administration (NASA), which aimed at refueling and relocating the Landsat-7 satellite in 2026, but was canceled in 2024. Several other industrial companies now seek to provide on-orbit satellite services, such as Starfish Space, Astroscale, ClearSpace, or Infinite Orbit, among others. Even though the target spacecraft of the aforementioned successful missions were still controlled, the assumption for OSAM operations is often that the target is uncontrolled. Thus, servicing operations are similar to ADR methods that are based on docking and the usage of robotic arms, as the general methodology is for a servicer to rendezvous and dock with an uncooperative target spacecraft. Illustrations of active debris removal and on-orbit servicing are shown in Fig. 1.1.

An area of research that has received increased attention for ADR and OSAM applications is spacecraft charging. Spacecraft build up electrostatic potentials in orbit due to various electric currents in the space environment [18]. The incoming electromagnetic radiation from the Sun excites electrons and causes them to escape from the spacecraft if the craft is charged negatively, leading to a positive photoelectric current. The plasma environment in space results in both positive and negative currents due to the ions and electrons that impact objects in space. In LEO, the plasma environment is cold (low particle energies) and dense. Thus, spacecraft such as the International Space Station (ISS) tend to charge a few volts positive in sunlight and a few volts negative in eclipse. In GEO and cislunar space, however, the plasma is hot and tenuous, resulting in high spacecraft electric potentials that can reach tens of kilo-volts. The Applied Technology Satellite 6 (ATS-6), for example, experienced a record potential of -19 kV while in eclipse in geostationary orbit [19]. Charging environments at night in lunar orbit or on the lunar surface may contain charging risks

similar to geostationary orbit during extreme space weather events [20].

High electric potentials affect spaceflight in several different ways. One of these effects is arcing. It is recommended by spacecraft design guidelines to build fully conducting satellites in order to mitigate unfavorable differential charging effects [21]. If the spacecraft is not fully conducting, some structures charge to different potentials than others, referred to as differential charging. This can lead to arcing between components, for example between the solar panel and the spacecraft bus, and consequently reduces the lifetime of the solar panel and the spacecraft [22, 23]. Arcing can occur between two spacecraft during docking operations if the electric potential difference between the two objects is large. This is possible if one spacecraft eclipses the other while docking, blocking out the light from the Sun that is responsible for the photoelectric current. For instance, the Lunar Gateway is oriented such that the Orion capsule's tail faces the Sun during docking operations [24], which can lead to hazardous spacecraft charging events.

One consequence from spacecraft charging are the electrostatic forces that result from electric potentials and the corresponding electric charges, a field of study that is referred to as charged astrodynamics. Two charged objects in proximity are subject to electrostatic forces proportional to the charging levels of the two objects. While opposite signs of the charges result in attractive forces, equal signs cause repelling forces. Thus, even if both objects are charged to the same potential, they are subject to a repelling force. This also leads to electrostatic torques if the center of charge of each object does not correspond to its center of mass [25, 26]. These electrostatic forces and torques can influence the relative motion and rotation during OSAM operations [25, 27]. In order to dock, a servicing spacecraft needs to match the rotational rates imposed on an uncooperative target spacecraft. This can cause the servicer to fail critical tasks such as aligning its solar panels with the sun for power generation or pointing the antenna toward Earth for communication. One can also take advantage of charged spacecraft and the resulting forces and torques. On the other hand, the Electrostatic Tractor ADR concept utilizes the electrostatic force to touchlessly relocate retired satellites from GEO to a graveyard orbit [28–30], and the electrostatic torque may even be used to touchlessly detumble retired satellites [31, 32].

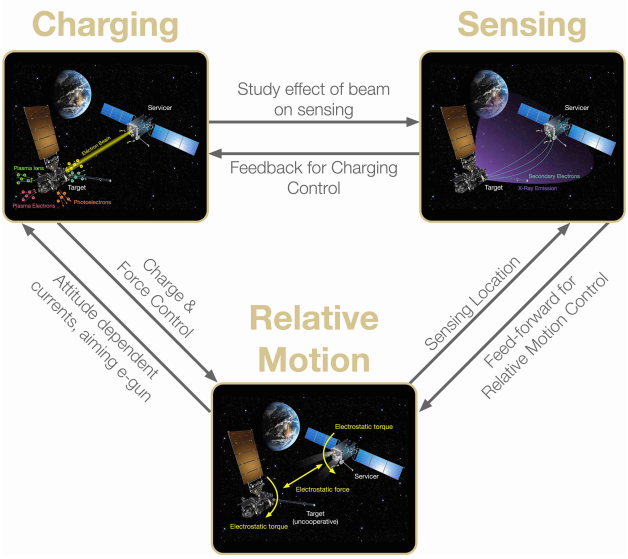

Figure 1.2: The three main topics of charged astrodynamics for OSAM and ADR: charging, sensing, and relative motion

To deal with electrostatic perturbations during OSAM operations and to utilize them for ADR methods, three major topics that are all connected with each other need to be studied: spacecraft charging, remote sensing of electric potentials, and the relative motion of the two charged spacecraft. Remotely sensing the electric potential of the target spacecraft can be used to feed forward the estimated electrostatic forces and torques to the relative motion control for ADR [33] and OSAM [34], and as feedback for charging control. Proposed methods for electric potential sensing utilize an electron beam that is emitted from the servicer and aimed at the target [35, 36]. Studying electron induced spacecraft charging enables us to investigate the effects of the electron beam on the remote sensing methods, as well as to develop charge control approaches in order to control the electrostatic forces. The relative position and orientation plays a role in aiming the electron gun for charging and also affects the sensing performance. Finally, controlling the relative motion subject to electrostatic forces and torques enables more robust on-orbit servicing operations as well as actively removing space debris from geostationary orbit. The connection between the three main topics is illustrated in Fig. 1.2.

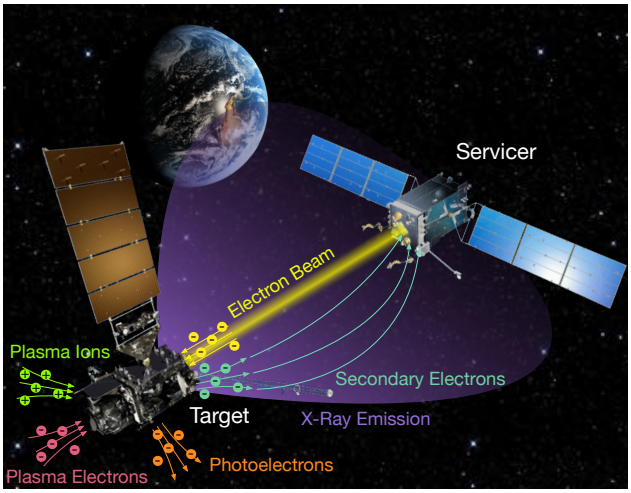

Figure 1.3: Illustration of spacecraft charging and sensing processes

1.2 Background and previous work

This section summarizes prior related work and highlights key aspects that have not been investigated previously. The necessary background for this dissertation about spacecraft charging, the remote sensing of electric potentials as well as space debris removal and servicing operations subject to electrostatic forces and torques is provided. Finally, the motivation for studying the relative motion of two spacecraft in the inertial frame is discussed.

1.2.1 Spacecraft charging and electric potential sensing

1.2.1.1 Electric potential sensing

To measure the electric potential of a spacecraft itself, a Langmuir probe [37, 38] or Retarding Potential Analyzer (RPA) [39] is frequently used. Such instrument is usually mounted on a long boom to avoid disturbances by the Debye sheath of the spacecraft itself and instead measure the ambient plasma.

Several methods to remotely sense electric potential of a nearby spacecraft have been proposed. While it is possible to use x-ray, optical, and radio emissions from GEO satellites to detect spacecraft charging and arcing events from LEO and even from Earth's surface [40], the proposed

method only indicates that a spacecraft is charged, but not to what level. Reference 41 proposes to estimate the electric potential of a nearby spacecraft from the relative motion evolution due to the perturbation by the electrostatic force between the two craft. However, the estimation accuracy of this method depends on the accuracy of the gravitational and relative motion models, only the potential of an effective sphere model is estimated, and it takes minutes to hours to update the charge estimate. Reference 42 proposes to estimate the electric potential and create a Multi-Sphere Model by measuring the electric field around the spacecraft, but the study does not consider the challenges of measuring an electric field in a tenuous plasma environment [43].

Two new methods to sense electric potentials of nearby spacecraft have been investigated in recent years: the electron method [35] and the x-ray method [36] (Fig. 1.3). The electron method employs a servicing spacecraft equipped with an electron beam that is aimed at a nearby object of interest. When electrons impact on a surface, they excite secondary electrons that leave the surface with nearly zero kinetic energy and are accelerated if the object is charged negatively. The kinetic energy of the electrons when they arrive at a servicing spacecraft corresponds to the potential difference between the object and the servicer. Thus, by measuring the energy of the secondary electrons with a servicing satellite at a known potential, the electric potential of the object is inferred. The x-ray spectroscopy method utilizes an electron beam on a servicing spacecraft to excite x-rays on a nearby object. Bremsstrahlung radiation is emitted from the object at a continuous spectrum of energies, and the maximum energy of the recorded spectrum corresponds to the landing energy of the impacting electrons. If the object is charged positively or negatively, the electrons are either accelerated or decelerated before they arrive at the object, which increases or decreases the maximum energy of the x-ray spectrum. Thus, measuring the potential of the servicing spacecraft using a Langmuir probe [38] and knowing the initial energy of the electrons (the electron beam energy), the electric potential of the object is estimated. Both methods have been validated experimentally [44, 45] for terrestrial conditions in the Electrostatic Charging Laboratory for Interactions between Plasma and Spacecraft (ECLIPS) research vacuum chamber [46]. This work focuses on the x-ray method.

Prior research developed the theoretical foundation for touchlessly determining electric potentials using x-ray spectroscopy [36]. The x-ray spectrum consists of characteristic radiation at discrete energies and continuous Bremsstrahlung radiation. Characteristic radiation is emitted at an energy that is distinct for each element, so the x-ray method can also be used for determining material composition [36]. The x-ray method is experimentally validated in Ref. 45, where it is shown that it is possible to estimate electric potentials of a flat plate with errors of less than 100 V for a wide range of potentials and for various angles between the x-ray detector and the electron beam. Reference 47 investigates the angular dependence of the x-ray method by conducting experiments with a rotating target plate and also by changing the angle between the detector and the electron beam. The results suggest that there is no relationship between the accuracy of this method and the angle of the target plate or the x-ray detector, but the number of photons detected by the x-ray detector (the signal availability) is affected by the plate angle. Reference 47 also shows that the accuracy of this method for the given x-ray detector decreases with increasing electron landing energy due to saturation of the detector, and suggests to control the electron beam energy as a function of the potential of the object (and of the servicing satellite, because the relative potential between the two objects determines the landing energy) to maintain a constant landing energy and enable better potential estimation. Reference 48 proposes to use the x-rays that are generated by the ambient plasma environment to passively determine the potential of a nearby object without using an active electron beam. The proposed method was tested experimentally [48] in a vacuum chamber using a broad-spectrum electron gun [49] that emits electrons of multiple energies at the same time.

However, all experiments for the x-ray method were conducted with a single flat plate that is homogeneously charged to a single potential. If the spacecraft is not fully conducting, some components charge to different potentials than others, referred to as differential charging. Thus, the effects of complex-shaped objects and differentially charged components on the performance of the x-ray remote sensing method were not studied.

1.2.1.2 Electron beam induced spacecraft charging

Spacecraft charging has been extensively reviewed in Ref. [18], and studied with emphasis on, among other topics, mitigation of charging [21], modeling of spacecraft charging [50], detection of discharging events [40] and characterization of the secondary electron yield [51] that plays an important role in spacecraft charging. Charging levels in various orbital regions have been investigated, such as Low Earth Orbit (LEO) [52], GEO [53] and cislunar space [54]. However, most research on spacecraft charging focuses on the effects of only the space environment, that is, how much a spacecraft charges naturally due to the ambient plasma environment. Charging induced by electron beam impact, electron beam emission, and ion beam emission is discussed relatively briefly in Chapters 9-12 of Ref. [18]. The coupled charging behavior of two spacecraft in close proximity, where one spacecraft emits an electron beam that hits the other spacecraft, has been studied for the application of the Electrostatic Tractor active debris removal method [55–58]. These papers specifically study the effect of the charging levels on the electrostatic force magnitude between the two spacecraft, with the goal of improving the performance of the Electrostatic Tractor, as a higher force magnitude leads to a reduction of the time required to reorbit retired satellites from GEO to a graveyard orbit. However, the coupled effect of electron emission and impact on the transients of the servicer and target spacecraft potentials, as well as the influence of the beam on remote sensing methods that estimate the electric potential of another spacecraft, have received little attention.

One key aspect of the remote sensing methods that has been ignored in prior theoretical and experimental work is the effect of the electron beam on the electric potential of the target. The electrons from the beam impose a negative current on the target object, which changes the equilibrium potential within a second, depending on the capacitance of the spacecraft. One might be interested in the natural potential of the object, that is, the potential resulting from the space environment without the influence of the electron beam. Therefore, any impact of the electron beam on the potential must be minimized, otherwise the potential being measured does not correspond to the natural potential. To what extent the electric potential is affected by the electron beam depends

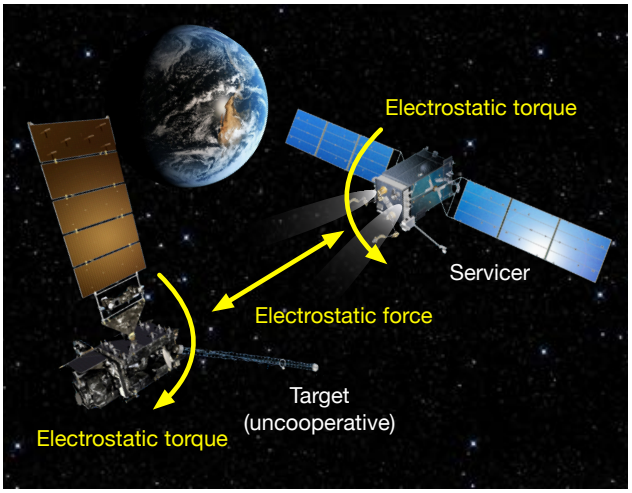

Figure 1.4: Illustration of charged proximity operations

on the conditions of the space environment and the electron beam parameters, i.e. the beam current and beam energy. The electron beam current and energy can be chosen such that the electron beam does not change the target potential significantly, however, the remote sensing methods impose restrictions on the beam parameters in order to generate a sufficient amount of secondary electrons and x-rays. In prior experimental work on the two sensing methods [33, 44, 45, 59], the potential of the target object was held constant during the experiments using high voltage power supplies, so the effect of the negative current due to the electron beam on the electric potential of the target was eliminated.

1.2.2 Charged proximity operations

1.2.2.1 Active debris removal

The Electrostatic Tractor (ET) has been proposed to touchlessly remove space debris from geostationary orbit by utilizing electrostatic forces [29]. A controlled spacecraft, referred to as a servicer or a tug, emits an electron beam onto an uncooperative or retired target satellite (debris). The emission of electrons raises the electric potential of the servicer to 10s of kilovolts, while the debris charges negatively due to the bombardment with electrons. Using thrusters, the resulting attractive Coulomb force in the order of milli-Newtons is utilized to pull the debris to a grave-

yard orbit without any contact. It has also been proposed to utilize the electrostatic torques to touchlessly detumble retired satellites [31, 32, 60–62].

Previous research on the ET focused on studying the applied spacecraft charging model [55] and analyzing the impact of spacecraft size [56], space weather [57, 58, 63] as well as pulsed electron beam configurations [64] on the electrostatic force levels between the two spacecraft. Reference 65 investigates the charged relative motion dynamics and control of the ET for two spherical spacecraft, and how charge uncertainty affects the control stability.

However, given the symmetric shape and charge distribution of a single sphere, attitude effects were not studied in prior work. Besides the direct effect of attitude on the electrostatic force, the effect of the debris attitude on the electric potential, which also affects the electrostatic force, has not been considered. The effect of Sun incidence angle on the electric potential and dynamics have been considered before, but only for individual lightweight Mylar debris that is subject to electromagnetic effects [66], and not for inter-spacecraft forces and torques during proximity operations.

1.2.2.2 Servicing

While the electrostatic forces and torques between two charged spacecraft may be utilized to detumble and relocate retired satellites, they may also perturb the relative motion of two nearby charged spacecraft. Reference 25 studies the impact of electrostatic perturbations on proximity and servicing operations with a servicer spacecraft and an uncooperative target object in High Earth Orbits. While the resulting accelerations due to the electrostatic force are negligible for the time of operation, the electrostatic torques impose significant rotational rates on the target object exceeding 0.1 deg/s. To maintain a constant relative position and orientation, the servicer needs to translate around the target object, which increases fuel consumption. Reference 34 proposes guidance strategies that minimize the electrostatic torques acting on the target upon approach by the servicer. This reduces the imposed rotational rates of the target object and results in less fuel consumption, because the servicer does not need to translate in order to maintain a constant relative position and orientation. Additionally, Ref. 34 feeds forward the expected electrostatic

torques to improve the control performance.

However, all prior work prescribed electric potentials of -10 kV for each spacecraft assuming extreme charging scenarios, without considering the interactions of the spacecraft with the plasma environment. Moreover, prior work on electrostatic proximity operations, both OSAM as well as active debris removal, assumed fully conducting spacecraft. The effects of differentially charged spacecraft on the inter-craft electrostatic forces and torques have not been studied. The focus of previous work was on GEO and did not investigate the complex cislunar plasma environment. In some regions in cislunar space (magnetosheath and solar wind), a plasma wake with a decreased ion density forms around spacecraft [67]. This results in higher electrostatic forces inside the wake when close to the leading spacecraft, compared to vacuum [68]. Thus, it may be beneficial to remain outside the plasma wake during approach. Approach trajectories that consider the plasma wake in cislunar space have also not been considered in previous work.

1.2.3 Inertial frame relative motion

The aforementioned plasma wakes form in the anti-ram-side direction behind the spacecraft if the ion thermal velocity is greater than the electron thermal velocity [67], where the ram-side is determined by the spacecraft velocity relative to the bulk velocity of the ions (Fig. 1.5). The plasma and spacecraft charging dynamics are more complex inside this wake, and inter-spacecraft electrostatic forces may also be stronger [68]. This motivates to stay inside the wake to study the plasma and spacecraft charging dynamics, or outside to minimize electrostatic perturbations [25]. In Low Earth Orbit (LEO), the ion bulk velocity is negligibly small, so the wake is approximately fixed in the spacecraft velocity frame [69] (or Hill frame for a circular orbit). Outside Earth's magnetosphere, in contrast, the ions move with the solar wind. If the spacecraft velocity is negligibly small compared to the solar wind velocity, the wake forms in the anti-sun direction and is quasi-inertially fixed [70]. Thus, the plasma wakes, especially in cislunar space, motivate a relative motion description in the inertial frame.

A large body of work exists in the literature about relative motion described in the Hill

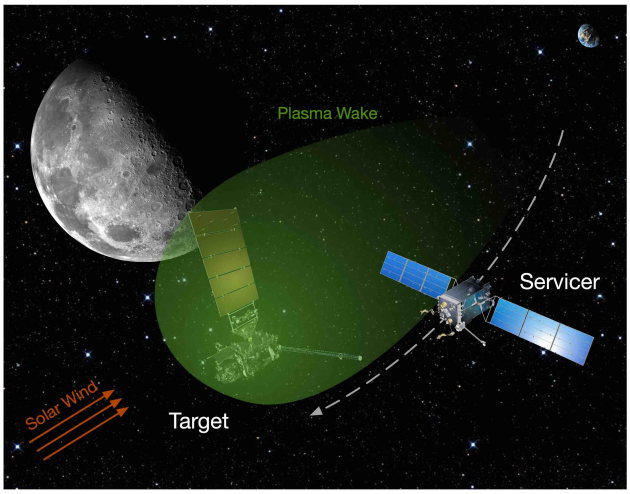

Figure 1.5: Illustration of plasma wake

frame, as extensively reviewed in Ref. 71. The various models may be categorized by the reference orbit, such as near-circular [72, Chapter 4] or eccentric orbit [73]; by the solution form, such as linear [74, 75] or nonlinear [76]; and by the perturbations considered in the dynamics, such as earth oblateness (J_2), atmospheric drag, thrust maneuvers, solar radiation pressure or third body effects by the Sun or Moon. Additionally, instead of using the cartesian relative position and velocity in the Hill frame as the state, some models use states that are based on relative orbit elements (ROEs), such as the Hill-Clohessy-Wiltshire (HCW) invariants [74, 77], mean orbit element differences (MOED) [78–83] or relative eccentricity and inclination vector (E/I-vector) [84, 85]. While mappings exist to map between the various state representations [71], they usually map the ROEs back to the cartesian state in the Hill frame. Some work exists for relative motion in the spacecraft velocity frame [86], which is especially advantageous for atmospheric entry trajectories of two spacecraft or highly eccentric chief orbits. Relative motion descriptions based on the relative state in the inertial frame have not been explored.

Constraints such as keep-in and keep-out zones are also usually described in the Hill frame or body frame of the target. Hill frame fixed keep-out zones are convenient for situations with larger spacecraft separation distances such as safety ellipses during approach of a spacecraft to the International Space Station [87]. Body frame fixed keep-out zones are often used for docking

operations [88]. Inertially constrained relative motion around a planet has only been studied for a very specific orbit to maximize the average power generation [89, 90], but keep-out zones or general orbits were not investigated.

1.3 Summary of contributions

The overarching purpose of the proposed research is to provide new insight into the complex and coupled dynamics of spacecraft charging and the corresponding relative motion. The goal is the development of methods to sense and control the electric potential of nearby spacecraft, in order to utilize electrostatic forces for active debris removal or to reduce the effect of such forces if they are undesired during servicing operations.

The first research thrust of this dissertation is focused on the remote electric potential estimation of spacecraft consisting of multiple components that are charged to different potentials and made of dissimilar materials using x-rays. This is important because the components of old spacecraft that have been exposed to the space environment for long periods of time may not all be connected to one common ground. The charge distribution and resulting electrostatic force of a differentially charged spacecraft differs from a fully conducting spacecraft, and the presence of multiple potentials may interfere with the x-ray based remote sensing method if not considered. This involves the deconvolution of the recorded x-ray spectrum to identify the presence of multiple potentials and materials. It is suggested to use theoretical x-ray spectra and the principle of superposition to estimate the potential of each individual component from one single measured spectrum. The proposed approach is experimentally tested in a vacuum chamber using a test object that approximates the shape of a spacecraft using a box and panels. The goal of this research thrust is to study the effect of multiple potentials and materials on the x-ray remote sensing method. This work is novel because previous work only considered simple test objects with one potential, such as a single flat plate, as opposed to complex shapes charged to multiple potentials. Additionally, estimating multiple potentials from one recorded spectrum was not attempted in previous work.

The second research thrust focuses on the coupled charging dynamics of the two spacecraft

due to electron beam emission from the target and electron beam impact on the target. The applied remote sensing methods utilize an electron beam that is impacting on the target object and the resulting current can significantly change the potential of the target during the measurement process, which was not considered in previous research. Knowing and understanding the charging dynamics and possible bifurcations is important for the robustness of remote potential sensing filters and active charging control. It is discovered that the electron beam induced current on the target can cause multiple equilibrium potentials to exist for both the servicer and the target. The goal is to investigate the criteria for multiple equilibria to exist, to study what could cause a jump from one equilibrium configuration to another, and to find potential implications and applications. Studying the impact of the electron beam current on the target equilibrium potential in GEO and cislunar space shows that the electron beam can significantly divert the potential from the natural potential of the target, especially in eclipse. This is undesired if one wants to sense the natural potential of a nearby spacecraft. Thus, it is proposed to use a pulsed electron beam instead of a continuous beam. The goal is to investigate the effects of a pulsed beam in GEO and cislunar space and develop pulsing strategies that minimize the impact of the electron beam on the potential of the target. This work is novel because the existence of multiple equilibria in a single-maxwellian plasma was not considered in prior work. Additionally, the effect of the beam current while sensing electric potentials was previously not studied. This will be studied in the proposed work, and the findings will support the development of charge control laws that utilize a pulsed beam.

The third research thrust involves the relative motion of the servicer and target, subject to the electrostatic forces and torques. This is important such that electrostatic forces can be utilized for active debris removal, and to minimize the impact of electrostatic perturbations on servicing operations. It was found that uncertainty in the electric potential of the target can cause the Electrostatic Tractor (ET) relative motion control to bifurcate, which may lead to a collision of the servicer with the target. These bifurcations are studied for complex shaped spacecraft models. The goal is to determine a strategy for choosing the feedback gain that is robust to electric potential estimation errors. Previous research discovered that electrostatic perturbations can cause high

rotational rates of the target spacecraft if the perturbations are not accounted for, and control laws were developed that feed forward on the expected electrostatic forces and torques during the docking phase. As part of this work, the effect of undetected differential charging on the electrostatic forces and torques is investigated. Additionally, a new approach is proposed that aims at staying outside the plasma wake created by the target during the approach phase. This is expected to reduce the electrostatic torque and consequently the rotational rate of the target spacecraft. Finally, inertial frame constrained relative motion is studied. The goal is to find natural relative orbits that obey keep-out zones that are fixed in the inertial frame or velocity frame. Such orbits can be used to approach a charged target spacecraft while staying away from the plasma wake in cislunar space, but can also be used more generally, for example to keep the servicer out of the Sun cast shadow of the target. The proposed work is novel because attitude effects on the ET relative motion were not investigated previously. Prior work on servicing relative motion did not consider the influence of wakes on the relative motion. Finally, inertially constrained relative motion was only studied for a very specific orbit, but not in a general way using an alternative relative motion description.

The goals of this dissertation are summarized as follows:

(1) Touchlessly measure the potentials of differentially-charged objects

   (a) Investigate effect of differential charging on inter-craft electrostatic forces and torques (Chapter 2)

   (b) Experimentally measure the potentials of differentially-charged objects and complex shapes using x-rays (Chapter 3)

(2) Explore the effects of electron beam emission and impact on the electric potentials of nearby spacecraft

   (a) Augment existing spacecraft charging models to account for attitude-dependent currents and allow for better numerical properties (Chapter 2)

   (b) Study the effects of a continuous beam, with a focus on multiple equilibria (Chapter 4)

(c) Study the effects of a pulsed beam, with a focus on potential control strategies (Chapter 5)

(3) Make the relative motion of two charged spacecraft more robust to electrostatic interactions

(a) Investigate the effect of electric potential uncertainty on the Electrostatic Tractor active debris removal method (Chapter 6)

(b) Develop a relative motion description in the inertial frame to better deal with cislunar plasma wakes (Chapter 7)

1.4 Publications

All publications that originated during this Ph.D. work and are related to this dissertation are listed below. Publications whose content does not appear in this dissertation are marked with an asterisk (*) symbol.

1.4.1 Journal Papers

8. **J. Hammerl** and H. Schaub, "Orbiting Spacecraft Relative Motion in the Inertial Frame", *Journal of the Astronautical Sciences*, submitted.

7. **J. Hammerl** and H. Schaub, "Reduced Order Spacecraft Charging Models for Electrostatic Proximity Operations", *IEEE Transactions on Plasma Science*, Vol. 52, No. 11, November 2024, pp. 5402–5413. doi:10.1109/TPS.2024.3503356

6. **J. Hammerl** and H. Schaub, "Coupled Spacecraft Charging Due to Continuous Electron Beam Emission and Impact", *Journal of Spacecraft and Rockets*, Vol. 61, No. 5, September 2024, pp. 1258-1271. doi:10.2514/1.A36010

5. **J. Hammerl**, A. López, Á. Romero Calvo and H. Schaub, "Touchless Potential Sensing of Differentially-Charged Spacecraft Using X-Rays", *Journal of Spacecraft and Rockets*, Vol. 60, No. 2, March–April 2023, pp. 648–658. doi:10.2514/1.A35492

4. * Á. Romero Calvo, **J. Hammerl** and H. Schaub, "Touchless Potential Sensing of Differentially-Charged Spacecraft Using Secondary Electrons", *Journal of Spacecraft and Rockets*, Vol. 59, No. 5, September – October 2022, pp. 1623–1633. doi:10.2514/1.A35355

3. * K. T. Wilson, **J. Hammerl** and H. Schaub, "Using Plasma-Induced X-ray Emission to Estimate Electrostatic Potentials on Nearby Space Objects", *Journal of Spacecraft and Rockets*, Vol. 59, No. 4, July–Aug 2022, pp. 1402–1405. doi:10.2514/1.A35161

2. K. Wilson, Á. Romero Calvo, M. Bengtson, **J. Hammerl**, J. Maxwell and H. Schaub, "Development and Characterization of the ECLIPS Space Environments Simulation Facility", *Acta Astronautica*, Vol. 194, May 2022, pp. 48–58. doi:10.1016/j.actaastro.2021.12.037

1. **J. Hammerl** and H. Schaub, "Effects of Electric Potential Uncertainty on Electrostatic Tractor Relative Motion Control Equilibria", *Journal of Spacecraft and Rockets*, Vol. 59, No. 2, March–April 2022, pp. 552–562. doi:10.2514/1.A35165

1.4.2 Conference Papers

12. **J. Hammerl** and H. Schaub, "Orbiting Spacecraft Relative Motion in the Inertial Frame for Inertially Fixed Constraints", AAS Space Flight Mechanics Meeting, Kauai, HI, January 19–23, 2025.

11. **J. Hammerl** and H. Schaub, "Pulsed Electron Beam For Electric Potential Sensing And Control", Spacecraft Charging and Technology Conference, Avignon, France, June 17–21, 2024.

10. **J. Hammerl** and H. Schaub, "Comparison of Reduced Order Spacecraft Charging Models for Electrostatic Proximity Operations", IEEE Aerospace Conference, Big Sky, MT, March 4–11, 2023.

9. * J. D. Walker, **J. Hammerl** and H. Schaub, "Experimental Validation of Touchless Electric Potential Sensing using a Pulsed Electron Beam", AIAA Science and Technology Forum and Exposition (SciTech), National Harbor, Maryland, January 23–28, 2023.

doi:10.2514/6.2023-1769

8. **J. Hammerl**, A. López and H. Schaub, "Electric Potential Estimation of Inhomogeneous and Differentially Charged Objects Using X-Rays", AIAA Science and Technology Forum and Exposition (SciTech), National Harbor, Maryland, January 23–28, 2023. doi:10.2514/6.2023-1398
7. * J. D. Walker, **J. Hammerl** and H. Schaub, "Design and Analysis for Experimental Validation of Touchless Charge Control Testing", AAS Astrodynamics Specialist Conference, Charlotte, North Carolina, August 7–10 2022. Paper No. AAS 22-661
6. **J. Hammerl**, A. López, Á. Romero Calvo and H. Schaub, "Measuring Multiple Potentials of a Rotating and Differentially-Charged Object Simultaneously Using X-rays" 16th Spacecraft Charging Technology Conference, Virtual, April 4–8, 2022.
5. **J. Hammerl** and H. Schaub, "Uncertainty Analysis of the Electrostatic Tractor Control Performance", AAS Guidance, Navigation and Control Conference, Breckenridge, CO, February 3–9, 2022.
4. **J. Hammerl**, Á. Romero Calvo, A. López and H. Schaub, "Touchless Potential Sensing of Complex Differentially-Charged Shapes Using X-Rays", AIAA SciTech Forum, San Diego, CA, January 3-7, 2022. doi:10.2514/6.2022-2312
3. * Á. Romero Calvo, **J. Hammerl**, H. Schaub, "Touchless Potential Sensing Of Complex Differentially-Charged Shapes Using Secondary Electrons", AIAA SciTech Forum, San Diego, CA, January 3-7, 2022. doi:10.2514/6.2022-2311
2. **J. Hammerl** and H. Schaub, "Debris Attitude Effects on Electrostatic Tractor Relative Motion Control Performance", AAS/AIAA Astrodynamics Specialist Conference, Big Sky, MT, August 8–12, 2021.
1. **J. Hammerl** and H. Schaub, "Effects of Electric Potential Uncertainty on Electrostatic Tractor Relative Motion Control", 8th European Conference on Space Debris, Darmstadt, Germany, April 20–23, 2021.

Chapter 2

Spacecraft charging and electrostatic force modeling

Spacecraft charge due to a multitude of electric currents in the space environment. The ambient plasma in space contains charged particles such as energetic electrons and ions. When these particles impact on the surface of a spacecraft, they transfer their charge to the spacecraft, resulting in what is referred to as the electron and ion plasma currents [18, Chapter 1]. At the same time, the impacting electrons and ions transfer their energy to neighboring electrons in the material. If enough energy is transferred, one or more secondary electrons leave the surface material with low energies of a few electron-volts (eV). This is referred to as secondary electron emission [18, Chapter 3]. It is also possible that an incident electron is backscattered and leaves the surface material again, resulting in backscattered electron emission [18, Chapter 3]. In contrast to the secondary electron emission, the emitted electron is the same as the incident electron, so the probability of generating a backscattered electron cannot exceed unity. In sunlight, the incoming electromagnetic radiation from the Sun excites photoelectrons from the surface of a spacecraft. These electrons are repelled if the spacecraft is charged negatively, leading to a positive photoelectric current [18, Chapter 7]. In addition to these naturally occurring currents, the electron beam that is used for the electric potential sensing methods described in Sec. 1.2.1.1, or for the Electrostatic Tractor debris removal method, imposes an artificial current. This current is negative for the target object due to the collection of negative charge [18, Chapter 9] and positive for the servicing satellite due to the emission of electrons [18, Chapter 10]. The electron beam impacting on the target also generates secondary and backscattered electrons. By computing all currents acting on a spacecraft, the

resulting equilibrium potential and charging transients can be determined.

Knowing the electric potential of two neighboring spacecraft, the charge distribution of the spacecraft is computed and subsequently the inter-spacecraft electrostatic force and torque. If each spacecraft is assumed to be spherical, the computation of the force is straightforward. For complex-shaped spacecraft, methods such as the Method of Moments (MOM) [91–93] or the Multi-Sphere Method (MSM) [94–96] are used to determine the charge distribution, force and torque.

This chapter presents the charging model (Sec. 2.1) and electrostatic force model (Sec. 2.2) used in this work. This is followed by a study of the natural electric potentials that may occur in cislunar space (Sec. 2.3) as well as an investigation on the effect of differential charging on the electrostatic force and torque (Sec. 2.4).

2.1 Spacecraft charging model

A charging model is used based on Ref. 55, but with improvements from Ref. 97 for the electron beam current and Ref. 98 for the faceted model. This model assumes a fully conducting spacecraft as well as orbit-limited attraction of the plasma particles. All charging is assumed to occur on the surface of the spacecraft (surface charging). With the orbit-limited approximation for the plasma currents, the environmental plasma electron and ion flux of a non-spherical shaped spacecraft are assumed to be equal to the fluxes incident on a sphere with the same potential [99]. In other words, the plasma electron and ion currents for a non-spherical spacecraft are assumed to be equal to those for a spherical spacecraft with the same surface area and potential. For orientation-dependent currents, such as the photoelectric current and occasionally the ion current, a faceted model is used to accurately compute the sun-facing area and ram-facing area [98]. A single-Maxwellian plasma distribution is assumed. Moreover, it is assumed that the only coupling between the servicer and the target is due to the electron beam [97]. A highly charged spacecraft perturbs the plasma distribution in its vicinity, which affects the plasma electron and ion current collected by a neighboring spacecraft. Additionally, a positively charged servicer attracts secondary and photoelectrons generated from a negatively (or less positively) charged target, resulting in a

target spacecraft that is charged more positively than one would expect according to the isolated charging model used in this work. Such interactions and effects of the electric fields of the satellites on each other are not considered in this work, but recommended for future work.

2.1.1 Naturally occurring currents

The plasma electron current is modeled as [100, Chapter 4]

$$I_e(\phi) = \begin{cases} -\dfrac{A_p q_0 n_e w_e}{4} e^{\phi/T_e} & \text{if} \quad \phi \leq 0 \\ -\dfrac{A_p q_0 n_e w_e}{4}\left(1 + \frac{\phi}{T_e}\right) & \text{if} \quad \phi > 0 \end{cases} \tag{2.1}$$

where A_p is the surface area of the spacecraft exposed to the plasma, q_0 is the elementary charge, and n_e and T_e are the electron density in units of m^{-3} and electron temperature in units of eV of the plasma, respectively. The (three-dimensional) thermal electron velocity is equal to $w_e = \sqrt{8T_e/(m_e\pi)}$, with electron mass m_e. The equation corresponds to the plasma current for a spherical spacecraft, because it is assumed that the plasma current for a non-spherical spacecraft are equal to those for a spherical spacecraft with the same surface area and potential. For a spherical spacecraft with radius R, the plasma exposed area equals $A_p = 4\pi R^2$. The plasma electron current is negative due to the negative charge of electrons. A negatively charged ($\phi < 0$) spacecraft repels electrons, resulting in a low current, while a positively charged spacecraft results in a high electron current due to the attraction of electrons.

Similarly to the electron current, the plasma ion current is approximated by [100, Chapter 4]:

$$I_i(\phi) = \begin{cases} \dfrac{A_p q_0 n_i w_i}{4}\left(1 - \frac{\phi}{T_i}\right) & \text{if} \quad w_i \geq v_{i,\text{bulk}}, \quad \phi \leq 0 \\ \dfrac{A_p q_0 n_i w_i}{4} e^{-\phi/T_i} & \text{if} \quad w_i \geq v_{i,\text{bulk}}, \quad \phi > 0 \\ A_{\text{ram}} q_0 n_i v_{i,\text{bulk}} & \text{if} \quad w_i < v_{i,\text{bulk}} \end{cases} \tag{2.2}$$

The variables are similar as above, but the subscript i (ions) replaces the subscript e (electrons). Additionally, the mesothermal case is considered when the bulk velocity $v_{i,\text{bulk}}$ of the ions (the average, directional velocity of the ion flow) with respect to the spacecraft is greater than the

thermal velocity w_i of the ions. In this case, the ions only impact on the ram-side of the spacecraft with area A_{ram}, and the resulting current does not depend on the spacecraft potential. The ram-side area A_{ram} is attitude dependent unless the spacecraft is spherical. Thus, in the mesothermal case, the plasma current depends on attitude but not potential. In a mesothermal environment, the ions may be collected from an area that is larger than simply the cross-sectional area when the spacecraft is negatively charged [52, 67]. Particle-in-cell simulations are required to determine this increased ion collection. Such enhancement is not considered here, but recommended for future work that focuses on the effects of spacecraft induced plasma wakes. For a spherical spacecraft $A_{\text{ram}} = R^2\pi$, and otherwise the ram-side area is computed using a faceted model in this work. In LEO, the mesothermal case ($w_i < v_{i,\text{bulk}}$) applies due to the low ion energies (< 1 eV) and high orbital velocities. In GEO, ions are more energetic (order of keV), so the thermal ion velocity dominates ($w_i > v_{i,\text{bulk}}$). In cislunar space, it depends on the location of the Moon, as the Moon can be inside or outside of Earth's magnetosphere and in the solar wind (Sec. 2.3). The charging code implemented for this work automatically compares the ion thermal velocity w_i to a specified ion bulk velocity $v_{i,\text{bulk}}$. It is assumed that the ion species consists of solely hydrogen ions (H^+). Thus, for the thermal ion velocity $w_i = \sqrt{8T_i/(m_i\pi)}$, it is assumed that the ion mass m_i equals the mass of a proton m_p. This is a valid assumption for geostationary orbit, as hydrogen is the dominant ion species in the magnetosphere with relative abundances of about 80% in GEO during low geomagnetic activity [101]. During high solar activity (planetary index $K_p \geq 4$), ionospheric outflow is enhanced, which delivers additional plasma – especially oxygen ions (O^+) – to higher altitudes, resulting in relative H^+ and O^+ abundances in GEO of about 50% each [101]. Depending on the location of the Moon with respect to Earth, the Moon is either inside Earth's magnetosphere (H^+ dominated) or outside in the solar wind. The solar wind primarily consists of about 95% electrons and protons and 4% helium nuclei [102, Chapter 3]. Thus, the assumption that the ion species consists of solely protons is also justified for cislunar space.

The secondary electron and backscattered electron emission current due to plasma electron

impact is calculated by

$$I_{\mathrm{SEE},B,e}(\phi) = \begin{cases} - < Y_{\mathrm{SEE},B,e} > \cdot I_e(\phi) & \text{if} \quad \phi \leq 0 \\ - < Y_{\mathrm{SEE},B,e} > \cdot I_e(\phi) e^{-\phi/T_{\mathrm{SEE}}} & \text{if} \quad \phi > 0 \end{cases} \tag{2.3}$$

and the secondary electron emission due to plasma ion impact is computed as

$$I_{\mathrm{SEE},i}(\phi) = \begin{cases} < Y_{\mathrm{SEE},i} > \cdot I_i(\phi) & \text{if} \quad \phi \leq 0 \\ < Y_{\mathrm{SEE},i} > \cdot I_i(\phi) e^{-\phi/T_{\mathrm{SEE}}} & \text{if} \quad \phi > 0 \end{cases} \tag{2.4}$$

The two cases are needed due to the fact that secondary electrons are emitted with very low energy, so the resulting current drops off quickly with increasing positive spacecraft potential ($T_{\mathrm{SEE}} = 5$ eV in this work) as the negatively charged secondary electrons are attracted back to a positively charged spacecraft. The mean yield over all particle energies $< Y >$ is computed by

$$< Y >= \frac{\int_L^\infty Y(E)\big(E/(E \pm \phi)\big) F(E \pm \phi) \mathrm{d}E}{\int_L^\infty \big(E/(E \pm \phi)\big) F(E \pm \phi) \mathrm{d}E} \tag{2.5}$$

where $Y(E)$ is a placeholder for the corresponding yield: secondary electron yield due to electron impact $Y_{\mathrm{SEE},e}$, backscattered electron yield Y_B, combined electron yield $Y_{\mathrm{SEE},B,e} = Y_{\mathrm{SEE},e} + Y_B$, or secondary electron yield due to ion impact $Y_{\mathrm{SEE},i}$. The energy of the incoming particle is denoted by E, and the particle flux distribution $F(E)$ (for electrons or ions) is given by [99]

$$F(E) = \sqrt{\frac{q_0}{2\pi T m}} \frac{E}{T} n \exp\left(-\frac{E}{T}\right) \tag{2.6}$$

for a Maxwellian plasma with plasma temperature T (measured in eV) and plasma density n. In Eq. (2.5), the positive sign of $\pm$ applies to ions and the negative sign to electrons. The lower bound L of the integral is 0 for the repelled particles (e.g. for electrons if $\phi < 0$) and $|\phi|$ for the attracted particles, and the upper bound is set as 1 MeV in this work. In the mesothermal case of Eq. (2.2), the mean ion induced secondary electron yield is simply $< Y_{\mathrm{SEE},i} >= Y_{\mathrm{SEE},i}(E)$, with $E = \frac{1}{2} m_i v_{i,\mathrm{bulk}}^2$ in units of eV.

The secondary electron and backscattered electron yield $Y_{\mathrm{SEE},B,e}$ is the average number of secondary and backscattered electrons generated per incident electron and is approximated using

the analytical model from Ref. [103]

$$Y_{\mathrm{SEE},B,e}(E) = 4 \cdot Y_{\max} \frac{E/E_{\max}}{(1 + E/E_{\max})^2} \tag{2.7}$$

where E is the landing (effective) energy of the incident electron when it impacts on the surface, $Y_{\max}$ is the maximum electron yield, and $E_{\max}$ is the landing energy at which this maximum occurs.

Note that the electron yield is relatively uncertain as it depends on many factors such as surface material, roughness and level of oxidation, and it changes after prolonged exposure to the space environment [51]. The yield for isotropic flux is assumed to be double the yield for normal incidence [99, 103]. Assuming a spacecraft made of aluminum, values of $Y_{\max} = 0.97$ and $E_{\max} = 300$ eV for normal incidence are used in this work [18, Chapter 3].

Secondary electrons can also be excited by incoming ions. The corresponding yield is modeled by [99]

$$Y_{\mathrm{SEE},i}(E) = \frac{\beta E^{1/2}}{1 + E/E_{\max,i}} \tag{2.8}$$

where E is the energy of the incident ion in keV, $E_{\max,i}$ is the energy of the maximum yield, β is a scaling parameter. Similarly to the electron induced secondary electron emission, the parameters for the electron yield due to incident ions are not well known, and the yield for isotropic flux is assumed to be double the yield for normal incidence [99, 103]. For aluminum, the energy that produces the maximum electron yield is assumed to be $E_{\max,i} = 230$ keV and a yield of $\beta = 0.244$ for 1 keV normally incident protons as extrapolated from data taken at energies greater than 10 keV is used.

The photoelectric current from solar radiation for normal photon incidence is [18, Chapter 7]

$$I_{\mathrm{ph}}(\phi) = \begin{cases} j_{\mathrm{ph},0} A_{\mathrm{ph}} & \text{if} \quad \phi \leq 0 \\ j_{\mathrm{ph},0} A_{\mathrm{ph}} e^{-\phi/T_{\mathrm{ph}}} & \text{if} \quad \phi > 0 \end{cases} \tag{2.9}$$

where A_{ph} is the area of the spacecraft that is in sunlight, and $j_{\mathrm{ph},0}$ and T_{ph} are the flux and temperature of the emitted photoelectrons, respectively. For a spherical spacecraft, $A_{\mathrm{ph}} = R^2\pi$. The flux $j_{\mathrm{ph},0}$ is in the order of 10 $\mu\mathrm{A/m}^2$, but depends on the surface material and can vary with

solar activity by a factor of up to 8 [104]. Similar to the secondary electron emission, photoelectrons are released with very low energy, requiring an equation with exponential drop-off for positive potentials. In this work, values of $j_{\mathrm{ph},0} = 20$ µA/m^2 and $T_{\mathrm{ph}} = 2$ eV are used [55]. Similar to the ram-side area, the sunlit area is also attitude dependent unless the spacecraft is spherical.

2.1.2 Electron beam induced currents

The electron beam current is modeled as

$$I_{EB,T}(\phi_T, \phi_S) = \begin{cases} -\alpha I_{EB}(1 - e^{-(E_{EB}-\phi_S+\phi_T)/T_{EB}}) & \text{if} \quad E_{EB} > \phi_S - \phi_T \\ 0 & \text{if} \quad E_{EB} \leq \phi_S - \phi_T \end{cases} \tag{2.10}$$

for the target spacecraft, where I_{EB} and E_{EB} are the electron gun current and operating energy (i.e. the kinetic energy of the electrons as they exit the electron gun), and ϕ_T and ϕ_S denote the electric potential of the target and the servicer, respectively. When the electron comes from an electron beam emitted from a servicer, rather than from the ambient plasma environment, the landing energy is computed as

$$E = E_{EB} - \phi_S + \phi_T \tag{2.11}$$

Due to the deflection and expansion of the electron beam [105], only a fraction α of the electrons emitted from the gun might reach the target. For simplicity, however, $\alpha = 1$ is assumed in this work. The electron beam electrons can only reach the target if the beam energy E_{EB} is greater than the electric potential difference between the two craft, $\phi_S - \phi_T$. That is, the landing energy of the electron beam electrons must be greater than zero, $E > 0$. Otherwise, the electrons do not reach the target and the net current due to the electron beam is approximately zero. In contrast to prior work [55, 56, 64], where the beam current is modeled as being equal to $-\alpha I_{EB}$ if $E_{EB} > \phi_S - \phi_T$ and zero if $E_{EB} \leq \phi_S - \phi_T$, an exponential drop-off is used here with $T_{EB} = 20$ eV. This removes the discontinuity at $E_{EB} = \phi_S - \phi_T$, which benefits numerical root finding of the equilibrium potential and the propagation of the charging dynamics with numerical methods [97].

The combined secondary and backscattered electron current emitted from the target object

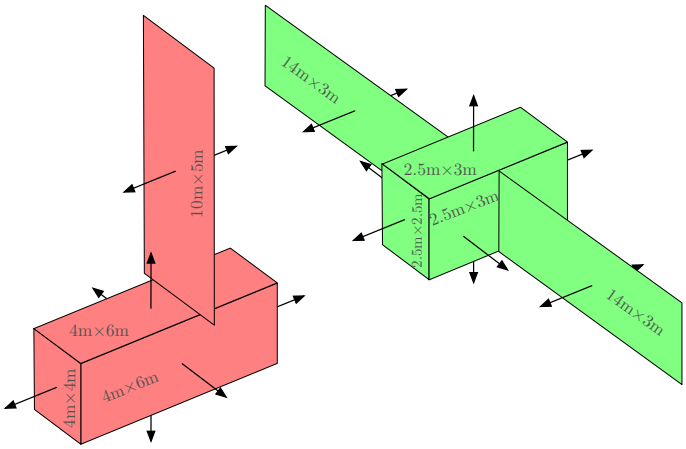

Figure 2.1: Faceted Spacecraft Model

due to the electron beam impact is equal to

$$I_{\mathrm{SEE},B,eb}(\phi_T,\phi_S) = \begin{cases} -Y_{\mathrm{SEE},B}(E)\cdot I_{EB,T} & \text{if} \quad \phi_T < 0 \\ -Y_{\mathrm{SEE},B}(E)\cdot I_{EB,T} e^{-\phi/T_{\mathrm{SEE}}} & \text{if} \quad \phi_T \geq 0 \end{cases} \tag{2.12}$$

where Eq. (2.11) is used to determine the energy E.

Similarly to the electron beam current on the target, the electron beam current on the servicer is modeled as

$$I_{EB,S}(\phi_T,\phi_S) = \begin{cases} I_{EB}(1-e^{-(E_{EB}-\phi_S+\phi_T)/T_{EB}}) & \text{if} \quad E_{EB} > \phi_S - \phi_T \\ 0 & \text{if} \quad E_{EB} \leq \phi_S - \phi_T \end{cases} \tag{2.13}$$

2.1.3 Faceted charging model

A faceted charging model is implemented to compute the projected sunlit area and ram-side area of the spacecraft, neglecting self-shadowing [98]. Self-shadowing refers to shadowing of components by other components of the individual spacecraft. In terms of one spacecraft shadowing the other, it is assumed that if that is the case, the entire shadowed spacecraft is in eclipse. Shadowing of part of a spacecraft by the other spacecraft is not considered. The spacecraft is divided into n facets with area A_i and normal vector $\hat{\boldsymbol{n}}_i$ of the i-th facet. The projected sunlit area

of the i-th facet is equal to

$$A_{\mathrm{ph},i} = \begin{cases} A_i \cos\theta_{s,i} = A_i \frac{\hat{\boldsymbol{s}}\cdot\hat{\boldsymbol{n}}_i}{|\hat{\boldsymbol{s}}|\cdot|\hat{\boldsymbol{n}}_i|} & \text{if} \quad \hat{\boldsymbol{s}}\cdot\hat{\boldsymbol{n}}_i > 0 \\ 0 & \text{if} \quad \hat{\boldsymbol{s}}\cdot\hat{\boldsymbol{n}}_i \leq 0 \end{cases} \tag{2.14}$$

where $\theta_{s,i}$ is the angle between the sun direction $\hat{\boldsymbol{s}}$ and the normal to the surface $\hat{\boldsymbol{n}}_i$. If the dot product $\hat{\boldsymbol{s}}\cdot\hat{\boldsymbol{n}}_i$ is negative, the area is facing away from the sun, so the sunlit area for that facet is set equal to 0. The total projected area of the spacecraft that is facing the sun is then

$$A_{\mathrm{ph}} = \sum_{i=1}^{n} A_{\mathrm{ph},i} \tag{2.15}$$

Similarly, the projected ram-side area of the i-th facet is equal to

$$A_{\mathrm{ram},i} = \begin{cases} A_i \cos\theta_{v,i} = A_i \frac{\hat{\boldsymbol{v}}_r\cdot\hat{\boldsymbol{n}}_i}{|\hat{\boldsymbol{v}}_r|\cdot|\hat{\boldsymbol{n}}_i|} & \text{if} \quad \hat{\boldsymbol{v}}_r\cdot\hat{\boldsymbol{n}}_i > 0 \\ 0 & \text{if} \quad \hat{\boldsymbol{v}}_r\cdot\hat{\boldsymbol{n}}_i \leq 0 \end{cases} \tag{2.16}$$

where $\theta_{v,i}$ is the angle between the spacecraft direction of motion with respect to the ion flow

$$\hat{\boldsymbol{v}}_r = \frac{\boldsymbol{v}_{S/C} - \boldsymbol{v}_{\mathrm{bulk}}}{|\boldsymbol{v}_{S/C} - \boldsymbol{v}_{\mathrm{bulk}}|} \tag{2.17}$$

with the spacecraft velocity $\boldsymbol{v}_{S/C}$ and the ion bulk velocity $\boldsymbol{v}_{bulk}$ (the direction of the ion flow). If the dot product $\hat{\boldsymbol{v}}_r\cdot\hat{\boldsymbol{n}}_i$ is negative, the area is facing away from the ion flow so the ram-side area for that facet is set equal to 0. The total projected ram-side area of the spacecraft is then

$$A_{\mathrm{ram}} = \sum_{i=1}^{n} A_{\mathrm{ram},i} \tag{2.18}$$

Figure 2.1 shows the faceted models for the GOES-R and SSL-1300 spacecraft used in this work, including the dimensions and normal vectors or the facets.

2.1.4 Equilibrium potentials and charging dynamics

Using all the above currents, the total current is

$$\begin{aligned} I_{\mathrm{tot},S}(\phi_T, \phi_S) = I_e(\phi_S) + I_i(\phi_S) + I_{\mathrm{ph}}(\phi_S) + I_{\mathrm{SEE},B,e}(\phi_S) + I_{\mathrm{SEE},i}(\phi_S) \\ + I_{EB,S}(\phi_T, \phi_S) \end{aligned} \tag{2.19}$$

for the servicing satellite and

$$I_{\text{tot},T}(\phi_T, \phi_S) = I_e(\phi_T) + I_i(\phi_T) + I_{\text{ph}}(\phi_T) + I_{\text{SEE},B,e}(\phi_T) + I_{\text{SEE},i}(\phi_T) + I_{EB,T}(\phi_T, \phi_S) + I_{\text{SEE},B,eb}(\phi_T, \phi_S) \tag{2.20}$$

for the target spacecraft.

To achieve an equilibrium potential, the total current on each spacecraft must be zero. Thus, the equilibrium potential of the spacecraft is found by setting Eqs. (2.19) and (2.20) equal to zero. No analytical solution exists, so this is solved numerically. In this work, the potential of the servicer is computed first. Knowing the servicer potential, the potential of the target is then determined by finding the root of Eq. (2.20). The natural potential of a spacecraft is found by setting the electron beam current equal to zero, $I_{EB} = 0$ µA.

Note that the electron beam current depends on the potential of both the target and the servicer. As mentioned above, for two-craft formations, the servicer potential is computed before the target potential within this work. When the servicer potential is computed, knowledge of the target potential is required to determine whether or not the beam is coming back to the servicer, resulting in a net zero electron beam current on the servicer. However, because the target potential is unknown at this point, the assumption is made that only the servicer potential determines whether or not the beam is coming back to the servicer. That is, it is assumed that $\phi_T = 0$ when computing the servicer equilibrium potential. This assumption is discussed and justified in Sec. 2.1.5.

The electric potential is propagated over time using the differential equations

$$\dot{\phi}_S = \frac{1}{C_S} \cdot I_{\text{tot},S}(\phi_T, \phi_S) \tag{2.21a}$$

$$\dot{\phi}_T = \frac{1}{C_T} \cdot I_{\text{tot},T}(\phi_T, \phi_S) \tag{2.21b}$$

where C is the capacitance of the spacecraft and is equal to $C = 4\pi\epsilon_0 R$ for a spherical spacecraft with radius R, with ϵ_0 being the vacuum permittivity. For propagations over time, the potential of the target is known from the previous time step, so the $\phi_T = 0$ assumption is not used when

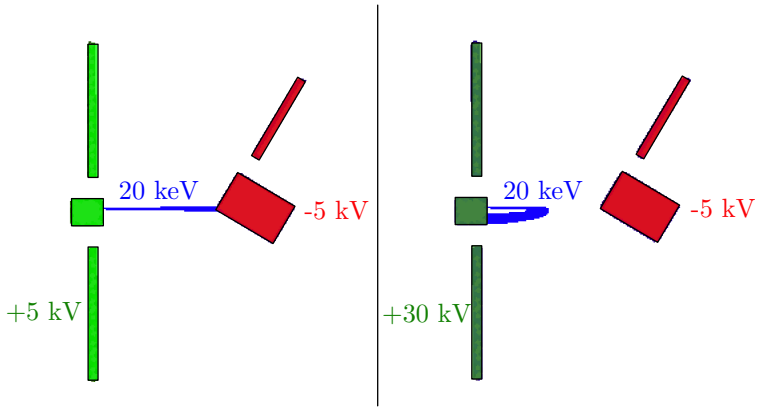

Figure 2.2: SIMION Simulation

computing the servicer currents. That is, the total current on the servicer and target are computed simultaneously for dynamic simulations, as opposed to sequentially (first for the servicer and then for the target) for the determination of equilibrium potentials.

2.1.5 Justification of electron beam assumptions

In Eq. (2.13), it is assumed that the presence of a charged target spacecraft does not affect whether or not the electron beam comes back to the servicing spacecraft. The benefit of this assumption is that the equilibrium electric potentials of the servicer and target can be computed sequentially by finding the root of Eq. (2.19), and then the root of Eq. (2.20). Alternatively, without this assumption, the equilibrium potentials could be computed either simultaneously by solving a bivariate root-finding problem for ϕ_S and ϕ_T, or by repeatedly finding the equilibrium potentials sequentially in a loop and using the knowledge of one potential to find the other until both solutions have converged. Both of these approaches come with increased complexity and computational effort. Because the charging model used in this work is approximate and to be used for the rapid computation of electric potentials, forces and torques, it is desired to keep computational effort low, as long as the assumptions are valid.

To validate the assumption, several simulations are performed with the particle tracing simu-

lation framework SIMION [1] . SIMION computes the electrostatic field by solving Laplace's equation and then propagates the particle trajectories using Newton's second law. The SIMION model does not account for space-charge effects, so the expansion of the electron beam and the effect of the electron beam on the electric field are not considered. Reference [105] shows that the trajectory of the beam center depends only very weakly on beam expansion. Because the main purpose of the SIMION model in this work is to simulate the beam landing area, the implemented model is considered sufficiently accurate, and computationally more expensive models such as particle-in-cell (PIC) are not considered.

A total number of 5292 SIMION simulations are run with electron beam energies of $E_{EB} = 10, 20, 30$ keV, target potentials ϕ_T between -30 and 0 kV with steps of 5 kV, servicer potentials ϕ_S between 0 and 30 kV with steps of 5 kV, separation distances of $15, 20, 30$ m and 12 different target orientations. The number of beam electrons that hit the target and servicer are recorded. The SIMION simulation setup is shown in Fig. 2.2. On the left, the entire beam hits the target for a beam energy of $E_{EB} = 20$ keV, target potential $\phi_T = -5$ kV, servicer potential $\phi_S = 5$ kV, separation distance of 15 m and target angle of 120 degrees. On the right, the entire beam comes back to the servicer for a target potential $\phi_T = -5$ kV, servicer potential $\phi_S = 30$ kV, and the remaining parameters being the same as on the left.

Figure 2.3 shows the percentage of the beam electrons that come back and hit the servicer as a function of target and servicer potential, for a beam energy of $E_{EB} = 20$ keV. In the figure, the average percent of servicer hits across all separation distances and target orientations is shown. The solid red line represents $\phi_S = \phi_T + E_{EB}$. For points below this line, the electron beam is energetic enough to reach the target, see Eq. (2.10). Note that, depending on the initial direction of the beam, the beam can come back to the servicer despite being energetic enough to reach the target. However, because the beam is aimed at the target in the simulations, the entire beam should hit the target, and no beam electrons are expected to hit the servicer. For points above the solid red line, the beam is not energetic enough to reach the target. When the potential of the servicer ϕ_S

[1] https://simion.com (Consulted on: 05/23/2025)

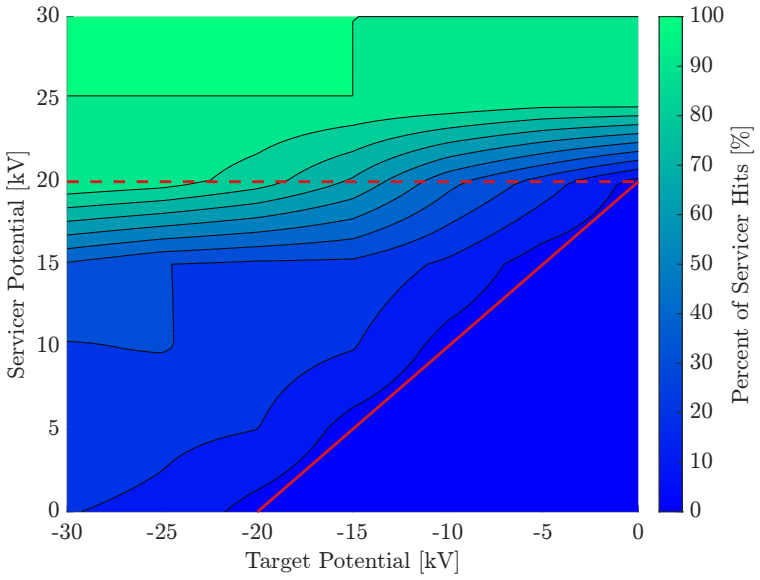

Figure 2.3: Percentage of electron beam that hits the servicer for a beam energy of 20 keV. Solid red line: $\phi_S = \phi_T + E_{EB}$. Dashed red line: $\phi_S = E_{EB}$

is computed, the potential of the target ϕ_T is undetermined, so this line is also unknown.

The dashed red line represents $\phi_S = E_{EB}$. This line is known when the potential of the servicer is computed. In Eq. (2.13), it is assumed that only the servicer potential influences whether or not the beam comes back to the servicer. If $\phi_S < E_{EB}$, the entire beam is assumed to leave the servicer, and if $\phi_S \geq E_{EB}$, the entire beam is assumed to come back to the servicer, resulting in a net zero current due to the electron beam. For this assumption to hold, the percentage of servicer hits in Fig. 2.3 must be 100% above the dashed red line and 0% below this line. As can be seen in the figure, this is true for most potential combinations. The percentage of servicer hits is close to 0% below the dashed red line and close to 100% above it. The main discrepancy occurs at the edge case $\phi_S = E_{EB}$. Given that the average percentage of servicer hits is close to the expected value, the assumption in Eq. (2.13) is considered justified.

2.2 Multi-sphere method for electrostatic force and torque approximation

Having computed the electric potential according to Sec. 2.1, the charge distribution and consequently the electrostatic force and torque between two spacecraft can be determined.

The electrostatic potential ϕ of an isolated object in vacuum is related to the charge q by

$$\phi = \frac{q}{C} \tag{2.22}$$

where C is the object's capacitance. If another object is in proximity, the charge on both objects changes due to mutual capacitance effects. For two spheres with radii R_1, R_2, potentials ϕ_1, ϕ_2, charges q_1, q_2, and separation distance L, the voltage to charge relationship changes to [106]:

$$\begin{bmatrix} \phi_1 \\ \phi_2 \end{bmatrix} = k_c \begin{bmatrix} 1/R_1 & 1/L \\ 1/L & 1/R_2 \end{bmatrix} \begin{bmatrix} q_1 \\ q_2 \end{bmatrix} \tag{2.23}$$

If the potentials on both spheres are constant, Eq. (2.23) is inverted to obtain the charges of the spheres. Knowing the charges q_1 and q_2, the electrostatic force between the two spheres is computed with Coulomb's law

$$F = k_c \frac{q_1 q_2}{r^2} \tag{2.24}$$

where $k_c = 8.988 \times 10^9$ N m^2 / C^2 is the Coulomb constant. However, general 3D geometries of a spacecraft and the resulting charge distribution cannot be modeled accurately with a single sphere. Additionally, single sphere models are unable to account for torques that result from two spacecraft with complex shapes. The Multi-Sphere Method (MSM) uses a number of spheres to represent general spacecraft geometries and to approximate the charge distribution of the objects [94, 96]. Knowing the charge on each sphere, the forces and torques between multiple bodies are computed accurately and faster-than-realtime. For multiple spheres, the voltage to charge relationship is

$$\begin{bmatrix} \phi_1 \\ \phi_2 \\ \vdots \\ \phi_n \end{bmatrix} = k_c \begin{bmatrix} 1/R_1 & 1/r_{1,2} & \cdots & 1/r_{1,n} \\ 1/r_{2,1} & 1/R_2 & \cdots & 1/r_{2,n} \\ \vdots & \vdots & \ddots & \vdots \\ 1/r_{n,1} & 1/r_{n,2} & \cdots & 1/R_n \end{bmatrix} \begin{bmatrix} q_1 \\ q_2 \\ \vdots \\ q_n \end{bmatrix} \tag{2.25}$$

or

$$\boldsymbol{\Phi} = [S]\boldsymbol{Q} \tag{2.26}$$

with the potential of the i-th sphere ϕ_i, charge q_i, sphere radius R_i, the vector $\boldsymbol{r}_{i,j}$ from the j-th to the i-th sphere, $r_{i,j} = |\boldsymbol{r}_{i,j}|$, and the elastance matrix $[S]$. Knowing the potentials ϕ_i, Eq. (2.25)

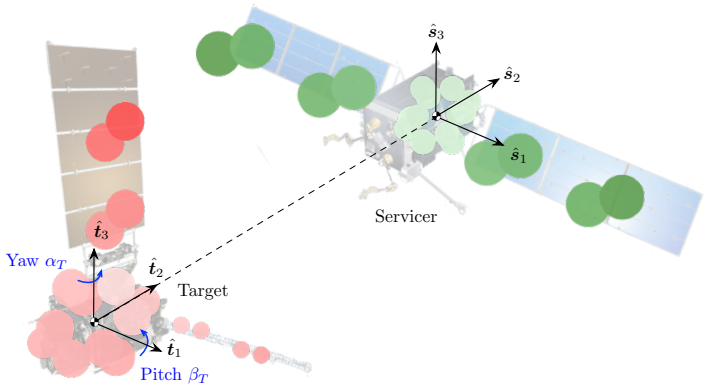

Figure 2.4: Multi-Sphere Spacecraft Models. Target spacecraft on the left, servicing spacecraft on the right

is inverted to obtain the charge of each sphere. For two charged bodies that consist of multiple spheres, Eq. (2.25) has the form

$$\begin{bmatrix} \boldsymbol{\Phi}_1 \\ \boldsymbol{\Phi}_2 \end{bmatrix} = \begin{bmatrix} S_1 & S_M \\ S_M^T & S_2 \end{bmatrix} \begin{bmatrix} \boldsymbol{Q}_1 \\ \boldsymbol{Q}_2 \end{bmatrix} \tag{2.27}$$

where S_M is the mutual capacitance block of the elastance matrix, which changes with the relative position of the two bodies. The diagonal blocks S_1 and S_2 remain constant and do not have to be updated for rigid bodies [25, 107]. Once the charge of each sphere is obtained, the resulting force and torque about point 0 acting on body 1 are computed using

$$\boldsymbol{F}_1 = -k_c \sum_{j=1}^{n_1} \boldsymbol{Q}_{1_j} \left(\sum_{i=1}^{n_2} \frac{\boldsymbol{Q}_{2_i}}{r_{i,j}^3} \boldsymbol{r}_{i,j} \right) \tag{2.28}$$

and

$$\boldsymbol{L}_{1,0} = -k_c \sum_{j=1}^{n_1} \boldsymbol{r}_j \times \boldsymbol{Q}_{1_j} \left(\sum_{i=1}^{n_2} \frac{\boldsymbol{Q}_{2_i}}{r_{i,j}^3} \boldsymbol{r}_{i,j} \right) \tag{2.29}$$

where $\boldsymbol{r}_j$ is the vector from point 0 to the j-th sphere.

An example MSM model used in this work is shown in Fig. 2.4. The target is based on the GOES-R satellite and is interesting due to its asymmetric shape, while the servicer is based on an SSL-1300 satellite bus. The GOES-R bus is modeled as a 4 × 4 × 6 m cuboid, the solar panel has dimensions of 5 × 10 m, and the magnetometer is about 10 m long. The servicing satellite on

Table 2.1: Cislunar plasma parameters (taken from DSNE)

Region	n_e [m^{-3}]	T_e [eV]	$v_{i,\text{bulk}}$ [km/s]	n_i [m^{-3}]	T_i [eV]
Magnetotail Lobes >100 km	6.2E+04	980	650	8.9E+04	3400
Plasma Sheet >100 km	5.0E+04	3700	1100	6.9E+04	4800
Magnetosheath Dayside >100 km	7.6E+04	1400	930	9.9E+04	3000
Magnetosheath Wake 100 km - 2000 km	4.3E+04	840	660	5.0E+04	3600
Magnetosheath Wake 2000 km - 12000 km	6.6E+04	920	770	9.2E+04	2900
Magnetosheath Wake >12000 km	7.7E+04	710	820	1.3E+05	1800
Solar Wind Dayside >100 km	6.6E+07	126	730	7.0E+07	121
Solar Wind Wake 100 km - 500 km	2.3E+04	430	720	3.6E+04	2300
Solar Wind Wake 500 km - 2000 km	5.0E+04	350	770	6.5E+04	2500
Solar Wind Wake 2000 km - 12000 km	3.5E+04	220	770	4.8E+04	2100
Solar Wind Wake >12000 km	1.5E+06	64	790	1.4E+06	800

the right is based on a 2.5 × 2.5 × 3 m SSL-1300 satellite bus with two 3 × 14 m solar panels. Figure 2.4 also shows the body frame of the target $\mathcal{T} : \{\hat{\boldsymbol{t}}_1, \hat{\boldsymbol{t}}_2, \hat{\boldsymbol{t}}_3\}$ and the servicer $\mathcal{S} : \{\hat{\boldsymbol{s}}_1, \hat{\boldsymbol{s}}_2, \hat{\boldsymbol{s}}_3\}$ in their nominal orientation. A 3-2-1 Euler rotation sequence with yaw angle α_T and pitch angle β_T is used to describe the orientation of the target. A roll rotation about the $\hat{\boldsymbol{t}}_2$ axis is assumed not to provide any additional insight, because the important orientations such as the solar panel facing (or not facing) the Sun as well as the solar panel pointing (or not pointing) at the servicer are covered using only yaw and pitch. Thus, the rotation about this axis is always set to zero to improve the visualization of the results by using only two rotation angles. The orientation shown in the figure has both frames aligned with the Hill frame. For any rotation of either spacecraft, the Hill frame is used as reference.

2.3 Cislunar space study of natural electric potentials

A qualitative study of the natural potentials in cislunar space is presented here using the charging model from Sec. 2.1. This allows for an identification of the cislunar regions where high electrostatic perturbations are most likely to occur.

Due to the low GEO orbital speed of the spacecraft and high ion temperatures, the ion thermal speed is greater than the ion bulk speed, and consequently the plasma ion current is assumed to

be independent of the spacecraft attitude and speed in GEO. In LEO, the ion bulk speed in the spacecraft reference frame is greater than the ion thermal speed, so charging does depend on the spacecraft orientation. However, due to electrostatic shielding and low electrostatic potentials, inter-craft electrostatic forces and torques are much smaller in LEO [28, 108]. In lunar orbit, the plasma temperatures as well as the ion bulk speed depend on the location of the Moon with respect to the magnetic field of the Earth. Four regimes are defined for spacecraft charging in cislunar space, as described in the NASA Design Specification For Natural Environments (DSNE) [109]: plasma sheet, magnetotail lobes, magnetosheath and solar wind. Depending on space weather and the regime that the spacecraft is located in, the ion bulk speed may be greater than the ion thermal speed, and consequently ram-side ion collection may apply. The electron and ion density and temperature as well as ion bulk speed are provided in DSNE for each regime. In the plasma sheet and magnetotail lobes regimes, the plasma properties are assumed to be the same for all altitudes above the Moon and regardless of whether the spacecraft is on the sun-facing or eclipsed side of the Moon. In the magnetosheath and solar wind regimes, the plasma properties are provided individually for various altitude regions. Additionally, a plasma wake exists in these regimes on the downwind side of the Moon due to the obstruction of the solar wind flow [110–112]. Thus, another differentiation for the plasma parameters is made in these regimes depending on whether the spacecraft is on the sun-facing (day-side) or eclipsed side (wake-side or night-side) of the Moon. The mean and max of the plasma parameters are provided in DSNE, and the max is used here to represent a high-charging environment. The cislunar plasma parameters used in this work are summarized in Tab. 2.1.

Using the plasma data from DSNE and the faceted spacecraft model from Sec. 2.1, the natural potentials are computed for the target for several spacecraft orientations with the given charging model and shown in Fig. 2.5. The minimum, maximum and average equilibrium potential across all orientations is recorded. Due to the high electron temperatures, the average natural equilibrium potential obtained for the plasma sheet is -7.64 kV. The range of potentials, depending on the spacecraft orientation, is between about -10.5 kV and -6 kV. If the target $\hat{\boldsymbol{t}}_2$ is perpendicular to

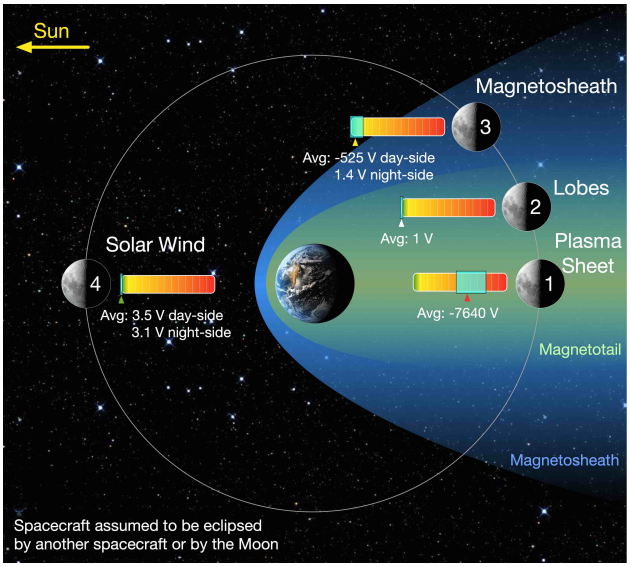

Figure 2.5: Natural potentials in cislunar space for an eclipsed spacecraft, obtained using a faceted model of the target. The teal area indicates the range of equilibrium potentials, depending on the spacecraft orientation. The average equilibrium potential across all orientations is also indicated.

the ion flow, the ram-side area is the smallest, and consequently the equilibrium potential is the most negative due to the reduced plasma ion current. The potential of -6 kV is obtained when the target $\hat{\boldsymbol{t}}_2$ is facing the same way as the ion flow, as this results in the maximum ram-side area for the given faceted model. In the magnetotail lobes, the ion thermal speed is greater than the ion bulk speed, so ram-side charging does not apply. The electron temperature is too low for the onset of charging, so the equilibrium potential is about 1 V positive for all orientations. In the magnetosheath regime, ram-side charging applies on the day-side and in the higher altitudes of the night-side, resulting in equilibrium potentials between -1.5 kV and 0 kV and an average of about -0.5 kV on the day-side. No significant charging occurs on the night side due to a lower electron temperature. Similarly, in the solar wind regime, ram-side charging applies on the day-side and in the higher altitudes of the night-side. Because the electron temperature here is low across all altitudes and on both sides of the Moon, the obtained equilibrium potentials are just slightly positive both on the day and night side.

Although more detailed spacecraft models and higher order charging models are needed to estimate the possible charging levels of mission specific satellites, the reduced order charging model

used here provides a qualitative study. Moreover, differential charging may lead to potential wells and barriers [18, Chapter 6], in which case the entire spacecraft may charge to much higher levels than determined by the current balance from Sec. 2.1. Thus, much higher potentials than the potentials here should be accounted for. In terms of electrostatic OSAM operations, the electrostatic perturbations resulting from spacecraft charging are considered to be the most concerning in the plasma sheet and the magnetosheath. The magnetosheath is especially interesting because both high electric potentials as well as plasma wakes are possible in this region.

2.4 Effect of differential charging on electrostatic force and torque

One aspect of spacecraft charging that has not been considered in prior work on electrostatic proximity operations and charged astrodynamics is differential charging, that is, when some components charge to different potentials than others. Differential charging affects the inter-spacecraft electrostatic force and torque and may affect the electric potential sensing methods. The effect of differential charging on the electrostatic force and torque is investigated here using the Multi-Sphere Method from Sec. 2.2.

To study the electrostatic forces for differentially charged spacecraft, various potentials are prescribed to the bus and panel of the target as well as the servicer. The levels of the prescribed potentials are similar to the natural potentials obtained in Sec. 2.3 for the cislunar regions. The resulting force and torque are then computed as a function of the target orientation, as shown in Figs. 2.6 and 2.8. Assuming a fully conducting servicer, several conditions are considered according to the following representation key:

- solid surface: servicer in sunlight (potential of approximately 0 kV)
- gridded surface: servicer in eclipse (potential of approximately -5 kV)
- black surface: target is fully conducting in eclipse (potential of approximately -5 kV)
- red surface: Target bus at 0 kV (B:0) and target panel at -5 kV (P:-5)

- blue surface: Target bus at -5 kV (B:-5) and target panel at 0 kV (P:0)

A yellow surface is added to highlight the zero-crossing of the force or torque. In differential charging cases, the magnetometer of the target is always assumed to be at 0 V.

Possible reasons for these differential charging scenarios include varying material properties of the non-conducting spacecraft components as well as differences in the exposure to sunlight. For example, consider a spacecraft with a potential of -5 kV (Sec. 2.3). If some component is electrically not connected to the rest of the spacecraft and made of a surface material with a higher secondary electron yield, then that component charges less negatively or possibly even only a few volts positive due to the increased emission of negatively charged secondary electrons. On the other hand, a partially eclipsed spacecraft may also differentially charge. Spacecraft in sunlight usually charge a few volts positive. If some electrically not-connected component is entirely on the shadowed side of the spacecraft, then it charges more negatively due to the missing photoelectric current [113, 114]. For more information, see Chapters 6 and 7 of Ref. 18.

First, the electrostatic force is investigated in Fig. 2.6. Instead of simply plotting the (unsigned) magnitude of the force, the signed force magnitude is plotted to indicate whether the force is attracting or repelling the two spacecraft. The sign ("polarity") p_F of the force is determined by looking at the component of the force along the direction from one spacecraft center to the other

$$p_F = \text{sign}(\boldsymbol{F}_{c,T} \cdot \boldsymbol{r}_{TS}) \tag{2.30}$$

where $\boldsymbol{F}_{c,T}$ is the electrostatic force acting on the target and $\boldsymbol{r}_{TS}$ is the vector from the servicer center to the target center. A positive force corresponds to the repelling case while a negative force corresponds to the attractive case.

If the servicer is in sunlight and the target is eclipsed (i.e. the servicer eclipses the target), the force is attractive (negative), and relatively small in magnitude for most target orientations because the servicer potential is approximately 0 kV. For those orientations where the target solar panel is pointed at the servicer, however, the force reaches a maximum magnitude of about 0.3 mN due to the small distance between the panel and the center of the servicer. If both spacecraft

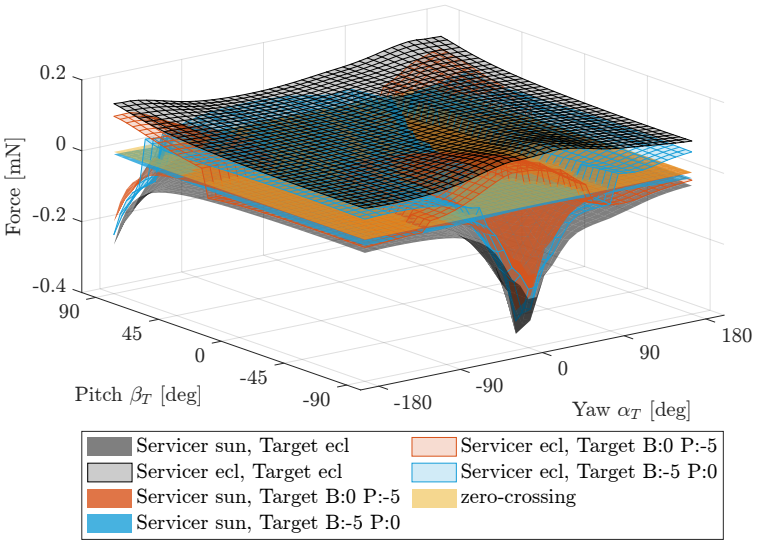

Figure 2.6: Electrostatic force as function of target orientation for differentially charged target

are eclipsed (for example, both spacecraft are behind the Moon), the force is repelling (positive). Although the force magnitude is also greater for orientations where the target panel comes closer to the servicer, the differences are not as significant as in the attractive case.

For the case where the servicer is in sunlight and the target is differentially charged, as shown by the solid red and blue surfaces in Fig. 2.6, the force magnitude is decreased with respect to the non-differentially charged baseline scenario for a sunlit servicer (solid black surface). If the target bus is at 0 kV and the panel at −5 kV, the force dependency on attitude is qualitatively similar to the fully conducting target case. In contrast, if the bus is charged to −5 kV and the panel to 0 kV, there is barely any attitude dependence. This is because the panel – which is primarily responsible for the attitude effects – and the servicer are both at a potential of 0 kV, resulting in forces that are negligible compared to those between the servicer and the target bus. The attitude of the bus of the target, however, does not affect the electrostatic force as much.

The case where the servicer is eclipsed and the target is differentially charged is more interesting, represented by the gridded red and blue surfaces in Fig. 2.6. Regardless of which part of the target is at 0 kV or −5 kV, the polarity of the force becomes dependent on the orientation of the target. If the bus is at 0 kV and the panel at −5 kV, the force is repelling when the panel

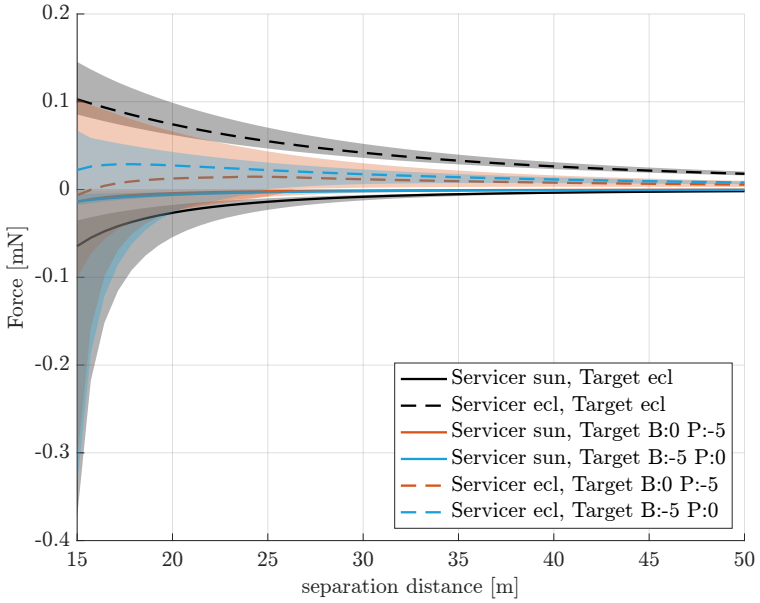

Figure 2.7: Differential charging effects over various separation distances. The shaded regions represent the range of forces for all target orientations, while the lines themselves indicate the average force across all orientations.

is directed at the servicer, similar to the scenario with an eclipsed servicer and fully conducting target, but attractive for some other orientations. If the bus is at -5 kV and the panel at 0 kV, the force is attractive when the panel is directed at the servicer, similar to the scenario with a sunlit servicer and fully conducting target, but repelling for most other orientations. This case is especially intriguing because the force magnitude is relatively large when the panel is pointing toward the servicer, but the force is of different polarity and actually more similar to the case of a sunlit servicer than the case of an eclipsed servicer (which is considered to be the baseline here). It should be noted again that the "polarity" of the force is simply determined looking at the force component that lies in the direction from one spacecraft center to the other. Thus, a switch in polarity of the force only implies that this specific component of the force switches sign, while the other components may be unaffected.

Figure 2.7 shows how the attitude effects decrease with increasing separation distance between the two spacecraft. The color scheme is the same as before, but here a solid line represents a sunlit servicer and a dashed line represents an eclipsed servicer. The shaded regions include the forces for

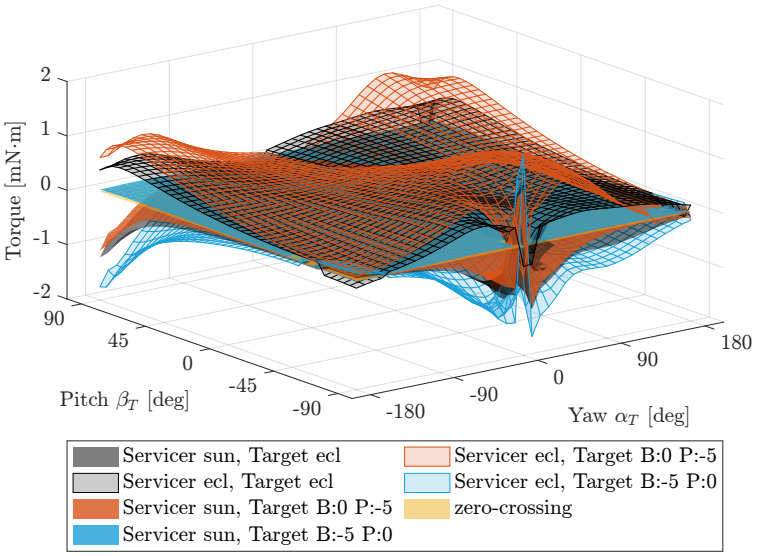

Figure 2.8: Electrostatic torque on the target as function of target orientation for differentially charged target

all target orientations, and the lines themselves indicate the average force across all orientations for a given separation distance. At close separations, the attitude effects are relatively high, and the polarity of the force may switch between one orientation and another. Starting at about 25 meters for the given spacecraft models and electric potentials, the polarity is the same for all orientations of one charging configuration. That is, the force polarity is not attitude dependent for distances greater than about 25 m, and the target appears as fully conducting from a force perspective. This implies that the polarity of the force for a differentially charged spacecraft is also dependent on the separation distance. Increasing the separation distance even more causes the shaded regions to almost vanish. At those separations, the attitude dependence on the force is negligible and the target appears as a fully conducting sphere from a force perspective.

Similarly to the force, the electrostatic torque acting on the target is plotted in Fig. 2.8 for several charging cases as a function of the target orientation. To determine the sign (polarity) of the torque, a reference point is chosen on the target to compute the equivalent force acting on that point to generate that torque. This reference point is chosen to be approximately at the far end of the solar panel of the target, ${}^{\mathcal{T}}\boldsymbol{r}_{PT} = [0, 0, 10]^T$ m, where the left superscript indicates that this

vector is described in the target frame $\mathcal{T} : \{\hat{\boldsymbol{t}}_1, \hat{\boldsymbol{t}}_2, \hat{\boldsymbol{t}}_3\}$. The sign p_L of the torque is determined by looking at the component of the equivalent force acting on the reference point along the direction from one spacecraft center to the other

$$p_L = \text{sign}((\boldsymbol{L}_{c,T} \times \boldsymbol{r}_{PT}) \cdot \boldsymbol{r}_{TS}) \tag{2.31}$$

where $\boldsymbol{L}_{c,T}$ is the electrostatic torque acting on the target center of mass. A positive torque corresponds to the repelling case where the torque is pushing the panel of the target away from the servicer while a negative torque corresponds to the attractive case where the torque is pulling the panel of the target toward the servicer. The torque on the target lies mostly in the $\hat{\boldsymbol{t}}_1$ - $\hat{\boldsymbol{t}}_2$ plane of the target frame, because the panel of the given target spacecraft provides little torque leverage around $\hat{\boldsymbol{t}}_3$.

Many of the observations from the force study also apply to the torque study, but two findings stand out in Fig. 2.8. First, across all orientations, the force of the differentially charged target appears to be bounded by the two scenarios with a fully conducting target and the servicer either eclipsed or in sunlight. This is demonstrated in Fig. 2.6 as the blue and red surfaces do not pierce through the gridded or solid black surfaces. For a differentially charged spacecraft with the given potentials, the net force is reduced in magnitude. This is not the case for the torque, as is evident in Fig. 2.8. For some orientations, the electrostatic torque is actually enhanced due to differential charging. For example, if the servicer is eclipsed, a target spacecraft with a bus potential of 0 kV and panel potential of -5 kV experiences enhanced repulsive torques. The solar panel provides more leverage for the torque with respect to the center of mass, so the negative charge concentrated on the panel combined with the negatively charged servicer lead to higher repulsive torques. Similarly, with the bus at -5 kV, the panel at 0 kV provides more leverage for the attractive torque, and consequently enhances the torque as well. The second finding is that the torque polarity of the differentially charged target may be switched with respect to the fully conducting target for almost all orientations, as opposed to only some specific orientations for the force polarity. The torque for an eclipsed servicer and fully conducting target is mostly repelling. However, if the target bus is

negatively charged to −5 kV and the panel is at 0 kV, the resulting torque is attractive for almost all orientations. Although, for a given orientation, the force is repulsive, for example, the torque may be attractive due to the greater leverage of the panel.

Not only does differential charging of large spacecraft components affect the magnitude of the electrostatic force and torque, but it can also lead to a switch of direction of the force component along the direction of separation. Additionally, while the magnitude of the electrostatic force is reduced by differential charging, the electrostatic torque may be enhanced due to greater leverage of protruding components such as solar panels. If the forces and torques resulting from a fully conducting spacecraft are considered to be the expected forces and torques, then differential charging can lead to large deviations with respect to the actual forces and torques. This is important to consider when using estimated forces and torques for feed-forward control during OSAM operations subject to electrostatic perturbations. Thus, identifying and measuring differential charging using the methods described in Chapter 3 and Refs. 59, 115 is important to generate a better model of the inter-spacecraft electrostatic forces and torques.

2.5 Conclusions

The charging model from Sec. 2.1 is used to compute the expected equilibrium potential in cislunar regions using lunar plasma data that corresponds to a high charging environment and assuming an eclipsed spacecraft. The highest risk of charging is found to be in the plasma sheet, with natural potentials between −10 kV and −6 kV, depending on the spacecraft orientation with respect to the ion flow. Despite lower natural potentials compared to the plasma sheet, the magnetosheath may be a challenging environment in terms of electrostatic perturbations due to the combination of high electric potentials and plasma wakes. High electric potentials in the order of the potentials found here for cislunar space lead to electrostatic perturbations that can affect On-Orbit Servicing, Assembly and Manufacturing operations [25].

Using the Multi-Sphere Method from Sec. 2.2, the effect of differentially charged spacecraft on the inter-craft electrostatic forces and torques is investigated. The results show that, if the

potential of the solar panel is different from the remaining spacecraft, the force and torque can differ significantly compared to a fully conducting spacecraft, depending on the potentials and the spacecraft orientation. In some cases, this can cause force and torque components to switch from being repulsive to being attractive. That is, instead of being pushed away, the spacecraft may be pulled towards each other. Moreover, the electrostatic torque, which has a more significant effect on proximity operations than the electrostatic force [25], may be enhanced due to greater leverage by protruding components such as solar panels. The deviation of the forces and torques of a differentially-charged spacecraft compared to those of a fully conducting spacecraft are important to consider for electrostatic force and torque based feed-forward control during OSAM and ADR operations. This highlights the importance of identifying and measuring differential charging with the electric potential sensing methods, which is investigated in the following Chapter 3.

Chapter 3

Electric potential sensing of complex shapes and differentially charged objects using x-rays

Remotely sensing the electric potential of a nearby spacecraft is a crucial part of electrostatic proximity operations. For the Electrostatic Tractor debris removal concept, estimating the potential of the debris allows for active spacecraft charging control with the electron beam, which in turn enables the control of the inter-spacecraft electrostatic force and torque. Additionally, the estimation of the debris potential, and consequently the force between the servicer and the debris, is needed for the feed-forward relative motion control proposed for the Electrostatic Tractor [33, 65]. For on-orbit servicing operations, sensing the electric potential of the target allows for the estimation of the electrostatic torque used for a feed-forward control to reduce the imposed rotational rates on the target [34], and knowing the relative potential between the servicer and target can prevent electrostatic discharged between the two spacecraft. Two methods have been recently proposed to estimate the potential of nearby spacecraft: the electron method [35] and x-ray method [36].

This chapter experimentally investigates the effect of complex shapes and differently charged objects on the estimation of electric potentials using the x-ray method. The relevant background for the x-ray method is reviewed in Sec. 3.1, including the theory of the method as well as a parametric study conducted in prior work. Section 3.2 provides an overview of the vacuum chamber facility used for the experiments. Experiments with differentially charged objects are presented in Sec. 3.3 and experiments with objects made of multiple materials are shown in Sec. 3.4. Finally, the sensing time required for the estimation with the x-ray method is investigated in Sec. 3.5.

3.1 Fundamentals of x-ray based electric potential estimation

3.1.1 Theory of x-ray spectroscopic potential estimation

Energetic electrons can interact with atoms in various ways. When an inner-shell electron is removed by an incoming energetic electron, an outer-shell electron of the atom fills the vacant spot of the inner-shell, and the difference in energy between the two shells is released as a characteristic x-ray photon [116, Chapter 10]. Because the energy difference between shells varies from element to element, the characteristic energy is specific to each element and allows for material identification. Another type of interaction occurs when an electron traverses closely to an atomic nucleus and is decelerated. Again, the loss in energy is emitted as an x-ray photon, called Bremsstrahlung (German for braking radiation) [116, Chapter 10]. However, because the interaction with the nucleus can occur in many different paths, the energy of the emitted x-ray is not distinct as for characteristic x-rays, but continuous. The maximum Bremsstrahlung energy is given by the Duane-Hunt law and is equal to the energy of the incident electron prior to the interaction with the atom [117], referred to as the landing energy (or effective energy). Thus, x-ray spectra can be used to estimate the landing energy of the electron beam electrons. The electron beam interacts with the electric field created by charged objects, and the change in kinetic energy of the electron beam corresponds to the difference in electric potential between the serving satellite (the initial location of the electron beam electrons) and the target object (the final location)

$$T_1 - T_0 = \phi_T - \phi_S \tag{3.1}$$

where T_1 and T_0 represent the kinetic energy of the electron beam in units of electron volts (eV) at the target and at the servicer, respectively, ϕ_T is the potential of the target and ϕ_S is the potential of the servicer. Therefore, measuring the electric potential of the servicing satellite ϕ_S using a Langmuir probe [38] or retarding potential analyzer (RPA) [39], knowing the initial electron beam energy $T_0 = E_{EB}$ (the electron beam operating energy), and estimating the landing energy of the electron beam from the maximum photon energy in the x-ray spectrum $T_1 = E_{\text{xray,max}}$, the

potential of the target object can be inferred [36, 45, 47]

$$\phi_T = \phi_S + E_{\text{xray,max}} - E_{EB} \tag{3.2}$$

Note that no assumptions are made about the polarity of the electric potential of either the servicer or the target. In contrast to the electron method [35, 44], the x-ray method also works for neutral or positively charged target objects. Regarding the servicer potential, it is assumed that it is being measured, and that the difference of electric potential between the servicer and the target is smaller than the electron beam energy. Otherwise, the electron beam is not energetic enough to reach the target.

For the experiments conducted in the vacuum chamber as part of this work, the electron gun is grounded, which corresponds to a neutral potential of the servicing satellite. Consequently, the change in energy of the electron beam is equal to the electric potential of the target object in the vacuum chamber. In general, the electron beam affects the potential of a target object in space. In the conducted experiments, the potential of the target is controlled using high voltage power supplies, so the potential of the target components remains nearly constant and is not affected by the electron beam.

3.1.2 Theoretical x-ray models

To gain some insight into what the resulting x-ray spectra look like, theoretical models may be employed. Thick target x-ray models are used, meaning that it is assumed that the incident electrons are completely stopped in the target object. The average path length Δx traveled by a charged particle penetrating into a material is computed using the continuous-slowing-down-approximation (CSDA) [118]

$$\Delta x = \int_0^{E_0} \frac{1}{S(E)\rho}\, \mathrm{d}E \tag{3.3}$$

where E is the kinetic energy of the particle, E_0 is the initial kinetic energy as the particle impacts on the material, ρ is the density of the material, and $S(E) = -\mathrm{d}E/\mathrm{d}x$ is the linear stopping power on the particle. Using the NIST ESTAR database for electron stopping powers [119], one finds that

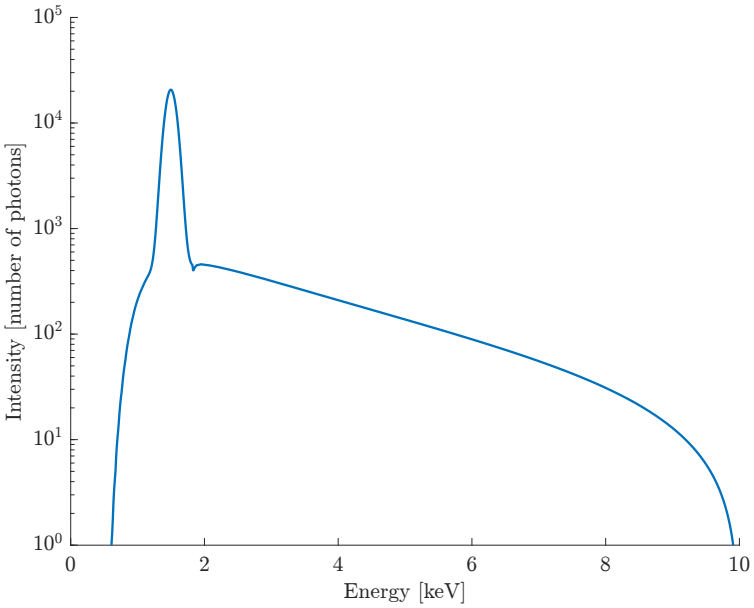

Figure 3.1: Sample Theoretical spectrum for aluminum with incident electron energy $E_e = 10$ keV

a 20 keV electron is stopped within 4.3 µm of aluminum, which is much thinner than the 0.75 mm aluminum panel used in the experiments.

Reference 120 is used to approximate the characteristic radiation of the theoretical spectrum. This model for the characteristic radiation is derived from x-ray tube measurements. The model assumes a thick target, that the plasma temperature is lower than the incident electron energy, and that there is no considerable ionization of the inner shell. The number of characteristic x-ray photons due to K_α transitions excited per incident electron with energy E_e is approximated by

$$N_{\mathrm{ph},c}(E_e) = \begin{cases} N\left(\frac{E_e}{E_k} - 1\right)^\alpha & \text{if } E_e \geq E_k \\ 0 & \text{if } E_e < E_k \end{cases} \tag{3.4}$$

where the parameters N, α and the characteristic energy E_k are material dependent. These photons are only emitted at a photon energy equal to E_k. For aluminum, $N = 1.4 \cdot 10^{-5}$, $\alpha = 1.63$ and $E_k = 1.49$ keV [120]. Since the characteristic energy E_k is the energy of the emitted characteristic photons, the energy of the incoming electron E_e must be greater than E_k to excite characteristic photons. Characteristic radiation is emitted isotropically. Even though characteristic x-rays are emitted at a discrete energy, the x-ray detector senses a Gaussian distribution with a width defined

by the full width at half maximum (FWHM). For the detector used in this work, the FWHM is approximately 200 eV and is converted to the standard deviation of the Gaussian distribution by

$$\sigma = \frac{\text{FWHM}}{2\sqrt{2\ln(2)}} \tag{3.5}$$

Given the standard deviation and the number of characteristic photons per incident electron with energy E_e, the theoretical characteristic radiation as observed by the detector is computed using the normal distribution

$$N_{\text{ph},c,\text{det}}(E, E_e) = \frac{N_{\text{ph},c}(E_e)}{\sigma\sqrt{2\pi}} \exp\left(-\frac{(E - E_k)^2}{2\sigma^2}\right) \tag{3.6}$$

The integral of this Gaussian distribution is $N_{\text{ph},c}(E_e)$, so the number of photons per incident electron are redistributed from a discrete energy E_k to a Gaussian distribution with standard deviation σ.

The Bremsstrahlung spectrum is approximated using an empirical model for thick targets from Ref. 121 that is based on experiments, and is valid for photon energies E ranging from 0.25 keV to 20 keV, atomic numbers Z between 4 and 83, and incoming electron energies between 5 and 38 keV. With this model, the number of Bremsstrahlung x-ray photons with energy between E_e and $E_e + \Delta E$ (with bin size ΔE) excited per incident electron with energy E_e is estimated by

$$\begin{aligned} N_{\text{ph},b}(E, E_e) = C\sqrt{Z}\frac{E_e - E}{E}\left(-73.90 - 1.2446E + 36.502\ln(Z) + \frac{148.5E_e^{0.1293}}{Z}\right) \\ \cdot \left(1 + (-0.006624 + 0.0002906E_e)\frac{Z}{E}\right)\Delta E \end{aligned} \tag{3.7}$$

using a scaling factor of $C = 3.35 \cdot 10^{-7}$ for aluminum. In contrast to characteristic radiation, Bremsstrahlung radiation is not emitted at a single energy, but at a continuous range of energies up to the landing energy of the incident electron [117]. Additionally, Bremsstrahlung radiation is emitted anisotropically, meaning that the intensity of the emitted radiation depends on the direction. For high energy electrons above 100 keV, the emitted radiation is mostly in the forward direction of the incident electron, but for lower energy electrons the photons are emitted in other directions as well. In other words, Bremsstrahlung radiation depends on both the energy and

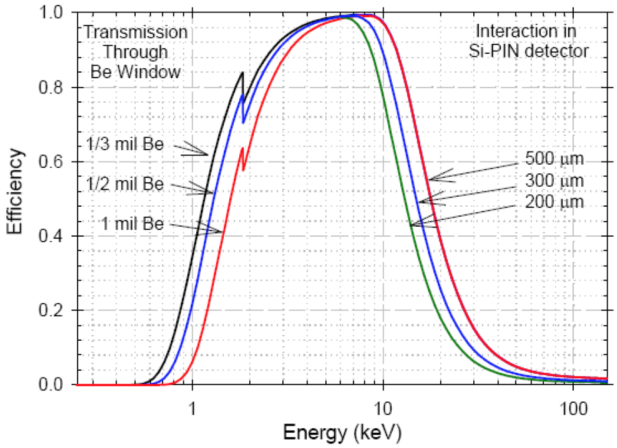

Figure 3.2: Efficiency of Si-Pin x-ray detector from Amptek. The detector used in this work has a 1 mil beryllium frontal window (red curve).

direction of the incoming electron, and varies with both the energy and direction of the emitted photon.

The total number of photons N_{ph} with an energy of E that are sensed by the detector during an accumulation time of t_{accum} is computed by

$$N_{\text{ph}}(E, E_e) = \frac{I_{EB}}{q}\Omega\Big[N_{\text{ph},c,\text{det}}(E, E_e) + N_{\text{ph},b}(E, E_e)\Big]t_{\text{accum}} \tag{3.8}$$

where I_{EB} is the electron beam current and $q = 1.602176634 \cdot 10^{-19}$ C is the elementary charge. The solid angle Ω is determined by $\Omega = \frac{A_{\text{det}}}{L^2}$, with the detector area A_{det} and the distance of the detector from the x-ray source L. A sample theoretical spectrum for aluminum with incident electron energy $E_e = 10$ keV and beam current $I_{EB} = 10$ µA is shown in Fig. 3.1.

Finally, the efficiency of the x-ray detector is considered. Low energy photons are filtered out by the Beryllium frontal window of the detector while high energy photons might not deposit a significant amount of their energy when transiting through the detector. To account for the attenuation of these photons, the energy dependent efficiency curve of the x-ray detector shown in Fig. 3.2 is applied for the computation of the theoretical x-ray spectrum [1] .

Reasons for inaccuracies of the theoretical model with respect to the experimentally observed

[1] https://www.amptek.com/products/x-ray-detectors/sipin-x-ray-detectors/sipin-x-ray-detectors (Consulted on: 05/23/2025)

Table 3.1: Theoretical x-ray model parameters

Element	N	E_k	α	Z	C
Aluminum (Al) [120]	1.4×10^{-5}	1.49 keV	1.63	16	3.35×10^{-7}
Copper (Cu) [120]	6.4×10^{-5}	8.05 keV	1.63	29	9.78×10^{-7}
Titanium (Ti) [120, 123]	2.2×10^{-5}	4.50 keV	1.55	22	3.20×10^{-7}

spectrum, especially in the case of the Bremsstrahlung model, include varying electron impact angles, varying observer angles, photons excited by backscattered electrons, photon absorption within the material, and uncertainty in the detector efficiency [121, 122].

The parameters for the characteristic and bremsstrahlung x-ray models are shown in Tab. 3.1 for aluminum, copper and titanium.

3.1.3 Parametric study

A parametric study using several experimental data sets was performed in Ref. 47 to find the main contributors of sensing errors with the x-ray method. The study included experiments with varying target object orientations (changing the electron impact angle on the target), varying detector locations (changing the observation angle w.r.t. the incoming electron direction), as well as several different electron beam energies (changing the impact energy). The results of the parametric study from Ref. 47 are reviewed and discussed here.

3.1.3.1 Review of previous findings

Electron incidence angle No statistically significant relation was found between the electron incidence angle and landing energy estimation error, using experiments with varying target object orientations. For these experiments, a titanium target plate was rotated between $-60°$ and $60°$.

Observation angle No statistically significant relation was found between observation angle and landing energy estimation error. This was investigated using experiments with varying

detector locations with respect to the incoming electron beam direction, with observation angles between $-30°$ and $30°$.

Electron landing energy A statistically significant relation was found between the true landing energy and the percentage error in the estimate of landing energy by using several different electron beam energies. The results indicate that an increasing electron landing energy leads to less accurate potential estimates, with an increase of about 0.35 % of the landing energy percentage error per 1 keV increase of true landing energy. For a 10 keV landing energy, the error is about 3.5 %. Note that this describes the percentage error of the landing energy estimate, not the percentage error of the electric potential estimate.

3.1.3.2 Discussion

For single-electron interactions, where an incoming electron only interacts with one single atom, the Bremsstrahlung radiation is highly anisotropic [124]. Especially with higher electron energies (100 keV), the emission of photons occurs predominantly in the forward direction of the electron. In thick targets, where the electron is assumed to be fully stopped within the target material, the incoming electron undergoes multiple interactions with atoms, which tends to randomize its direction before it comes to rest. Such thick target interactions are studied experimentally in Ref. 125, where the effects of photon absorption within the target and the angular distribution of the Bremsstrahlung radiation are investigated. The experiments are conducted with a high-purity target plate of various metals and beam energies from 10 to 30 keV, and the experimental setup allows for a range of different incidence angles and observation angles.

As shown in Ref. 125, the absorption of photons within the target is the greatest for normal incidence of the electrons, due to the deeper penetration of electrons into the material, and for shallow (along the surface) emission (i.e., observation) angles, due to the longer path length of the photons inside the target. Especially the x-ray emission at lower photon energies is greatly reduced due to absorption. Additionally, the higher the incident energy, the longer the range of electrons within the material, and the greater the absorption. For a certain incident energy

and normal incidence, low energy photons experience the greatest absorption at shallow observing angles due to the long path length of the photons. High energy photons actually have a high intensity at shallow angles, because the increased emission normal to the beam direction dominates the absorption at shallow observation angles. The angular distribution of the total number of Bremsstrahlung x-rays becomes more asymmetric as the electron beam becomes more oblique to the target. These experimental results indicate that even for thick targets, the Bremsstrahlung radiation is anisotropic.

The angular distribution of thick-target Bremsstrahlung radiation is also studied in Ref. 126 using experiments with electrons with energies between 10 and 20 keV and incident on Silver. The results show that thick target Bremsstrahlung radiation is more anisotropic at higher photon energies (closer to the incident energy of the electron). Low energy photons (w.r.t to the energy of the incident electron) are produced throughout the deceleration process within the material, including after the electron has been significantly scattered. This scattering randomizes the emission direction, making low energy Bremsstrahlung more isotropic. High energy photons are generally emitted earlier in the path of the electron, when the electron still retains much of its original direction. Because no significant scattering has occurred at this point, the angular distribution of the photons retains more of the original beam direction, like in single-electron interactions.

The increased anisotropy of photons with energies close to the landing energy of the electron beam is relevant to this work, because the higher energy end of the spectrum is used for the estimation of the electric potential via x-ray spectroscopy. While an anisotropy of the emitted x-ray spectrum does not necessarily imply an angular dependence of the x-ray method, a relationship between the observation angle and the accuracy of the x-ray method is found experimentally in Ref. 45 for observation angles between 15° and 135°. Thus, the lack of statistically significant angular dependence of the x-ray method found in Ref. 47 may be explained by the smaller range of angles included in that work.

The energy dependence of the x-ray method found in Ref. 47 may be explained by the increased anisotropy of Bremsstrahlung radiation for higher incident electron energies [125], as well

as by detector-specific characteristic such as the energy dependent detector efficiency. In addition to the relationship between the true landing energy and the percentage error of the landing energy estimate, characteristic peaks in the higher end of the recorded spectrum may also influence the accuracy of the estimation, as discussed in Sec. 3.4. If the landing energy is close to a characteristic peak, that characteristic peak may interfere with the estimation process.

Although not studied in Ref. 47, the beam current is another important parameter of the x-ray method. Generally, the higher the beam current, the more x-ray photons are excited and the better the signal-to-noise ratio. Thus, a higher beam current improves the sensing errors. However, care must be taken to avoid saturation of the x-ray detector. If too many x-rays are processed at once by the x-ray detector, the detector saturates and the recorded x-ray spectrum becomes unreliable. Thus, there exists an upper limit for the electron beam current to avoid such saturation.

3.2 ECLIPS space environment simulation facility

The experiments are conducted in the Electrostatic Charging Laboratory for Interactions between Plasma and Spacecraft (ECLIPS) Space Environments Simulation Facility [46]. This vacuum chamber facility is specifically designed for the experimental study of spacecraft charging and charged astrodynamics related topics. Several experiments have been conducted in ECLIPS related to the estimation of electric potentials using x-rays [45], secondary electrons [44] or photoelectrons [127]. Other studies focused on charged particle optics to enable plasma wake experiments [128, 129] as well as active charging control [130]. The facility includes several sources, probes and various other ancillary components to allow for a wide range of experiments, as described in great detail in Ref. 46. The components relevant to the experiments conducted as part of this work are highlighted in this Section.

The stainless steel bell-jar style vacuum chamber was donated to the Autonomous Vehicle Systems (AVS) Laboratory at the University of Colorado Boulder in 2016 by the Air Force Research Laboratory (AFRL) and is about 75 cm in diameter and 1 m tall. After reception from AFRL,

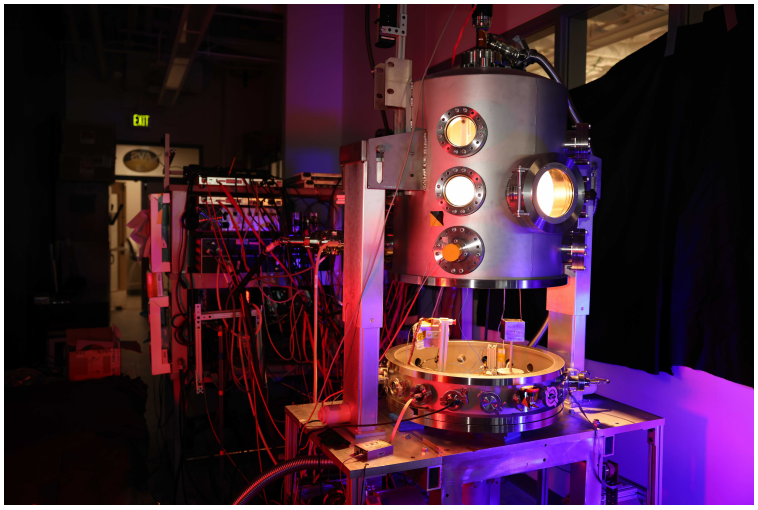

Figure 3.3: ECLIPS vacuum chamber facility

several viewports and flanges were added to allow for visual observation of experiments as well as the installation of crucial components such as the electron gun and high-voltage feedthroughs. The pumping system consists of an Agilent IDP-15 scroll pump and an Agilent Turbo-V 1001 Navigator turbo pump and enables operating pressures in the order of 10^{-7} Torr. An Agilent ConvecTorr gauge is used to measure the chamber pressure from atmosphere down to 10^{-4} Torr, and an Agilent IMG-100 IMG is used to monitor the pressure below 10^{-4} Torr. A photo of the chamber facility is shown in Fig. 3.3.

The main source used in this work is the EMG-4212C electron gun from Kimball Physics. This electron gun is capable of emitting an electron beam with energies from 1-30 keV and currents from 1 µA to 100 µA. The focus of the electron beam is adjustable, which allows to either hit a large area (spot size of about 25 mm) of the target object with electrons, or to focus the electron beam on a small spot with a diameter of about 500 µm for the separation distance of roughly 15-20 cm used in this work. Additionally, the electron gun is capable of beam pulsing, which provides a way for active charging control, as discussed in Chapter 5. A Matsusada AU-30R1 and a Spellman SL300 high voltage power supply are used to separately control the potentials of various components inside the chamber, such as components of the target object or the grid of the RPA, and are able to provide potentials up to 30 kV and 1 kV, respectively. The orientation of the target object inside

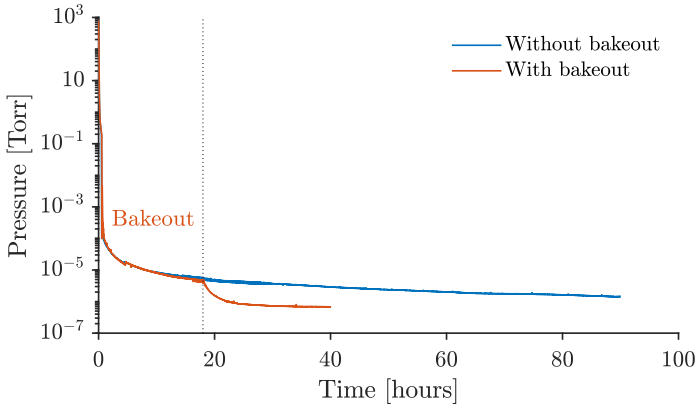

Figure 3.4: Pressure evolution with time with and without bakeout

the chamber with respect to the electron beam is varied with a RM-3 vacuum compatible rotary stage from Newmark Systems, and measured with an incremental rotary high-vacuum Renishaw Tonic encoder. A 3.8 cm diameter Kimball Physics Rugged Phosphor Screen is attached to the backside of the test object to verify the landing spot of the unperturbed electron beam (i.e. when the test object is not charged).

An Amptek X123 X-ray spectrometer with a 6 mm^2 Si-PIN diode is used to detect x-rays and record x-ray spectra. The detector has a 1 mil (0.0254 mm) thick beryllium frontal window which effectively attenuates photons with energies less than 0.9 keV, as visible in Fig. 3.2. The detector efficiency decreases for higher energies, as incoming photons with such high energy pass through the detector without depositing all of their energy. Another important characteristic of the x-ray detector is the maximum count rate of $10,000$ photons per second. At count rates exceeding this maximum rate, the detector saturates and the recorded x-ray spectrum becomes unreliable. The detector is calibrated with an Fe-55 radioisotope x-ray source, which emits x-rays at energies of 5.89 and 6.49 keV. For on-orbit calibration of the x-ray method, sample spectra may be taken of targets with well known energies of characteristic peaks, such as Earth or Moon. Additionally, the background radiation may be characterized prior to any estimation of the electric potential of a target spacecraft.

One key addition to the chamber facility that was led by the author is the bakeout system. A

VB-1 Vacuum Bakeout Package from RBD Instruments with one IRB-600 infrared emitter is used to accelerate the pump down process and clean the components inside the chamber. The temperature inside the chamber is controlled using a type J thermocouple located about 15 cm away from the heat emitter to provide temperature feedback. Although higher temperatures are achievable with this bakeout system, a temperature of 70° C is maintained while pumping down in the ECLIPS vacuum facility. This temperature increases the outgassing speed and decreases the pump down time sufficiently while ensuring that the temperature limits of sensitive chamber components are not exceeded. Without the bakeout system, the pumping down process from atmosphere to about 10^{-6} Torr takes approximately four days, as shown in Fig. 3.4. However, the application of a 70° C bakeout for the first 17 h reduces this interval to just 24 h, enabling rapid advancement of experimental campaigns. The bakeout system is usually turned on manually shortly after the activation of the scroll pump.

3.3 Differential charging

As shown in Sec. 2.4, differential charging of a spacecraft can lead to significant differences of the electrostatic force and torque compared to those of a fully conducting spacecraft. Identifying and measuring differential charging with the x-ray method allows for a better approximation of the electrostatic force and torque to be used for feed-forward control with the Electrostatic Tractor or during OSAM operations.

3.3.1 Experimental setup

The experimental setup is shown in Fig. 3.5 and consists of an electron beam, an x-ray detector, and a box-and-panel shaped object on a rotary stage representing a spacecraft bus with one solar panel. The bus of the spacecraft-like target object is a $70 \times 70 \times 70$ mm cube and the panel is a 145×60 mm flat plate. Both components are made of aluminum. Non-conducting Polyetheretherketone (PEEK) screws and washers are used to connect the panel with the cube to electrically isolate the components from each other. Additionally, a Retarding Potential Analyzer (RPA) is

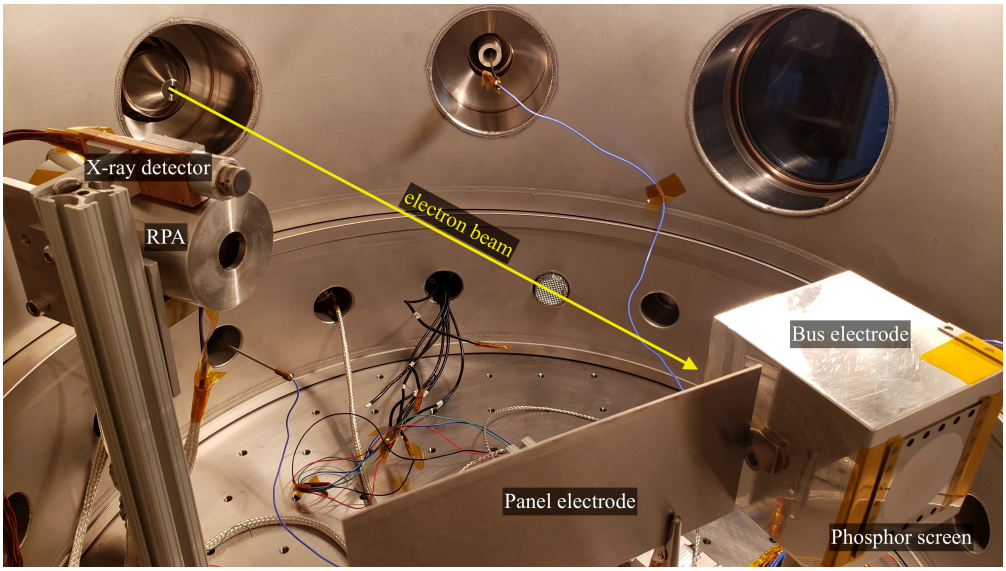

Figure 3.5: Experimental setup with a box-and-panel object representing a spacecraft

included in the setup and used to touchlessly estimate potentials with the electron method [59], but is not required for the x-ray method. The line between the x-ray detector and the test object approximately forms a 16° angle with the electron beam.

The orientation of the spacecraft with respect to the electron beam is varied with the rotary stage, and measured with the encoder. The phosphor screen is attached to the backside of the test object to verify the landing spot of the unperturbed electron beam (i.e. when both the bus and panel potential are grounded). The unperturbed landing spot of the electron beam is also used as a reference point for the setup of the numerical simulation with the particle tracing software described in the next section. The angle that describes the orientation of the target object is defined to be zero when the panel is facing the electron beam (aligned with the unperturbed, straight electron beam).

When measuring electric potentials using x-rays excited by an electron beam, the beam current, the energy, and the focus can be adjusted. A high beam current is generally desired, because it will result in more x-rays being generated and thus yields a stronger signal. However, one must take into account the possibility of detector saturation. The Amptek X123 X-ray spectrometer with a 6 mm^2 Si-PIN diode used in this work has a maximum count rate of $10,000$ photons per

second. Therefore, the electron beam current should be chosen such that this maximum count rate is not exceeded during the 20 second accumulation time frame of the x-ray detector. Using Eq. (3.8) with an approximate distance between the detector and the x-ray source of 20 cm, one finds that an electron beam current $I_{EB} = 1$ µA yields a count rate of about $10,000$ photons per second for a beam energy of 10 keV and a grounded target object. Thus, to stay below the $10,000$ photons per second, an electron beam current of 1 µA is used for all experiments in this work. The code used for the data analysis rejects any recorded spectrum with a count rate that exceeds the maximum count rate of $10,000$ photons per second, but this did not occur for any of the experiments. Naturally, the electron beam interacts with the electric field created by the charged target object and is deflected to some degree [105]. To reduce deflection, a high electron beam energy of $E_{EB} = 10$ keV is used in this work. Finally, the electron beam focus is varied from experiment to experiment to provide either a narrow (half-cone angle of 0.2°), medium (0.5°), or a wide beam spot (2°). A narrow beam spot is used to excite x-rays from a small source region on the target object. Ideally, the electron beam hits only one spacecraft component for a given orientation and consequently each potential of a differentially charged object is measured individually. On the other hand, a wide beam spot is used to excite x-rays from multiple spacecraft components at once and thus measure multiple potentials simultaneously.

3.3.2 Particle tracing simulation framework

A phosphor screen is used to center the electron beam for a specific orientation (−30°) of the uncharged target object, but the exact landing spot of the electron beam changes with the orientation of the object and the electric potential of the spacecraft bus and panel. However, to validate the experimental results, it is important to know if the electron beam is hitting the bus or panel, because both components are charged to different potentials. Thus, the particle tracing simulation software SIMION [2] is configured to assist the interpretation of the experimental results. SIMION solves Laplace's equation to derive the electrostatic field and then computes the particle

[2] https://simion.com (Consulted on: 05/23/2025)

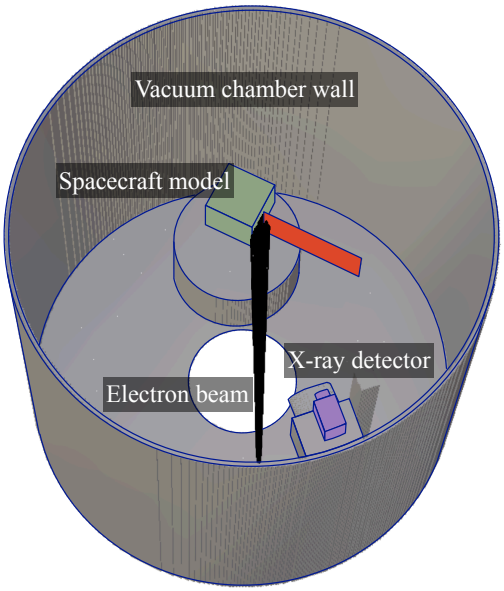

Figure 3.6: SIMION Model

trajectory from Newton's second law. The implementation of the SIMION simulation framework for remote sensing of electric potentials is discussed in greater detail in Ref. 59. Space-charge effects are not accounted for in the SIMION model, so the expansion of the electron beam and the effect of the electron beam on the electric field are not considered. As shown in Ref. 105, electrostatic repulsion is negligible for the beam divergence angles employed in the ECLIPS chamber, and the trajectory of the centroid of the beam depends only very weakly on beam repulsion. Because the main purpose of the SIMION model in this work is the validation of the beam landing spot, the implemented model is considered sufficiently accurate, and computationally more expensive models such as particle-in-cell (PIC) are not considered. The implication of not considering space-charge is described further in Ref. 59. The trajectories of the secondary electrons excited by the electron beam are also modeled in SIMION, but not shown or discussed here as they are irrelevant for the x-ray method. Figure 3.6 shows the SIMION model of the experimental setup.

Figure 3.7: Narrow Electron Beam for measuring each component individually

3.3.3 Measuring each component individually

A small electron beam spot with a half-cone angle of about 0.2° is centered on the phosphor screen for a spacecraft angle of −30° and grounded components, as shown in Fig. 3.7. The half-cone angle θ is required for the SIMION simulations and is approximated by estimating the beam spot radius R_b on the phosphor screen and using

$$\tan\theta = \frac{R_b}{L_{t,eb}} \tag{3.9}$$

where $L_{t,eb}$ is the distance from the electron beam source to the landing location. For the experiments, the angle of the target object is changed between −20° and 80° in 10° steps, where an angle of 0° corresponds to the panel pointing towards the electron gun. The x-ray spectra are taken for a static target object orientation and using an x-ray accumulation time of 20 seconds, meaning that the x-ray detector counts photons for 20 seconds. Each experiment run is repeated five times.

Figure 3.8 shows some sample x-ray spectra for various target object angles. The electric potential of the bus is set to $\Phi_B = -500$ V and the potential of the panel is set to $\Phi_P = -1500$ V. To estimate the landing energy, it is not sufficient to simply take the energy of the highest energy photon observed by the x-ray detector due to the noise of the measurement. Instead, a more robust method is recommended by Ref. 131. Taking advantage of the approximately linear shape of the Bremsstrahlung spectrum close to the landing energy, a linear curve is fitted to the upper energy part of the x-ray spectrum. The energy where this fitted line intersects the x-axis corresponds to

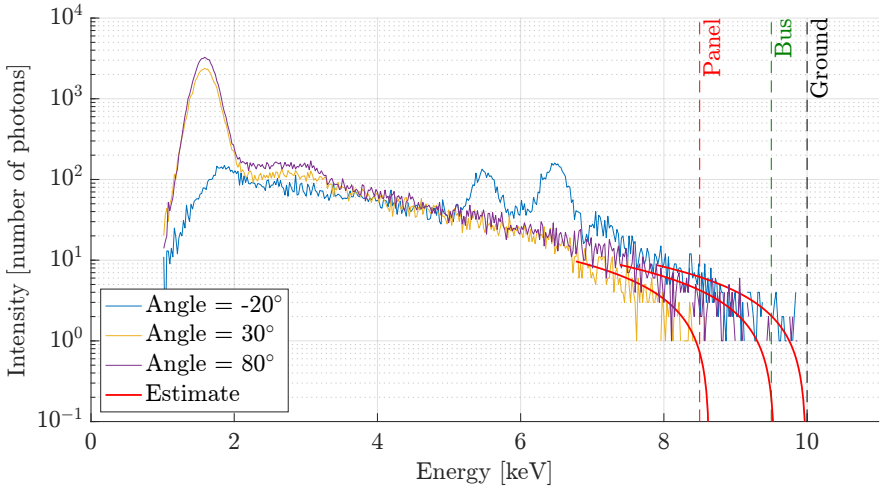

Figure 3.8: X-ray spectra for different target object angles. $\Phi_B = -0.5$ kV, $\Phi_P = -1.5$ kV

the estimated landing energy. This procedure is explained in greater detail in Refs. 45 and 47. The uncertainty of the estimated landing energy can be determined using the bounding lines of the linear fit to cover 95 % of the sampled data points. The interception of these bounding lines with the x-axis are then used to determine the uncertainty of the landing energy estimate, showing uncertainties of about 200 V for the x-ray method [132]. The fitted lines for each sample spectra are shown by the red curves in Fig. 3.8, labeled as "Estimate". Note that the log-scale of the plot distorts the linear shape of the fitted Estimate line.

For a target object angle of $-20°$, the resulting x-ray spectrum includes characteristic peaks at approximately 5.4 keV and 6.4 keV. These peaks match with the characteristic energies of Chromium (Cr, K_α transition at 5.41 keV) and Iron (Fe, K_α transition at 6.4 keV) [133], indicating that the electron beam hits the stainless steel chamber wall. The estimated landing energy is approximately 10 keV. For an electron beam energy of 10 keV, this corresponds to an estimated potential of 0 V. This supports the claim that the beam is deflected from the target object and impacting on the chamber wall, because both electrodes are charged to non-zero potentials and the rest of the chamber is grounded. The x-ray spectra for an angle of 30° and 80° both include a characteristic peak at 1.5 keV, which agrees with the characteristic energy of Aluminum (Al, K_α transition at 1.49 keV) provided by Ref. 133. This suggests that the electron beam hits the

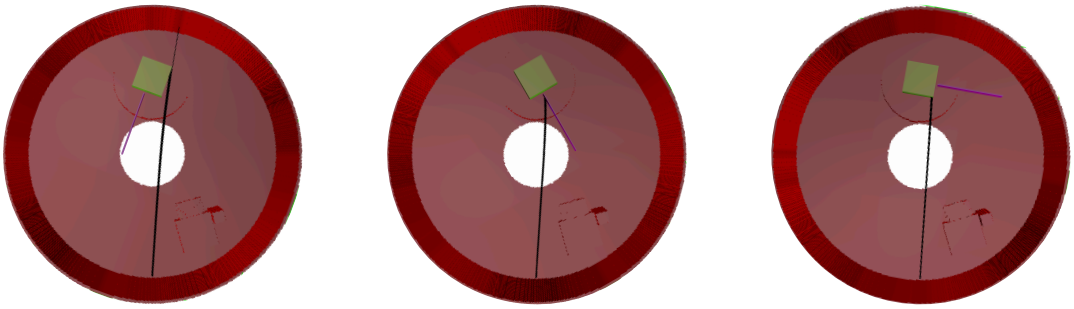

(a) −20° (b) 30° (c) 80°

Figure 3.9: Narrow Beam trajectories from SIMION simulation. $\Phi_B = -0.5$ kV, $\Phi_P = -1.5$ kV

aluminum target object. The estimated potential is approximately −1400 V for 30° and −500 V for 80°, indicating that the electron beam impacts on the panel for the former orientation and the spacecraft bus for the latter. If the target was charged to a positive potential, the landing energy of the electron beam electrons (and thus the maximum recorded x-ray energy) would be higher than the initial electron beam energy – opposed to being lower in the case of a negative target potential. Which object or component is observed in the x-ray spectrum for each orientation is confirmed by the simulated electron trajectories, as shown in Fig. 3.9.

The estimated potential as a function of the target object orientation is presented for two different voltage combinations in Fig. 3.10 using box-plots. The horizontal line inside of each box corresponds to the median of the data, and the bottom and top edges of the box represent the 25% and 75% percentiles. The black whiskers indicate the minimum and maximum of each data set, excluding outliers. Outliers are represented by circles and are values that are more than $1.5 \cdot IQR$ away from the bottom or top of the box, where IQR is the difference between the top and bottom box edges (interquartile range). Depending on the angle of the target object, the potential of either the chamber wall, the bus, or the panel is measured. If the maximum photon count per energy bin is less than 100 photons, or the total number of photons counted is less than 1500 photons, the corresponding x-ray spectrum is rejected by the data analysis code due to a lack of an x-ray signal. That is, this threshold is used to determine whether or not there is an x-ray signal at all due to the impact of the electron beam. This is the case for an angle of 10°, and the reason why Figs. 3.10a

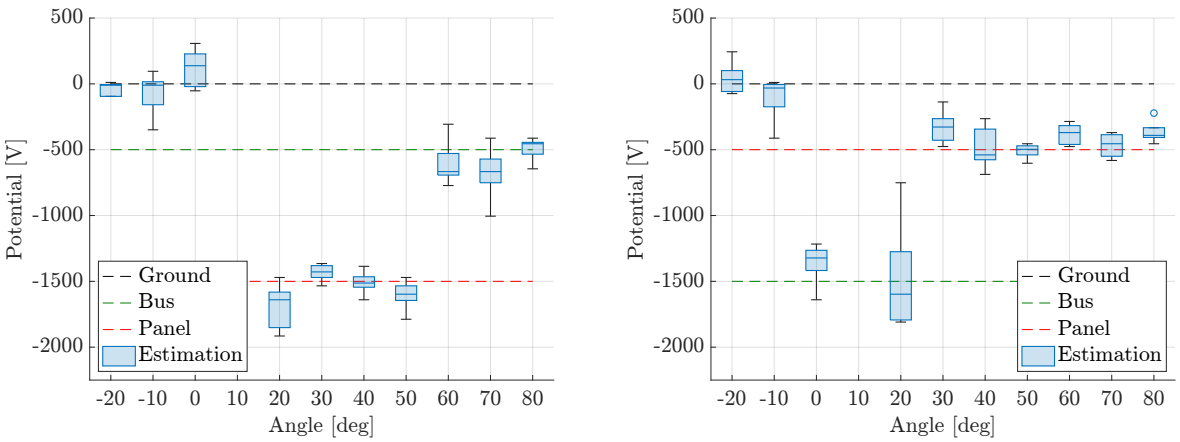

(a) $\Phi_B = -500$ V, $\Phi_P = -1500$ V

(b) $\Phi_B = -1500$ V, $\Phi_P = -500$ V

Figure 3.10: Narrow Beam Results

and 3.10b do not include any data for 10°. The consistent lack of signal at an angle of 10° over all experiment runs is a consequence of the experimental setup. As mentioned earlier, the x-ray detector and the electron beam are about 16° apart from each other, and the target object angle is defined as the angle between the panel and the source location of the electron beam. Thus, for an angle of 10°, the electron beam impacts on the panel on one side, but the x-ray detector is located on the other side of the panel, reducing the x-ray signal significantly. Even for an angle of 20°, the location of the detector is unfavorable, resulting in a weakened signal and consequently larger 2σ values. For angles below $-10°$, the electron beam is deflected and hits the chamber wall, and consequently the potential of the grounded chamber wall is measured. For the remaining angles, either the bus or panel potential is detected.

3.3.4 Target observability

The previous subsection demonstrates that the orientation of the target object affects which component the electron beam impacts on and which potential is observed by the x-ray detector. The electric field due to the two electrodes varies from one orientation to the other, which changes the way the electron beam is deflected. Consequently, the landing spot of the electron beam is a function of the target object's orientation and the electric potential of its components. For low

Table 3.2: X-ray Observations. (a) $\Phi_B = -0.5$ kV, $\Phi_P = -1.5$ kV, (b) $\Phi_B = -1.5$ kV, $\Phi_P = -0.5$ kV

	Angle	$-20°$	$-10°$	$0°$	$10°$	$20°$	$30°$	$40°$	$50°$	$60°$	$70°$	$80°$
(a)	Experimental	CW	CW	CW	LOS	P	P	P	P	B	B	B
	SIMION	CW	CW	CW	LOS	P	P	B/P	B/P	B	B	B
(b)	Experimental	CW	CW	B	LOS	B	P	P	P	P	P	P
	SIMION	B	CW	B	LOS	P	P	P	P	B/P	B	B

CW...chamber wall, B...bus, P...panel, B/P...both bus and panel, LOS...loss of signal

electric potentials as applied in this set of experiments ($\leq$ 1.5 kV), however, the effect of the beam deflection is not as significant as the influence of the orientation of the target object. Which potential is measured essentially depends on the landing location of the beam. Table 3.2 provides an overview of which potential is measured by the x-ray detector, compared to the landing location of the electron beam as predicted by the SIMION simulation. The possible observations are the chamber wall (CW), the bus (B), the panel (P), both the bus and the panel (B/P) or loss of signal due to an insufficient number of photons (LOS). The outcome CW essentially means that the electron beam does not hit the spacecraft. Thus, in an in-orbit scenario, the outcome CW corresponds to a loss of signal.

In general, the observations by the x-ray detector agree well with the predictions by SIMION. For electrode configuration (a) and an angle of 40°-50°, the x-ray detector measures the potential of the panel even though the SIMION simulation predicts the electron beam to hit both the bus and the panel. However, small modeling inaccuracies of the experimental setup geometry have a large effect on the accuracy of the SIMION simulation. Reference 59 shows that there is a shift of about 3° between the experimental results for the electron method and the SIMION simulation, for the same chamber setup as in this work. Thus, this discrepancy is explained by geometric imprecisions of the SIMION chamber model. More interestingly, for electrode configuration (b) and angles between 60° and 80°, the potential of the panel is measured although the electron beam hits either the bus

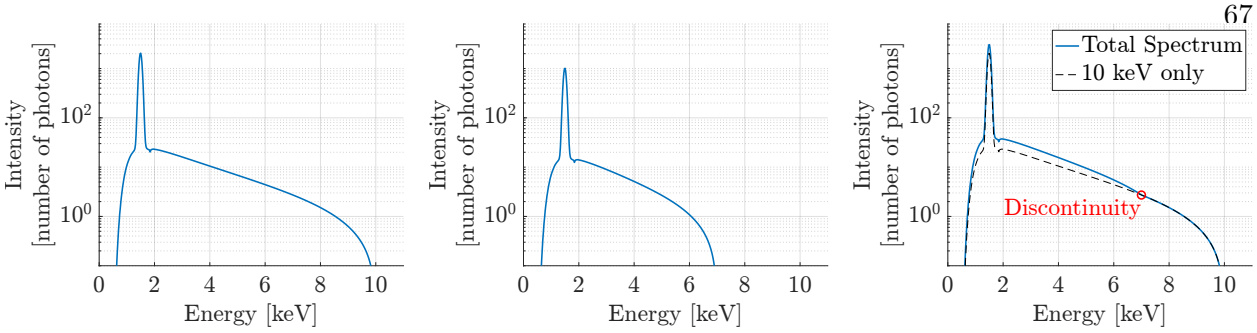

(a) 10 keV Spectrum (b) 7 keV Spectrum (c) Total Spectrum

Figure 3.11: Theoretical superposition of X-ray spectra

or both the bus and the panel in the SIMION simulation. In addition to an approximate SIMION chamber model, this is explained by the following phenomenon. If the electron beam impacts on two components charged to different potentials, then the electron landing energy is different for each component. However, only the higher landing energy is measured by the x-ray spectroscopy method explained in Sec. 3.1.1. Thus, if the electron beam hits two components with dissimilar electric potentials, only the higher potential is measured. That is, either the potential that is less negative or more positive. Because only negative potentials are used in the experiments within this work, only the potential that is smaller in magnitude is measured. For electrode configuration (b), this corresponds to the panel at $\Phi_P = -0.5$ kV.

3.3.5 Measuring multiple potentials simultaneously

The analysis of target observability shows that, if the electron beam hits two components with different electric potentials, only the higher potential is detected when measuring the maximum photon energy to infer the electric potential per the Duane-Hunt law. This raises the question as to whether it is possible to measure multiple potentials simultaneously using a single x-ray spectrum. To investigate this, theoretical x-ray spectra are created for two different landing energies, representing two different potentials.

Figure 3.11 shows the individual theoretical spectra for landing energies of 10 keV and 7 keV. For an electron beam energy of 10 keV, this corresponds to electric potentials of 0 kV and -3 kV,

respectively. If an electron beam hits two components charged to different potentials at the same time, then the resulting total spectrum is obtained by superimposing the individual spectra of each landing energy. This is illustrated in Fig. 3.11c for potentials of 0 kV and −3 kV, assuming that the same number of electrons impact both components. A discontinuity in the slope is produced in the total spectrum at an energy of 7 keV, which corresponds to the landing energy of the lower-energy individual spectrum. Thus, the lower potential can be estimated by locating this discontinuity in the total spectrum, while the higher potential is estimated from the maximum photon energy of the spectrum (Sec. 3.1.1).

In a real x-ray spectrum, however, this discontinuity is not easily identified due to the noise in the spectrum. Instead, it is proposed to estimate the higher potential from the maximum photon energy of the total spectrum, and to compute a theoretical spectrum using the corresponding estimated landing energy [115]. Subtracting the theoretical spectrum from the total spectrum yields a residual spectrum that approximates the individual spectrum of the lower potential component. The lower potential is then estimated by finding the maximum photon energy of the residual spectrum. That is, the recorded x-ray spectrum is deconvoluted to split it up into two individual spectra that both contain information about the individual components. For example, in Fig. 3.11, one would estimate the maximum photon energy from the total spectrum (Fig. 3.11c) and compute the corresponding higher landing energy spectrum (Fig. 3.11a). The residual spectrum (Fig. 3.11b) then provides an estimation of the lower landing energy. The two potentials are inferred from the two estimated landing energies.

3.3.5.1 Experiments with wide electron beam

To investigate the proposed method experimentally, a wide electron beam spot with a half-cone angle of about 2° is centered on the phosphor screen for a spacecraft angle of −30° and grounded components, as shown in Fig. 3.12. For the experiments, the angle of the target object is changed between −20° and 80° in 10° steps. The x-ray spectra are taken for a static target object orientation and using an x-ray accumulation time of 20 seconds. Each experiment run is repeated

Figure 3.12: Wide Electron Beam for measuring multiple potentials simultaneously

five times.

For this experiment, a target object orientation must be found where the electron beam impacts on both the bus and the panel. SIMION shows that, for electrode potentials of $\Phi_B = 0$ kV and $\Phi_P = -3$ kV, the beam hits both components if the angle is 30° and only the bus if the angle is 80°, as shown in Fig. 3.13.

A spectrum for 80° is presented in Fig. 3.14a. The maximum photon energy of about 10 keV is determined using a linear curve fit in the higher energy part of the spectrum as described in Sec. 3.3.3. For a beam energy of 10 keV, this corresponds to a potential of 0 kV, i.e. the potential of the spacecraft bus. A theoretical x-ray spectrum is computed for the estimated landing energy of about 10 keV using the models provided in Sec. 3.1.2. The computed theoretical spectrum agrees well with the measured spectrum (Fig. 3.14a), and the resulting residual spectrum (the difference between the measured and theoretical spectrum, Fig. 3.14b) is low in intensity. This suggests that only one potential is detected, and that is the bus potential of 0 kV. Note that the lower limit of the y-axis in Fig. 3.14 is 1 as this is the smallest non-zero integer number of photons that can be measured by the detector. The theoretical number of photons, however, can be a fraction of a photon. Thus, even though the theoretical curve in Fig. 3.14a intersects the x-axis at about 9 keV (indicating a potential of −1 kV), it approaches an intensity of 0 photons at about 10 keV, corresponding to a potential of 0 kV (compare with Fig. 3.11). The experimental result is also confirmed by numerical simulations with SIMION that show that the beam only impacts

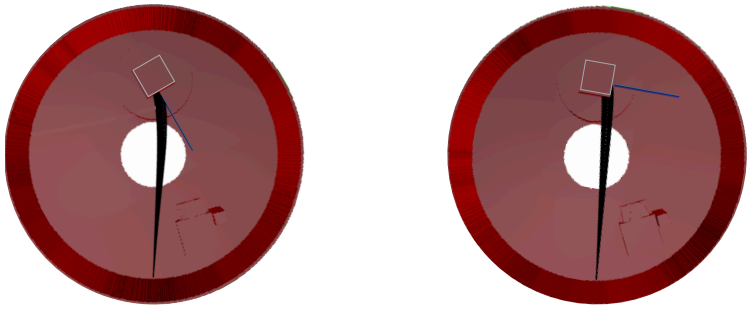

(a) 30° (b) 80°

Figure 3.13: Wide Beam trajectories from SIMION simulation. $\Phi_B = 0$ V, $\Phi_P = -3000$ V

the spacecraft bus for an orientation of 80° (Fig. 3.13b). No theoretical spectrum is shown in Fig. 3.14b due to the lack of a notable residual spectrum. A low-pass filtered curve of the data is plotted to illustrate the trend of the data. This low-pass filtered curve is used to identify and remove characteristic peaks using the Matlab function `findpeaks`. However, the least-square estimation itself is done using the raw data. Thus, aside from the number of data points removed through the removal of characteristic peaks, the low-pass filtering is not expected to significantly change the measurement characteristics.

The intensity of the theoretical x-ray spectrum needed to match the recorded spectrum is not exactly known. While it could be computed in theory using Eq. (3.8), such approximation depends on several factors such as the number of electrons impacting the target, the distance between the x-ray source location and the detector, and the solid angle field of view of the detector. It also assumes that no structures of the target object block the x-ray detector field of view of the source region. These variables are uncertain in a real application, especially if the x-rays are emitted from multiple sources with different potentials, and an accurate intensity of the theoretical spectrum is crucial for the proposed method. Thus, instead of computing the intensity theoretically, the right scaling factor β of the intensity is determined by minimizing the root-mean-squared error between the actual spectrum and theoretical spectrum. The fitting region is a 1.5 keV window in the upper end of the spectrum. For example, if the estimated landing energy is 10 keV, then the fitting region is between 8.5 keV and 10 keV. However, this imposes limits on the detection of

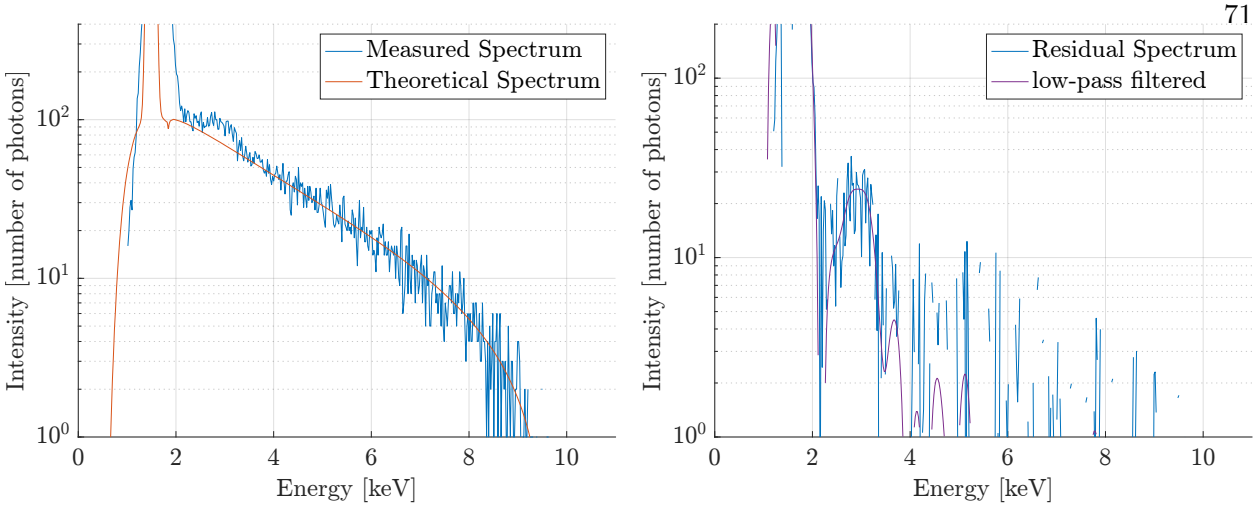

(a) Total Spectrum

(b) Residual Spectrum

Figure 3.14: Sample Spectrum for 80°. $\Phi_B = 0$ kV, $\Phi_P = -3$ kV

differential charging. For a fitting window of 1.5 keV, potential differences less than 1.5 kV cannot be detected. This also limits how many different potentials can be detected. Only six 1.5 keV windows fit into a spectrum with a maximum energy of 10 keV, restricting the theoretical number of potentials that can be detected to six. The attenuation of low energy x-rays within the x-ray detector likely decreases this number even further. Characteristic peaks inside the fitting window can be removed using the Matlab function `findpeaks` to avoid any interference of the peaks with the fitting process. This procedure is recommended in Ref. 45 to filter out characteristic radiation from the bremsstrahlung radiation.

Figure 3.15a shows a spectrum for 30°, where the electron beam impacts on both the bus and the panel. The maximum photon energy is determined and the corresponding theoretical spectrum computed. Here, the measured spectrum clearly deviates from the theoretical one. The residual spectrum in Fig. 3.15b is relatively high in intensity and approximately resembles an individual x-ray spectrum including both characteristic radiation and Bremsstrahlung radiation. The estimated landing energy for the residual spectrum is approximately 7 keV, which yields an estimated potential of about -3 kV. Using the estimated landing energy, another theoretical spectrum is computed, which approximately matches the residual spectrum.

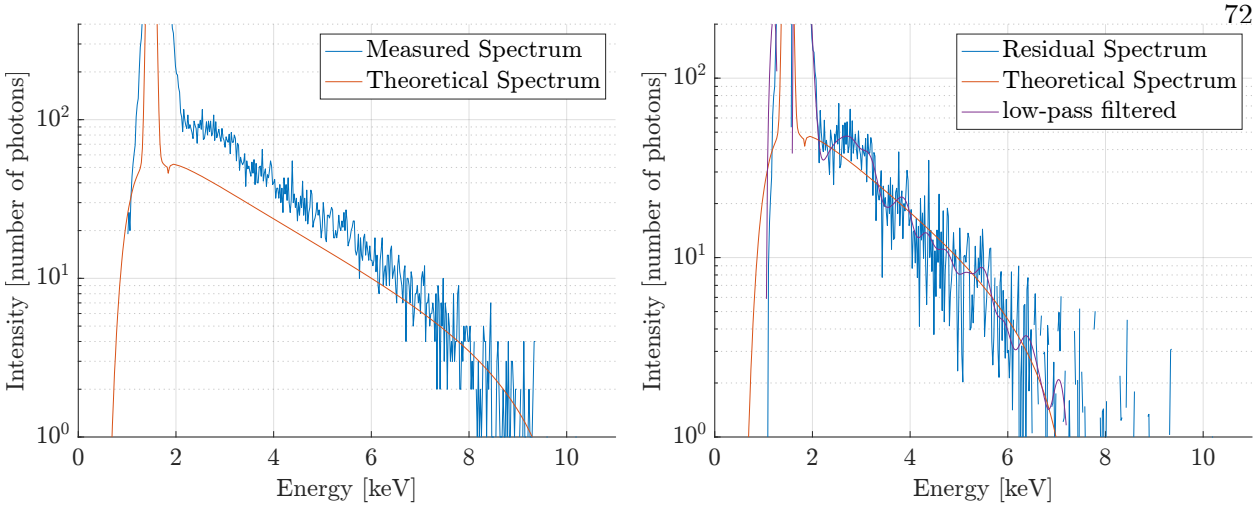

(a) Total Spectrum

(b) Residual Spectrum

Figure 3.15: Sample Spectrum for 30°. $\Phi_B = 0$ kV, $\Phi_P = -3$ kV

The estimated potential as a function of the target object orientation for the given electrode configuration ($\Phi_B = 0$ kV, $\Phi_P = -3$ kV) is presented in Fig. 3.16. Estimation 1 employs the total measured spectrum and always measures the highest potential (least negative or most positive potential). Estimation 2 uses the residual spectrum. The recorded x-ray spectrum is strictly positive (positive number of photon counts), with the highest number of bremsstrahlung x-ray photons in the 2-4 keV energy range due to the x-ray detector efficiency (Fig. 3.2). If the recorded x-ray spectrum includes information of two individual potentials, then the residual spectrum is also expected to be positive in this energy range (Fig. 3.15b). However, if the photon count in the 2-4 keV energy range is very low or even negative, it is likely just noise and does not represent a separate signal from another component (Fig. 3.14b). Thus, no second estimation is performed if the intensity of the residual spectrum is below a certain threshold between 2 keV and 4 keV, as this is an indicator that likely no second potential is present in the recorded spectrum (in this context, the second potential is the more negative potential). A threshold of 15 photons per energy was found to be effective for the given experimental setup, but might have to be adjusted for a different electron beam current, accumulation time and distance between the x-ray source and the detector, as this affects the intensity of the measured spectrum. This means that the residual spectrum is

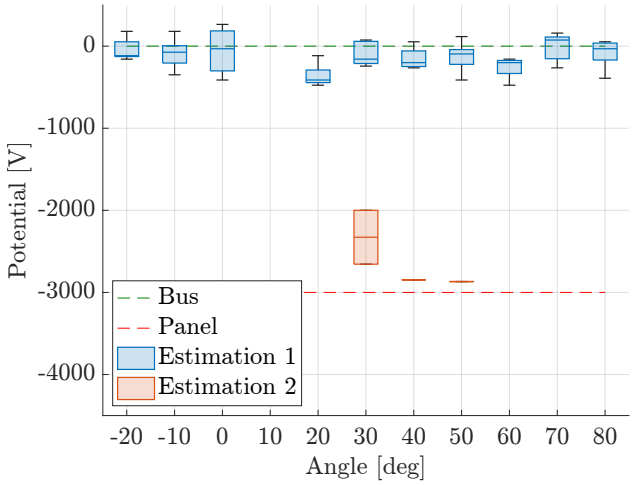

Figure 3.16: Wide Beam Results. $\Phi_B = 0$ V, $\Phi_P = -3000$ V

rejected and no second estimation is performed if the low-pass filtered residual spectrum is below 15 photons at some point between 2 keV and 4 keV. Alternatively a relative threshold could be used, for example 1% of the maximum intensity of the recorded spectrum. The first estimation always measures the highest potential, which is equal to 0 kV. When the beam impacts on both target object components (30°), the second estimation measures the lower potential of −3 kV. The low intensity of the residual spectrum results in a bad signal-to-noise ratio, which is disadvantageous for estimating the electric potential and likely the reason for the low accuracy of the second estimation. For orientations of 40° and 50°, all but one residual spectra are rejected due to low intensity, and the corresponding box-plots consist of only a horizontal line representing the single second estimation attempted for that angle.

The results suggest that it is possible to detect two potentials simultaneously with a single x-ray spectrum, using a theoretical Bremsstrahlung model. The theoretical model depends on the atomic number of the target element, so the material of the target must either be known or identified by the characteristic peaks of the measured spectrum. However, the occasion of an electron beam simultaneously hitting multiple components charged to different potentials is rather rare and highly dependent on the geometry of the target object and the electric field. A more realistic scenario is that the electron beam impacts multiple spacecraft components of a rotating object during a given

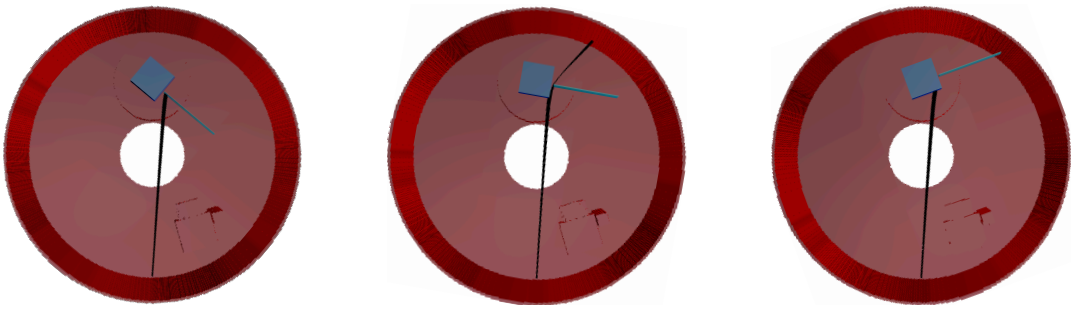

(a) 50° (b) 80° (c) 110°

Figure 3.17: Beam trajectories for dynamic experiment from SIMION simulation. $\Phi_B = -3$ kV, $\Phi_P = -1$ kV

sensing interval. Here a beam is moving across the spacecraft surface and exciting surface elements at different potentials in a sequential rather than parallel manner.

3.3.5.2 Dynamic experiments with rotating object

All experiments in prior electric potential sensing work were static, meaning that the target object did not move while the x-rays were counted with the detector. Objects in space such as retired or uncooperative satellites might tumble with rotational rates of several degrees per second [11, 12] due to solar radiation pressure or impacts of micro-meteoroids, which motivates dynamic experiments with rotating target objects. This is especially interesting for measuring multiple potentials simultaneously as the electron beam moves from one component to another during the sensing time frame.

An electron beam spot with a half-cone angle of about 0.5° is centered on the phosphor screen for a spacecraft angle of −30° and grounded components. The target object is rotated 30° with different starting angles, and the stepper motor speed is chosen such that this takes about 20 seconds. While the object is rotating, an x-ray spectrum is recorded using an accumulation time of 20 seconds, meaning that x-rays of all energies between a few eV and 20 keV are recorded simultaneously during a time frame of 20 seconds. Thus, if the electron beam impacts different components during the rotation of the target object, the resulting x-ray spectrum includes x-rays

excited from both components. Experiments are performed with starting rotation angles between 0° and 80°, in 10° steps. Each experiment is repeated 20 times.

Figure 3.17 illustrates the electron beam trajectories for a bus potential of $\Phi_B = -3$ kV and a panel potential of $\Phi_P = -1$ kV. For angles up to about $70° - 80°$, the electron beam impacts only on the panel. At about 80°, the beam transitions to the spacecraft bus, and at 110° the beam impacts only on the bus. Angles above 110° are not possible for the given experimental setup, as the spacecraft panel comes too close to the chamber wall.

The experiments conducted for this section include a bus potential of -3 kV and panel potentials of 0 kV and -1 kV. Figure 3.18a shows the estimated potential for a bus potential of -3 kV and panel potential of -1 kV as a function of the orientation of the target object. Estimation 1 accurately measures the potential of the spacecraft panel over all angles. Estimation 2 measures the potential of the cube for higher angles, where the beam impacts the cube. The reason why the second estimation is not as accurate is the low intensity of the residual spectrum. In one case ($40° - 70°$), a second estimation is attempted for one of the 20 samples, even though no second potential should be detected for these angles. Figure 3.18b shows the experimental results for a bus potential of -3 kV and panel potential of 0 kV. The results are similar to Fig. 3.18a. The first estimation measures the potential of the panel relatively accurately, while the second estimation is less accurate due to the low intensity of the residual spectrum. The presence of a second potential is detected for orientations between 70° and 110°.

3.3.6 Detectability of differential charging of a rotating object

To detect the presence of multiple potentials in a realistic scenario of application, the electron beam needs to irradiate the corresponding component for a sufficient amount of time. This determines how fast the target spacecraft can rotate such that a measurement is still possible. Some of the residual spectra of the experiments here introduced have a total number of photons as low as $N_{\min} = 20,000$. Taking this as the minimum required value for the residual spectrum to detect the second potential, the maximum rotational rate is determined by the flux of photons arriving

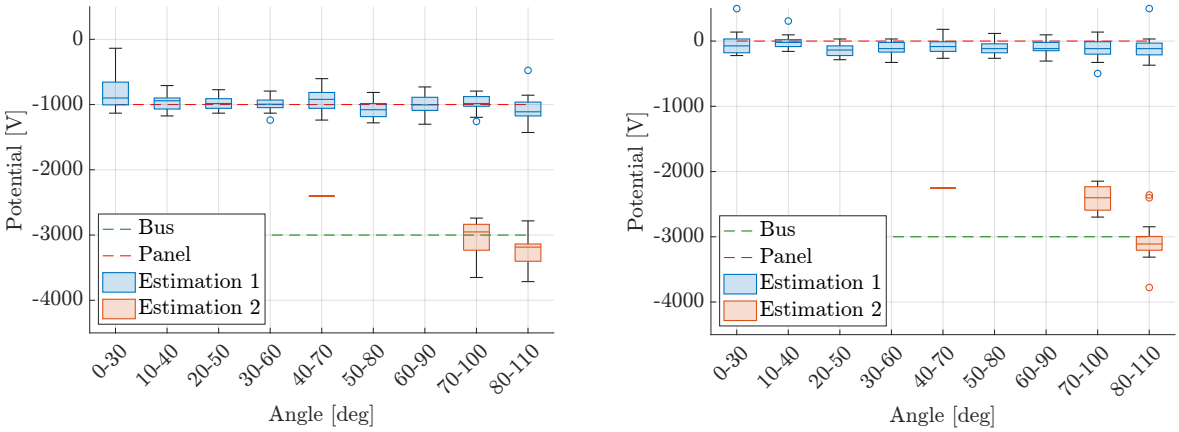

(a) $\Phi_B = -3000$ V, $\Phi_P = -1000$ V

(b) $\Phi_B = -3000$ V, $\Phi_P = 0$ V

Figure 3.18: Dynamic Experiment Results

at the detector. Using the theoretical x-ray models provided in Sec. 3.1.2 and Eq. (3.8) with a distance between the detector and the target of $L = 15$ m and a detector area of $A_{\text{det}} = 70$ mm^2, a count rate of about $f = 3,400$ photons per second is found for an electron beam current of $I_{EB} = 100$ µA and a beam energy of 10 keV. Therefore, the target spot needs to be irradiated for at least $t_{\min} = N_{\min}/f = 5.9$ s. Assuming for simplicity a spherical aluminum spacecraft of $R_{\text{SC}} = 1$ m radius and a characteristic co-centered beam spot radius of $R_b = 1.5$ cm at 15 m [105], the maximum rotational rate that allows the collection of x-ray photons from a small component with a width of $L_t = 20$ cm located on the equator of the sphere becomes

$$\omega_{\max} = \frac{(L_t + 2R_b)/t_{\min}}{R_{\text{SC}}} \tag{3.10}$$

which returns 2.2 deg/s for the problem under consideration. Larger components will be irradiated for longer times, increasing the maximum allowed rotational rate. A Silicon Drift Detector (SSD) with an area of 70 mm^2 is the largest x-ray detector available from Amptek and is capable of count rates over 1,000,000 counts per second.[3] The maximum rotational rate can be increased by using several detectors to increase the effective detector area. In the case of the experimental setup used in this work, the beam impacts the cube (the component with the second potential) over more than

[3] https://www.amptek.com/products/x-ray-detectors/fastsdd-x-ray-detectors-for-xrf-eds/fastsdd-silicon-drift-detector (Consulted on: 05/23/2025)

20 degrees, allowing for rotational rates of more than 5 deg/s with a 6 mm^2 detector and a beam current of 1 µA.

3.4 Multiple materials

It is demonstrated in the previous section that it is possible to identify differential charging and measure multiple potentials simultaneously using the x-ray method. However, the experimental setup from Sec. 3.3.1 only allows for two different potentials, so the residual spectrum approach can only be applied once. Additionally, both the cube and panel used in the previous experiments are made of aluminum. With a characteristic peak at 1.49 keV, the characteristic peak of aluminum is far away from the the higher energy part of the spectrum that is used to fit the intensity of the theoretical spectrum and to estimate the landing energy. A characteristic peak in the higher energy part of the spectrum is expected to interfere with the estimation of the potential. As recommended in Ref. 45, characteristic peaks are removed from the recorded spectrum using Matlab's `findpeaks` function. This process removes the data points within the energy range of the characteristic peak, which also removes any information about the bremsstrahlung radiation in this energy range. Valuable data points needed for the generation of the theoretical spectrum as well as the estimation of the landing energy are consequently missing, which affects the linear fitting that is performed.

This set of experiments aims at identifying differential charging under more difficult conditions, including measuring three instead of just two potentials and the presence of characteristic peaks in the higher end of the x-ray spectrum.

3.4.1 Experimental Setup

The experimental setup is for the most part similar to that described in Sec. 3.3.1 and used in Sec. 3.3. Instead of one aluminum panel, two panels are attached to the cube and charged to different potentials, as shown in Fig. 3.19. One panel is made of copper (Cu) and the other panel is made of titanium (Ti). The dimension of both panels is $155 \times 50 \times 0.85$ mm. The angle that

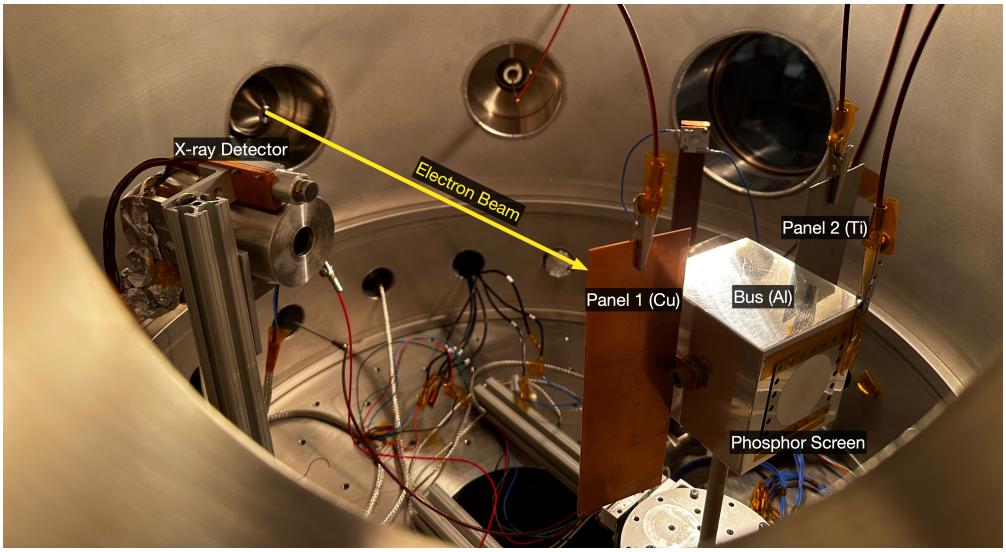

Figure 3.19: Experimental setup with two panels

describes the orientation of the target object is defined to be zero when the phosphor screen is facing the electron beam (perpendicular to the unperturbed, straight electron beam). Finally, the potential of the three components (i.e. cube, copper panel and titanium panel) is controlled by three high voltage power supplies. Two Matsusada AU-30R1 power supplies are used to control the potential of the cube and the titanium panel, capable of providing potentials up to 30 kV. The potential of the copper panel is maintained by a Spellman SL300 power supply that is limited to potentials of up to 1 kV.

3.4.2 Beam steering

The electron gun of the ECLIPS facility has the capability to steer the electron beam in the X and Y direction (perpendicular to the direction of the beam) by applying a voltage between -300 V and $+300$ V to two separate deflection grids located near the exit of the electron gun. By changing the deflection voltages, one can aim the electron beam at different locations and components without changing the orientation of the target. This capability is employed here to excite x-rays separately from each of the three target components and the chamber wall. An electron beam energy of $E_{EB} = 12$ keV is used with a beam current of $I_{EB} = 5$ µA. The beam

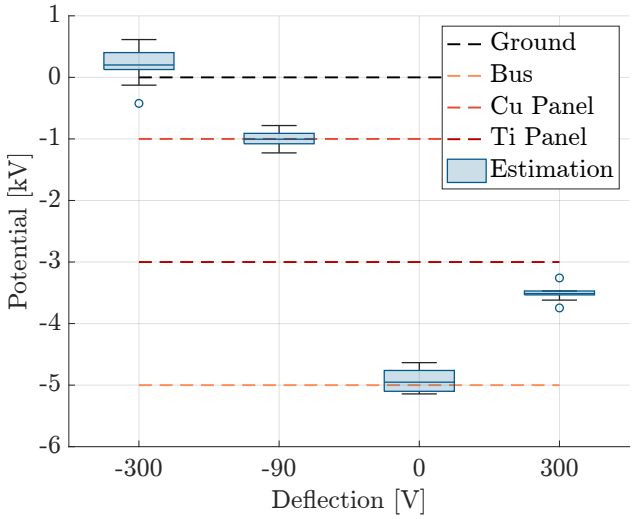

Figure 3.20: Estimated potentials for different beam deflections

focus is set to $V_F = 6$ V, resulting in a spot size of about 3 mm in diameter, and the orientation of the target is set to an angle of 210 degrees. Various deflections in the X direction between -300 V and $+300$ V are used, and 10 spectra are recorded for each deflection, over a time period of 20 seconds. All components of the target are at different potentials, with the bus (Al) at $V_B = -5$ kV, panel 1 (Cu) at $V_{P1} = -1$ kV, and panel 2 (Ti) at $V_{P2} = -3$ kV.

Figure 3.20 shows a box plot with the estimated potential for each value of deflection. The horizontal line inside of each box corresponds to the median of the data, and the bottom and top edges of the box represent the 25% and 75% percentiles. The black whiskers indicate the minimum and maximum of each data set, excluding outliers. Outliers are represented by circles and are values that are more than $1.5 \cdot IQR$ away from the bottom or top of the box, where IQR is the difference between the top and bottom box edges (interquartile range). The estimated potentials are reasonable accurate, with the exception of the titanium panel. One possible reason for this could be the relatively weak x-ray signal from the titanium panel, as the panel is located on the far side of the cube with respect to the x-ray detector, and part of the cube is blocking the sensor's view of the panel.

3.4.3 Simultaneous estimation

One of the limitations of the proposed approach is that the signal of some components may be significantly lower than that of other components, which makes the estimation of the potential less accurate. To investigate how many different potentials can be estimated from a single spectrum in a best-case-scenario, the spectra from the individual components used in Sec. 3.4.2 are manually super-imposed (without the spectrum from the chamber wall). This way, the signal from each component is similar in intensity. A sample super-imposed spectrum is shown in Fig. 3.21a, with the characteristic peaks for aluminum, titanium and copper visible. The highest (least negative) potential is estimated from this total spectrum, corresponding to the -1 kV of the copper panel. A theoretical spectrum for copper is generated and subtracted from the total spectrum, yielding the residual shown in Fig. 3.21b. The next potential is estimated the same way as the first one, but using the residual spectrum from the first estimation (Fig. 3.21c), corresponding to the -3 kV of the titanium panel. By subtracting the theoretical spectrum for titanium and for the given landing energy, another residual spectrum is obtained as shown in Fig. 3.21d and used to estimate the potential of the bus at -5 kV (Fig. 3.21e). The final residual spectrum in Fig. 3.21f is mostly noise.

Note that, even though the characteristic peaks are shown, the are identified using Matlab's `findpeaks()` function and removed for the estimation of the landing energy with the linear curve fit [45]. However, the presence of characteristic peaks in the upper energy part of the spectrum may still interfere with the estimation of the electric potential. First, removing the peaks essentially reduces the number of data points used for the linear fit. Linearly interpolating between the two endpoints of the removed characteristic peak is also disadvantageous because the least-squares solution would over-fit to the linearly interpolated part. Second, a characteristic peak in the upper end of the spectrum may also interfere with fitting the intensity of the theoretical spectrum, which in turn affects the estimated potential from the following residual spectrum. These challenges are not encountered in Sec. 3.3 on differential charging, because only aluminum components were used with a characteristic peak at 1.5 keV that is far away from the upper energy part of the spectrum.

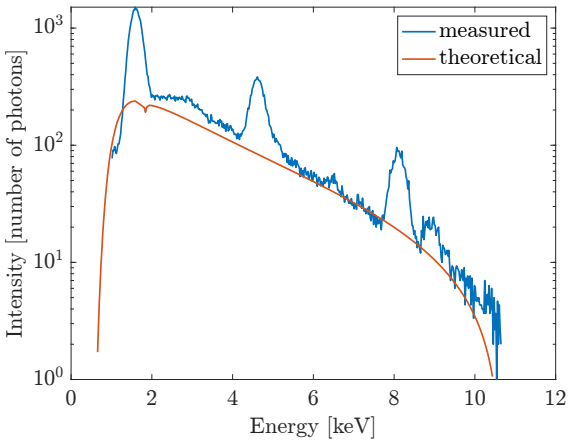

(a) original recorded spectrum

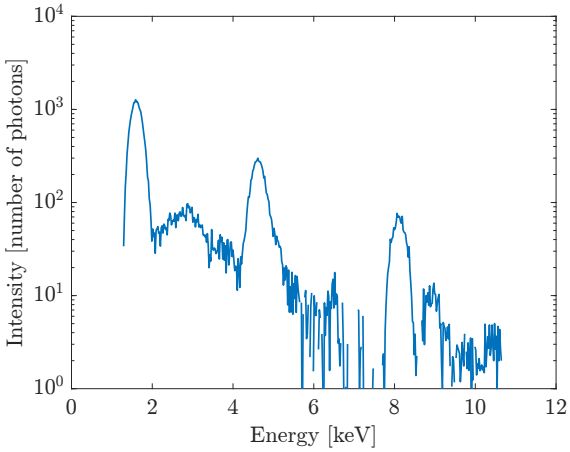

(b) first residual spectrum

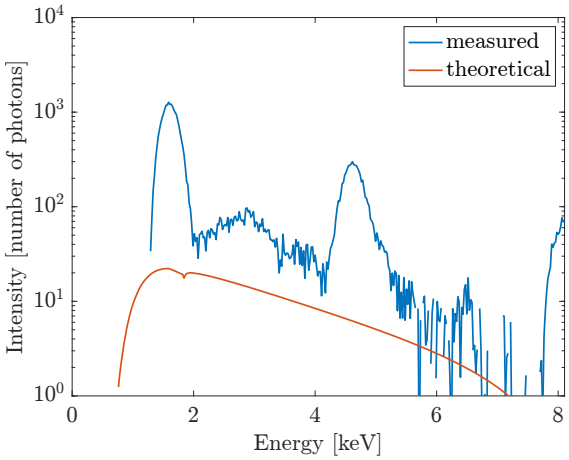

(c) residual spectrum from first estimation

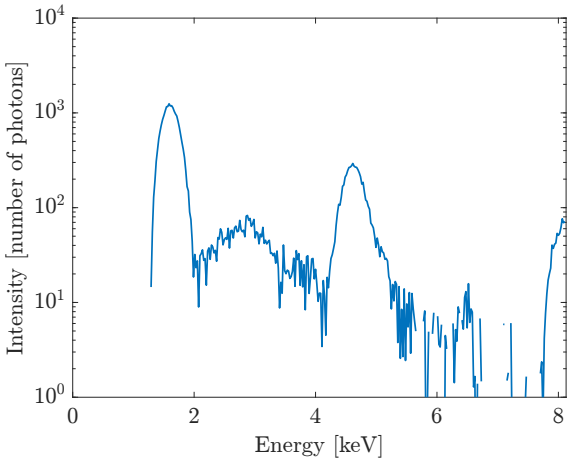

(d) second residual spectrum

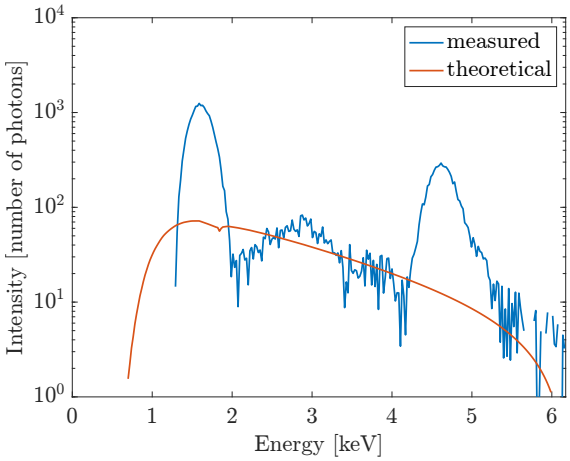

(e) residual spectrum from second estimation

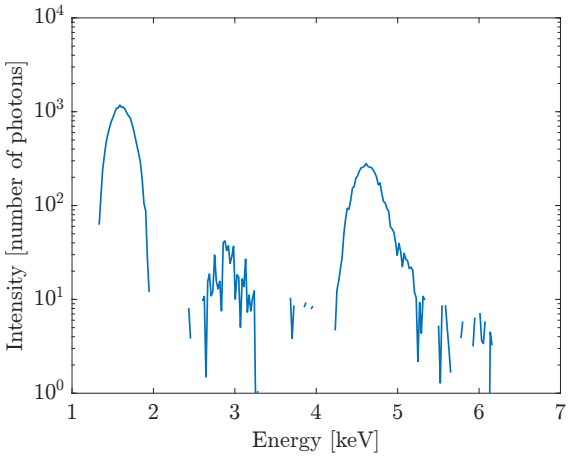

(f) third residual spectrum

Figure 3.21: Sample spectra for two-panel test object with multiple materials

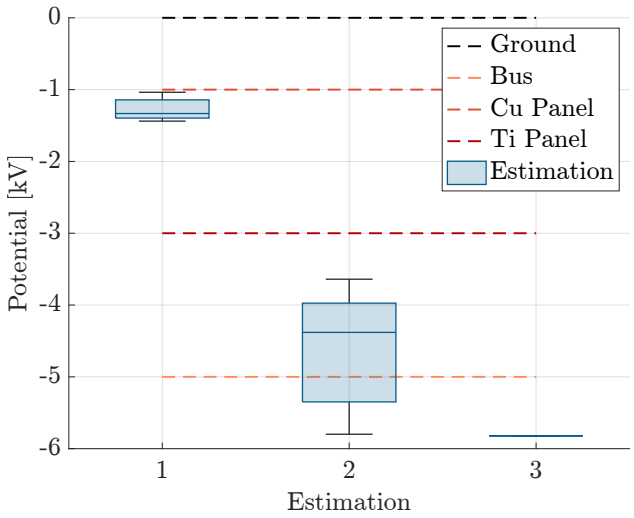

Figure 3.22: Simultaneous estimation of potentials

Figure 3.22 shows a boxplot with the estimated potentials for each estimation step. Estimation 1 measures the highest potential, and each following estimation step measures the next lower potential. The errors of each estimation affect the next estimation, so the estimations become less accurate with every step. Additionally, a misfit of the intensity of the computed theoretical spectrum may decrease the intensity of the following residual spectrum, which also makes the next estimation less accurate. A beam energy of 12 keV was chosen for this set of experiments to clearly show all characteristic peaks, including copper at 8.05 keV. However, such a high beam energy negatively affects the accuracy of the x-ray method [45], also contributing to larger errors in this experimental set.

3.5 Sensing time

All experiments within this work are conducted with an x-ray accumulation time of 20 seconds, meaning that x-rays are measured continuously for 20 seconds to create the recorded spectra shown in various figures. While a longer accumulation time improves the signal-to-noise ratio, it also affects the temporal resolution of the x-ray method when several spectra are recorded in a row to allow for a continuous estimation of the electric potential. Conversely, a shorter accumulation time improves the temporal resolution, but at the cost of the signal quality. It is of interest to

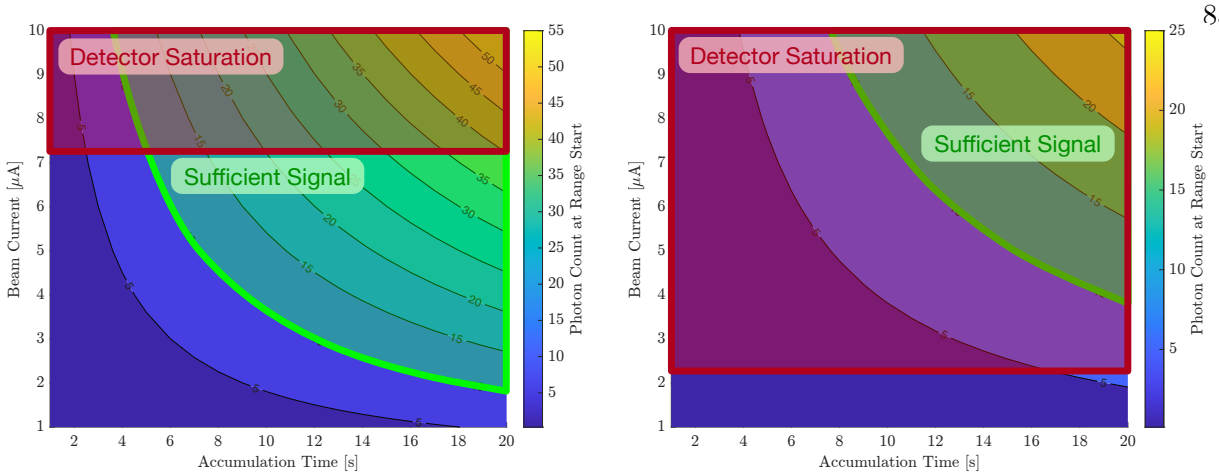

(a) 10 keV landing energy

(b) 20 keV landing energy

Figure 3.23: Photon count at range start of estimation linear fit as function of accumulation time and beam current for chamber conditions

find the shortest possible x-ray accumulation time while ensuring a sufficient signal. Similar to the accumulation time, a higher beam current also results in a better signal as more photons are excited per second (see Eq. (3.8)), so the minimum sensing time depends directly on the beam current. However, there exists an upper limit for the beam current to avoid detector saturation. The number of photons detected by the x-ray sensor per second also depends on geometric factors such as the distance L between the detector and the x-ray source region on the target object (the location where the beam impacts the target) and the detector area A_{det}. The number of detected photons is also influenced by other factors such as the fraction of the beam that actually impacts the target as well as components of the target possibly obscuring the field of view of the x-ray sensor. Because these two factors are unknown, they are not considered in this analysis. To investigate this, theoretical spectra are created for a given landing energy according to Sec. 3.1.2 and scaled by the accumulation time t_{accum}, beam current I_{EB}, detector-source distance L and detector area A_{det}. The analysis includes both the experimental conditions in ECLIPS as well as potential in-orbit conditions.

3.5.1 Chamber conditions

First, the minimum sensing time is investigated for the conditions in the ECLIPS chamber, corresponding to the experiments in Secs. 3.3 and 3.4. For the chamber setup, values of $L = 20$ cm and $A_{\text{det}} = 6$ mm^2 are used, and the maximum photon count rate to avoid detector saturation is equal to $10,000$ photons per second. As explained in Sec. 3.3.3, a linear fit is performed within an energy range in the higher energy part of the spectrum to estimate the landing energy and consequently the electric potential. The experiments in this chapter showed that a photon count of 10 at the lower end of that energy range is needed to obtain good estimation results. Thus, this is considered to be the threshold for a sufficient signal to obtain an accurate measurement for this analysis. Figure 3.23 shows this theoretical photon count as a function of accumulation time and beam current for two different landing energies. As expected, the critical photon count increases with increasing accumulation time and increasing beam current. Figure 3.23a shows the results for a landing energy of 10 keV. Because the photon intensity of the recorded spectrum scales linearly with both accumulation time t_{accum} and beam current I_{EB}, as can be seen in Eq. (3.8), two different accumulation times and beam currents for a given photon count and landing energy are related through

$$I_{EB,1} \cdot t_{\text{accum},1} = I_{EB,2} \cdot t_{\text{accum},2} \tag{3.11}$$

For a beam current of 2 µA, an accumulation time of 20 seconds is needed. Increasing the beam current to 6 µA reduces the required sensing time to approximately 6 seconds. In theory, the beam current could be increased even further to enable a sensing time of 1 second, for example. However, the detector saturation count rate limit of $10,000$ photons per second limits the maximum beam current. This maximum beam current is about 7.3 µA for the given scenario, limiting the minimum sensing time to about 5 seconds. The figure also illustrates that when a lower beam current than 2 µA is desired, for example to avoid significantly changing the target potential while sensing (Sec. 4.3), the accumulation time must be increased to more than 20 seconds.

Figure 3.23b shows the results for a landing energy of 20 keV. Because a higher landing

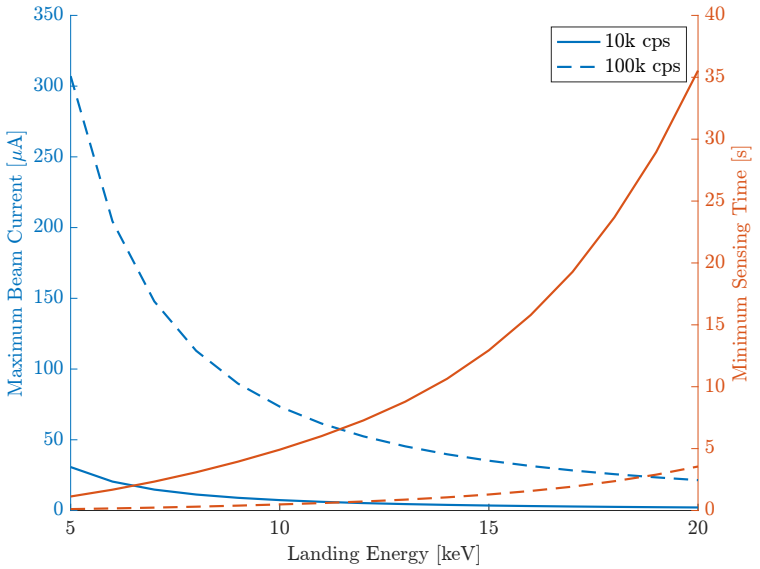

Figure 3.24: Sensing time and max. beam current to avoid detector saturation for chamber conditions

energy excites photons from a wider range of photon energies, the number of photons excited for a given beam current is higher than for a lower landing energy. Thus, the maximum beam current for 20 keV is only about 2.1 µA. Additionally, because the photons are distributed over a wider range of energies, it takes more accumulation time or a higher beam current to obtain a sufficient photon count at the range start of the linear fit. Consequently, the minimum sensing time for a landing energy of 20 keV is about 35 seconds.

The effect of landing energy on the sensing time and maximum beam current is summarized in Fig. 3.24. The maximum beam current to avoid detector saturation is determined for a given landing energy. Using this beam current, the minimum sensing time is then computed. Because the maximum beam current decreases with increasing landing energy, the minimum sensing time increases. For a landing energy of 5 keV, the minimum sensing time is about 2 seconds, while a landing energy of 20 keV requires a minimum sensing time of about 35 seconds. One way to reduce the minimum sensing time is to use an x-ray detector with a higher maximum count rate.[4] The higher possible count rate increases the maximum beam current, which in turn decreases the

[4] https://www.amptek.com/products/x-ray-detectors/fastsdd-x-ray-detectors-for-xrf-eds/fastsdd-silicon-drift-detector (Consulted on: 05/23/2025)

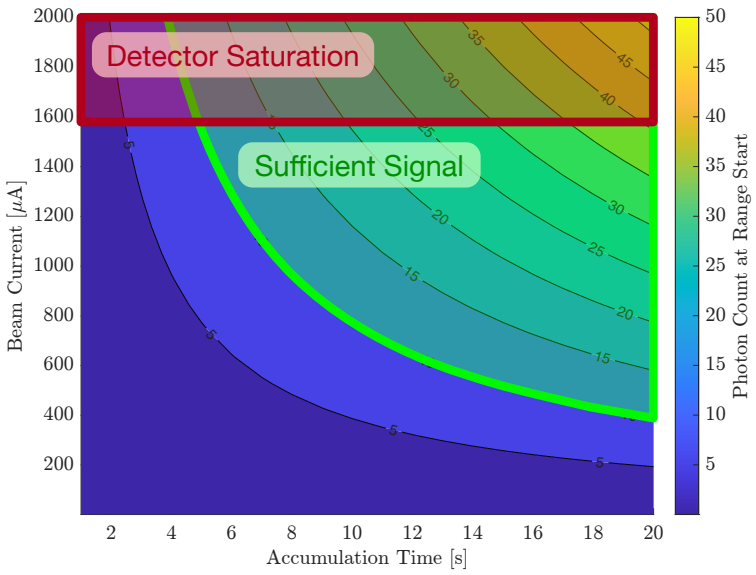

Figure 3.25: Photon count at range start of estimation linear fit as function of accumulation time and beam current for orbital conditions and landing energy of 10 keV

minimum sensing time. This is shown by the dashed lines in Fig. 3.24 for a maximum photon count rate of 100,000 counts per second (cps). The Fast-SDD detector from Amptek has a maximum count rate of about 1,000,000 cps, but a limit of 100,000 cps is chosen here for illustration purposes. A detector with such a saturation limit would decrease the minimum sensing time to a fraction of a second for 5 keV and to about 3.5 seconds for 20 keV. Note that the effect of the electron beam on the potential of the target (Sec. 4.3) is not considered here. To reduce that effect, a lower beam current is desired, which in turn increases the required sensing time for a sufficient signal.

3.5.2 In-orbit conditions

To simulate in-orbit conditions, a detector-source distance of $L = 10$ m and a detector area of $A_{\text{det}} = 70$ mm^2 are assumed. This corresponds to the largest available detector from Amptek, with the same maximum photon count rate to avoid detector saturation of 10,000 photons per second. The threshold for a sufficient signal is still assumed to be 10 photons at the lower end of the energy range used for the linear fit. Figure 3.25 shows this theoretical photon count at the range start as a function of accumulation time and beam current for a landing energy of 10 keV

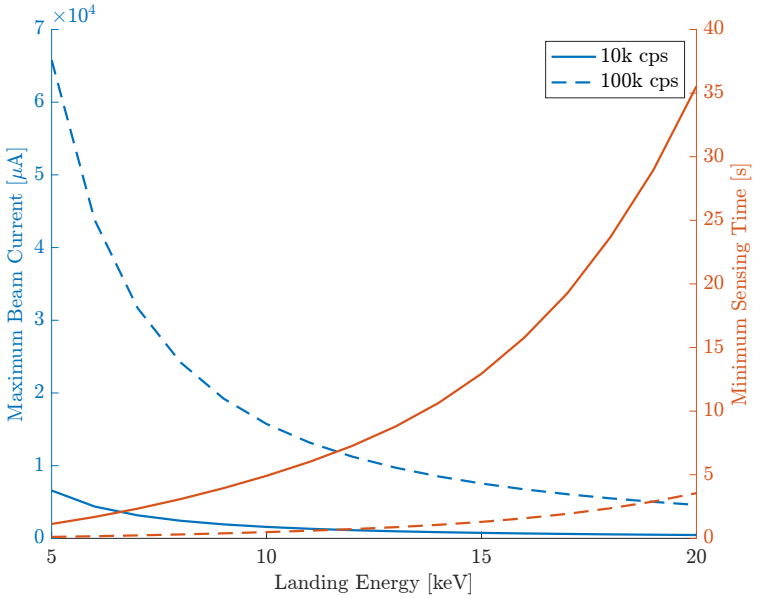

Figure 3.26: Sensing time and max. beam current to avoid detector saturation for orbital conditions

and in-orbit conditions. The general trend of Fig. 3.25 is similar to that of Fig. 3.23, but much higher beam currents are needed to produce a sufficient signal for the given range of accumulation times. This is because the solid angle $\Omega = A_{\text{det}}/L^2$ is much smaller for this orbital scenario than in the ECLIPS chamber. For a beam current of 400 µA, an accumulation time of 20 seconds is needed. Increasing the beam current to 1 mA reduces the required sensing time to approximately 8 seconds. The maximum beam current to avoid detector saturation is about 1.57 mA for the given scenario, limiting the minimum sensing time to about 5 seconds. To achieve very low beam currents to avoid significantly changing the target potential while sensing, while also ensuring a sufficient signal, much longer accumulation times are needed. For example, for a beam current of 10 µA, an accumulation time of almost 800 seconds (about 13 minutes) is required. Within this long period of time, the charging conditions (spacecraft orientation, plasma conditions, etc.) may have already changed drastically, leading to a different equilibrium potential.

Figure 3.24 illustrates the effect of landing energy on the sensing time and maximum beam current for orbital conditions. Because of the smaller solid angle, the maximum beam current is much higher for the in-orbit conditions compared to the chamber conditions in Fig. 3.24. The

maximum beam current is in the order of milli-Amperes for a maximum count rate of $10,000$ photons per second, and in the order of 10s of milli-Amperes for $100,000$ cps. However, the minimum sensing time for orbital conditions is the same as for chamber conditions. This is because for both conditions, the resulting maximum beam current yields a count rate equal to the maximum count rate. For chamber conditions, this is achieved by a larger solid angle $\Omega = A_{\text{det}}/L^2$, while for orbital conditions it is achieved by a higher beam current.

3.5.3 Implications for active debris removal and on-orbit servicing

The conditions and goals for electric potential sensing are different for active debris removal and on-orbit servicing. For active debris removal with the Electrostatic Tractor method, a high beam current in the order of hundreds of micro-Amperes to milli-Amperes is used to achieve electric potentials of $\pm$20-30 kV on each spacecraft. The goal is to use the estimation of the electric potential as feedback for the control of the electric potential via active charging control, as well as for an approximation of the electrostatic force to be fed-forward to the relative motion control. Thus, the findings for the maximum beam current and minimum sensing time are promising, as short sensing times are achievable with beam currents that are in the order of magnitude of the beam currents to be used for the Electrostatic Tractor. For on-orbit servicing, both spacecraft are assumed to be at their natural potential. In this case, one may want to measure the natural potential of the target without actually changing the potential. This requires low beam currents in the order of a few micro-Amperes of even lower (Sec. 4.3). According to Fig. 3.25, such low currents require accumulation times in the order of 10s to 100s of seconds. The potential of the target may change drastically within that time due to a different spacecraft orientation or varying plasma conditions. Thus, these results indicate that the active sensing methods with an electron beam [35, 36] may not be beneficial for on-orbit servicing scenarios. Instead, passive methods that do not require an electron beam to sense the potential of the target can be used [48] for on-orbit servicing applications.

3.6 Conclusions

The estimation of electric potentials of complex-shaped differentially charged objects is investigated using x-ray spectroscopy. A shape primitive with box and panels charged to different potentials is used as a test object. The experiments show that the orientation of the target object and the deflection of the electron beam affect the landing location of the electron beam. This is also confirmed by numerical simulations with SIMION. Thus, the orientation of the object affects which component's potential is measured. Using a focused electron beam with a small landing spot size helps to excite x-rays from only one component at a time. For such an electron beam configuration and a non-rotating object, several x-ray spectra taken from different angles are required to measure the potential of multiple components.

To estimate multiple potentials simultaneously from a single x-ray spectrum, the beam must hit multiple components during the sensing time frame. This is achieved by either a wide electron beam that excites x-rays from multiple components simultaneously, or by a rotating target object that causes the beam to impact on different components over time. However, with the conventional x-ray spectroscopic method that was proposed in prior work and used in this work (see Sec. 3.1.1), only the higher potential of the two components can be measured. That is, only the potential that is either less negative or more positive is detected. A new method is proposed that uses theoretical x-ray models and the principle of superposition of individual x-ray spectra to measure multiple potentials using a single recorded x-ray spectrum. Experiments are conducted with a rotating target object to excite x-rays from multiple components during the sensing time frame, demonstrating that this new method can be used for simultaneous measurements. This is promising for the electric potential estimation of tumbling objects where the landing location of the electron beam changes during the recording time frame. Experiments with three components made of different materials and charged to different potentials show that the presence of characteristic peaks in the upper energy part of the x-ray spectrum provides some challenges for the potential estimation, and that the estimation becomes more inaccurate with every additional potential that is measured from a

single spectrum.

Finally, a theoretical study of the required sensing time shows that minimum sensing times in the order of a few seconds or even less than a second are possible with the beam currents used for the Electrostatic Tractor. However, for on-orbit servicing, where very low beam currents may be required to avoid changing the potential of the target, sensing times in the order of 10s to 100s of seconds are required to produce a sufficient x-ray signal. This makes the passive x-ray method [48] more promising for on-orbit servicing applications.

Chapter 4

Spacecraft charging using a continuous electron beam

An electron beam enables both the estimation of the electric potential as well as the active and controlled charging of a nearby target satellite. For active debris removal with the Electrostatic Tractor method, high beam currents in the order of hundreds of micro-Amperes to milli-Amperes are used to achieve electric potentials of ±20-30 kV on each spacecraft. Additional to the high beam current needed to overcome the plasma currents and the photoelectric current, a high beam energy of 60 keV is required to achieve such high potentials of the target and servicer. For on-orbit servicing, the assumption is made that the natural potential of the target is supposed to be measured, so low beam currents are needed to avoid changing the potential of the target. Investigating the effects of a continuous electron beam on the transients and equilibria of the servicer and target potential enables the development of electric potential control strategies for the Electrostatic Tractor. Moreover, it provides insight into how much the beam current affects the equilibrium potential of the target while sensing the electric potential for on-orbit servicing operations.

This chapter investigates the effects of electron emission and impact on the transients and equilibria of the servicer and target potential. Section 4.1 highlights the different effects of beam current and beam energy. As discovered within this work, the electron beam causes multiple equilibria to exist under certain conditions [97], even in a single-Maxwellian plasma. This is studied in Sec. 4.2. Finally, the equilibrium potentials due to the electron beam in geostationary orbit and cislunar space are investigated in Sec. 4.3.

4.1 Electron beam parameters: current and energy

In Chapter 11 of Ref. [18], spacecraft charging due to electron beam emission is figuratively compared to digging a hole. To dig a deeper hole, the amount of dirt thrown out of the hole must exceed the amount of dirt that falls into the hole. However, once the hole is as deep as one can throw, all the dirt that is attempted to be thrown out, falls back into the hole. That is, the initial kinetic energy of the dirt is not high enough to overcome the gravitational potential difference between the top and bottom of the hole, and the maximum depth of the hole is reached. Similarly, for a spacecraft that emits an electron beam, the outgoing electron beam current must be greater than the incoming currents. Because negatively charged electrons are emitted, the electron beam current on the servicer is positive, and must exceed the negative currents acting on the servicer in order to charge positively. The physical limit on how much the servicer can charge depends on the electron beam energy. Because the servicer charges positively, the emitted electrons are attracted back to the servicer. Once the electric potential of the servicer is as high as the beam energy, the electron beam electrons are unable to escape and come back to the servicer, resulting in a net zero electron beam current. In contrast to the simplified analogy of digging a hole with a constant amount of dirt going in and out of the hole, however, the final electric potential does not only depend on the electron beam energy, but also on the electron beam current. As the servicer charges positively, more electrons from the ambient plasma environment are attracted to the servicer. That is, the incoming currents increase, and a higher electron beam current is required to charge more positively. Without a higher electron beam current, the servicer cannot charge to the physical limit determined by the beam energy. The presence of another charged spacecraft, in this case the target spacecraft, affects the charging limits. The initial beam energy must be high enough to overcome the electric potential difference between the servicer and the target to ensure that the beam can reach the target and is not coming back to the servicer.

For a spacecraft that is irradiated by an electron beam, the secondary electron yield of the surface material plays an important role. As electrons impact on the surface, secondary electrons

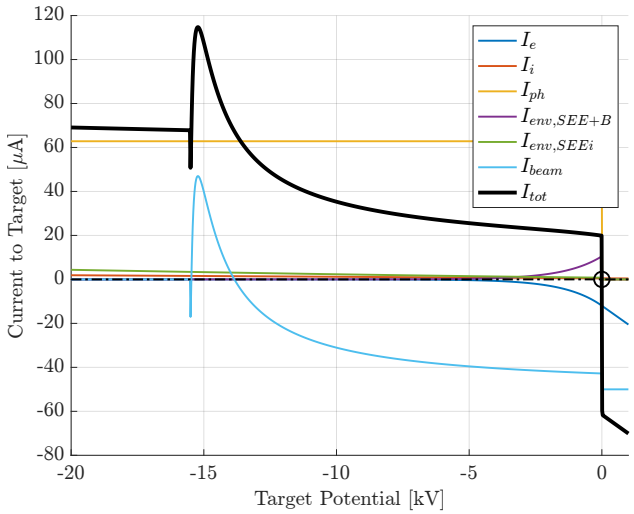

Figure 4.1: Currents vs. Potential of Target. $I_{EB} = 50$ µA, $E_{EB} = 20$ keV, resulting servicer equilibrium potential of about +4.5 keV

are excited that leave the material. If the spacecraft is charged negative, these secondary electrons are repelled by the spacecraft, resulting in a positive current due to the loss of negatively charged electrons. In a similar fashion, incoming electrons can also be backscattered, when the same electron enters and exits the surface material. The average number of secondary electrons generated per incoming electron depends on the effective energy of the incoming electron and is characterized by the secondary electron yield. The effective energy, also called landing energy or impact energy, is the kinetic energy of the incoming electron as it impacts on the surface. For some materials and effective energies, the secondary electron yield can exceed unity. This leads to the interesting charging behavior where an object is charged positively despite being irradiated with negatively charged electrons. Note that secondary electrons and backscattered electrons are different and can be modeled with two separate yield curves (the secondary electron yield and backscattered electron yield). Both are relatively uncertain and can change after long exposure to the space environment [51]. In this work, both yield curves are modeled combined with the model presented in Ref. [103], and the resulting combined yield is generally referred to here as secondary electron yield. Within this chapter, the servicer and target spacecraft are assumed to be spherical with radii equal to $R_S = R_T = 1$ m.

The photoelectric current and secondary electron currents induced by the ambient plasma electrons and ions as well as by the incoming electron beam are all excited from the surface with low kinetic energies. Thus, all of these currents are strong for a negatively charged spacecraft that repels the released electrons, but quickly drop to zero if the spacecraft is charged positively. This drop of current at about 0 V is clearly visible in Figure 4.1, where the various currents from Sec. 2.1 are shown as a function of the target potential. For this figure, an electron beam current of 50 µA and energy of 20 keV is used, resulting in a servicer potential of about +4.5 kV. Due to the relatively strong photoelectric current of over 60 µA, the equilibrium potential of the target is about 0 V (marked by the black circle).

Examining the total current (black line in Fig. 4.1) acting on the target as a function of the target potential helps to build understanding of electron beam induced spacecraft charging. Starting at the left side of the figure, the electron beam is not energetic enough to reach the target, so the net electron beam current is zero, and the photoelectric current and plasma ion current dominate. Given the servicer equilibrium potential of about +4.5 kV and the initial beam energy of 20 keV, the beam is energetic enough to reach the target for target potentials less negative than −15.5 kV. The total current quickly decreases by the intensity of the beam current of 50 µA, before increasing again due to the secondary electron emission induced by the electron beam. Note that the I_{beam} current in the figure includes both the beam current $I_{EB,T}$ and the resulting secondary and backscattered electron emission $I_{SEE,B,eb}$, that is, $I_{\text{beam}} = I_{EB,T} + I_{SEE,B,eb}$. Due to the maximum secondary electron yield of $Y_{\text{max}} = 2$ used here, the total current is even more positive than without electron beam impact. Progressing to the right in the figure, the total current is affected by the secondary electron yield, as well as the properties of the ambient plasma electrons and ions. At about 0 V, the total current drops quickly, because the photoelectrons and secondary electrons are attracted back to the positively charged spacecraft. This drop in current at 0 V explains the threshold of electron beam current required for the onset of charging. For the target spacecraft, a higher electron beam current essentially shifts the total current curve downward. The total current line is nearly vertical at 0 V, so if the equilibrium potential is about 0 V, it barely changes with

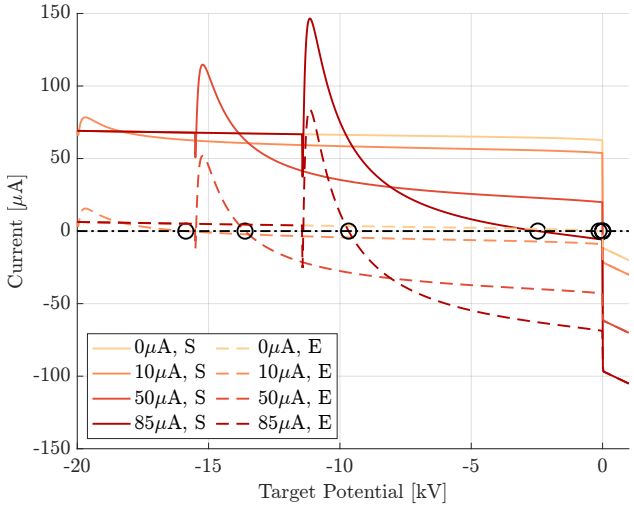

Figure 4.2: Current vs. Potential of Target for various beam parameters. $E_{EB} = 20$ keV

increasing or decreasing electron beam current. Once the chosen electron beam current exceeds a certain threshold (in Fig. 4.1 about 20 µA more, so a total of 70 µA), the total current line crosses 0 µA to the left of the vertical drop at 0 V, and the target charges negatively. Similar observations can be made for the servicing spacecraft, where a certain electron beam current is required in order to charge the servicer positively (for the servicer, the total current curve shifts upward with increasing electron beam current).

The effect of different beam currents on the equilibrium potential of the target is shown in Fig. 4.2. The equilibrium potentials are again marked with circles. The plasma parameters used here are $n_e = 0.95$ cm^{-3}, $T_e = 1400$ eV, $n_i = 0.75$ cm^{-3}, $T_i = 7100$ eV. A beam energy of 20 keV is chosen and the servicer and target spacecraft radii are $R_S = 1$ m and $R_T = 1$, respectively. Two different cases are considered. In one case, both the servicer and target are in sunlight (indicated by S). In the other case, the servicer is in sunlight but eclipses the target (indicated by E). Looking first at the sunlight cases (solid lines), the equilibrium potential is approximately zero for most beam currents. Only a beam current of 85 µA is strong enough to charge the target negatively in sunlight. For an eclipsed target, the natural potential (zero electron beam current) is also close to zero for the given plasma properties. Increasing the beam current drastically affects the potential of the target in eclipse, with equilibria of about -16 kV for 10 µA, -13 kV for 50 µA and -10 kV

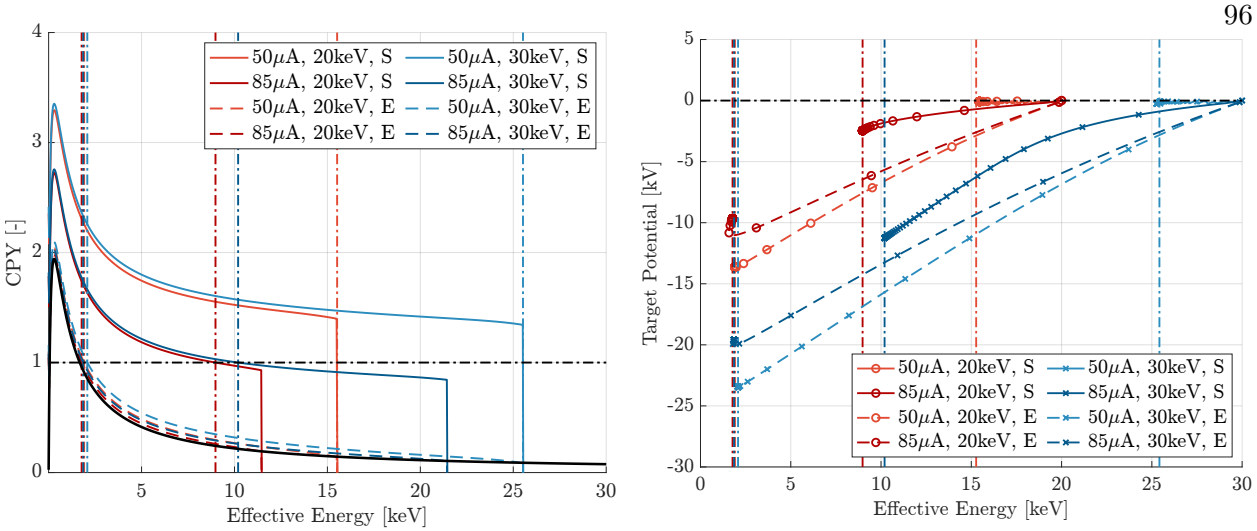

(a) Charged Particle Yield

(b) Transients

Figure 4.3: Charging as function of effective energy

for 85 µA. Notice that, for the given selection of beam currents, the equilibrium potential is more negative for a smaller beam current of 10 µA than for 85 µA. This relatively unintuitive effect is due the charging of the servicer. For a stronger beam current, the servicer charges more positively, thus decreasing the energy of the electron beam as it reaches the target and limiting the most negative possible potential of the target.

The secondary electron emission plays an important role in spacecraft charging. To generalize the idea of the secondary electron yield, the charged particle yield (CPY) is introduced, defined as

$$\mathrm{CPY}(\phi_T) = \frac{I_{\mathrm{tot},T}(\phi_T)}{I_{EB}} + 1 \tag{4.1}$$

That is, the CPY represents the number of outgoing electrons (and incoming ions) per incoming beam electron. For CPY = 1, the system is at equilibrium. Similarly to the secondary electron yield (SEY), the CPY is shown as a function of the effective energy $E_{\mathrm{eff}} = E_{EB} - \phi_S + \phi_T$ of the beam in Fig. 4.3a. The SEY used in this work is represented by the black line. If the system consisted solely of the electron beam hitting the target and the resulting secondary electron emission, this would also correspond to the CPY. The CPY for the 50 and 85 µA cases (both in sunlight S and eclipse E) from Fig. 4.2 are shown again for a beam energy of 20 keV in red, and additionally for

30 keV in blue. As discussed in the introduction, the x-ray and secondary electron methods for remotely estimating electric potential yield more information in certain ranges of effective energies. For the x-ray method, higher effective energies are preferred, because more elements of the surface can be identified while sensing the potential. For the secondary electron method, lower effective energies are preferred due to the higher secondary electron emission in this energy range, resulting in a better signal. Thus, plotting the CPY as a function of the effective energy quickly illustrates which sensing method is better suited for a given charging scenario. In the figure, the CPY = 1 line is represented by the black dash-dotted line, and the effective energy for the equilibria of the various cases is indicated by the dash-dotted line in the corresponding color.

Figure 4.3b shows the dynamic charging behavior for the parameters from Fig. 4.3a. Starting at the natural potential of close to zero volts (no electron beam), the electron beam is turned on to charge both spacecraft. The lines approach the equilibrium effective energy on the horizontal axis and the equilibrium target potential on the vertical axis, and markers are placed at time steps of 10 ms to illustrate the time scale. The shape and orientation of the trajectories indicates whether or not the servicer is charging. If the line is horizontal, only the servicer is charging, and the effective energy is decreasing until the servicer has reached its equilibrium. If the line is straight but with a downward trend, only the target is charging, and a curve indicates that both spacecraft are charging at that moment. For an electron beam current of 50 µA in sunlight, only the servicer charges, while the target remains at approximately 0 V. In all other cases, both spacecraft are charging at the beginning, but the servicer reaches its equilibrium potential first. This plot illustrates nicely the effect of changing the electron beam energy. Increasing the electron beam energy by 10 keV essentially shifts the lines 10 keV to the right. If this barely changes the equilibrium potential of the servicer, then the charging trajectory intersects the line of the equilibrium effective energy approximately 10 kV lower than for the less energetic beam, resulting in a target equilibrium potential that is 10 kV more negative than before.

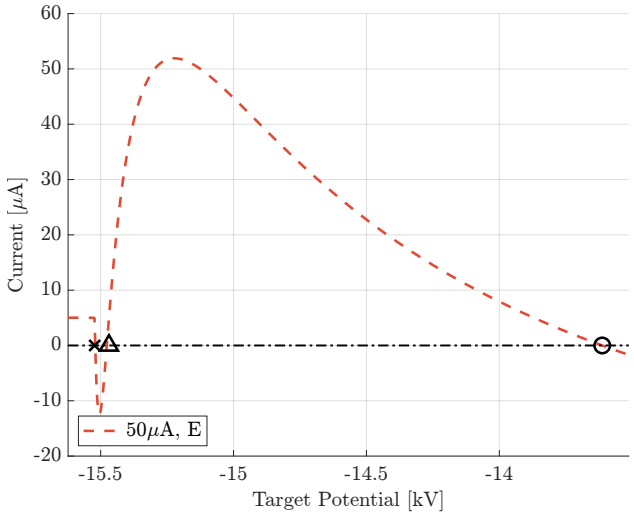

Figure 4.4: Multiple Equilibria: Left and right equilibria are stable, center equilibrium is unstable.

4.2 Multiple equilibria

4.2.1 Overview

Under specific circumstances the secondary electron emission due to electron beam impact can cause multiple equilibria to exist. This is also indirectly shown in [18, Chapter 9], but not in detail and any other currents besides electron beam induced currents are not considered. Multiple equilibria for spacecraft charging are known to exist for double-maxwellian plasma as discussed in [18, Chapter 5], but have not been recognized for single-maxwellian plasma. For example, multiple equilibria due to electron beam impact exist for the case of 50 µA in eclipse in Fig. 4.2, and is highlighted in Fig. 4.4. As discussed in Sec. 2.1, the equilibrium potential corresponds to the potential for which the total current is equal to zero. This occurs three times in Fig. 4.4 for the given charging model. There is a significant jump in current at the potential at which the electron beam is not energetic enough to reach the target, at about −15.5 kV in the figure (the servicer potential in this figure is +4.5 kV and the beam energy is 20 keV). If the total current is positive without the electron beam hitting the target, but smaller in magnitude than the electron beam current, then there is a zero crossing at this potential, corresponding to an equilibrium (×). Due to the secondary electron emission, which is especially high for effective energies below approximately 1-2

keV, the total current increases again with increasing potential, resulting in another zero crossing and equilibrium (Δ). With increasing potential (increasing effective energy of the electron beam electrons), the secondary electron emission weakens, resulting in another equilibrium potential where the total current is zero ($\circ$). The left and right side equilibria are stable, while the center equilibrium is unstable. For a slight negative deviation of the potential from the center equilibrium, the current is negative, so the potential drifts away further from the equilibrium. Similarly, for a slight deviation of the potential in the positive direction, the current is positive. Thus, the center equilibrium represents a divergence point. For multiple equilibria to exist, the conditions

$$I_{EB} > I_{tot,T}(\phi_T = \phi_S - E_{EB}, \phi_S) \tag{4.2a}$$

$$Y_{SEE,B,eb,\max} > 1 - \frac{I_{tot,T}(\phi_T = \phi_S - E_{EB} + E_{\max}, \phi_S)}{I_{EB}} \tag{4.2b}$$

must be fulfilled. If the first condition is not fulfilled, the beam current is not strong enough to dominate the natural current from the space environment, and only the right side equilibrium exists. Without the second condition, the secondary electron emission is not significant enough and only the left side equilibrium exists. In either edge case, the center equilibrium aligns with either the right or left equilibrium.

Note that Fig. 4.4 only shows the total current for one specific servicer potential, i.e. for the servicer equilibrium potential of +4.5 kV. For a different servicer potential, the total current on the target shifts, and so do the equilibria of the target. This is due to the coupling effect of the electron beam, as the potential difference between the two spacecraft can only be as high as the energy of the electron gun. For example, the currents in Fig. 4.1 are computed for a servicer potential of +4.5 kV. If the servicer potential was +5.5 kV, the electron beam induced currents on the target would shift by 1 kV to the right, also affecting the total current. Thus, some of the equilibria in Fig. 4.4 may not be achievable unless the servicer maintains a potential of +4.5 kV.

Figure 4.5 shows the time responses of the target potential (Fig. 4.5a) and servicer potential (Fig. 4.5b) for the same charging scenario as in Fig. 4.4 and for several initial conditions. The initial servicer potentials are $0, 1.5, 3, 4.5, 6$ kV and are indicated by the color of the lines. For each initial

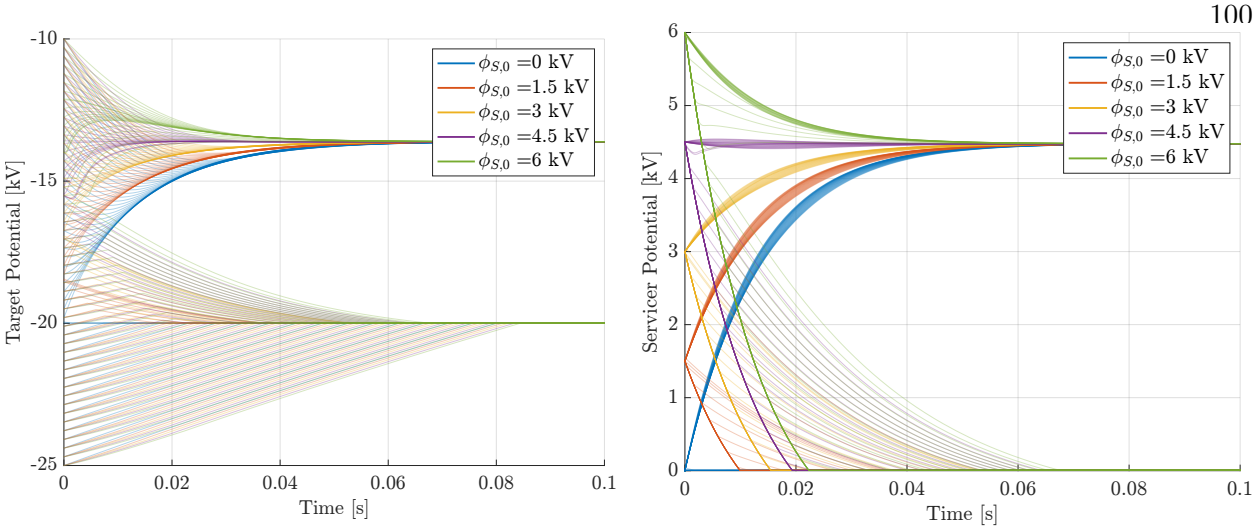

(a) Target

(b) Servicer

Figure 4.5: Multiple Equilibria Transients for various initial servicer potentials $\phi_{S,0}$

servicer potential, 50 initial target potentials are linearly spaced between -25 kV and -10 kV. As visible in the figures, both the target and servicer converge to different equilibrium potentials. One set of equilibria corresponds to the right side target equilibrium: due to electron beam emission, the servicer charges to $+4.5$ kV, while the target charges to about -13.5 kV due to the electron beam impact and the resulting secondary electron emission. For the other set of equilibria, the servicer converges to about 0 V and the target converges to about -20 kV. This corresponds to the case where the electron beam is initially unable to reach the target, and comes back to the servicer. This causes the target to charge in the positive direction and to converge to a left side equilibrium, i.e. the most negative potential possible for a given electron beam energy. The servicer converges to its natural potential, as the returning electron beam results in a net-zero beam induced current.

For some initial conditions with the target starting between about -20 kV and -15 kV, the target initially charges positively, but then charges negatively after some time and ends up at the equilibrium of -20 kV. This behavior can be explained in the following way. Initially, the beam is not able to reach the target and comes back to the servicer. Consequently, due to the net-zero beam induced current on both spacecraft, the target and servicer are slowly de-charging

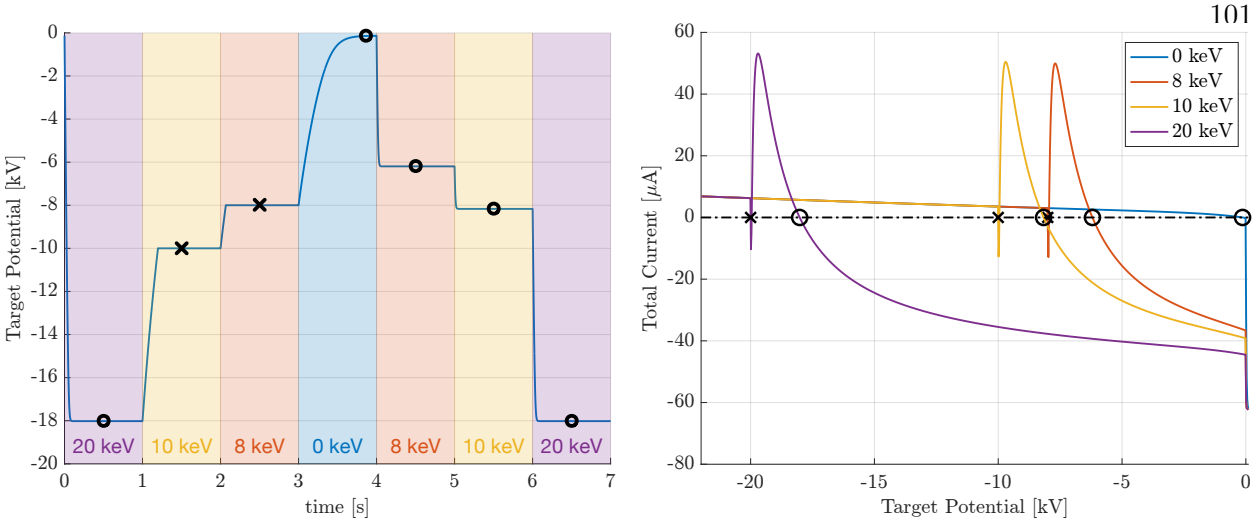

(a) Transients (b) Currents

Figure 4.6: Change of Equilibria due to Electron Beam Energy Variation. $I_{EB} = 50$ µA

to their natural potential of about 0 V, so the target charges in the positive direction while the servicer charges in the negative direction. This decreases the potential difference between the two spacecraft. After some time, the potential difference is small enough for the beam to hit the target. Once the beam hits the target, the target charges negatively and converges to -20 kV. As the beam is just barely able to reach the target and leave the servicer (modeled with the exponential drop-off in Eq. (2.13)), the servicer keeps charging negatively and converges to 0 V.

4.2.2 Change of equilibrium

As shown above, which equilibrium the target and servicer spacecraft settle to depends on the initial potential of both the servicer and the target, and whether or not the beam is initially energetic enough to reach the target. However, this leaves the questions of how to get to a state where the beam is unable to reach the target in the first place, and what could cause a jump from one equilibrium to another.

One way of changing the type of equilibrium (left side vs. right side) is to simply vary the electron beam energy, as illustrated in Fig. 4.6 for the same charging environment as in Fig. 4.4. In this simulation, the servicer potential is held at 0 V. This makes the illustration simpler by

eliminating the effect of the servicer potential on the charging response of the target. Figure 4.6a shows the response of the target potential over time as the beam energy is changed, while Fig. 4.6b shows the total current on the target for each beam energy as a function of target potential. The left side equilibria are indicated by $\times$ and the right side equilibria by $\circ$. The target starts at the natural potential of about 0 V. When hit by a 20 keV electron beam, the potential quickly changes to about -18 kV, corresponding to the right side equilibrium. When the electron beam energy is changed to 10 keV, the potential converges to -10 kV, corresponding to the left side equilibrium for this beam energy. That is, the equilibrium switched from the right side to the left side (although, for different beam settings), because the electron beam is initially unable to reach the target once the beam energy is reduced from 20 keV to 10 keV. Similar observations are made when changing the beam energy from 10 keV to 8 keV. When the electron gun is turned off (0 keV), there is only one possible equilibrium, i.e. the natural potential of the target. Now, if the beam energy is increased, the right side equilibrium is achieved for every beam energy. To reach a left side equilibrium again, the beam energy needs to be reduced such that the beam is initially unable to reach the target. Figure 4.6a clearly illustrates that the same charging environment and beam settings (e.g. 10 keV) can result in two different final potentials depending on the initial conditions. Note that the time it takes the electron gun to adjust its beam energy is not considered here. That is, it is assumed that the beam energy changes faster than the spacecraft charge.

Varying the electron beam energy is a controlled (intentional) way of switching between left and right side equilibria. However, a switch of equilibria could also occur naturally. For a rotating (non-spherical) spacecraft, the sunlit area changes over time, and consequently the photoelectric current changes. If the resulting change in current is significant enough, the requirement for multiple equilibria in Eq. (4.2a) may not be fulfilled anymore. As a result, only the right side equilibrium exists, causing a jump to that potential. This is illustrated in Fig. 4.7. Figure 4.7a shows the response of the target potential over time as the sunlit area of the target changes, while Fig. 4.7b shows the total current on the target for each fraction of sunlit area as a function of target potential. The servicer is assumed to be either fully eclipsed or fully sunlit. Again, the left side equilibria are

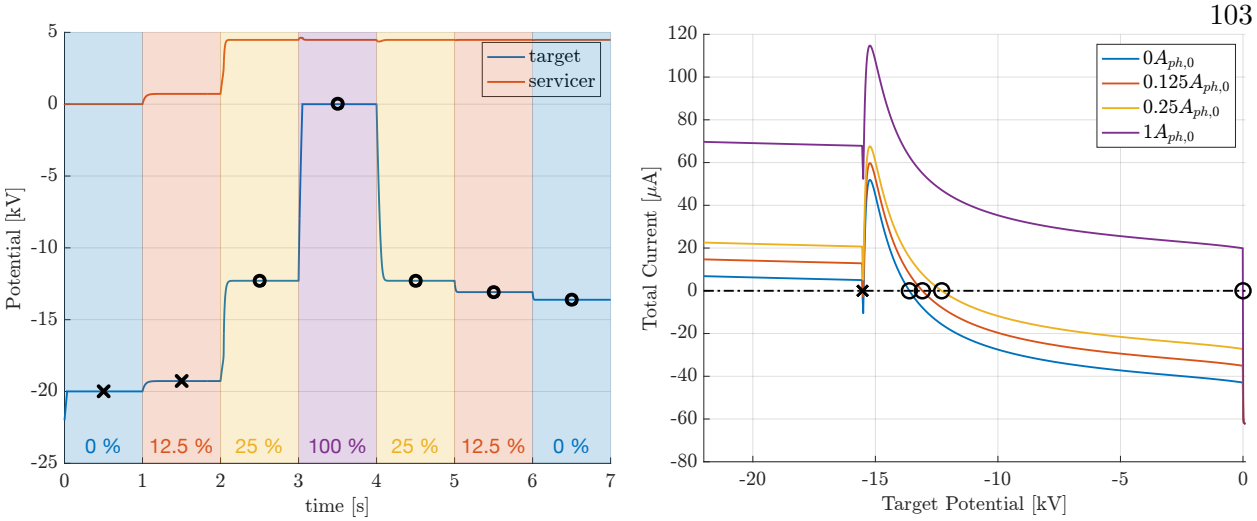

(a) Transients

(b) Total Current on Target (Servicer at 4.5 kV)

Figure 4.7: Change of Equilibria due to Sunlight Variation. $I_{EB} = 50$ µA

indicated by $\times$ and the right side equilibria by $\circ$.

Starting at a potential of -22 kV with both spacecraft in eclipse (0% sunlit area), the target potential converges to the left side equilibrium of -20 kV. After one second, both spacecraft exit eclipse, with the servicer being entirely sunlit, while only 12.5% of the nominal photoelectric current area $A_{ph,0}$ of the target is sunlit. The resulting transients are interesting. If the entire electron beam escapes the servicer, the servicer charges to about +4.5 kV; if the entire beam comes back to the servicer, the servicer remains at about 0 V. Yet, the servicer converges to about 0.7 kV and the target to -19.3 kV. This is one of the cases from Sec. 2.1.5 where the target potential influences the charging of the servicer (as the target is highly charged). The increase in photoelectric current from 0% to 12.5% results in an increase in total current on the target that is constant over all negative potentials (Eq. (2.9)), essentially shifting the total current line in Fig. 4.7b upwards. This upward shift causes the left-most zero crossing to shift slightly to the right, and consequently the left side target equilibrium to shift a few volts in the positive direction. This allows the servicer to charge a bit more positively, as the potential difference between the two spacecraft can only be as high as the electron beam energy (without the presence of a charged target spacecraft, the servicer

would charge to +4.5 kV). In turn, due to the limitation on the potential difference, the increased positive potential of the servicer causes the target potential to shift in the positive direction. This continues until the servicer and target potentials converge to 0.7 kV and −19.3 kV, respectively. This highlights one of the limitations of the assumption that the target potential does not influence whether or not the beam is able to leave the servicer as discussed in Sec. 2.1.5. With the root-finding procedure highlighted in Sec. 2.1, these (left-side) equilibrium potentials cannot be found. A more complex, bivariate root-finding algorithm is needed. Instead of solving for the equilibrium potential of the servicer and target sequentially, both equilibria must be computed simultaneously. At equilibrium, the current on both spacecraft must be zero, so the one-dimensional function

$$I_{\text{sum}}(\phi_T, \phi_S) = \sqrt{I_{\text{tot},T}(\phi_T, \phi_S)^2 + I_{\text{tot},S}(\phi_T, \phi_S)^2} \tag{4.3}$$

is used to represent the sum of both currents. This current sum is shown in Fig. 4.8 as a function of the two spacecraft potentials, with the corresponding right side and left side equilibria highlighted. Using this function, one can use a bivariate root-finder to compute the potentials of both spacecraft simultaneously in a case where the more complex left side equilibrium is of interest. For the case where the beam is initially energetic enough to reach the target, resulting in the right side equilibrium, the root-finding procedure from Sec. 2.1 can be used.

As the sunlit area of the target increases to 25% of the nominally sunlit area $A_{ph,0}$, the target potential jumps from the left side equilibrium to the right side one. In fact, the left side equilibrium disappears: the increase in photoelectric current shifts the total current line in Fig. 4.7b so far upward that the requirement in Eq. (4.2a) for the left side equilibrium is not fulfilled anymore. That is, the electron beam current is not significant enough for the given space environment such that the left side equilibrium can exist. As a result of the jump to the right side equilibrium, the servicer converges to the corresponding equilibrium at +4.5 kV. With an increase to 100% of the nominally sunlit area $A_{ph,0}$ of the target, the target potential converges to about 0 V, i.e. the electron beam current is not strong enough to charge the target at all for the given space environment. Any subsequent variations in sunlit area cause the equilibrium potential of the target

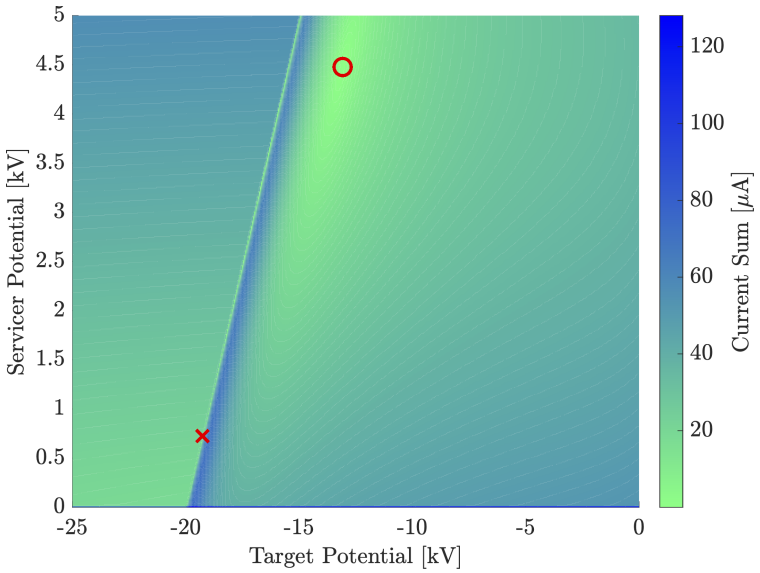

Figure 4.8: Current Sum for bivariate root-finding. $I_{EB} = 50$ µA, $E_{EB} = 20$ keV

to change, but the potential remains at the right side equilibrium, even when both spacecraft are eclipsed again. To achieve a left side equilibrium again, another variation needs to be included, such as a change in the electron beam energy.

Note that the two ways of changing the type of equilibrium (left side vs. right side) presented here are fundamentally different. One way, by changing the electron beam energy, puts the current target potential into a different region of convergence by essentially shifting the total current line left or right. In this way, one can change the type of equilibrium in both directions: from left side equilibrium to the right side, and vice-versa. This way of changing the type of equilibrium can also be achieved by varying the potential of the servicer using some additional current such as, for example, an extra electron or ion beam that is uncoupled from the target by facing in the other direction. The other way, by changing the target spacecraft orientation and the resulting photoelectric current, removes the left side equilibrium and thereby enforces the right side equilibrium, by essentially shifting the total current line upwards. In this way, however, one can change the type of equilibrium only in one direction: from left to right. To go back to the left side equilibrium, one needs to change another charging source, such as the electron beam energy. Any current fluctuations (change in plasma environment, variations in electron beam current, etc.), if significant

enough, can cause the left side equilibrium to disappear and consequently a jump to the right side equilibrium (Eq. (4.2a)).

4.2.3 Significance and potential applications

As shown in this section, changes in the charging environment can cause a jump from one type of equilibrium to another, such as from the right side equilibrium to the left side one. If the charging environment allows for multiple equilibria and the electron beam energy is reduced by several keV (corresponding to approximately the difference in kV between the left and right side equilibrium), the potential of the target may converge to the left side equilibrium. Not only is this an unexpected charging behavior, but it also affects the remote sensing of the electric potential. For the left side equilibrium, the impact energy of the electron beam on the target is close to zero, and barely any secondary electrons or x-rays are excited, which are needed for the electric potential sensing methods.

From a charge control perspective, where the potentials of the servicer and target are controlled by adjusting the electron beam current and energy, the left side equilibrium provides a new potential control algorithm. Instead of implementing a closed-loop control that uses feedback of the potential of the servicer and target to control the beam parameters accordingly, the beam energy is reduced to make sure a left side equilibrium is obtained. The value of that equilibrium potential is approximately $\phi_T \approx \phi_S - E_{EB}$, so as long as the potential of the servicer is measured, no estimation of the target potential is required. One drawback of this open-loop control is that no secondary electrons or x-rays are excited. This results in a similar signal as if the beam does not hit the target at all, so it cannot be verified if the electron beam is charging the target at all. Potential solutions to solve this ambiguity are to passively estimate the potential [48] using the x-rays and secondary electrons excited by the ambient plasma are used to, to use a pulsed beam with varying energy (Chapter 5), or to determine whether or not the beam is coming back to the servicer. The other drawback is that the left side equilibrium results in a low servicer potential. For the Electrostatic Tractor, high magnitude potentials with opposing signs are desired for both

spacecraft to maximize the attractive electrostatic force between the two vehicles. To achieve a more positive servicer potential, an additional electron beam can be used that is uncoupled from the target by facing in the other direction.

These findings are also important when using numeric root-finders to compute the equilibrium potential. If the right-most equilibrium is of interest (as in this work), then the limits for the root-finding algorithm are set to only accept an equilibrium potential greater than $\phi_T \geq \phi_S - E_{EB} + E_{\max}$, where $E_{\max}$ is the effective energy where the maximum secondary electron yield occurs. This limit ensures that the two equilibria to the left are ignored. However, for a small enough maximum secondary electron yield, the right-most equilibrium and the unstable equilibrium may not exist. Moreover, a more complex bivariate root-finding algorithm may be required as opposed to the sequential root-finding approach used in this work.

4.3 Study of electron beam effects around Earth and Moon

Using the charging model from Sec. 2.1 and the findings from Sec. 4.2, the equilibrium potentials induced by the electron beam are studied in geostationary earth orbit (GEO) and cislunar space. Only right side equilibria are considered, so the bounds for the numerical root finder are set accordingly as described in Sec. 4.2.3. The left side equilibrium is achieved if the beam is initially not energetic enough to reach the target, due to a large potential difference between servicer and target or a reduction in electron beam energy. Thus, the right side equilibrium is generally more likely when starting from natural potentials, which motivates the focus on it within this study.

4.3.1 Geostationary Earth Orbit

The plasma environment data for GEO is taken from Ref. [134], which provides the electron and ion temperature and density (T_e, n_e, T_i, n_i) as a function of local time and Kp index. The data comes from averaging in-orbit measurements from satellites flown by the Los Alamos National Laboratory between 1990 and 2001. Local time represents the location in GEO, where a local time of 12 hours indicates that the spacecraft is between Sun and Earth, and a local time of 24

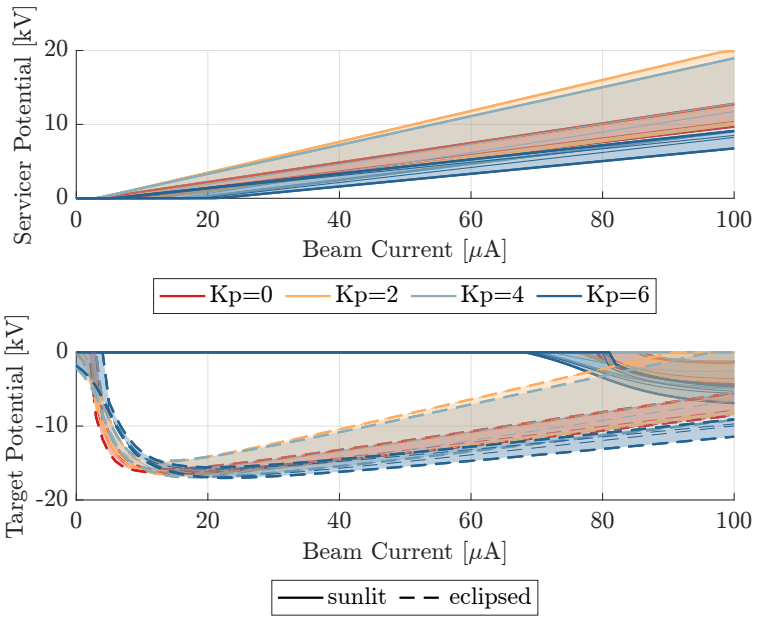

Figure 4.9: Equilibrium Potential vs. Electron Beam Current in GEO. $E_{EB} = 20$ keV

hours corresponds to the spacecraft being behind Earth with respect to the Sun. The Kp index, or planetary K-index, characterizes the intensity of geomagnetic activity. The enhanced electron fluxes within the ring current and plasma sheet in the GEO region during geomagnetic storms frequently lead to more severe spacecraft charging levels [135]. Thus, the plasma parameters are a function of the local time and Kp index. While the servicer is assumed to always be in sunlight in GEO, two cases are considered for the target: either the target is also in sunlight, or it is eclipsed by the servicer (resulting in no photoelectric current on the target).

Figure 4.9 shows the equilibrium potential of the servicer and target as a function of electron beam current, for several Kp indices and a beam energy of 20 keV. The shaded regions represent the various local times for each Kp index, i.e. these regions are bounded by the minimum and maximum equilibrium potential across all local times obtained for a given beam current and Kp index. The solid lines indicate that the target is in sunlight, while the dashed lines indicate that the target is eclipsed by the servicer. The servicer equilibrium potential increases approximately linearly with increasing beam current. It takes some minimum current for the servicer to charge. This can be explained with Fig. 4.1 (note that this figure shows the currents on the target, but

the currents on the servicer are similar despite the beam currents of the opposite sign). At 0 V, there is a significant current drop-off because the secondary electron and photoelectric currents reduce exponentially with increasing positive potential. Thus, it requires some minimal current to overcome this drop-off. This is provided by the electron beam current, which essentially shifts the total current upward for the servicer. Similarly to the servicer, it takes some minimal current to charge the target negatively. This can also be explained using Fig. 4.1, but in this case the total current is shifted downwards by the electron beam on the target. For the eclipsed target, the equilibrium potential is up to a few kV negative even without the electron beam (0 µA). With increasing beam current, the equilibrium potential increases quickly in the negative direction before approaching zero volts again, approximately linearly. This is interesting as one might expect that a higher beam current results in a more negative target potential. However, the electron beam couples the charging of the servicer and target. With increasing beam current, the servicer charges more positively, and less energy of the electron beam is left to charge the target [55, 57]. While a higher Kp index is associated with more negative charging due to more energetic electrons at increased geomagnetic activity, the Kp indices of 2 and 4 show less negative charging than a Kp index of 0. This is due to a decreased electron density for Kp indices between 2 and 5 in the data. Consequently, the servicer charges more positively and less energy is left to charge the target.

As a satellite orbits around Earth in GEO, it moves through various plasma environments throughout the day, specified by the local time (LT). Figure 4.10 shows the equilibrium potential of the servicer and target as a function of local time, for several beam currents. The shaded regions represent the various Kp indices, i.e. these regions are bounded by the minimum and maximum equilibrium potential across all Kp indices obtained for a given local time and beam current. In Fig. 4.10a, both spacecraft are in sunlight and high beam currents between 60 and 90 µA are used. The natural potential (zero beam current) of both the servicer and target is a few volts positive across all local times. In the dawn and dusk hours, the target charges the most negatively, while the servicer charges the most positively a little after noon. Most natural charging is negative and occurs in the dawn and dusk hours [18, Chapter 1]. The electron beam induced potentials follow the

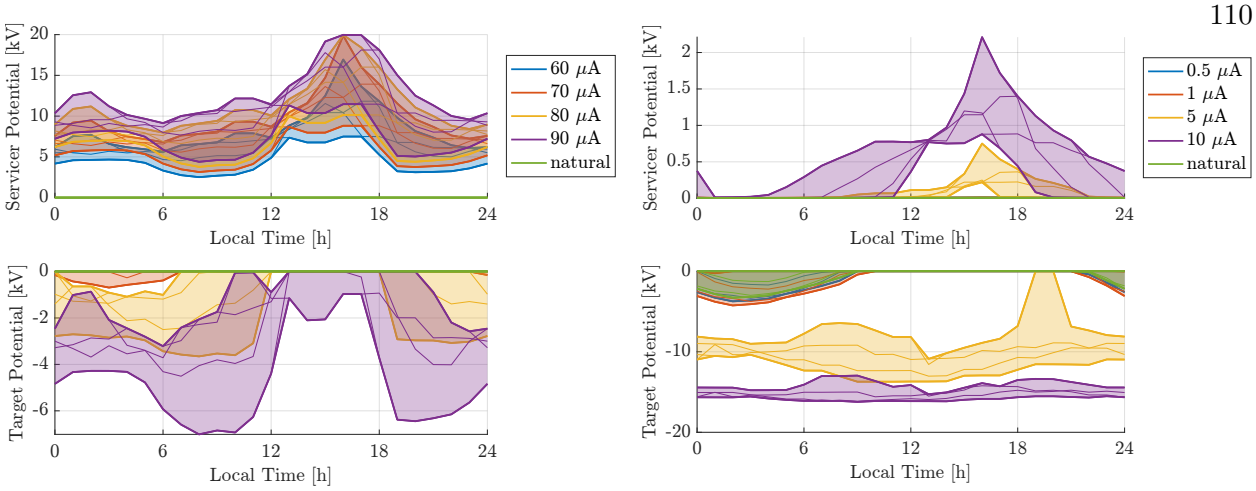

(a) Sunlight

(b) Eclipse

Figure 4.10: Equilibrium Potential vs. GEO Local Time. $E_{EB} = 20$ keV

same trend. Note that the equilibrium potential of the servicer varies more than 15 kV throughout the day for the same beam parameters. These differences in charging during one day affect the electrostatic force between the two spacecraft and can consequently impact the performance of the multi-month reorbit process of the Electrostatic Tractor debris removal method. With the servicer in sunlight and the target eclipsed by the servicer only small beam currents are needed to significantly charge the target, as the natural potential of the eclipsed spacecraft can already be a few kilo-volts, as shown in Fig. 4.10b. The trends throughout the day are similar as to when the target is in sunlight, with small differences due to the weaker electron beam current.

The significant charging levels of the eclipsed target for small beam currents of only a few micro-amperes raise the question how much this influences the remote sensing methods. For these methods, when applied during on-orbit servicing operations, it is desired to measure the electric potential without significantly changing the potential during the estimation process. Figure 4.11 shows the maximum current that is allowed to not change the potential of the target by more than 200 V from its equilibrium, as a function of GEO local time and for various Kp indices. For a Kp index of 0, the maximum allowed current is a few micro-amps for all local times. For higher geomagnetic activity, the maximum allowed current drops to 0.1 to 1 μA for the night-side local

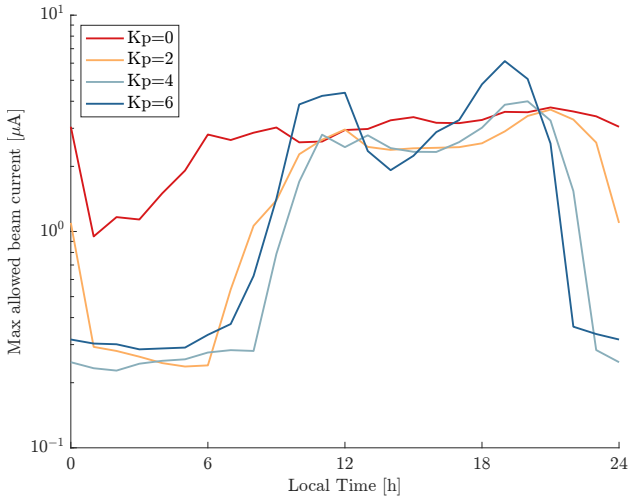

Figure 4.11: Maximum Allowed Current in GEO eclipse

times. Such low currents may not be feasible for the electron gun used by the servicing satellite. Instead, one could quickly pulse the electron beam to reduce the average current and let the target object periodically recharge to its natural potential. Note that such a low current also affects the signal strength for the sensing methods, as a low current results in less secondary electrons and x-rays to be generated. However, because the beam is pulsed at a known frequency, one can strengthen the signal using a band-pass filter. The charging dynamics of a pulsed beam and the potential benefits of pulsing for electric potential sensing and control are investigated in Chapter 5.

4.3.2 Cislunar space

Another region with high spacecraft charging levels is cislunar space. As explained in Sec. 2.3, the Moon moves through different regions of Earth's magnetic field and into the solar wind as it orbits Earth. Thus, for spacecraft charging considerations, four regimes are defined for cislunar space according to the NASA Design Specification For Natural Environments (DSNE) [109]: the plasma sheet (PS), the magnetotail lobes (ML), the magnetosheath (MS) and the solar wind (SW). The DSNE provides the electron and ion temperature and density as well as the ion bulk velocity $v_{i,\text{bulk}}$ for these cislunar environment regimes (see Tab. 2.1). In the magnetosheath and solar wind, a plasma wake with a depletion of plasma density forms on the downwind side of the Moon because

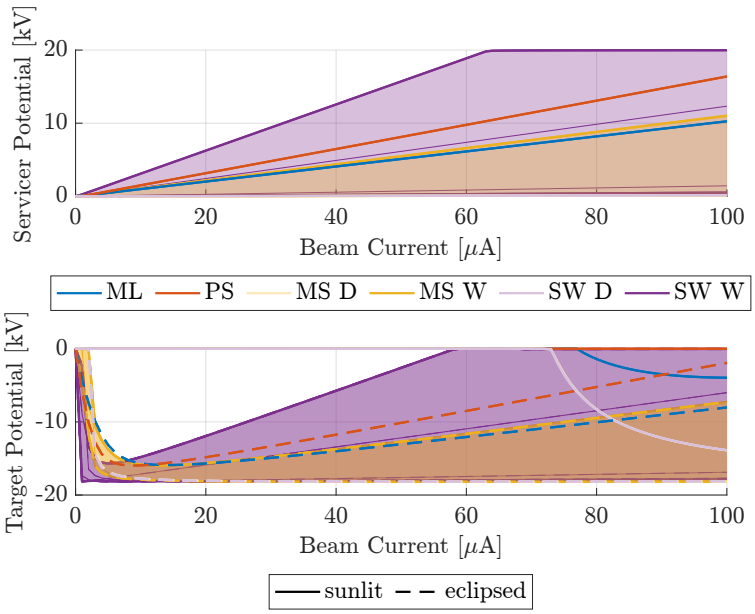

Figure 4.12: Equilibrium Potential vs. Electron Beam Current in cislunar space. $E_{EB} = 20$ keV

the Moon obstructs the flowing solar wind [110–112]. Thus, the plasma data for the magnetosheath and solar wind regions is given separately for the day-side (D) and wake-side (W) of the Moon. In addition, the data is altitude dependent in the magnetosheath wake-side and solar wind wake-side regions, with three altitude ranges for the magnetosheath and four for the solar wind. This results in a total of 11 different cislunar regions for spacecraft charging. The DSNE provides the mean and max for the plasma data, but only the mean is used here. It is assumed here that both spacecraft are eclipsed in the magnetosheath and solar wind wake-side regions. In the day-side regions, the servicer is always assumed to be in sunlight and the target is either in sunlight or eclipsed by the servicer.

Figure 4.12 shows the equilibrium potential of the servicer and target as a function of electron beam current for the various cislunar regions and a beam energy of 20 keV. The shaded regions represent the various altitudes, i.e. these regions are bounded by the minimum and maximum equilibrium potential across all altitudes obtained for a given beam current and cislunar region. The charging behavior in the plasma sheet and magnetotail lobes is similar to GEO, with beam currents of about 70 µA required for the onset of charging if the target is in sunlight, and with a

maximum target potential magnitude for a beam current of about 10 µA if the target is eclipsed. The charging behavior for a sunlit target is also similar in the magnetosheath and solar wind day-side regions, although the target is charging to more negative potentials. This is due to the higher electron density in these regions, causing the servicer to barely charge positively and leaving more electron beam energy to charge the target. Another reason for the higher charging levels of the target is that the bulk velocity $v_{i,\text{bulk}}$ of the ions with respect to the spacecraft is greater than the thermal velocity w_i of the ions in these regions, in which case the third case in Eq. (2.2) is applied. Consequently, the ion induced secondary electron emission is reduced, allowing for more negative target potentials. Due to the servicer potential being close to neutral in the magnetosheath and solar wind day-side regions, the equilibrium potentials for an eclipsed target are highly negative for beam currents above ≈ 5 µA, without a steady increase in potential with increasing beam current. In the magnetosheath and solar wind wake-side regions, where both the servicer and target are eclipsed, the charging levels of the target are altitude dependent due to the plasma data being provided for different altitude regions. For lower altitudes, the ion bulk velocity is less than the ion thermal velocity, and the maximum potential magnitude is around 10 µA, similar to an eclipsed target in the plasma sheet or magnetotail lobes. For higher altitudes, the ion bulk velocity is greater than the ion thermal velocity, and the equilibrium potential is highly negative for most beam currents, similar to an eclipsed target in the magnetosheath and solar wind day-side regions.

4.4 Conclusions

The electron beam is only energetic enough to reach the target if the initial beam energy is greater than the potential difference between the two spacecraft. This relationship between the beam energy and the electric potentials of the spacecraft leads to a coupling of charging dynamics between the servicer and target. Multiple electric potential equilibria are found to exist for the servicer and target in a single-maxwellian plasma. This is due to the emission of secondary electrons that are excited by the electron beam impacting on the target, and due to the energy-potential relation of the electron beam. The existence of multiple equilibria depends on the magnitude of the

beam current relative to the currents induced by the space environment, as well as the secondary electron yield of the surface material of the target. Jumps between the stable equilibrium configurations are possible due to a fast decrease in beam energy or increase in servicer potential; or due to current fluctuations caused by a rotating spacecraft (resulting in a time-varying photoelectric current), changes in beam current or the plasma environment. These findings are important for active charging and remote electric potential sensing methods that utilize an electron beam. Potential applications that utilize the knowledge about multiple equilibria include an open-loop charge controller that takes advantage of the stability of the most negative equilibrium potential of the target.

Moreover, the spacecraft charging levels due to the electron beam are studied in geostationary orbit and cislunar space, and the effect of the electron beam on remote electric potential sensing methods is investigated. It is found that, especially when the target is eclipsed, the electron beam may significantly divert the electric potential of the target from its natural equilibrium while the potential is measured.

Chapter 5

Spacecraft charging using a pulsed electron beam

The sensing methods described in Sec. 1.2.1 strongly depend on the electron beam parameters, that is, the electron beam current I_{EB} and electron beam (operating) energy E_{EB}. However, the x-ray method and electron method benefit from electron beam configurations that conflict each other. The higher the beam current, the more electrons are impacting on the target and the more x-rays and secondary electrons are emitted from the target. Thus, a high beam current is preferred for a better signal, although the saturation of the x-ray detector (when too many x-rays are detected at once) should be considered. In terms of beam energy, a high beam energy that results in landing energies of at least 5 to 10 keV is preferred for the x-ray method. As shown in Sec. 3.4, characteristic x-ray peaks may interfere with the x-ray method if they are close to the landing energy (maximum energy in the x-ray spectrum). With a high landing energy, one can avoid that low-energy characteristic x-ray peaks (e.g. aluminum at 1.5 keV and titanium at 4.5 keV) are close to the maximum x-ray energy that is used for the estimation. Moreover, the wider energy spectrum of the x-rays allows for more materials to be identified. However, it should be taken into account that the landing energy affects the accuracy of the x-ray method (Sec. 3.1.3). The electron method, on the other hand, benefits from a lower beam energy. The secondary electron yield (the average number of secondary electrons emitted per impacting primary electron) depends on the impact energy of the incoming electron. Although there are many uncertainties involved with the secondary electron yield, the maximum yield occurs at an impact energy of less than 1 keV for most materials [18, Chapter 3]. Above this specific energy, the secondary electron yield decreases

continuously with increasing impact energy. Thus, a landing energy of less than 1 keV or only a few keV results in more secondary electrons being emitted from the target and consequently a stronger signal for the electron method.

Another consideration for the beam parameters is the deflection of the electron beam due to the interaction with the electric field generated by the two charged spacecraft [105]. With a lower beam energy, the beam deflects more. This can cause the beam to impact on a different component of the target spacecraft than desired, and consequently the electric potential of the wrong component is estimated. If the beam is significantly deflected or not energetic enough to reach the target, the beam misses the target entirely. Thus, no signal is produced for the electron method or the x-ray method. In the case of such a loss-of-signal of the active sensing methods that utilize an electron beam, passive methods such as the passive x-ray method [48] may be used as a back-up. In addition to the loss-of-signal, the servicer is also unable to actively charge the target if the beam misses the target. For the Electrostatic Tractor, this results in a loss of the attractive electrostatic force needed for reorbiting the target. Thus, unrelated to the signal produced, a high electron beam energy is beneficial because the electron beam is deflected less if it has a higher energy. Upper limits on the beam energy are imposed by the capabilities of the electron gun (30 keV for the electron gun used in Sec. 3), prevention of melting the target surface material (30 to 150 keV are usually used for electron beam welding), and prevention of detector saturation (Sec. 3.5).

Given the conflicting desired electron beam configurations, a pulsed beam is proposed to quickly switch between beam settings. For example, by alternating between a low and high electron beam energy, one can create conditions that, on average, are beneficial for both sensing methods. Additionally, the pulsed beam enables a way of open-loop charging control as proposed in Sec. 4.2.3. Previously, the pulsed beam has been proposed for the Electrostatic Tractor to increase the efficiency of the ET debris reorbit process [64].

This chapter provides an initial study of using a pulsed beam for charging control as well as to enhance the remote electric potential sensing methods. The parameters of the pulsed beam are

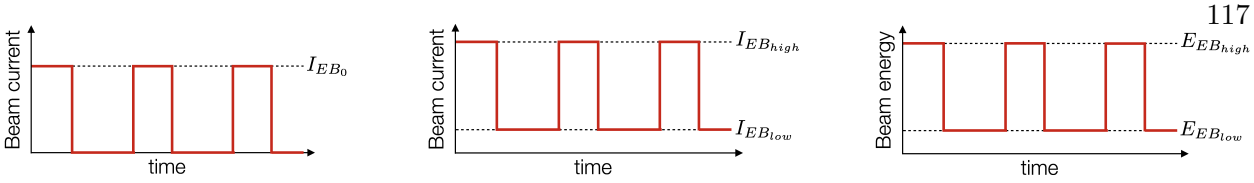

(a) On-Off Pulsing (b) Current Pulsing (c) Energy Pulsing

Figure 5.1: Types of Pulsing

reviewed in Sec. 5.1. Section 5.2 looks into open-loop pulsing strategies, and Sec. 5.3 looks into closed-loop pulsing.

5.1 Pulsing Parameters

Three types of pulsing are considered: on-off pulsing, current magnitude pulsing, and beam energy pulsing. For on-off pulsing (Fig. 5.1a), the beam is periodically turned off, providing some nominal current $I_{EB,0}$ during the on-time and no current during the off-time. For current pulsing (Fig. 5.1b), the beam switches between a high beam current $I_{EB,\text{high}}$ and a low current $I_{EB,\text{low}}$. Finally, for energy pulsing (Fig. 5.1c), the beam alternates between a high beam energy $E_{EB,\text{high}}$ and a low energy $E_{EB,\text{low}}$. Current pulsing is equivalent to on-off pulsing if $I_{EB,\text{low}} = 0$. In a less obvious way, on-off pulsing can also be achieved under certain conditions with energy pulsing. If the low energy is smaller than the difference of electric potentials, i.e. $E_{EB,\text{low}} < \phi_S - \phi_T$, the beam is not energetic enough to reach the target [97]. This results in zero current due to the electron beam during the low energy period of the pulse cycle, and is consequently comparable to on-off pulsing. In addition to the low and high current/energy levels, two more parameters are needed to describe the pulsing cycle: the pulsing frequency f and the duty cycle d. The frequency is equal to

$$f = \frac{1}{T_{\text{pulse}}} \tag{5.1}$$

where $T_{\text{pulse}} = t_{\text{high}} + t_{\text{low}}$ is the period of one pulse cycle, t_{high} is the duration of the high cycle, and t_{low} is the duration of the low cycle. For on-off pulsing, t_{high} corresponds to the time that the

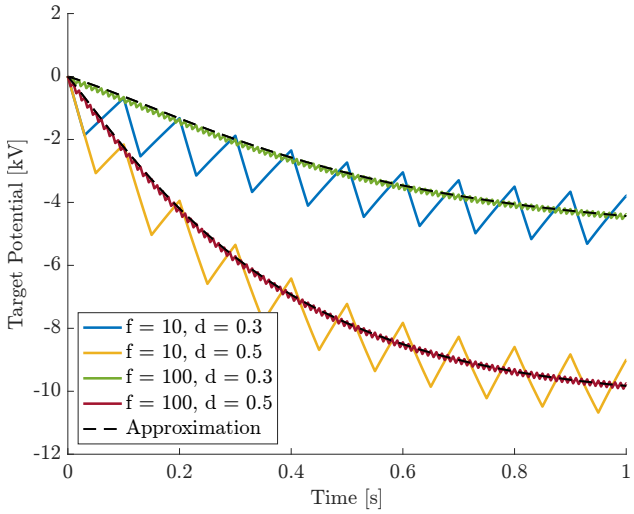

Figure 5.2: Duty Cycle d and Pulsing Frequency f

beam is on and t_{low} to the time that the beam is off. The duty cycle is

$$d = \frac{t_{\text{on}}}{T_{\text{pulse}}} = \frac{t_{\text{high}}}{t_{\text{high}} + t_{\text{low}}} \tag{5.2}$$

and consequently $0 \leq d \leq 1$.

In this chapter, the spacecraft radii are equal to $R_S = R_T = 1$ m and plasma parameters of $n_e = 0.55$ cm^{-3}, $T_e = 600$ eV, $n_i = 0.55$ cm^{-3} and $T_i = 8100$ eV are used. The target is assumed to be eclipsed, and the servicer potential is assumed to be equal to 0 V at all times to allow for a better focus on the charging behavior of the target.

5.2 Open-loop pulsing

5.2.1 On-Off pulsing

On-off pulsing is shown in Fig. 5.2 for different duty cycles and pulsing frequencies, and a nominal beam current of $I_{EB,0} = 10$ µA and beam energy $E_{EB} = 20$ keV. During the on-cycle, the beam charges the target just like a continuous beam would. During the off-cycle, the beam current is zero, so the target recharges slightly towards its natural equilibrium potential. This essentially reduces the net current due to the electron beam. For on-off pulsing, the duty cycle reduces the effective beam current by approximately $I_{EB,\text{eff}} = d \cdot I_{EB,0}$ and consequently affects the obtained

equilibrium potential. The frequency only determines the amplitude of the oscillations, but has no effect on what potential the target converges to. In Fig. 5.2, the Approximation lines correspond to a continuous beam with a current of $I_{EB} = I_{EB,\text{eff}}$.

For electric potential sensing purposes, on-off pulsing may be beneficial in multiple ways. First, when estimating the natural (no electron beam current) equilibrium potential of the target, any current from the electron beam affects the target potential itself. Thus, it is desired to keep the beam current as low as possible while still producing a sufficient x-ray and secondary electron signal to accurately measure the potential. By pulsing the electron beam, one can reduce the net beam current to levels below the capabilities of the electron gun for a continuous beam. Second, the excited x-rays and secondary electrons are emitted at a specific frequency (the pulsing frequency), allowing for band-pass filtering of the signal. Thus, for the same effective beam current, pulsing can provide a better signal-to-noise ratio. Finally, the pulsed beam can also increase the efficiency of the Electrostatic Tractor debris removal method [29], as it increases the average electrostatic force for the same power used for the electron beam [64]. In the last case, however, the pulsing frequencies are much lower than the ones discussed and used here.

5.2.2 Energy pulsing

The drawback of on-off pulsing for electric potential sensing purposes is that it does not significantly affect the landing energy of the electron beam and therefore might only be well-suited for one estimation method. For example, in Fig. 5.2, the landing energy is between approximately 16 and 18 keV for $d = 0.3$ and between 10 and 12 keV for $d = 0.5$. Given that the servicer potential is held constant at 0 V and the beam energy is constant, the oscillations of the landing energy are purely a result of the oscillating target potential. Such high landing energies are only beneficial for the x-ray method, due to the limited number of secondary electrons being excited for this range of landing energies.

To alternate the landing energy between two levels that are favorable for one estimation method at a time, the beam energy can be pulsed. Pulsing the beam energy while maintaining a

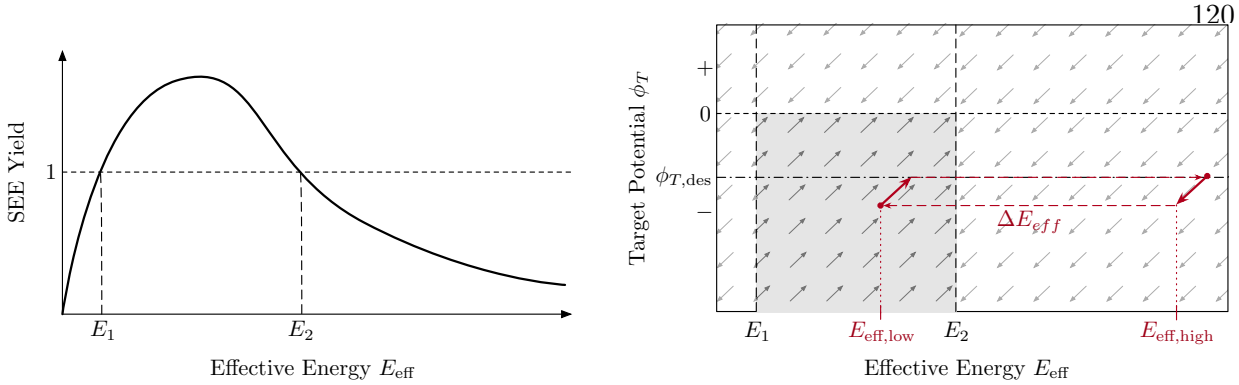

(a) SEE yield vs. effective energy

(b) target potential vs. effective energy

Figure 5.3: Illustration for energy pulsing

constant servicer potential allows for an alternating effective energy (landing energy) of the electron beam as the beam arrives at the target. Due to the secondary electron emission, charging of the target is strongly connected to the beam energy and effective energy [18, Chapter 9], as discussed in Sec. 4.1 and illustrated in Fig. 5.3. If the secondary electron emission (SEE) yield has a maximum yield greater than 1, there are two effective energies E_1 and E_2 for which the yield is equal to 1 (Fig. 5.3a). Assuming that the only currents acting on the target are the electron beam current and the secondary electron emission current, then the total current on the target is positive if the effective energy E_{eff} is between E_1 and E_2 ($E_1 < E_{\text{eff}} < E_2$) due to the SEE yield being greater than 1, leading to more outgoing than incoming electrons. If $E_{\text{eff}} < E_1$ or $E_{\text{eff}} > E_2$, the total current is negative because there are more incoming than outgoing electrons. If $E_{\text{eff}} = E_1$ or $E_{\text{eff}} = E_2$, the total current is zero and the target potential is at equilibrium. Because secondary electrons are only able to escape the target if the target potential is negative, this effective energy dependent charging behavior only applies to a negatively charged spacecraft. If the target is charged positively, the secondary electrons are attracted back to the target, resulting in no net SEE current. Consequently, only the electron beam current acts on the target and the total current is negative.

The charging behavior of a target subject to electron beam impact is illustrated in Fig. 5.3b. The total current is only positive if $E_1 < E_{\text{eff}} < E_2$ and the target potential is negative ($\phi_T < 0$),

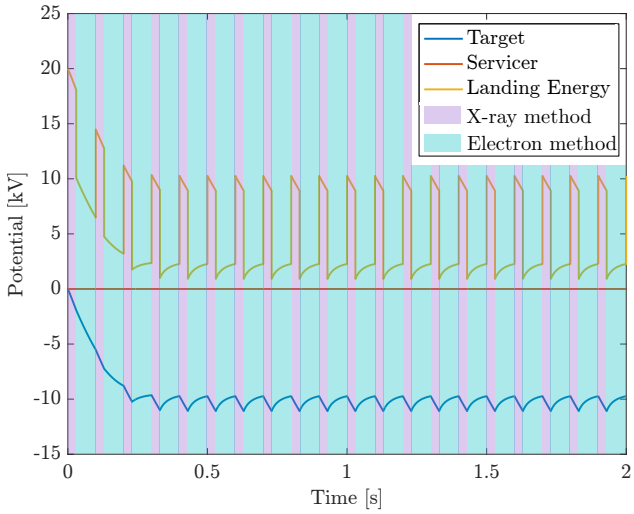

Figure 5.4: Open Loop Energy Pulsing: color shading indicates which sensing method benefits from a better signal

as illustrated by the shaded region. Otherwise, the total current is negative. For a constant beam energy and servicer potential, a change in the target potential results in an equal change in the effective energy. This is evident when taking the time derivative of Eq. (2.11), $E_{\text{eff}} = E_{EB} - \phi_S + \phi_T$, resulting in $\dot{E}_{\text{eff}} = \dot{\phi}_T$ if the beam energy and servicer potential are constant. Consequently, the charging trend follows the 45° tilted arrows displayed in Fig. 5.3b. For some initial condition $E_{\text{eff},0}$ and $\phi_{T,0}$, the charging trajectory in E_{eff}-ϕ_T space in Fig. 5.3b follows a 45° tilted line until it intersects the vertical line E_2. That is, the effective energy E_2 corresponds to a stable equilibrium while E_1 corresponds to an unstable equilibrium, as illustrated by the arrows. This charging behavior can be utilized by a pulsed energy beam to achieve conditions beneficial for both the x-ray method and the electron method. By alternating between a low and high beam energy, the total current switches between positive and negative. Consequently, the time period with low effective energy $E_{\text{eff,low}}$ is beneficial for the electron method and the time period with high effective energy $E_{\text{eff,high}}$ is beneficial for the x-ray method, all while the target potential oscillates around a desired target potential $\phi_{T,\text{des}}$.

Energy pulsing is demonstrated in Fig. 5.4 for $d = 0.3$, $f = 10$ Hz and $I_{EB,0} = 10$ µA. The high beam energy is $E_{EB,\text{high}} = 20$ keV and the low beam energy is $E_{EB,\text{low}} = 12$ keV. In

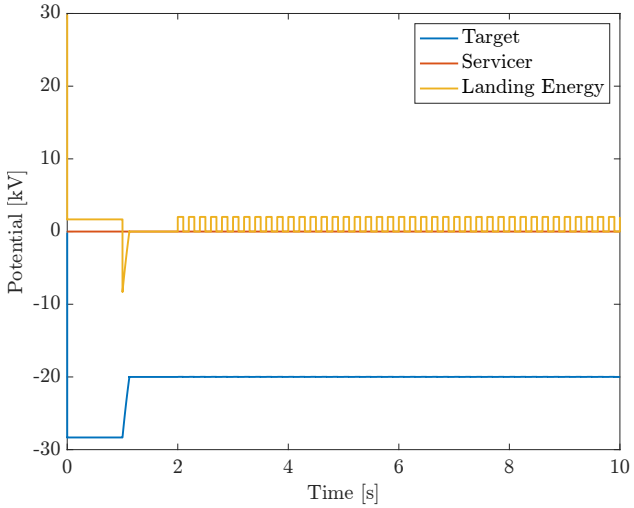

Figure 5.5: Open Loop Potential Control

contrast to the illustration in Fig. 5.3, environmental currents according to the plasma parameters in Sec. 5.1 are also present. At the beginning of the simulation, both beam energy levels result in landing energies above approximately 3 keV, which causes the target to charge negatively in either cycle. However, after about 0.3 seconds, the target potential stops decreasing and instead oscillates around -10 keV. During the high energy cycle, the target still charges negatively, and the corresponding landing energy of about 10 keV is beneficial for the x-ray method. However, during the low energy cycle, the effective energy is within a range where the secondary electron yield is greater than 1 ($E_1 < E_{\text{eff}} < E_2$), causing the electron beam to actually charge the target positively. Due to the increased number of secondary electrons being excited, the low energy cycle is beneficial for the secondary electron method.

5.2.3 Open-loop potential control

The aforementioned pulsing strategies may be beneficial for sensing purposes, but they change the potential of the target to an initially unknown value. It may be desired to charge the target to a specific potential. The estimated potential could be used as feedback for a closed-loop control. However, as proposed in Sec. 4.2.3, one can take advantage of the multiple equilibria that may exist for the target potential [97] using an open-loop control approach. One of the stable equilibrium

potentials is close to the point where the beam is just barely energetic enough to reach the target. If the potential is slightly less negative than the equilibrium, the beam is able to reach the target and charges it negatively until it reaches the equilibrium. If the potential is slightly more negative than the equilibrium, the beam is unable to reach the target (resulting in zero beam current), and the natural currents drive the potential back in the positive direction until the beam is hitting the target again. Thus, for a zero servicer potential, this equilibrium point of the target potential is approximately equal to the beam energy, but negative. The drawback of this control approach is that the landing energy is close to approximately zero, so no x-rays or secondary electrons are excited, and no potential can be estimated. The resulting x-ray and secondary electron signal looks just like the beam is missing the target entirely. This ambiguity is quite significant: either the beam is hitting the target and the potential is equal to the beam energy (e.g. -20 kV), or the beam is missing the target and the potential is equal to the natural potential, which may even be around 0 V. Pulsing the beam between two energy levels can solve this ambiguity.

As shown in Fig. 5.5, the beam energy is 30 keV for one second, charging the target to about -28 kV, followed by a one second phase with an energy of 20 keV. Due to the decrease of beam energy, the beam is now unable to reach the target, indicated by a negative landing energy in the figure. This brings the potential to the stable equilibrium around -20 kV where the 20 keV beam is just barely energetic enough to reach the target, corresponding to a change in equilibrium according to Sec. 4.2.2. Now, the beam is pulsed between energies of 20 and 22 keV, with $d = 0.5$, $f = 5$ Hz and $I_{EB,0} = 50$ µA. During the 20 keV phase, the potential is at -20 kV. During the 22 keV phase, the potential changes slightly, but the landing energy increases to about 2 keV. Thus, secondary electrons and x-rays are excited that can be used for the estimation of the electric potential, and to confirm that the beam is hitting and charging the target spacecraft.

5.3 Closed-loop pulsing

The potential estimation from the sensing methods may also be used as feedback for charge control to maintain a desired potential on the target. For on-off pulsing, the duty cycle can be

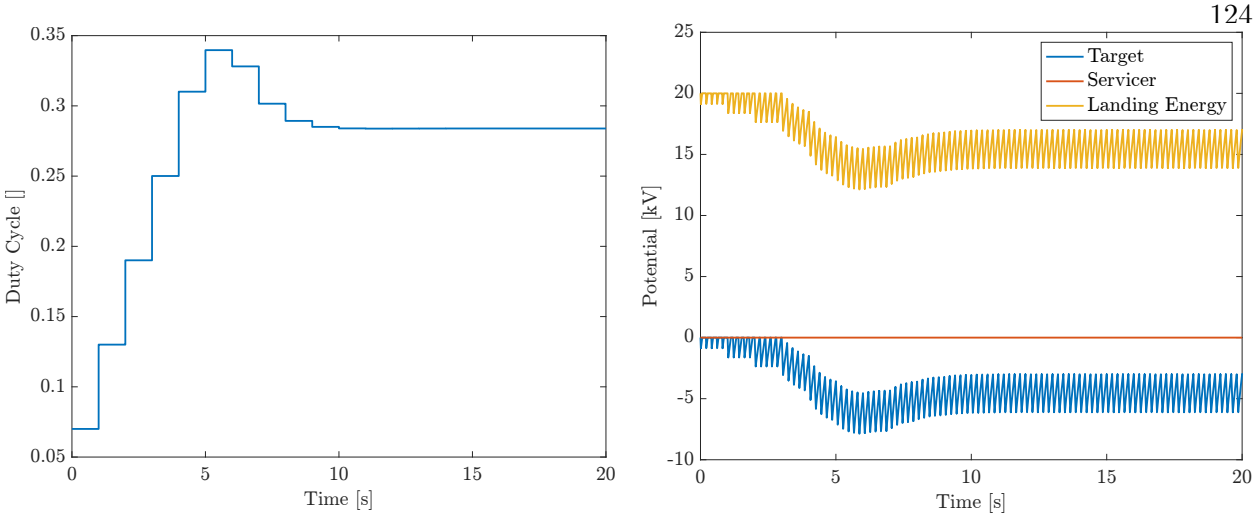

(a) Duty Cycle

(b) Potentials

Figure 5.6: Closed Loop On-Off Pulsing

controlled in a way such that the effective current delivered to the target results in the desired equilibrium potential. The simple feedback law

$$d_k = d_{k-1} + K_d(\hat{\phi}_T - \phi_{T,\text{des}}) \tag{5.3}$$

is used to update the duty cycle, where d_k and d_{k-1} are the duty cycles from the current and previous control period, respectively, K_d is the feedback gain, $\hat{\phi}_T$ is the most recent estimate of the target potential, and $\phi_{T,\text{des}}$ is the desired potential of the target. In this example, the control update rate is 1 Hz. Moreover, a method is implemented to simulate the estimation of the target potential. When only measuring one potential at a time (as opposed to multiple potentials, e.g. in the case of a differentially charged spacecraft), the x-ray method detects the potential corresponding to the highest landing energy in the recorded x-ray spectrum (the most positive or least negative electric potential) [33], as discussed in detail in Sec. 3.3. Thus, if the x-ray detector records x-rays over a certain time and the target potential changes during that time period (while the beam energy remains constant), the estimated potential corresponds to the least negative potential. Here, the estimation time window is 1 second, and the implemented estimation method simply takes the highest potential during that time frame.

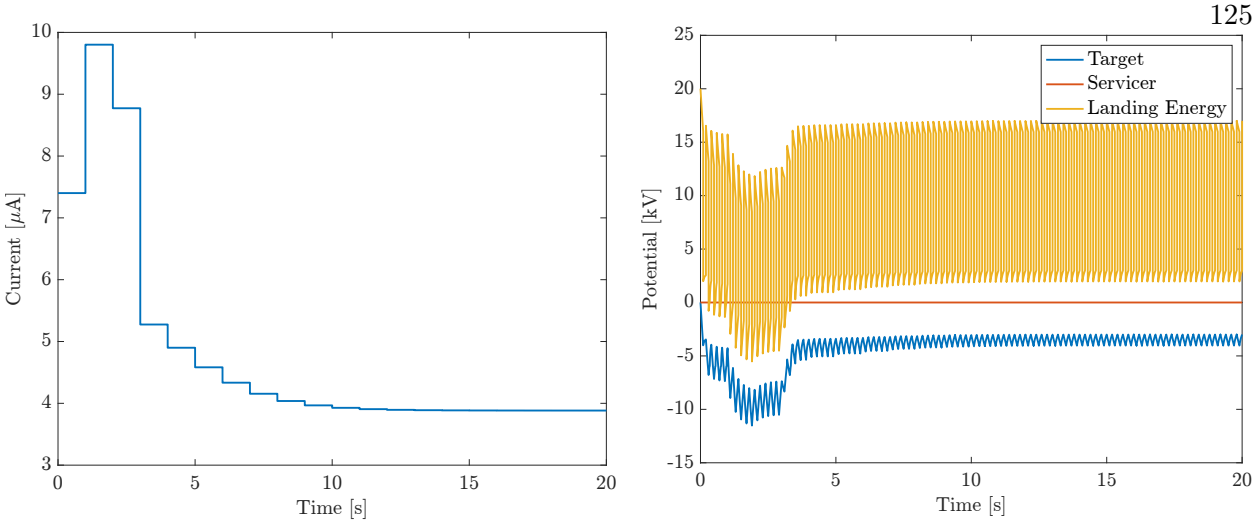

(a) Nominal Beam Current

(b) Potentials

Figure 5.7: Closed Loop Energy Pulsing

The simulation results for closed-loop on-off pulsing are shown in Fig. 5.6 for a desired potential of -3 kV and a feedback gain of $K_d = 2 \cdot 10^{-5}$. The beam energy is 20 keV and the nominal beam current $I_{EB,0} = 10$ µA. Starting at 0 V and a duty cycle of less than 0.1, the duty cycle ramps up to achieve the desired potential of -3 kV. Because the simplified estimation method that is implemented in the simulation takes the highest potential as the measurement, the converged potential has an upper bound of -3 kV, while there are some oscillations due to the pulsed beam that cause a lower potential as well.

This pulsed control strategy has the benefits of the on-off pulsed beam described earlier, but does not improve the signal for both estimation methods due to the lack of energy pulsing. For energy pulsing control, the control law

$$I_{EB,0,k} = I_{EB,0,k-1} + K_c(\hat{\phi}_T - \phi_{T,\text{des}}) \tag{5.4}$$

is used to update the nominal beam current $I_{EB,0}$, with feedback gain K_c. The simulation results for closed-loop energy pulsing are shown in Fig. 5.7 for a desired potential of -3 kV and a feedback gain of $K_c = 8 \cdot 10^{-10}$. The beam energy switches between 20 and 6 keV, and the pulse duty cycle and frequency are 0.5 and 5 Hz, respectively. In the simulation, the beam current settles just below

4 µA, resulting in the desired target potential. During the high energy phases, the target charges negatively and the high landing energy is favorable for the x-ray method. For the other half of one pulse cycle (due to the duty cycle of 0.5), the low beam energy results in a lower landing energy that causes the target to charge positively again. During some time periods, the low beam energy results in a negative landing energy in the figure, meaning that the beam is unable to reach the target. In this case, the target charges positively due to the environmental currents, and no x-ray or secondary electron signal is produced. With this control, the beam energy levels for both the high and low phase can be adjusted to maintain favorable landing energies for each method.

5.4 Conclusions

The electron and x-ray sensing methods benefit from dissimilar beam parameters. Pulsing the beam allows to quickly switch between beam settings that benefit one method at a time. Multiple ways of pulsing the beam are showcased to provide better signals for sensing as well as to provide means for charging control. Using on-off pulsing reduces the effective beam current delivered to the target, such that the target potential is perturbed less while sensing. This may be desired for electric potential sensing during on-orbit servicing operations. Energy pulsing allows to switch between a low landing energy (beneficial for the secondary electron method) and high energy (beneficial for the x-ray method), consequently establishing conditions that are beneficial for both methods as opposed to just one. The estimated potential can then be used for a feedback control where the duty cycle or the beam current is adjusted to maintain a desired potential of the target. Finally, energy pulsing enables a better way for the open-loop charging control proposed in Sec. 4.2.3 by providing a signal that can be used to confirm that the beam is actually hitting the target.

Chapter 6

Electrostatic tractor relative motion control

The Electrostatic Tractor (ET) has been proposed to touchlessly remove space debris from geostationary orbit using electrostatic forces [29, 30]. For the proposed ET relative motion control [65], the predicted inter-craft electrostatic force between the controlled tug and the uncontrolled debris is feed-forward to the control algorithm. To predict the force, the electrostatic potential of both spacecraft must be estimated to subsequently approximate the charge distribution as well as the force and the torque. As evident in Chapter 3, the remote estimation of the electric potential of a nearby object in space may be subject to errors of several hundred volts. Such estimation errors lead to an under-prediction or over-prediction of the electrostatic force, and consequently affect the relative motion control. Prior work for the ET only considered spherical spacecraft. Thus, attitude effects of complex-shaped spacecraft on the relative motion control could not be considered.

This chapter studies the performance of the Electrostatic Tractor relative motion control for spacecraft with complex shapes. The dynamics and control of the ET are reviewed in Sec. 6.1. Section 6.2 includes a detailed study of the effects of electric potential estimation errors on the relative motion control equilibria. In Sec. 6.3, the effect of the debris attitude on the control performance is investigated, including dynamic simulations. A comparison with a simple feed-back control law without the feed-forward term is presented in Sec. 6.4, and a comparison of higher and lower fidelity charging and force models is provided in Sec. 6.5.

6.1 Dynamics and control model

6.1.1 Electrostatic Tractor relative motion dynamics

The relative motion dynamics are derived in Ref. 65 and are revisited here for convenience. A Hill frame $\mathcal{H} : \{\hat{\boldsymbol{h}}_r, \hat{\boldsymbol{h}}_\theta, \hat{\boldsymbol{h}}_h\}$ with origin at the servicer's center of mass is defined by

$$\hat{\boldsymbol{h}}_r = \frac{\boldsymbol{r}_S}{r_S}, \quad \hat{\boldsymbol{h}}_\theta = \hat{\boldsymbol{h}}_h \times \hat{\boldsymbol{h}}_r, \quad \hat{\boldsymbol{h}}_h = \frac{\boldsymbol{r}_S \times \dot{\boldsymbol{r}}_S}{|\boldsymbol{r}_S \times \dot{\boldsymbol{r}}_S|} \tag{6.1}$$

where $\boldsymbol{r}_S$ is the inertial position vector of the servicer (tug), $\dot{\boldsymbol{r}}_S$ is the inertial velocity vector, and $r_S = |\boldsymbol{r}_S|$. The position of the target (debris) is described with the relative position vector $\boldsymbol{\rho}$:

$$\boldsymbol{r}_T = \boldsymbol{r}_S + \boldsymbol{\rho} \tag{6.2}$$

Solving for $\boldsymbol{\rho}$

$$\boldsymbol{\rho} = \boldsymbol{r}_T - \boldsymbol{r}_S \tag{6.3}$$

and taking two inertial time derivatives gives

$$\ddot{\boldsymbol{\rho}} = \ddot{\boldsymbol{r}}_T - \ddot{\boldsymbol{r}}_S \tag{6.4}$$

The inertial acceleration of the servicer is

$$\ddot{\boldsymbol{r}}_S = -\frac{\mu}{r_S^3}\boldsymbol{r}_S + \frac{\boldsymbol{F}_c}{m_S} + \boldsymbol{u}_S \tag{6.5}$$

where $\mu = 3.986 \times 10^{14}$ m^3 s^{-2} is Earth's gravitational parameter and m_S is the mass of the servicing satellite. The first term in Eq. (6.5) corresponds to the gravitational acceleration, $\boldsymbol{F}_c$ is the electrostatic force acting on the servicer due to the charged debris, and $\boldsymbol{u}_S$ is the thruster control acceleration generated by the servicer's inertial thrusters to perform a low-thrust semimajor axis orbit change. Similarly, the inertial acceleration of the debris is

$$\ddot{\boldsymbol{r}}_T = -\frac{\mu}{r_T^3}\boldsymbol{r}_T - \frac{\boldsymbol{F}_c}{m_T} \tag{6.6}$$

with the mass of the debris m_T. Substituting Eqs. (6.5) and (6.6) into Eq. (6.4) yields the relative Equations of Motion (EOM):

$$\ddot{\boldsymbol{\rho}} = -\frac{\mu}{r_T^3}\boldsymbol{r}_T + \frac{\mu}{r_S^3}\boldsymbol{r}_S - \frac{\boldsymbol{F}_c}{m_T} - \frac{\boldsymbol{F}_c}{m_S} - \boldsymbol{u}_S \tag{6.7}$$

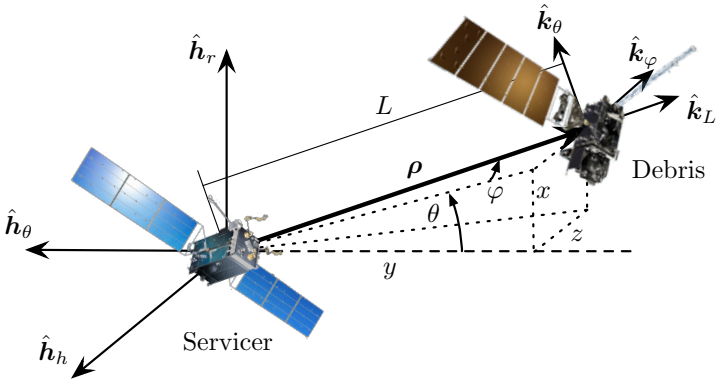

Figure 6.1: Hill frame $\mathcal{H}$ and Spherical frame $\mathcal{K}$

Combining the thruster control acceleration $\boldsymbol{u}_S$ and the electrostatic force $\boldsymbol{F}_c$ to the total control acceleration vector

$$\boldsymbol{u} = -\boldsymbol{F}_c \left(\frac{1}{m_S} + \frac{1}{m_T} \right) - \boldsymbol{u}_S \tag{6.8}$$

brings the EOM to a form that is equivalent to the Clohessy-Wiltshire-Hill (CWH) relative motion EOM:

$$\ddot{\boldsymbol{\rho}} = -\frac{\mu}{r_T^3}\boldsymbol{r}_T + \frac{\mu}{r_S^3}\boldsymbol{r}_S + \boldsymbol{u} \tag{6.9}$$

The linearized form of Eq. (6.9) is obtained using the relative position vector expressed in the Hill frame ${}^{\mathcal{H}}\boldsymbol{\rho} = [x, y, z]^T$:

$$\ddot{x} - 2n(t)\dot{y} - 3n^2(t)x = u_x \tag{6.10a}$$

$$\ddot{y} + 2n(t)\dot{x} = u_y \tag{6.10b}$$

$$\ddot{z} + n^2(t)z = u_z \tag{6.10c}$$

Because a semi-major axis orbit change is performed, the mean motion $n = \sqrt{\mu/a^3}$, with semimajor axis a, is not constant but a function of time, $n = n(t)$. The electrostatic force is in the order of milli-Newtons and requires low thrust in the same range. Thus, the orbit angular acceleration $\dot{n}$ is in the order of n^3 and is not considered [65].

The cartesian form of the EOM in Eq. (6.10) is not convenient for control design because the equations are coupled. A spherical frame $\mathcal{K} : \{\hat{\boldsymbol{k}}_L, \hat{\boldsymbol{k}}_\theta, \hat{\boldsymbol{k}}_\varphi\}$ is introduced with separation distance

L between the servicer and debris, in-plane rotation angle θ, and out-of-plane rotation angle φ, as illustrated in Fig. 6.1. The angles θ and φ are a 3-2 Euler angle rotation sequence with respect to the Hill frame $\mathcal{H}$. The direction cosine matrix (DCM) that maps from $\mathcal{H}$ to $\mathcal{K}$ is:

$$[KH] = \begin{bmatrix} \cos\varphi\sin\theta & -\cos\varphi\cos\theta & -\sin\varphi \\ \cos\theta & \sin\theta & 0 \\ \sin\theta\sin\varphi & -\cos\theta\sin\varphi & \cos\varphi \end{bmatrix} \tag{6.11}$$

The relations between the Hill frame and spherical frame coordinates are

$$L = \sqrt{x^2 + y^2 + z^2} \tag{6.12a}$$

$$\theta = \arctan\left(\frac{x}{-y}\right) \tag{6.12b}$$

$$\varphi = \arcsin\left(\frac{-z}{L}\right) \tag{6.12c}$$

and

$$\begin{bmatrix} x \\ y \\ z \end{bmatrix} = [KH]^T \begin{bmatrix} L \\ 0 \\ 0 \end{bmatrix} = \begin{bmatrix} L\sin\theta\cos\varphi \\ -L\cos\theta\cos\varphi \\ -L\sin\varphi \end{bmatrix} \tag{6.13}$$

Taking the time derivative of Eq. (6.13) twice and substituting into Eq. (6.10) yields the spherical relative equations of motion:

$$\begin{bmatrix} \ddot{L} \\ \ddot{\theta} \\ \ddot{\varphi} \end{bmatrix} = [\boldsymbol{F}(L, \theta, \varphi, \dot{L}, \dot{\theta}, \dot{\varphi})] + [G(L, \varphi)]\ {}^{\mathcal{K}}\boldsymbol{u} \tag{6.14}$$

with the control

$${}^{\mathcal{K}}\boldsymbol{u} = \begin{bmatrix} u_L \\ u_\theta \\ u_\varphi \end{bmatrix} \tag{6.15}$$

the dynamics

$$[\boldsymbol{F}] = \begin{bmatrix} \frac{1}{4}L\left(n^2\left(-6\cos(2\theta)\cos^2\varphi + 5\cos(2\varphi) + 1\right) + 4\dot{\theta}\cos^2\varphi\left(2n + \dot{\theta}\right) + 4\dot{\varphi}^2\right) \\ \left(3n^2\sin\theta\cos\theta + 2\dot{\varphi}\tan\varphi\left(n + \dot{\theta}\right)\right) - 2\frac{\dot{L}}{L}\left(n + \dot{\theta}\right) \\ \frac{1}{4}\sin(2\varphi)\left(n^2\left(3\cos(2\theta) - 5\right) - 2\dot{\theta}\left(2n + \dot{\theta}\right)\right) - 2\frac{\dot{L}}{L}\dot{\varphi} \end{bmatrix} \tag{6.16}$$

and the control mapping

$$[G] = \begin{bmatrix} 1 & 0 & 0 \\ 0 & \frac{1}{L\cos\varphi} & 0 \\ 0 & 0 & -\frac{1}{L} \end{bmatrix} \tag{6.17}$$

Note that this description is singular for out of plane motions where $\phi \to \pm\frac{\pi}{2}$.

6.1.2 Rotational dynamics

The electrostatic force also induces an electrostatic torque if the center of mass of an object does not align with its center of charge. Since the debris is uncontrolled, its attitude generally changes during the reorbit process as a result of the electrostatic torque. The rotational dynamics of the debris are given by [136, Chapter 4]

$$[I_T]\dot{\boldsymbol{\omega}} = -[\tilde{\boldsymbol{\omega}}][I_T]\boldsymbol{\omega} + \boldsymbol{L}_c \tag{6.18}$$

where $\boldsymbol{\omega}$ is the inertial angular velocity of the debris, $[\tilde{\boldsymbol{\omega}}]$ is the skew-symmetric matrix of $\boldsymbol{\omega}$ and is used as the cross-product equivalent matrix operator, $[I_T]$ is the inertia matrix of the debris, and $\boldsymbol{L}_c$ is the torque that acts on the debris due to the electrostatic forces. The inertia matrix is obtained from a CAD model of the target that is generated using publicly available size and mass information of a GOES-R satellite [47]. The attitude of the servicing satellite is held constant at its nominal orientation during the simulation, so no rotational dynamics are required for the servicer.

6.1.3 Electrostatic Tractor relative motion control design

A globally asymptotically stabilizing feedback-control is developed in Ref. 65

$${}^{\mathcal{K}}\boldsymbol{u} = [G(L,\varphi)]^{-1}\Big(- [P]\dot{\boldsymbol{X}} - [K](\boldsymbol{X} - \boldsymbol{X}_r) - [\boldsymbol{F}(L,\theta,\varphi,\dot{L},\dot{\theta},\dot{\varphi})]\Big) \tag{6.19}$$

where $\boldsymbol{X} = [L,\theta,\varphi]^T$, $\boldsymbol{X}_r$ includes the desired steady-state values L_r, θ_r, φ_r, and $[K]$ and $[P]$ are positive definite gain matrices. As in Eq. (6.8), the total control acceleration ${}^{\mathcal{K}}\boldsymbol{u}$ includes both the electrostatic force and the acceleration by the thrusters:

$${}^{\mathcal{K}}\boldsymbol{u} = -{}^{\mathcal{K}}\boldsymbol{F}_c\left(\frac{1}{m_S} + \frac{1}{m_T}\right) - {}^{\mathcal{K}}\boldsymbol{u}_S \tag{6.20}$$

Using Eq. (6.19) to obtain ${}^{\mathcal{K}}\boldsymbol{u}$, the required thruster control acceleration is computed by

$$ {}^{\mathcal{K}}\boldsymbol{u}_S = -{}^{\mathcal{K}}\boldsymbol{u} - {}^{\mathcal{K}}\boldsymbol{F}_c \left(\frac{1}{m_S} + \frac{1}{m_T} \right) \tag{6.21} $$

The thruster acceleration consists of a feedback term ${}^{\mathcal{K}}\boldsymbol{u}$ and a feed-forward term of the electrostatic force $\boldsymbol{F}_c$. Uncertainty in the estimation of the electrostatic potential of debris results in an inaccurate prediction of the Coulomb force. This motivates the analysis of the electrostatic potential uncertainty effects on the Electrostatic Tractor relative motion control.

Thruster plume impingement can exert additional forces on the debris [137, 138]. These forces are not considered, and no thrust direction keep-out zones are considered to reduce plume impingement. Additionally, it is assumed that the thrusters are able to fire continuously and without thruster saturation.

If the electron gun fails and is unable to create an electrostatic force between the two spacecraft, the servicer would initially pull away from the debris due to the missing attractive force. This is favorable compared to an electrostatic pusher configuration, where a sudden loss of the repelling force would require an immediate avoidance maneuver to prevent a collision [139]. Another scenario is the case of a complete failure of all thrusters. In this situation, the electron gun would have to be turned off to stop the attractive electrostatic force from pulling the two spacecraft toward each other. Note that, even without an active electron gun, spacecraft can charge naturally up to a few kV in GEO [18, Chapter 1]. However, if both spacecraft are charged to the same sign, this results in a repelling force.

The Multi-Sphere Method described in Sec. 2.2 is used to compute the electrostatic force and torque acting between the two spacecraft, and Fig. 2.4 shows the MSM models used in this work. The setup shown in Fig. 2.4 represents the standard (or nominal) configuration. In this configuration, the spacecraft center of mass locations are 20 m apart in the $\hat{\boldsymbol{k}}_L$ direction, and the axes of the debris frame $\mathcal{T} : \{\hat{\boldsymbol{t}}_1, \hat{\boldsymbol{t}}_2, \hat{\boldsymbol{t}}_3\}$ align with the corresponding axes of the servicer frame $\mathcal{S} : \{\hat{\boldsymbol{s}}_1, \hat{\boldsymbol{s}}_2, \hat{\boldsymbol{s}}_3\}$.

6.2 Effects of electric potential uncertainty on relative motion equilibria

The relative motion control requires knowledge of the electrostatic force between the two spacecraft. This force depends on the charge distribution of the two bodies, which in turn depends on the electrostatic potentials. Thus, an accurate determination of the potentials is necessary for a desired control behavior. Because the advantage of the Electrostatic Tractor over other ADR methods is that it does not require any physical contact, remote electrostatic potential sensing techniques are essential to keep this ADR method fundamentally touchless.

The sensing methods described in Sec. 1.2.1 provide two promising ways of touchlessly determining the potential of a neighboring satellite. However, even though these remote sensing methods provide means to touchlessly measure the electrostatic potential of the debris, the estimation might be off by a few percent [44, 45]. Measurement uncertainty arises due to inaccuracies of the implemented models and noise. It is important to know how the corresponding estimation errors affect the closed-loop response of the relative motion control.

6.2.1 Equilibria under standard conditions

If the gain matrices $[K]$ and $[P]$ are selected to be orthogonal, the spherical relative EOM in Eq. (6.14) decouple as

$$\ddot{L} + P_L\dot{L} + K_L(L - L_r) = 0 \tag{6.22a}$$

$$\ddot{\theta} + P_\theta\dot{\theta} + K_\theta(\theta - \theta_r) = 0 \tag{6.22b}$$

$$\ddot{\varphi} + P_\varphi\dot{\varphi} + K_\varphi(\varphi - \varphi_r) = 0 \tag{6.22c}$$

which allows for better analysis of the closed-loop response. If the potential of the debris is estimated, the first equation becomes

$$\ddot{L} + P_L\dot{L} + K_L(L - L_r) = (F_c - F_{c,\text{est}})\left(\frac{1}{m_S} + \frac{1}{m_T}\right) \tag{6.23}$$

where $F_{c,\text{est}}$ is the Coulomb force according to the estimated potential and F_c is the actual Coulomb force. Both $F_{c,\text{est}}$ and F_c are the $\hat{\boldsymbol{k}}_L$ components of the electrostatic force vectors $\boldsymbol{F}_{c,\text{est}}$ and $\boldsymbol{F}_c$.

Defining

$$\mu_{ST} = \left(\frac{1}{m_S} + \frac{1}{m_T} \right) \tag{6.24}$$

yields a compact form for the equilibrium solutions of the closed-loop response:

$$K_L(L - L_r) = (F_c - F_{c,\text{est}})\mu_{ST} \tag{6.25}$$

Note that, for constant servicer and debris potentials ϕ_S and ϕ_T, the actual force $F_c = F_c(L)$ depends on the separation distance L between the servicer and the debris. Assuming perfect knowledge of the servicer potential ϕ_S, the estimated force $F_{c,\text{est}} = F_{c,\text{est}}(L, \Delta\phi)$ is a function of L and the estimation error of the debris potential

$$\Delta\phi = \frac{\phi_T - \phi_{T,\text{est}}}{\phi_T} \cdot 100\% \tag{6.26}$$

where ϕ_T is the actual potential and $\phi_{T,\text{est}}$ is the estimated potential of the debris. Thus, Eq. (6.25) is rewritten as

$$K_L(L - L_r) - \Big(F_c(L) - F_{c,\text{est}}(L, \Delta\phi) \Big) \mu_{ST} = 0 \tag{6.27}$$

where the forces are computed using MSM. The feedback gain K_L must be chosen to compute the equilibrium solutions of Eq. (6.27). Reference [65] shows that

$$K_L \geq \frac{27 \mu_{ST} k_c |\Delta Q|}{4 L_r^3} \tag{6.28}$$

is required to ensure that an equilibrium solutions with a positive value of L exist for the two-sphere model. This formulation considers a charge estimation error

$$\Delta Q = q_S q_T - q_{S,\text{est}} q_{T,\text{est}} \tag{6.29}$$

instead of an electrostatic potential estimation error $\Delta\phi$. In the equation above, q_S and q_T are the charges of the servicer and the debris, and $q_{S,\text{est}}$ and $q_{T,\text{est}}$ are the estimated charges. Equation (6.28) depends on the masses of the spacecraft, the reference separation distance, and requires some knowledge about the expected magnitude of the charge estimation error ΔQ. If the feedback gain K_L is chosen according to Eq. (6.28), then equilibrium solutions with a positive value of L exist

Table 6.1: Parameters used in this analysis

m_S	m_T	ϕ_S	ϕ_T	$\Delta\phi_{\max}$
2000 kg	2857 kg	25 kV	-25 kV	10 %

for charge estimation errors that are smaller than the expected estimation error magnitude that was selected for determining the feedback gain. Comparing Eq. (6.28) to Eq. (2.24) shows that the term $k_c|\Delta Q|/L_r^2$ corresponds to the difference between the actual force and the estimated force:

$$K_L \geq \frac{27\mu_{ST}}{4L_r}\left|F_c(L_r) - F_{c,\text{est}}(L_r, \Delta\phi)\right| \tag{6.30}$$

The required minimal gain K_L depends on the expected potential uncertainty $\Delta\phi$ and the desired reference separation distance L_r. The feedback gain is obtained by substituting the maximum expected potential error $\Delta\phi_{\max}$:

$$K_L = \frac{27\mu_{ST}}{4L_{r,KL}}\left|F_c(L_{r,KL}) - F_{c,\text{est}}(L_{r,KL}, \Delta\phi_{\max})\right| \tag{6.31}$$

Note that L_r is replaced by $L_{r,KL}$ to distinguish between the desired distance L_r and the configuration distance $L_{r,KL}$ that is used to compute the gain, as these two values sometimes differ in the following sections. Equation (6.27) is solved numerically for the standard spacecraft orientation as shown in Fig. 2.4, using the parameters given in Table 6.1 and $L_r = 20$ m. The resulting equilibrium locations L_{eq} are shown in Fig. 6.2.

If the electrostatic potential of the debris is underestimated ($\Delta\phi < 0$), the estimated negative debris potential $\phi_{T,\text{est}}$ increases in magnitude. Thus, the force is over-predicted and the relative motion control settles to an equilibrium separation distance that is greater than the desired distance L_r. If the debris potential is overestimated ($\Delta\phi > 0$), the magnitude of the estimated potential $\phi_{T,\text{est}}$ decreases, and the resulting force is under-predicted. In this case, either two positive and one negative equilibrium solutions exist or only one negative solution, depending on the error $\Delta\phi$. The under-estimation of the electrostatic force pulls the servicing satellite closer to the debris. Only one of the positive equilibria is stable, depicted by the solid line in the figure, while the other positive

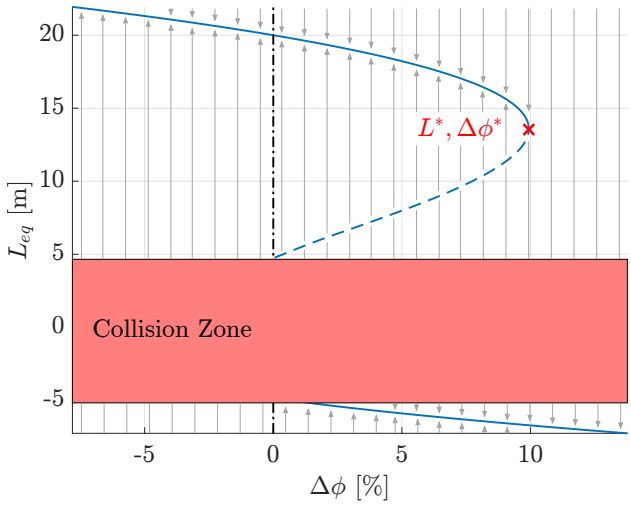

Figure 6.2: Equilibrium locations L_{eq} of the closed-loop response for potential estimation error $\Delta\phi$ and $L_r = 20$ m: the solid lines correspond to stable equilibria, the dashed line represents unstable equilibria.

equilibrium solution is unstable and represented by a dashed line. The arrows in Fig. 6.2 illustrate the domain of attraction.

The closed-loop response bifurcates at the critical point $(L^*, \Delta\phi^*)$. A potential error that is greater than the critical error $\Delta\phi^*$ results in one negative root. As the relative motion control settles towards this negative equilibrium location, the servicing satellite would have to pass through the debris, causing a collision. The separation distances where the two spacecraft geometries intersect are represented by the shaded region in Fig. 6.2 and labeled as the Collision Zone. An equilibrium location that is within this region, or a negative equilibrium solution, causes the two spacecraft to collide. Thus, an estimation error that is greater than the critical error $\Delta\phi^*$ must be avoided as it would cause a collision. Note that the critical error is approximately equal to the expected maximum estimation error, which is 10 % in this analysis, if the feedback gain is computed using Eq. (6.31).

The location of the critical point can also be approximated by replacing the complex spacecraft models with effective spheres. Reference 65 shows that

$$L^* = \frac{2}{3} L_r \tag{6.32}$$

for a two-sphere model. While this relation is exact for the two-sphere model, it only holds approximately for general 3D geometries. The charge estimation error at this distance is:

$$\Delta Q^* = -\frac{4K_L L_r^3}{27 k_c \mu_{ST}} \tag{6.33}$$

This critical value is also obtained with Eq. (6.29):

$$\Delta Q^* = q_S q_T - q^*_{S,\text{est}} q^*_{T,\text{est}} \tag{6.34}$$

The charges q_S and q_T correspond to the actual spacecraft potentials ϕ_S and ϕ_T, while $q^*_{S,\text{est}}$ and $q^*_{T,\text{est}}$ result from the critical potential estimation error $\Delta\phi^*$. Assuming perfect knowledge of the servicer potential, the charges are determined by inverting Eq. (2.23):

$$q_S = \frac{L^*(L^* R_S \phi_S - R_S R_T \phi_T)}{k_c(L^{*2} - R_S R_T)} \tag{6.35a}$$

$$q_T = \frac{L^*(L^* R_T \phi_T - R_S R_T \phi_S)}{k_c(L^{*2} - R_S R_T)} \tag{6.35b}$$

$$q^*_{S,\text{est}} = \frac{L^*(L^* R_S \phi_S - R_S R_T \phi_T(1+\Delta\phi^*))}{k_c(L^{*2} - R_S R_T)} \tag{6.35c}$$

$$q^*_{T,\text{est}} = \frac{L^*(L^* R_T \phi_T(1+\Delta\phi^*) - R_S R_T \phi_S)}{k_c(L^{*2} - R_S R_T)} \tag{6.35d}$$

Substituting Eq. (6.35) into Eq. (6.34) gives

$$\Delta Q^* = \frac{L^{*2} R_S R_T}{k_c^2 (L^{*2} - R_S R_T)^2} \cdot \left[L^* R_T \Delta\phi^{*2} + \left(2L^* R_T \phi_T - (L^{*2} + R_S R_T)\phi_S\right)\Delta\phi^* \right] \tag{6.36}$$

This expression depends on the radii of the effective spheres R_S and R_T. The self-capacitance of a sphere is given by

$$C = 4\pi\varepsilon_0 R = \frac{R}{k_c} \tag{6.37}$$

where ε_0 is the vacuum permittivity. Since the self capacitance of the spacecraft is known from the MSM models, the effective sphere radii are approximated by:

$$R_S = C_S k_c = 4.8 \text{ m} \qquad R_T = C_T k_c = 4.4 \text{ m} \tag{6.38}$$

Note that Eqs. (6.35) and (6.36) are singular if $L^{*2} - R_S R_T = 0$. However, for two spheres that do not overlap, i.e. $R_S + R_T < L^*$, it can be shown that $L^{*2} - R_S R_T > 0$ is always true. Equating

Eq. (6.33) with Eq. (6.36) and using Eq. (6.32) yields the quadratic formula

$$\Delta\phi^{*2} + b\Delta\phi^* + c = 0 \tag{6.39}$$

where

$$b = 2 - \frac{3}{2L_r R_T}(\frac{4}{9}L_r^2 + R_S R_T)\frac{\phi_S}{\phi_T} \tag{6.40a}$$

$$c = \frac{K_L k_c(\frac{4}{9}L_r^2 - R_S R_T)^2}{2R_S R_T^2 \mu_{ST}\phi_T^2} \tag{6.40b}$$

The solution of Eq. (6.39) is

$$\Delta\phi^*_{1,2} = -\frac{b}{2} \pm \sqrt{\frac{b^2}{4} - c} \tag{6.41}$$

Examining the terms in Eq. (6.40) shows that only the minus sign in front of the square root yields a reasonable solution. The equation above is only exact for two spheres with known radii, but provides an approximation of the critical error for two complex shaped spacecraft that are replaced by two effective spheres:

$$\Delta\phi^* \approx -\frac{b}{2} - \sqrt{\frac{b^2}{4} - c} \tag{6.42}$$

6.2.2 Change over distance

It is interesting to see how the closed-loop response is affected by changes to the reference spacecraft separation distance L_r. This analysis considers two cases:

- Case 1: Changes to the reference distance L_r without adjustment of the feedback gain K_L
- Case 2: Changes to the reference distance L_r with a feedback gain K_L that is adjusted to the new reference distance

Equation (6.31) shows that the gain K_L is configured for a certain reference distance $L_{r,KL}$. Thus, it is expected that the closed-loop response changes if the desired distance L_r of the controller differs from the configuration distance $L_{r,KL}$. While one would not intentionally change the reference distance without adjusting the feedback gain, this can happen for other reasons. For example, erroneous relative position measurements essentially change the reference distance L_r.

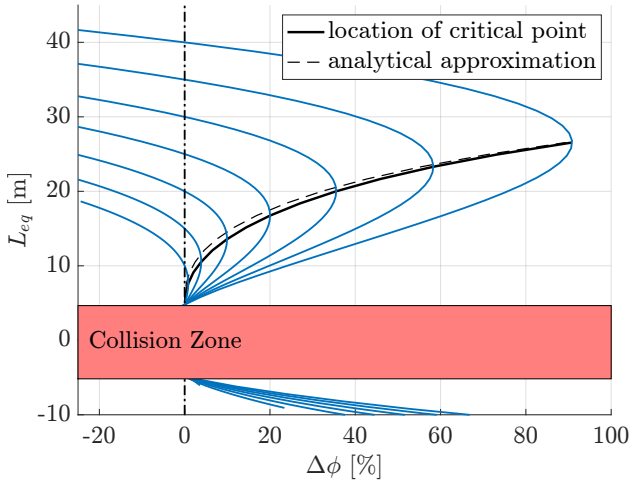

Figure 6.3: Changes to the reference distance L_r without adjustment of the gain K_L, for $L_{r,KL} = 20$ m

The effects of changes to the reference distance without adjustment of the feedback gain (Case 1) are shown in Fig. 6.3 for a configuration distance of $L_{r,KL} = 20$ m. If $L_r = L_{r,KL}$, the critical potential estimation error is approximately equal to the maximum expected error, $\Delta\phi^* \approx \Delta\phi_{\max} = 10$ %, since the controller was set up for this separation distance. The magnitude of the electrostatic force decreases proportional to $1/L^2$, so increasing the reference distance such that $L_r > L_{r,KL}$ results in a larger critical error. Thus, a larger uncertainty of the debris potential can be handled without causing a collision. At some point, the critical error exceeds 100 %. However, if $\Delta\phi > 100$ %, the estimated debris potential is positive even though the actual potential of the debris is negative, so the controller would expect a repelling force instead of an attractive force. This drastically changes the dynamics of the relative motion control, so estimation errors greater than 100 % are not considered in this analysis. If $L_r < L_{r,KL}$, the critical error decreases, because the electrostatic force is stronger in closer proximity. This means that an estimation error that is smaller than the maximum expected error leads to a collision of the spacecraft.

Figure 6.3 also displays the location of the critical points, represented by the solid black line, and the corresponding approximation according to Eq. (6.42), denoted by the dashed line. For small separation distances, where the electrostatic forces are strong and the difference between the

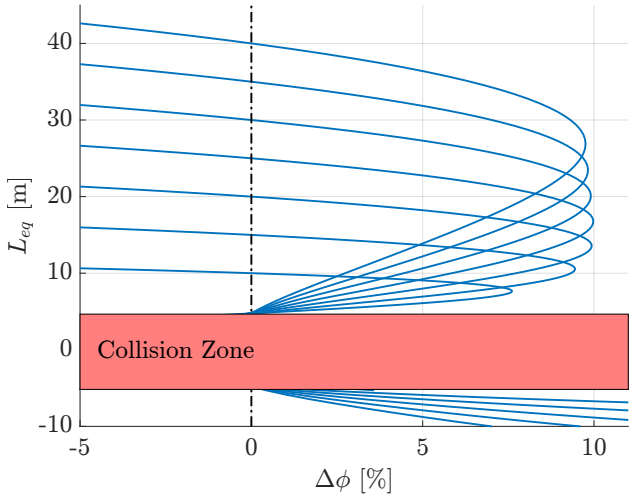

Figure 6.4: Changes to the reference distance L_r with adjusted feedback gain K_L

two-sphere model and the MSM model are of greater importance, the approximation deviates from the actual locations. However, for greater distances, the locations are approximated well.

Figure 6.4 shows how changes to the reference distance affect the equilibrium locations if the feedback gain is adjusted for each value of L_r. Because the gain K_L, according to Eq. (6.31), is set up such that the critical error approximately equals the maximum expected error, $\Delta\phi^* \approx 10$ % for each reference distance. However, Eq. (6.31) is based on a two-sphere model. For small separation distances, the differences between the two-sphere-model and the MSM model become more significant, so the critical potential estimation error deviates from the maximum expected error.

6.2.3 Change over attitude

The implementation of MSM models enables the study of attitude effects on the closed-loop response for generally shaped spacecraft. According to Fig. 2.4, the debris is re-oriented by changing the yaw α and the pitch β, where $-180° < \alpha < 180°$ and $-90° < \beta < 90°$. The yaw axis aligns with the solar panel of the GOES-R satellite, the pitch axis points in the direction of the magnetometer, and the geometric center of the debris serves as the pivot point. This analysis of the attitude effects only considers the case where $\Delta\phi = \Delta\phi^*$.

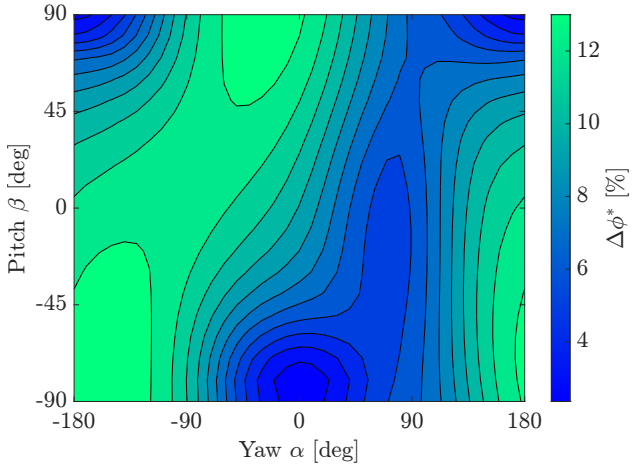

Figure 6.5: Attitude effects on the critical potential estimation error $\Delta\phi^*$

Figure 6.5 shows how different spacecraft orientations affect the critical estimation error $\Delta\phi^*$. For the standard orientation ($\alpha = 0°, \beta = 0°$) that was considered in the previous sections, the critical error is about 10 % if $L_r = L_{r,KL}$. However, this critical error reaches values as low as 2 % for some debris orientations, meaning that a potential estimation error of just 2 % already causes a collision. The green areas correspond to debris orientations that increase the critical error, so a larger estimation error can be tolerated without causing the two satellites to collide. These regions generally correlate with those orientations where both the solar panel and the magnetometer point away from the servicer. The blue areas, on the other hand, designate the orientations that decrease the critical error. This poses a risk because the servicer would collide with the debris at an estimation error that is smaller than the maximum expected error. The dark blue regions at ($\alpha = 0°, \beta = -90°$) and ($\alpha = \pm 180°, \beta = 90°$) correspond to orientations where the solar panel of the debris satellite is directed towards the servicing satellite, and the valley at $\alpha = 90°$ is due to the magnetometer pointing to the servicer.

Essentially, the distance between the center of charge of each spacecraft decreases if one of the debris' features, such as the solar panel or the magnetometer, is directed towards the servicer. In an effective two-sphere model, this corresponds to a scenario where the two spheres are separated by a distance that is smaller than the reference distance L_r. As shown in the previous section, a smaller

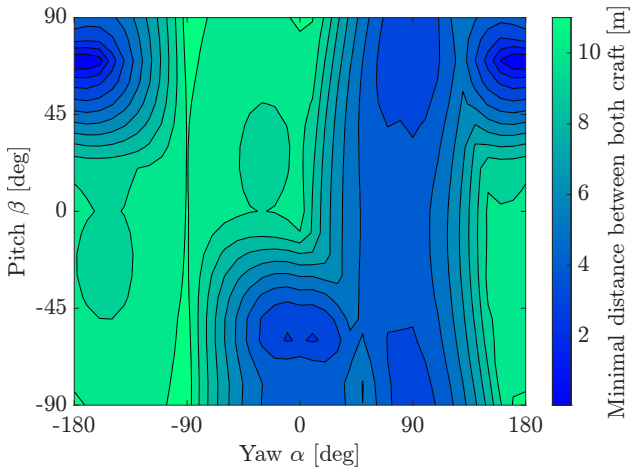

Figure 6.6: Attitude effects on the minimal distance between the debris and the servicer, for $\Delta\phi = \Delta\phi^*$

reference distance decreases the critical error, and vice-versa, if the feedback gain is not adjusted (Fig. 6.3). For the worst case orientations, where the solar panel is aimed at the servicing satellite, the critical error decreases drastically to only about 2 %, even though the maximum expected estimation error is 10 %. For the best case orientation, however, the critical error increases only marginally to a little over 13 %.

The effects of debris attitude on the minimal distance between both spacecraft in the $\hat{\boldsymbol{k}}_L$ direction is displayed in Fig. 6.6. For each debris orientation, the length of the line connecting the two closest points between the tug and the debris is computed. The long peak at $\alpha = -90°$ and the valley at $\alpha = 90°$ correspond to the magnetometer of the debris pointing away and towards the servicer, respectively, and the dark blue circular regions accord to the orientations where the solar panel is directed towards the servicer.

The minimal distance between the debris and the servicer is significantly lower than the reference distance $L_r = 20$ m due to the following reasons. First, since this attitude analysis is done for an estimation error of $\Delta\phi = \Delta\phi^*$, the center-to-center equilibrium separation distance of the two spacecraft is about two thirds of the reference distance, or about 13 m, according to Eq. (6.32). Second, the reference distance is based on the distance between the center of the debris and the center of the servicer, so the size of the spacecraft buses further decreases the minimal space

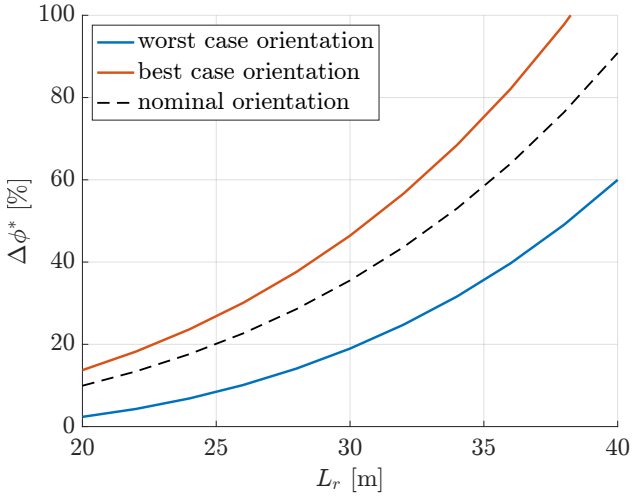

Figure 6.7: Attitude effects over distance, without adjustment of the gain K_L, for $L_{r,KL} = 20$ m

between the two craft by a few meters. In the case where the debris' solar panel or magnetometer – both of which are about 10 m long – is directed towards the servicer, the minimal distance reduces severely to less than 1 meter, despite a reference distance of 20 m.

Note that the regions of low critical error in Fig. 6.5 generally match with the areas of low minimal distance in Fig. 6.6. If one of the debris' features points towards the servicer, induced charging effects move the center of charge of each spacecraft closer to the other one, which decreases the critical estimation error. At the same time, this reduces the minimal distance due to the length of these structures. While intriguing, this offers a clear choice for a worst case scenario, which can be used to select the feedback gain of the relative motion control accordingly. This limits the closest reference distance that can be achieved, unless a control law is implemented that adjusts the separation distance according to the debris orientation.

Figure 6.7 and Fig. 6.8 show how these attitude effects are affected by changes to the reference distance L_r by looking at the worst and best case scenarios. The worst case orientation is at $(\alpha = 0°, \beta = -90°)$, where the critical error drops to 2.4 %, and the best case orientation is at $(\alpha = -30°, \beta = 90°)$, where the critical error rises to 13.7 %. Like in the previous section, it is differentiated between adjusting the feedback gain for every reference distance, and keeping the same gain across all distances. The nominal orientation corresponds to the scenario shown in

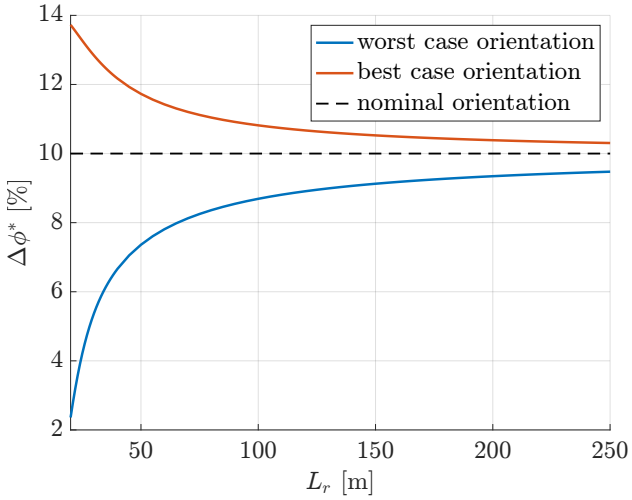

Figure 6.8: Attitude effects over distance, with adjusted feedback gain K_L

Fig. 2.4.

In Fig. 6.7, the feedback gain is not updated. The distance effects dominate the attitude effects, because the critical error increases for both the worst and best case scenario.

Figure 6.8 displays the attitude effects over distance for the case where the feedback gain is adjusted for every reference distance. The curves from both the worst and best case scenario converge to the critical estimation error of 10 % that corresponds to the standard orientation. The attitude effects are quite significant for distances up to 50 m, and even at 150 m the deviation from the standard critical error is still noteworthy. Note that Debye shielding is not considered in this analysis, which would decrease the impact of electrostatic forces at greater distances, and consequently reduce the attitude effects as well. At a distance over 200 m in GEO, Debye screening essentially prevents the two charged spacecraft from exerting electrostatic forces on each other. However, these results suggest that attitude effects should be considered at any separation distance in a tugging scenario where electrostatic forces are effective.

It is important to differentiate between errors of the estimated landing energy and errors of the estimated potential. Figure 6.5 shows critical estimation errors of the target potential of 2 %, which should not be exceeded. For a target potential of -25 kV, a critical estimation error of 2 % corresponds to 500 V. In Chapter 3, estimation errors of 200 V can be seen, which corresponds

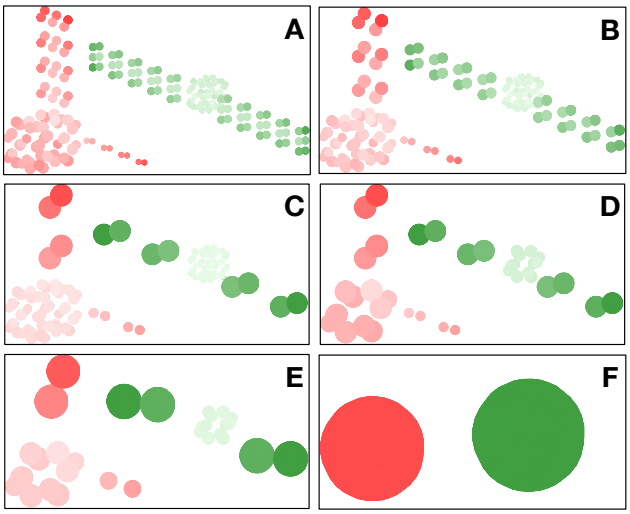

Figure 6.9: MSM Models

to 20 % for an applied potential of 1 kV, for example. However, the sensing methods are used to estimate the landing energy of the electron beam and subsequently infer the electric potential of the target. As shown in Ref. 47, the estimation error scales with landing energy, not with electric potential. Thus, similar sensing estimation errors are expected for a target potential of -25 kV (as opposed to 1 kV), as long as the landing energy remains the same.

6.2.4 Multi-Sphere model comparison

The analysis in the previous sections is based on a debris MSM model with 80 spheres and a servicer model with 108 spheres. However, a large number of spheres increases the computational costs. Thus, the effects of lower-fidelity MSM models are investigated in this section.

For the surface MSM models, the spacecraft surfaces are discretized into triangles, and each sphere of the MSM model is placed at the centroid of a triangle [96]. Consequently, at least two spheres are required for a rectangular surface, which limits the minimum number of spheres for the spacecraft MSM models. For example, each spacecraft bus consists of six rectangular sides, so at least $6 \times 2 = 12$ spheres are required for the bus.

Figure 6.9 and Table 6.2 show the different MSM model configurations that are used in this analysis. The number of feature spheres corresponds to the number of spheres that are used for

Table 6.2: MSM Model configurations

Configuration ID	Debris			Servicer		
	# of bus spheres	# of feature spheres	total # of spheres	# of bus spheres	# of feature spheres	total # of spheres
A	48	32	80	48	60	108
B	48	18	66	48	32	80
C	48	8	56	48	8	56
D	12	8	20	12	8	20
E	12	4	16	12	4	16
F	-	-	1	-	-	1

geometries like the solar panel and magnetometer. For the lowest-fidelity model (Configuration F), a single effective sphere represents the spacecraft, and is placed at the center of charge of the corresponding spacecraft. The center of charge is computed using the Configuration A MSM models in their standard orientations as shown in Fig. 2.4.

6.2.4.1 Standard conditions

First, the equilibrium locations are computed for the standard spacecraft orientations and for a reference distance of $L_r = L_{r,KL} = 20$ m (Fig. 6.10). Most of the equilibria curves agree with the highest-fidelity MSM model (Configuration A). Only Configuration F, which consists of one effective sphere placed at the center of charge of each spacecraft, deviates significantly. The deviation of $\Delta\phi$ at the critical point ($L^* = 2/3\ L_r$) corresponds to the difference between the analytical approximation of the critical point and the actual value for $L_r = 20$ m as seen in Fig. 6.3.

6.2.4.2 Attitude

Next, the critical estimation error $\Delta\phi^*$ is computed for the worst and best case orientation using the different MSM model configurations. The absolute difference between the computed values

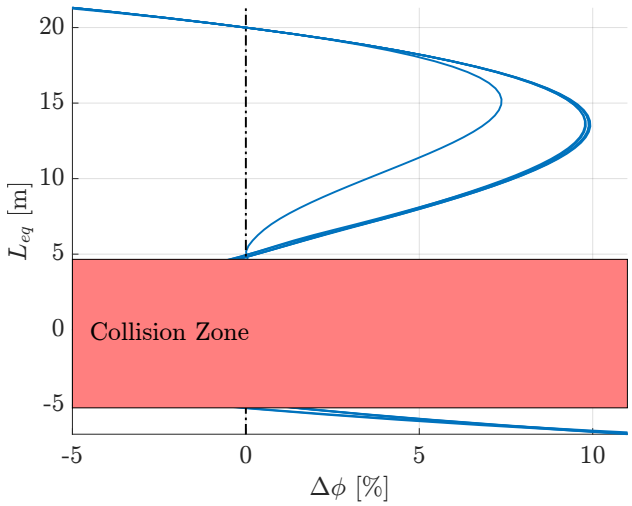

Figure 6.10: MSM model effects for standard scenario

and the corresponding values using Configuration A is shown in Fig. 6.11, for each configuration. Note that the critical error is already given in units of %. A difference of +1 %, for instance, means that the lower-fidelity MSM model predicts a critical error of 3 % if the highest-fidelity MSM model yields a value of 2 %. Configuration B and C deviate just slightly from Configuration A. For the worst case orientation, there is almost no difference going from configuration C to D. Even though the number of spheres on the debris decreases from 56 to 20, this change only comes from a reduced number of bus spheres, while the number of feature spheres remains the same. On the other hand, the difference between configuration D and E is significant despite only reducing the total spheres by four, as the number of feature spheres decreases while the modeling of the bus does not change.

The effects of the two sphere effective sphere model (Configuration F) are interesting, as the deviation of the best case orientation increases significantly (as expected), while the deviation of the worst case orientation actually decreases with respect to Configuration E. This is due to the following reasons. First, since the effective sphere of the debris is placed at the spacecraft's center of charge, and rotated about the geometric center of the actual spacecraft to represent different debris orientations, some attitudes are represented more accurately than others. The center of charge is computed for the standard orientation of the debris, but varies if the orientation is changed. Second, a single sphere cannot account for any induced charging effects due to the other spacecraft, which

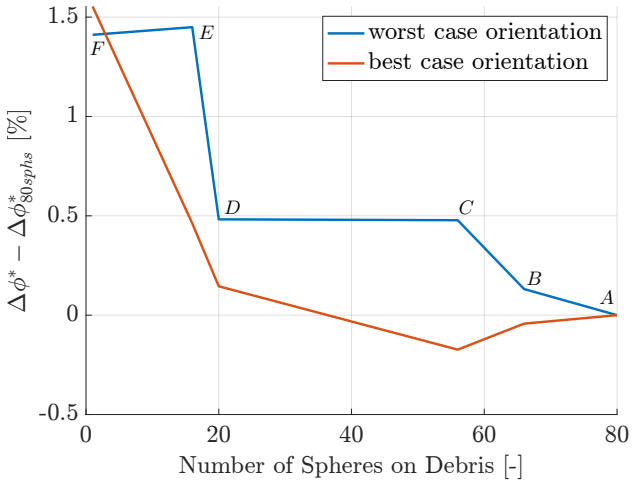

Figure 6.11: MSM model effects on critical estimation error of worst and best case scenario

generally accumulates charge at the sides of the spacecrafts that face each other. These induced charging effects are even more significant when some of the debris' features point towards the servicing satellite, which is the case for the worst case orientation. Finally, according to Fig. 6.10, the critical error for the standard orientation of Configuration F is already almost 3 % lower than that of the other configurations. Because the critical error is smaller for the worst case orientation, the negative offset of Configuration F at the standard orientation gives the two-sphere model a head start and reduces the $\Delta\phi^*$ deviation.

The results imply that priority must be given to the distribution of spheres on the spacecraft's features – such as solar panels, magnetometers, and other protruding structures – while the spacecraft's bus can be modeled with a minimal number of spheres. Charge accumulates at the edges and corners of conducting objects. For spacecraft, this corresponds to the protruding structures, noticeable in Fig. 2.4. Thus, it is important to accurately model these structures with MSM. The deviations are reasonably small for all models, including Configuration F. However, the strong dependency of the effective sphere model on the location of the center of charge at the standard orientation makes the two-sphere model unfavorable. A center of charge that is located at or near the geometric center of the satellite, which serves as the pivot point for the debris rotations, would prevent any information of the attitude effects.

Table 6.3: Computation time ratios with respect to Configuration A

Configuration	A	B	C	D	E	F
# of Spheres	80	66	56	20	16	1
t/t_A	1	0.80	0.44	0.16	0.13	0.05

6.2.4.3 Computation time

Lastly, the reduction in computation time due to a decrease in the number of spheres is investigated. For this analysis, the data in Fig. 6.5 is computed with each MSM model configuration, and the computation times are compared to that of Configuration A. Table 6.3 shows the ratio of the computation time t of each configuration to the computation time t_A of Configuration A. As expected, the computation time decreases with a reduction in the number of spheres, and the effective sphere model is significantly faster than Configuration A. However, Configuration D is just slightly slower than Configuration F, at a much higher accuracy according to Fig. 6.10 and Fig. 6.11.

For the given spacecraft, Configuration D is recommended due to the high computation speed and reasonable accuracy. For the Surface Multi-Sphere Method, a minimum of two spheres is required for a rectangular area. The analysis suggests that two spheres per solar panel significantly reduce the accuracy (Configuration E), so at least four spheres per protruding structure are recommended.

In general, the distribution of spheres should be focused on protruding structures like solar panels, while a spacecraft's bus can consist of a smaller number of spheres. The implementation of effective spheres that are placed at the center of charge of higher fidelity spacecraft models is not recommended due to the dependency on the location of the center of charge, and because the reduction in computational effort is marginal compared to low fidelity Multi-Sphere models.

6.2.5 Servicer electric potential uncertainty

Because the remote electric potential sensing methods that are being developed [35, 36] estimate the relative potential between the target and the servicer, the estimated absolute potential of the target also depends on the estimated potential of the servicer. Thus, estimation errors of the servicer are also considered here. An electric potential estimation error for the servicer

$$\Delta\phi_S = \phi_{S,\text{est}} - \phi_S \tag{6.43}$$

is applied, where $\phi_{S,\text{est}}$ is the estimated potential of the servicer. For the debris, the error of the relative potential between the debris and the servicer

$$\Delta\phi_{T,\text{rel}} = \phi_{T,\text{rel,est}} - \phi_{T,\text{rel}} = (\phi_{T,\text{est}} - \phi_{S,\text{est}}) - (\phi_T - \phi_S) \tag{6.44}$$

is used because it is the actually measured value. The estimated absolute potential of the debris

$$\phi_{T,\text{est}} = \phi_{S,\text{est}} + \phi_{T,\text{rel,est}} \tag{6.45}$$

also depends on the estimated potential of the servicer. Reference 34 derives the sensitivity ratio of the (estimated) electrostatic force between two spheres to errors in the electric potentials

$$\frac{\partial F/\partial\phi_S}{\partial F/\partial\phi_{T,\text{rel}}} = \frac{(2\phi_S + \phi_{T,\text{rel}})(\rho^2 + R_S R_T) - 2R_S\phi_S\rho - 2R_T\rho(\phi_S + \phi_{T,\text{rel}})}{\phi_S(\rho^2 + R_S R_T) - 2R_T\rho(\phi_S + \phi_{T,\text{rel}})} \tag{6.46}$$

where ρ is the separation distance between the two spheres, R_S and R_T are the radii of the spheres, and ϕ_S and $\phi_{T,\text{rel}}$ are the absolute potential of the servicer sphere and relative potential of the debris sphere, respectively. If both spheres are charged to the same potential ($\phi_{T,\text{rel}} = 0$), the repulsive electrostatic force is more sensitive to errors in the servicer potential ϕ_S. This is the case in Ref. 34. On the other hand, if $\phi_S = 25$ kV and $\phi_{T,\text{rel}} = -50$ kV, as it is the case for the electrostatic tractor, then the magnitude of the sensitivity ratio is less than 1, indicating that the force is more sensitive to errors in the relative potential $\phi_{T,\text{rel}}$.

6.3 Debris attitude

While estimation errors of the target electric potential have some effect on the reorbit performance, these effects are enhanced by the some orientations of the target due to the effectively

closer distance between the two spacecraft and consequently stronger electrostatic force (Sec. 6.2). The effect of the debris attitude itself is further analyzed here.

The Basilisk[1] astrodynamics simulation framework is used for this set of simulations [140]. This open source software package uses a set of C/C++ modules, and the scripts are written in Python. The simulations are set up easily using the Python scripts, while the C/C++ based modules allow for fast computations. Basilisk is capable of computing the electrostatic forces between several spacecraft using the Multi-Sphere Method, which makes this software package especially appealing for work on charged astrodynamics.

The simulation is set up in the following way. The servicing spacecraft starts at the desired position $\boldsymbol{X} = \boldsymbol{X_r}$ with $\theta_r = 0$ and $\varphi_r = 0$, and the attitude of the servicer is held constant at its nominal orientation according to Fig. 2.4. The initial attitude of the debris varies from one analysis to the other, and the attitude is either prescribed (meaning that it is held at a constant orientation) or freely rotating according to the rotational dynamics given in Eq. (6.18). The debris is then reorbited to a graveyard orbit at an altitude of $\Delta a = 300$ km above GEO, where the semi-major axis difference between the graveyard orbit and GEO is Δa. Table 6.1 shows the simulation parameters used in this analysis. The electric potentials of the servicer and the debris are denoted by ϕ_S and ϕ_T, respectively. Fully conducting spacecraft are assumed, so all spheres have the same electric potential as the corresponding spacecraft. The reference separation distance L_r is equal to 20 m and a feedback gain $K_L = 1.356 \cdot 10^{-7}$ is used which is determined according to Eq. 6.31 for a maximum expected electric potential estimation error of the debris of $\Delta\phi_{\max} = 10$ %.

6.3.1 Prescribed attitude

The effects of the debris attitude on the performance of the Electrostatic Tractor are investigated for prescribed attitudes. The attitude of the debris is set using yaw α and pitch β according to Fig. 2.4, where $-180° < \alpha < 180°$ and $-90° < \beta < 90°$. This orientation of the debris is held constant throughout the entire simulation.

[1] https://avslab.github.io/basilisk/ (Consulted on: 05/23/2025)

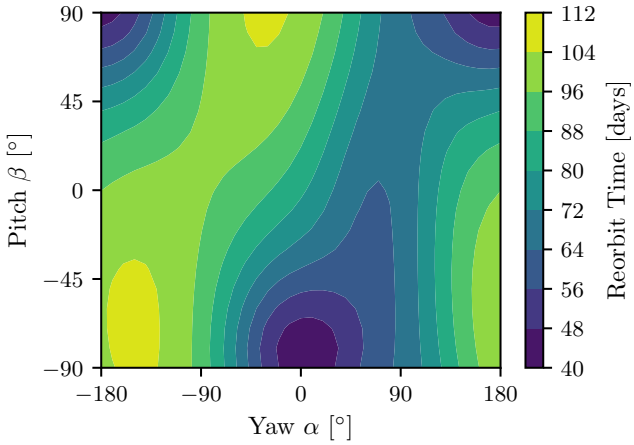

Figure 6.12: Reorbit Times for 300 km altitude raise with prescribed attitude

Figure 6.12 shows the time it takes to increase the semi-major axis of the debris orbit by 300 km, as a function of the yaw and pitch angle of the debris. For three orientations (dark blue regions) at $(\alpha = 0°, \beta = -90°)$ and $(\alpha = \pm 180°, \beta = 90°)$, the required reorbit time is significantly lower than for the other orientations. At these debris orientations, the solar panel of the debris is pointing toward the servicing satellite. Similarly, the reorbit time is generally lower at $\alpha = 90°$, where the magnetometer is directed toward the servicer. Essentially, the center of charge of the debris is closer to the servicer for these orientations, which increases the electrostatic force between the two spacecraft. Due to the higher electrostatic force, the thruster acceleration in the opposite direction increases as well to prevent the servicer from coming closer to the debris (Eq. (6.21)). Thus, as a result of the higher inertial thrust, the two satellites reorbit faster.

Figure 6.12 suggests that the ideal orientation in terms of reorbiting time for a GOES-R debris satellite is at $(\alpha = 0°, \beta = -90°)$, where the single solar panel of the GOES-R points toward the servicing satellite. Many retired satellites in GEO are tumbling [11], so the debris must be detumbled and then held at the desired orientation. It has been proposed to touchlessly detumble objects in GEO using electrostatic forces [31]. The electrostatic detumble control has been investigated for target objects with cylindrical shapes [61, 141] and satellite shapes including solar panels and magnetometers [62]. However, the main objective in these references is to reduce the angular velocity of the target object to a minimum such that docking becomes possible. That

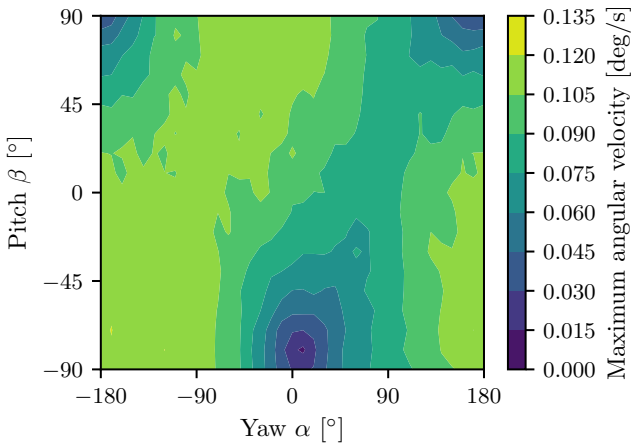

Figure 6.13: Maximum angular velocity during 300 km altitude raise

is, the object is detumbled without interest in the final attitude. Reference 60 demonstrates that it is possible to control the orientation (i.e. the final attitude after detumbling) of a cylindrical object using electrostatic forces, and the simulation results are validated experimentally. This provides a promising way of touchlessly holding the debris in a desired orientation to reduce the reorbiting time with the Electrostatic Tractor.

6.3.2 Freely rotating debris

Studying prescribed attitudes is valuable to identify optimal debris orientations for the Electrostatic Tractor concept. However, unless the attitude of the dysfunctional debris is externally controlled by the servicer using electrostatic torques and charge control, the desired orientation of the debris can generally not be maintained. Moreover, one of the advantages of the ET compared to other ADR methods is that the debris does not need to be detumbled prior to reorbiting. Some other ADR methods require low rotational rates of the debris to make capture with harpoons, nets or robotic arms possible [13]. Thus, freely rotating debris are studied as well.

Similarly to the previous subsection, the initial orientation of the debris is set using yaw α and pitch β according to Fig. 2.4. However, the orientation of the debris is not held constant throughout the simulation as in the case for a prescribed attitude. Instead, the debris rotates freely according to the rotational dynamics given in Eq. (6.18).

The simulation is started with no initial angular velocity of the debris. Figure 6.13 shows the maximum angular velocity magnitude of the debris during reorbit. Overall, the figure looks similar to Fig. 6.12: the maximum and average angular velocity magnitude is low for those initial orientations where protruding structures such as the solar panel or the magnetometer are directed toward the servicer, and high when these structures are initially pointing away from the servicer.

For conducting objects, electric charge generally accumulates at the corners and edges due to the repulsion of like charges within the object. Fully conducting spacecraft are assumed in this work, so electric charge gathers at the protruding solar panels of both spacecraft, as apparent in Fig. 2.4. Thus, for the GOES-R spacecraft model that is used as the debris here, the center of charge is shifted from the geometric center toward the solar panel. Note, however, that the charge distribution depends on the location and orientation of both satellites. The debris is subject to electrostatic torques if its center of charge does not align with its center of mass. The greater the distance from the center of charge of the debris perpendicular to the line that connects the center of mass of the debris with the center of charge of the servicer, the greater the torque. If, however, the center of charge of the debris lies on this line, no electrostatic torque is applied to the debris. This corresponds to the $\hat{\boldsymbol{k}}_L$ direction if the center of mass of each spacecraft aligns with the geometric center and the center of mass of the servicer coincides with its center of charge. This is visible in Fig. 6.13, as the maximum angular velocity magnitude is low whenever the debris' initial orientation minimizes the perpendicular distance between the debris' center of charge and $\hat{\boldsymbol{k}}_L$ (e.g., when the solar panel points toward the servicer). A similar discussion on electrostatic torques is provided in Ref. 25 for servicing and proximity operations.

This is advantageous for the case where one tries to hold the debris at a fixed attitude using charge-control of the servicer, because the orientation that is optimal for reorbit performance (solar panel pointing toward servicer) also results in a small electrostatic torque acting on the debris. While the specific favorable orientation strongly depends on the spacecraft shapes, this advantage is generally applicable. The reorbit time decreases with decreasing distance between the center of charge of each spacecraft due to the stronger electrostatic force. If the debris' center of

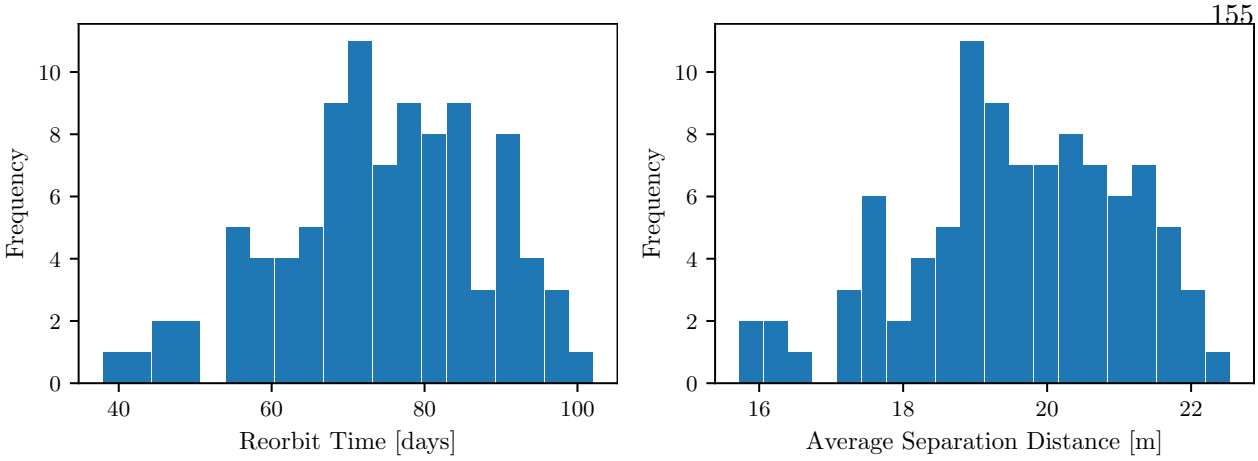

(a) Reorbit Times (b) Separation Distances

Figure 6.14: Histograms for 300 km altitude raise and randomized potential error

charge lies on the line connecting each center of mass and on the side of the debris that is closer to the servicer, then both the reorbit time and the electrostatic torque are minimized.

6.3.3 Debris attitude effects including electric potential error

To analyze the control sensitivity to electric potential sensing errors for a freely rotating debris, a Monte Carlo simulation with 100 runs similar to the simulation in the previous subsection is performed. Instead of assuming perfect knowledge of the debris potential, a randomized estimation error is imposed that is sampled from a normal distribution with a mean μ of 0 and variance σ^2 of 25, that is $\Delta\phi \sim \mathcal{N}(0, 25)$.

The histograms of the reorbit time and average separation distance between the two spacecraft are shown in Figs. 6.14a and 6.14b. The separation distance deviates from the desired reference distance of 20 m due to the constant electric potential estimation error $\Delta\phi$ that is applied as a bias throughout the entire simulation. Consequently, the reorbit time also varies. Out of 100 simulation runs, the servicer collides with the debris in three cases due to an excessive estimation error (at $\Delta\phi = 9.5\ \%, 9.6\ \%, 13.4\ \%$). The controller is set up to tolerate estimation errors of 10 % for the nominal spacecraft orientations (Fig. 2.4), but the critical estimation error at which the control response bifurcates is much lower for some orientations [33]. This suggests that the rotation of

the debris reduces the sensitivity to estimation errors of the controller, because it is essentially averaged over several debris orientations. However, the issue of the bifurcation is not eliminated by the tumbling debris, as there are still cases where an estimation error of less than 10 % causes the spacecraft to collide. This issue can be solved by setting up the controller to tolerate an estimation error of 10 % for the most critical orientation (target panel pointing toward the servicer) as opposed to the nominal orientation, which leads to a higher feedback gain K_L. In this scenario, the feedback gain tuned for the most critical orientation of the target for a separation distance of 20 m is equal to $K_L = 2.646 \cdot 10^{-7}$ as opposed to $K_L = 1.356 \cdot 10^{-7}$ for the nominal orientation.

6.4 Control without feed-forward of electric potential

The sensitivity to estimation errors of the debris electric potential of the control method proposed in Ref. 65 raises the question whether or not a simple feedback controller without any feed-forward term is sufficient for the ET relative motion control. To investigate such a control, the force feed-forward term in Eq. 6.21 is dropped, resulting in the simple control

$$^{\mathcal{K}}\boldsymbol{u}_S = -^{\mathcal{K}}\boldsymbol{u} \tag{6.47}$$

where $^{\mathcal{K}}\boldsymbol{u}$ is computed according to the feedback law from Eq. 6.19. The reorbit process is simulated with Basilisk for one orbit revolution, similar to the simulations in Sec. 6.3, with no potential estimation errors, and the control methods with and without the feed-forward term are compared. The debris starts with zero angular velocity, but rotates freely subject to the electrostatic torque.

First, this comparison is done without navigation errors. Given a certain feedback gain K_L with $1 \cdot 10^{-6} \leq K_L \leq 1 \cdot 10^{-3}$, the average and the standard deviation σ of the separation distance during one orbit are recorded. The results are shown in Fig. 6.15, where the solid line indicates the average, and the shaded region represents the $\pm 3\sigma$ bounds. With the feed-forward term, the average separation distance is approximately equal to the reference distance of $L_r = 20$ m, with little variation. Without feeding forward the estimated electrostatic force, the control settles at a separation distance less than the desired 20 m, resulting in an average separation distance that

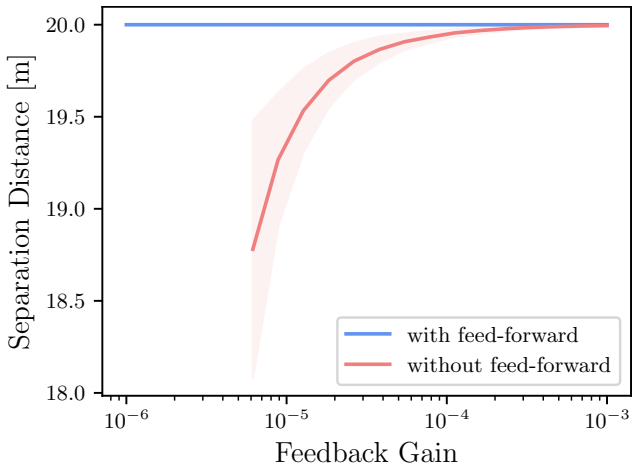

Figure 6.15: Average separation distance and $\pm 3\sigma$ during one orbit revolution as function of feedback gain K_L

deviates from the 20 m, unless a higher feedback gain is used. The standard deviation of the separation distance is also greater without the feed-forward term, in part due to the rotation of the debris which results in a variation of the electrostatic force over time that is not accounted for. If the feedback gain is too small, the servicer settles at a separation distance so close to the target that the two spacecraft may collide. In case of a collision, the simulation is terminated, which is indicated by a missing data point in Fig. 6.15. In this scenario, this is the case for feedback gains less than about $K_L = 6 \cdot 10^{-6}$ without feed-forward.

Similar to the control with feed-forward, there is a minimum feedback gain for the control without feed-forward to avoid a collision. To determine this minimum feedback gain for a control without feed-forward, Eq. (6.31) may be used with an estimated force magnitude equal to $F_{c,\text{est}} = 0$ N. Essentially, using no feed-forward term corresponds to a maximum expected potential estimation error of $\Delta\phi_{\max}$ in Sec. 6.2. For the given scenario, the obtained minimum feedback gain for the control without feed-forward is equal to $K_L = 1.393 \cdot 10^{-6}$, which is about five times greater than the feedback gain needed with feed-forward to be robust to estimation errors up to 10 % for the worst case orientation, as mentioned in Sec. 6.3.3. The minimum feedback gain in Fig. 6.15 required to avoid collisions is greater than the obtained minimum gain due to the freely rotating debris.

Table 6.4: Navigation Error Parameters

Position Std. Dev.	Velocity Std. Dev.	Position Error Bound	Velocity Error Bound
$1 \cdot 10^{-2}$ m	$1 \cdot 10^{-4}$ m/s	$1 \cdot 10^{-1}$ m	$1 \cdot 10^{-3}$ m/s

The above analysis is idealized due to missing noise such as navigation errors. Thus, the analysis is repeated including navigation errors of the servicer according to Tab. 6.4, with the results shown in Fig. 6.16. As expected, the navigation errors lead to larger variations of the separation distance for both control methods, but the average separation distance is not affected as much. Similar to the analysis without navigation errors, the minimum feedback gain to avoid a collision is greater without feed-forward control than with feed-forward control. The behavior of both control methods is similar for higher feed-back gains, but these higher feedback gains come at the cost of increased control effort.

6.5 Comparison of reduced order charging and force models

The photoelectric effect provides a strong, naturally occurring current in the space environment that is scaled by the sunlit area of the spacecraft. If a spherical shape is used for the charging model, the sunlit area is independent of the orientation. However, for more complex shapes such as satellites, the sunlit area can vary significantly. The faceted model described in Sec. 2.1.3 is implemented to account for these variations. The plasma parameters used here correspond to a local time of $LT = 12$ h in geostationary orbit and a planetary K-index of $K_p = 2$ according to Ref. 134, and are equal to $n_e = 6 \cdot 10^5$ m^{-3}, $T_e = 700$ eV, $n_i = 6.5 \cdot 10^5$ m^{-3} and $T_i = 8,000$ eV. The plasma being slightly non-neutral is a result of how the energetic particles arrive in geostationary orbit. The energetic electrons and ions in GEO typically come from the magnetotail. As they arrive at Earth, electrons travel eastward (into the dawn region) and ions travel westward (into the dusk region) due to Earth's magnetic field [18]. This results in a reduced electron density compared to the ion density in the dusk region. Ref. 134 shows that this low electron/ion density ratio can

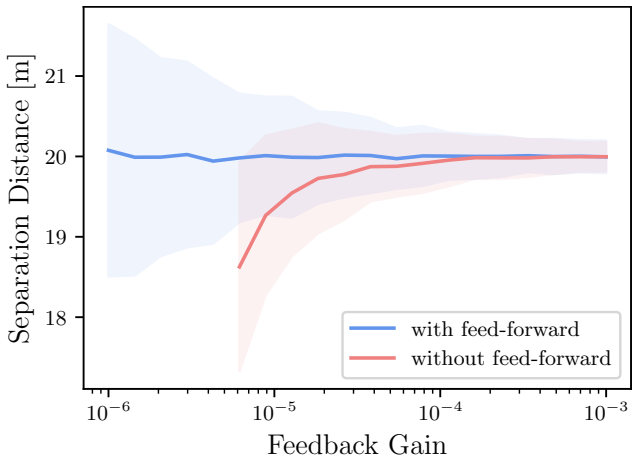

Figure 6.16: Average separation distance and $\pm 3\sigma$ during one orbit revolution as function of feedback gain K_L, with navigation errors

extend into the noon region. An electron beam is included with an energy of $E_{EB} = 30$ keV and a current of $I_{EB} = 1$ mA. The spacecraft centers are 15 m apart, with their nominal orientation shown in Fig. 2.4, and the sun direction is aligned with the nominal $\hat{\boldsymbol{t}}_1$ direction.

Figure 6.17 shows the equilibrium potential of the GOES-R target satellite as a function of its orientation, as obtained with the faceted model. The orientation of the target is changed using yaw and pitch 3-2-1 Euler rotations as depicted in Fig. 2.4, while the servicer remains at the nominal orientation. For orientations where the yaw angle is close to $\alpha_T = \{-180°, 0°, 180°\}$ or the pitch angle is close to $\beta_T = \{-90°, 90°\}$, the equilibrium potential is highly negative, while it is approximately zero for all other orientations. The aforementioned angles correspond to those orientations where the solar panel of the GOES-R satellite is edge on with the sun, that is, the normal vectors of the two panel facets are (nearly) perpendicular to the sun direction $\hat{\boldsymbol{s}}$. If the solar panel normal vector is more aligned with the sun direction, the sunlit area is increased, providing a greater photoelectric current. Because the released photoelectrons are attracted back to the spacecraft once it is positively charged, the target settles to an equilibrium potential that is only a few volts positive (close to zero). The equilibrium potential of the servicer is about +7 kV due to the electron beam current. It should be noted that a roll rotation about the $\hat{\boldsymbol{t}}_2$ axis also affects the resulting potential, force and torque. As described in Sec. 2.2, it is neglected here because the

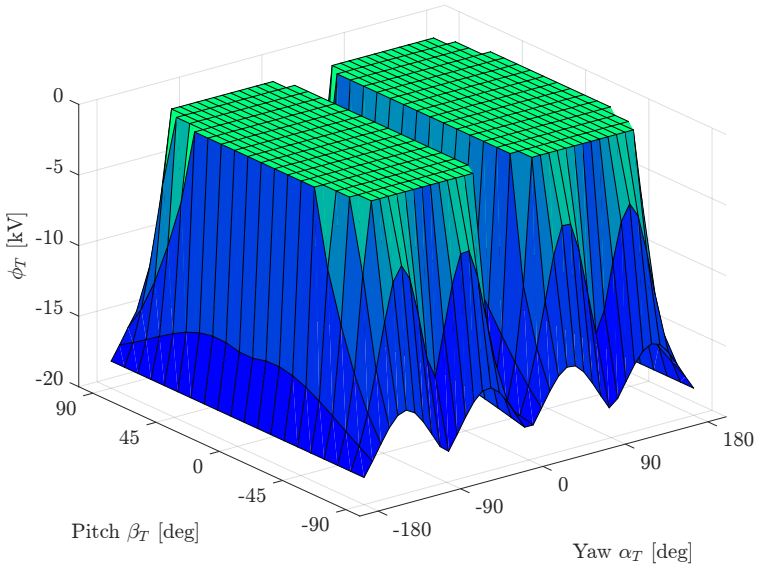

Figure 6.17: Electric Potential of the target ϕ_T as function of target orientation

most important orientations are covered using only yaw and pitch.

To study the effect of the orientation-dependent equilibrium potential on electrostatic proximity operations, four different models are considered to compute the electrostatic force and torque as a function of the target orientation. The highest-fidelity model uses the faceted model to compute the electric potential of the spacecraft and the multi-sphere model (MSM) to calculate the resulting force and torque (Model 1 – "faceted, MSM"), while the lowest-fidelity model uses a spherical spacecraft to determine the potential and a 1-sphere model (1SM) to approximate the force and torque (Model 4 – "spherical, 1SM"). Two more models are studied that are a mix of the highest and lowest fidelity models (Model 2 – "spherical, MSM" and Model 3 – "faceted, 1SM"). The radius R_{eff} of the single sphere is chosen to match the self-capacitance C of the MSM model

$$R_{\text{eff}} = \frac{C}{4\pi\epsilon_0} \tag{6.48}$$

where ϵ_0 is the vacuum permittivity. This radius is referred to as the effective radius, and is equal to 4.4438 m for the GOES-R and 4.7984 m for the SSL-1300 satellite. Essentially, the faceted model accounts for the effect of the orientation on the equilibrium potential (which affects the force and torque), while the MSM model accounts for the direct effect of the orientation on the electrostatic

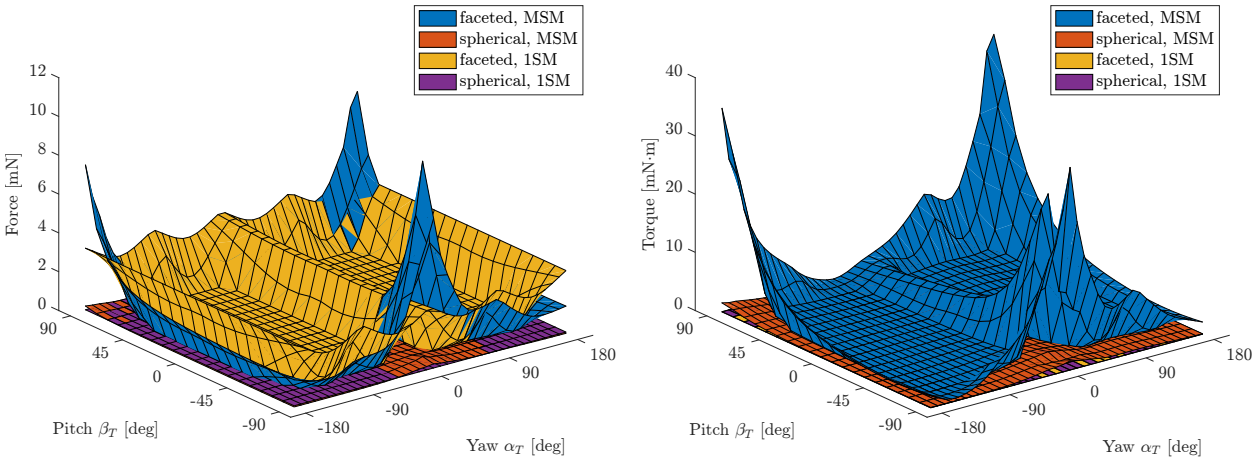

(a) Force (b) Torques

Figure 6.18: Electrostatic force and torque magnitude as function of target orientation, using different models

force and torque.

Figure 6.18a shows the electrostatic force between the servicer and target as a function of the target orientation for the different models. There are three clear peaks in force magnitude for the highest-fidelity model. These peaks also exist for the "spherical, MSM" model and are a consequence of the solar panel of the target pointing towards the servicer. However, this effect is pronounced for the highest-fidelity model, because the solar panel is edge on with the sun for these orientations, leading to a more negative electric potential that further increases the electrostatic force. The force magnitude for the "faceted, 1SM" model essentially corresponds to Fig. 6.17, but flipped upside down. When the electric potential is more negative, the force is greater due to the positively charged servicing spacecraft. Finally, the force for the "spherical, 1SM" model is constant across all orientations.

The electrostatic torque as a function of yaw and pitch angles is shown in Fig. 6.18b. For the 1-sphere models (Models 3 and 4), the torque is zero across all orientations, because the center of charge is always aligned with the center of mass for a single sphere, producing no torque. The observations for the torque of the MSM models (Models 1 and 2) are similar to the observa-

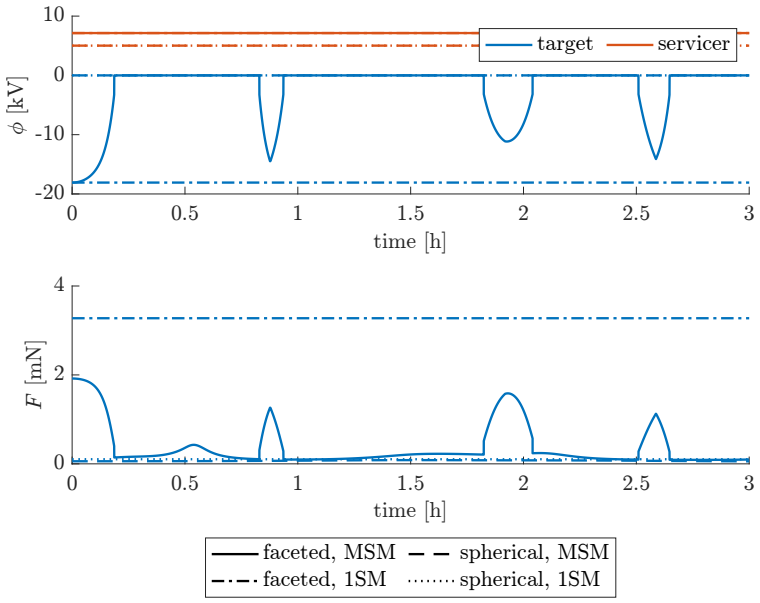

Figure 6.19: Electric potential ϕ of target and servicer and force magnitude F over time during the Electrostatic Tractor debris reorbit scenario

tions above for the force magnitude. Model 2 accounts for the torque variations due to different orientations, but, for the given GOES-R spacecraft model, these variations are enhanced by the orientation-dependent equilibrium potential.

A rotational dynamic simulation is performed, where the relative position of the two spacecraft and the attitude of the servicer are held constant, but the target satellite is free to rotate given the electrostatic torque that is acting on it (Fig. 6.19). The rotational dynamics are modeled according to Eq. 6.18. The initial attitude corresponds to the nominal orientation shown in Fig. 2.4, with zero angular velocity. Due to the electrostatic torque, the target starts rotating. Because the 1-sphere model cannot account for any torques if the center of mass is at the center of the sphere, the orientation of the target stays constant throughout the simulation and neither the potential nor the force change. In case of the "faceted, 1SM" model, the potential remains at about -18 kV, because the sunlit area of the faceted model at its initial (and in this case constant) orientation is rather small, causing a strong force, but no torque.

The cases of the multi-sphere models are more interesting. Due to the large cross-section of the 4.4438 m radius GOES-R effective sphere that is facing the Sun, the equilibrium potential

is about 0 V for the "spherical, MSM" model, at all times. Regardless of the 0 V potential, the electrostatic force and torque are non-zero due to induced charging effects [139]. The force and torque are rather small in magnitude, so the rotational rate of the target is small as well. Finally, the "faceted, MSM" model provides the most detail as it is the highest-fidelity model used here. Initially, the potential of the target spacecraft is at about -18 kV. As the target starts rotating due to the electrostatic torque, the sunlit area increases, which makes the equilibrium potential less negative. At some point, the potential is close to zero and the force is significantly lower than at the beginning. After about 0.8 hours, only a small area of the target spacecraft is in sunlight once again, causing a spike in the equilibrium potential and the electrostatic force. The differences between these models depend on the specific shapes of the spacecraft, but the results demonstrate that the charge distribution and dynamics can be misrepresented by a spherical or 1-sphere model.

These results have two main implications for the Electrostatic Tractor debris removal method. First, the electron beam current I_{EB} must be sufficiently high to charge the debris regardless of the orientation of the debris. In the example used here, the beam current is not sufficiently high, causing debris potentials of only a few volts for those orientations where the photoelectric current is the strongest. This results in large force fluctuations throughout the reorbit process that directly affect the time needed to reorbit the debris. Second, although one of the advantages of the Electrostatic Tractor compared to other proposed active debris removal methods is that it is not required to detumble the retired satellite before reorbiting, the results from this work suggest that a detumbled debris may be beneficial. In Sec. 6.2, it is found that the sensitivity of the ET relative motion control to uncertainty of the debris electric potential is higher for some orientations than others [33]. Following work in Sec. 6.3 demonstrates that this sensitivity is averaged out if the debris is tumbling [26]. Although the variation of the force and resulting change in reorbit time due to the varying debris orientation was taken into account in prior work, the potentially amplifying effect of the varying spacecraft potential on the electrostatic force and reorbit time was not considered. In addition to the fluctuating debris potential and electrostatic force, a tumbling debris may introduce other complications, such as periodically differentially charged

debris components as they move in and out of the shadow of the spacecraft, or relative navigation challenges. Thus, holding the debris at a favorable orientation as discussed in Sec. 6.3 may be preferred [26] . It is recommended for future work on the Electrostatic Tractor to investigate whether a tumbling or detumbled retired satellite is beneficial for the reorbit process, and how to maintain a debris orientation using electrostatic torque control. It should also be noted that, if the orientation of the debris with respect to the servicer remains constant while reorbiting, the inertial attitude and consequently the sun-facing area and electric potential do change. Thus, it should be differentiated whether an inertially fixed or Hill frame fixed debris orientation is beneficial.

6.6 Conclusions

The effects of electrostatic potential uncertainty on the Electrostatic Tractor (ET) relative motion control is investigated for complex spacecraft geometries. If the estimation error of the debris potential exceeds the critical value, the closed-loop response bifurcates and causes the servicing satellite to collide with the debris. The critical value decreases drastically if the debris is oriented in a way that protruding structures such as solar panels are directed towards the servicer, and this attitude also reduces the minimal distance between the two spacecraft significantly, limiting the smallest possible reference separation distance that is used for the controller. Additionally, these consequences of different debris orientations are significant for any reasonable ET separation distance. Thus, attitude effects must be considered when choosing a reference separation distance. One way to mitigate the attitude effects is to select a feedback gain based on the worst case orientation, which generally corresponds to the orientation described above.

The reorbit time is minimized if protruding structures of the debris are pointing toward the servicing spacecraft, motivating work to control the debris attitude using electrostatic torques. Additionally, such orientations reduce the electrostatic torque on the debris, making such orientations favorable to be maintained during the reorbit process. If not controlled, the debris generally starts to tumble while being reorbited due to electrostatic torques. The sensitivity of the relative motion control to estimation errors of the debris electric potential is decreased for a tumbling debris, but

not eliminated. Thus, even for tumbling debris, higher feedback gains are recommended to reduce the sensitivity to electric potential estimation errors. Regardless of the sensitivity to electric potential estimation errors, the ET relative motion control proposed in prior work is found to be more suitable for the ET than a simple feedback control law by allowing for lower feedback gains.

A comparison of reduced order charging and force models shows great variations of the electric potentials and the electrostatic force between the tug and the debris if the debris is rotating. Thus, for any realistic simulations for the ET, the use of Multi-Sphere force models as well as faceted charging models is recommended. These results suggest that it may be beneficial to detumble and maintain a constant debris orientation while reorbiting, as opposed to letting the debris tumble freely.

Chapter 7

Spacecraft relative motion in the inertial frame

During on-orbit servicing operations, plasma wakes form in the anti-ram-side direction behind the spacecraft if the ion thermal velocity is greater than the electron thermal velocity [67], where the ram-side is determined by the spacecraft velocity relative to the bulk velocity of the ions. Because the inter-spacecraft electrostatic forces may be stronger inside the wake [68], it is proposed to stay outside the wake to minimize electrostatic perturbations. Additionally, it may be beneficial for electric potential sensing considerations to stay outside the wake while sensing [142]. On the other hand, it may be of interest to stay inside the wake to study the complex plasma and spacecraft charging dynamics of a plasma wake. In LEO, the wake is approximately fixed in the velocity frame (or Hill frame for a circular orbit) due to the negligibly small ion bulk velocity [69], as shown in Fig. 7.1a. Outside Earth's magnetosphere, however, the wake forms in the anti-Sun direction and is quasi-inertially fixed because the ions move with the solar wind and the spacecraft velocity is negligibly small compared to the solar wind velocity [70], as illustrated in Fig. 7.1b. Such cislunar plasma wakes extend several spacecraft widths behind the leading spacecraft, resulting in wake lengths in the order of 10s of meters [142]. Thus, while the relative motion of two spacecraft is commonly described in the Hill frame due to benefits such as the existence of simple analytical solutions for circular orbits and the resulting intuitive shape of the relative orbits in the Hill frame, a relative motion description in the inertial frame may be beneficial for scenarios such as servicing operations in cislunar space. That is, instead of expressing the relative position and velocity vectors of the deputy with respect to the chief in a rotating frame, it may be beneficial to describe these

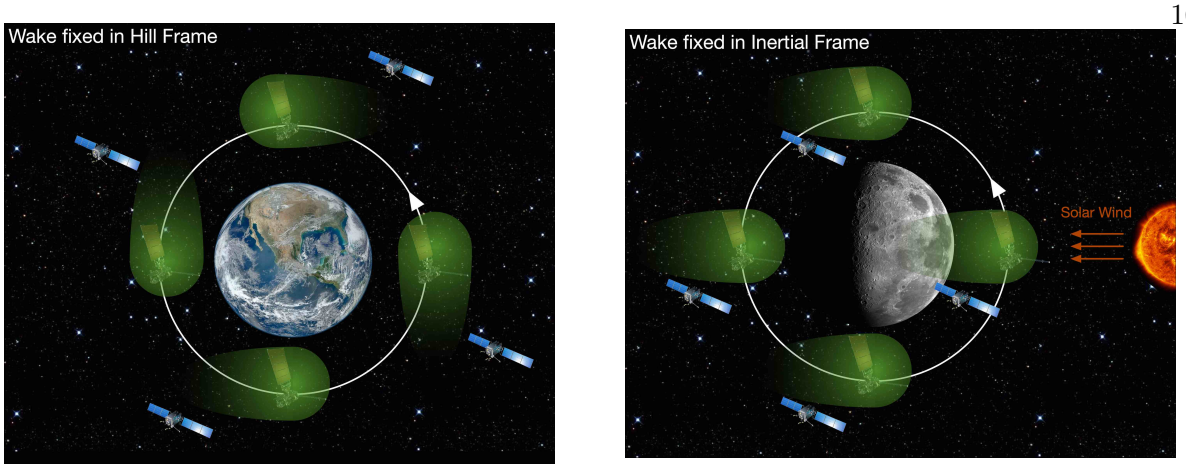

(a) Wake in LEO

(b) Wake in cislunar space

Figure 7.1: Plasma wake orientations in different orbital regimes

vectors in inertial frame components.

For the problem at hand, the inertially fixed constraint imposed by the plasma wake could be treated as a time-varying constraint in the Hill frame. However, the motivations of describing the relative motion of two spacecraft in the inertial frame extend beyond the interests related to this dissertation, calling for a more general approach to this problem. For example, during rendezvous it may be beneficial to maintain certain lighting conditions, or to keep line-of-sight with another inertially fixed target. Relative motion constraints for docking operations are often described in the body frame of the target spacecraft. If the target satellite is not rotating, the body frame of the target remains aligned with the inertial frame, and the insights from the inertial frame relative motion can be applied to the body frame. Thus, a more general approach is used here to better understand the motion in the inertial frame, as opposed to dealing with time-varying constraints in the Hill frame.

Aside from general on-orbit servicing and rendezvous operations, distributed space telescopes may also benefit from such a description. Distributed space telescopes have been proposed for large-aperture telescope architectures that cannot be realized with a single spacecraft [143, 144]. Instead of having one spacecraft with all telescope components, a two-spacecraft formation consisting of

one spacecraft equipped with the lens and another spacecraft equipped with the sensor is used. The VIrtual Super Optics Reconfigurable Swarm (VISORS) mission is a demonstration for such a concept [145]. Because a space telescope is commonly aligned with inertial targets, the description of relative motion is beneficial in the inertial frame, despite inertial frame relative orbits being more complex. Missions such as New World Observer [146], where a giant starshade [147] is used to block the light from a star while searching for exoplanets, may also benefit from a description in the inertial frame. Other missions such as the Terrestrial Planet Finder [148] (TPF, canceled in 2011) and Large Interferometer For Exoplanets [149] (LIFE, in development) proposed to use a nulling interferometer consisting of multiple spacecraft to search for exoplanets. Such exoplanet search missions are planned to be located around the Sun-Earth L2 Lagrange point. Thus, the relative motion occurs within the regime of the three body problem and requires different dynamics models [150–153], in contrast to the relative motion of two spacecraft orbiting one planet as explored in this current work. Other mission concepts call for formations where the spacecraft never eclipse each other, or where one spacecraft is desired to be in the shadow of the other for prolonged periods. For example, the Project for On-Board Autonomy 3 (PROBA-3) mission is a formation flying demonstration mission that launched in December 2024, consisting of an occulter spacecraft that casts the Sun's shadow on a coronagraph spacecraft to study the Sun's faint corona [154]. For spacecraft orbiting Earth, this imposes a keep-out or keep-in zone that is fixed in a quasi-inertial frame (because the Sun direction changes slowly).

This chapter develops an elegant analytical description of the relative motion of two spacecraft in the inertial frame, where new geometrically meaningful relative motion invariants are introduced. A background about relevant coordinate frames and relative motion descriptions in the Hill frame is provided in Sec. 7.1. The solution of the relative motion in the inertial frame and the inertial frame relative orbit elements are derived and discussed for circular chief orbits in Sec. 7.2 and for elliptic chief orbits in Sec. 7.3. A control law based on this new set of relative orbit elements is derived and implemented in Sec. 7.4. Finally, the inertial relative orbit design is applied to an on-orbit servicing example with plasma wakes in Sec. 7.5.

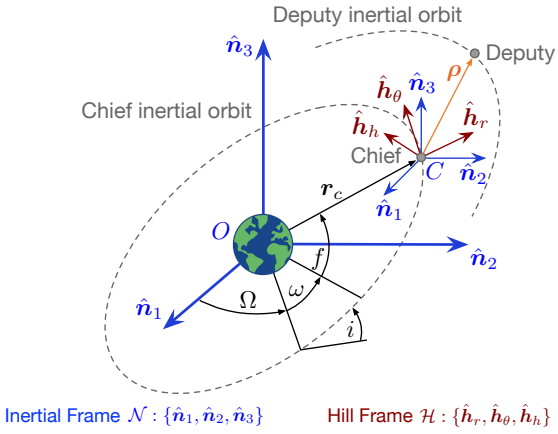

Figure 7.2: Illustration of Hill frame and Inertial frame: The Hill frame $\mathcal{H}$ is centered at the chief and rotates as the chief orbits the central body, with $\hat{\boldsymbol{h}}_r$ aligned with the orbit radial direction of the chief and $\hat{\boldsymbol{h}}_h$ aligned with the orbit normal direction. The inertial frame $\mathcal{N}_O$ is located at the central body with fixed directions of the frame axes. A moving frame $\mathcal{N}_C$ is used that is centered at the chief, but its axes remain aligned with the inertial frame.

7.1 Background

Two spacecraft are orbiting a central body in close proximity to each other. Given the inertial position of the chief (target spacecraft) $\boldsymbol{r}_c$ and the deputy (servicing spacecraft) $\boldsymbol{r}_d$, the relative position vector is defined as

$$\boldsymbol{\rho} = \boldsymbol{r}_d - \boldsymbol{r}_c \tag{7.1}$$

and used to describe the relative motion of the two spacecraft.

7.1.1 Relevant coordinate frames

The relative motion is commonly described in a rotating frame $\mathcal{H}: \{\hat{\boldsymbol{h}}_r, \hat{\boldsymbol{h}}_\theta, \hat{\boldsymbol{h}}_h\}$ centered at the chief C with axes

$$\hat{\boldsymbol{h}}_r = \frac{\boldsymbol{r}_c}{|\boldsymbol{r}_c|} \tag{7.2a}$$

$$\hat{\boldsymbol{h}}_\theta = \hat{\boldsymbol{h}}_h \times \hat{\boldsymbol{h}}_r \tag{7.2b}$$

$$\hat{\boldsymbol{h}}_h = \frac{\boldsymbol{r}_c \times \dot{\boldsymbol{r}}_c}{|\boldsymbol{r}_c \times \dot{\boldsymbol{r}}_c|} \tag{7.2c}$$

where $\dot{\boldsymbol{r}}_c$ is the inertial velocity of the chief. This frame is referred to as the Hill frame [155] and is similar to the Local-Vertical-Local-Horizon (LVLH) frame $\mathcal{L} : \{\hat{\boldsymbol{l}}_1 = \hat{\boldsymbol{h}}_\theta,\ \hat{\boldsymbol{l}}_2 = -\hat{\boldsymbol{h}}_h,\ \hat{\boldsymbol{l}}_3 = -\hat{\boldsymbol{h}}_r\}$. The first axis of the Hill frame is aligned with the orbit radial direction of the chief, the third axis is aligned with the orbit normal direction, and the second axis completes the right-handed coordinate frame. Another frame $\mathcal{N} : \{\hat{\boldsymbol{n}}_1, \hat{\boldsymbol{n}}_2, \hat{\boldsymbol{n}}_3\}$ is used with inertially fixed directions of the frame axes $\hat{\boldsymbol{n}}_1, \hat{\boldsymbol{n}}_2, \hat{\boldsymbol{n}}_3$. Figure 7.2 illustrates the Hill frame and Inertial frame.

The direction cosine matrix (DCM) $[HN]$ to map from the inertial frame $\mathcal{N}$ to the Hill frame $\mathcal{H}$ may be obtained using the chief orbit elements. Using the DCMs for a generic rotation θ about the first frame axis

$$[M_1(\theta)] = \begin{bmatrix} 1 & 0 & 0 \\ 0 & \cos\theta & \sin\theta \\ 0 & -\sin\theta & \cos\theta \end{bmatrix} \tag{7.3}$$

and the generic DCM about the third frame axis

$$[M_3(\theta)] = \begin{bmatrix} \cos\theta & \sin\theta & 0 \\ -\sin\theta & \cos\theta & 0 \\ 0 & 0 & 1 \end{bmatrix} \tag{7.4}$$

the DCM for a (3-1-3) Euler angle rotation (Ω, i, ω) is written as [136]

$$[PN(\Omega, i, \omega)] = [M_3(\omega)][M_1(i)][M_3(\Omega)] \tag{7.5}$$

where Ω is the right ascension of the ascending node (RAAN), i is the orbit inclination, and ω is the argument of periapsis. The frame $\mathcal{P} : \{\hat{\boldsymbol{p}}_1, \hat{\boldsymbol{p}}_2, \hat{\boldsymbol{p}}_3\}$ is the perifocal frame, in which the first axis points from the focus of the orbit (the central body) to periapsis, the third axis points in the chief orbit angular momentum direction, and the second axis completes the right-handed coordinate frame. To map from the perifocal frame $\mathcal{P}$ to the Hill frame $\mathcal{H}$, another rotation around the third frame axis is performed using the true anomaly f

$$[HP(f)] = [M_3(f)] \tag{7.6}$$

Thus, the DCM to map from the inertial frame to the Hill frame is equal to

$$[HN(\Omega, i, \omega, f)] = [HP][PN] = [M_3(f)][M_3(\omega)][M_1(i)][M_3(\Omega)] \tag{7.7}$$

7.1.2 Cartesian coordinate description

The relative position vector $\boldsymbol{\rho}$ of the deputy relative to the chief in Hill-frame components is

$${}^{\mathcal{H}}\boldsymbol{\rho} = \begin{bmatrix} x \\ y \\ z \end{bmatrix} \tag{7.8}$$

where the left superscript indicates that the vector is expressed in Hill frame $\mathcal{H}$ components, and x, y, z are the relative position coordinates in the Hill frame. In this frame, x and y describe the relative motion in the chief orbit plane while z describes any out-of-plane motion. Assuming a circular chief orbit (eccentricity $e = 0$) and small separation distances between the two spacecraft ($|\boldsymbol{\rho}| \ll |\boldsymbol{r}_c|$), the relative equations of motion (EOM) in the Hill frame are equal to [155]

$$\ddot{x} - 2n\dot{y} - 3n^2 x = 0 \tag{7.9a}$$

$$\ddot{y} + 2n\dot{x} = 0 \tag{7.9b}$$

$$\ddot{z} + n^2 z = 0 \tag{7.9c}$$

These relative EOM are known as the Clohessy-Wiltshire-Hill (CWH) equations. Using the semi-major axis a of the chief orbit and the standard gravitational parameter μ of the central body, the mean motion n is determined by $n = \sqrt{\mu/a^3}$. The analytical solution to the CWH equations is equal to [136, 156]

$$x(t) = A_0 \cos(nt + \alpha) + x_{\text{off}} \tag{7.10a}$$

$$y(t) = -2A_0 \sin(nt + \alpha) - \frac{3}{2} n t x_{\text{off}} + y_{\text{off}} \tag{7.10b}$$

$$z(t) = B_0 \cos(nt + \beta) \tag{7.10c}$$

with the velocities

$$\dot{x}(t) = -A_0 n \sin(nt + \alpha) \tag{7.11a}$$

$$\dot{y}(t) = -2A_0 n \cos(nt + \alpha) - \frac{3}{2} n x_{\text{off}} \tag{7.11b}$$

$$\dot{z}(t) = -B_0 n \sin(nt + \beta) \tag{7.11c}$$

The six relative motion parameters in Eq. (7.10) are called the CW constants or linearized relative orbit elements (LROEs) and are the invariants of the linearized relative motion:

- In-plane sinusoidal amplitude A_0
- In-plane phase angle α
- Orbit-radial offset x_{off}
- Along-track offset at epoch y_{off}
- Out-of-plane sinusoidal amplitude B_0
- Out-of-plane phase angle β

The corresponding LROE state vector is

$$\delta \boldsymbol{oe}_{CW} = \begin{bmatrix} A_0 & \alpha & x_{\text{off}} & y_{\text{off}} & B_0 & \beta \end{bmatrix}^T \tag{7.12}$$

These geometrically insightful invariants of motion are determined through the initial conditions or cartesian state according to Eq. (A.1) and fully define the relative motion under the given assumptions.

Examining Eq. (7.10), one finds that the in-plane motion corresponds to a 2-by-1 ellipse in which the along-track amplitude is twice the orbit-radial amplitude, and the out-of-plane motion corresponds to an unforced oscillator. The motion may be offset in the y-direction with y_{off} or the x-direction with x_{off}. An offset x_{off} causes a drift in the along-track direction y over time due to the difference in semi-major axis of the two spacecraft. Thus, x_{off} must be zero for bounded motion. For a simple lead-follower formation, all relative motion parameters besides y_{off} are zero. Some relative orbit shapes in the Hill frame are shown in Fig. 7.3.

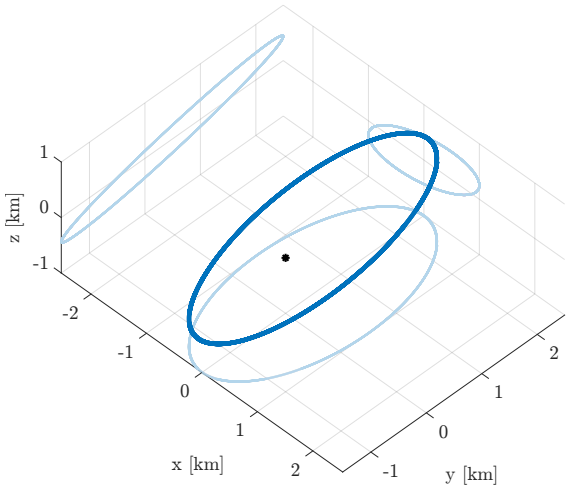

(a) Motion 1: $A_0 = 1$ km, $\alpha = -60$ deg, $x_{\text{off}} = 0$ km, $y_{\text{off}} = 0.5$ km, $B_0 = 0.5$ km, $\beta = 0$ deg

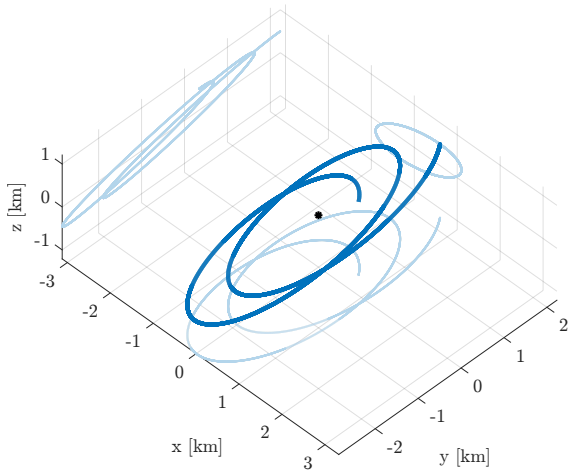

(b) Motion 2: $A_0 = 1$ km, $\alpha = -60$ deg, $x_{\text{off}} = 0.1$ km, $y_{\text{off}} = 0.5$ km, $B_0 = 0.5$ km, $\beta = 0$ deg

Figure 7.3: Relative motion in Hill frame for a circular chief orbit: A_0 creates a 2-by-1 relative orbit ellipse that is offset in the y-direction by y_{off}. Drift motion is induced by x_{off}. The projections of the relative orbit on the three planes are shown in lighter color.

7.1.3 Orbit element difference description

Given the general orbit elements

$$\boldsymbol{oe} = \begin{bmatrix} a & e & i & \Omega & \omega & M_0 \end{bmatrix}^T \tag{7.13}$$

with semi-major axis a, eccentricity e, inclination i, right ascension of the ascending node Ω, argument of periapsis ω and initial mean anomaly M_0, the orbit element differences between the deputy and the chief spacecraft are equal to [78, 136]

$$\delta\boldsymbol{oe} = \boldsymbol{oe}_d - \boldsymbol{oe}_c = \begin{bmatrix} \delta a & \delta e & \delta i & \delta\Omega & \delta\omega & \delta M_0 \end{bmatrix}^T \tag{7.14}$$

where $\boldsymbol{oe}_d$ and $\boldsymbol{oe}_c$ are the orbit elements of the deputy and chief, respectively. This differential orbit elements (DOEs) description does not make any assumptions on the eccentricity of the orbits. A semi-major axis difference δa between the two spacecraft causes the mean anomaly difference δM to drift over time. The relation between the differences in mean anomaly at time t and time

t_0 is equal to

$$\delta M = \delta M_0 - \frac{3}{2}\frac{\delta a}{a}(M - M_0) \tag{7.15}$$

where M and M_0 are the mean anomalies of the chief at time t and time t_0, respectively. Assuming small relative orbit sizes, the relative position coordinates x, y, z can be expressed in terms of the orbit element differences and as a function of the chief true anomaly f for general orbit eccentricities

$$x(f) = \frac{r}{a}\delta a + \frac{ae\sin f}{\eta}\delta M - a\cos f\delta e \tag{7.16a}$$

$$y(f) = \frac{r}{\eta^3}(1 + e\cos f)^2\delta M + r\delta\omega + \frac{r\sin f}{\eta^2}(2 + e\cos f)\delta e + r\cos i\delta\Omega \tag{7.16b}$$

$$z(f) = r(\sin\theta\delta i - \cos\theta\sin i\delta\Omega) \tag{7.16c}$$

with the relation $\eta = \sqrt{1 - e^2}$, the true latitude $\theta = \omega + f$ and the chief orbit radius

$$r = \frac{p}{1 + e\cos f} = \frac{a(1 - e^2)}{1 + e\cos f} = \frac{a\eta^2}{1 + e\cos f} \tag{7.17}$$

Note that most terms in Eq. (7.16) include the orbit radius r, which varies with true anomaly f for an elliptic chief orbit.

7.2 Circular chief orbits

7.2.1 Inertial frame relative orbit elements

First, the inertial relative motion is investigated for circular chief orbits using the Clohessy-Wiltshire equations. To express the relative motion in the inertial frame, the relative position $\boldsymbol{\rho}$ is mapped from the Hill frame $\mathcal{H}$ to the inertial frame $\mathcal{N}$ with the DCM $[NH] = [HN]^T$:

$${}^{\mathcal{N}}\boldsymbol{\rho} = {}^{\mathcal{N}}\begin{bmatrix} X \\ Y \\ Z \end{bmatrix} = [NH]\cdot {}^{\mathcal{H}}\boldsymbol{\rho} = [HN]^T\cdot {}^{\mathcal{H}}\boldsymbol{\rho} \tag{7.18}$$

For general chief orbit elements (Ω, i, ω) and relative orbit parameters, this results in a rather complex analytical expression that is difficult to analyze. Thus, to begin, it assumed that $\Omega = i =$

$\omega = 0$. This corresponds to a description in the perifocal frame $\mathcal{P}$:

$$^{\mathcal{P}}\boldsymbol{\rho} = \begin{bmatrix} X_p \\ Y_p \\ Z_p \end{bmatrix}^{\mathcal{P}} = [HN(0,0,0,f)]^T \cdot {}^{\mathcal{H}}\boldsymbol{\rho} = [HP]^T \cdot {}^{\mathcal{H}}\boldsymbol{\rho} \tag{7.19}$$

Once the relative motion is understood in the perifocal frame, it is rather straightforward to consider general chief orbit orientations. For a circular orbit, $f = nt$, so using Eqs. (7.10) and (7.19) as well as significant simplification results in the analytical expression

$$^{\mathcal{P}}\begin{bmatrix} X_p(t) \\ Y_p(t) \\ Z_p(t) \end{bmatrix} = {}^{\mathcal{P}}\begin{bmatrix} \frac{1}{2}\left(3A_0\cos\alpha - A_0\cos(\alpha+2nt) + 3ntx_{\text{off}}\sin(nt) + 2x_{\text{off}}\cos(nt) - 2y_{\text{off}}\sin(nt)\right) \\ \frac{1}{2}\left(-3A_0\sin\alpha - A_0\sin(\alpha+2nt) - 3ntx_{\text{off}}\cos(nt) + 2x_{\text{off}}\sin(nt) + 2y_{\text{off}}\cos(nt)\right) \\ B_0\cos(\beta+nt) \end{bmatrix} \tag{7.20}$$

Using the identities

$$A\sin t + B\cos t = \sqrt{A^2+B^2}\cos\left(t - \arctan\left(\frac{A}{B}\right)\right) \tag{7.21a}$$

$$A\sin t + B\cos t = -\sqrt{A^2+B^2}\sin\left(t - \arctan\left(\frac{B}{-A}\right)\right) \tag{7.21b}$$

and other well-known trigonometric identities, Eq. (7.20) is rewritten to significantly reduce its complexity:

$$X_p(t) = 3d_i\cos\alpha_i - d_i\cos(2nt-\alpha_i) - 2r_i\cos(nt-\phi_i) \tag{7.22a}$$

$$Y_p(t) = 3d_i\sin\alpha_i - d_i\sin(2nt-\alpha_i) - 2r_i\sin(nt-\phi_i) \tag{7.22b}$$

$$Z_p(t) = B_i\cos(nt-\beta_i) \tag{7.22c}$$

Here, the inertial frame relative state vector

$$\delta\boldsymbol{\alpha}\boldsymbol{e}_i = \begin{bmatrix} r_i & \phi_i & d_i & \alpha_i & B_i & \beta_i \end{bmatrix}^T \tag{7.23}$$

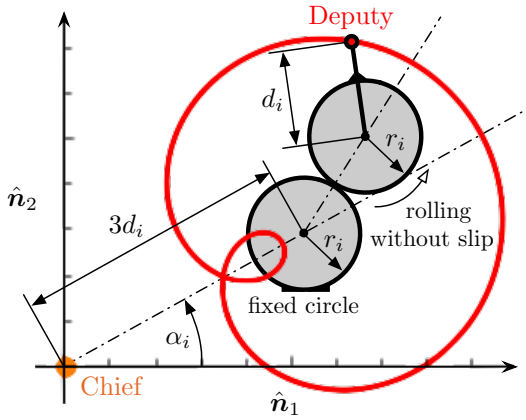

Figure 7.4: Inertial frame relative orbit elements: The relative motion in the inertial frame traces an epitrochoid curve, in which a circle with radius r_i rolls without slip on a fixed circle with radius r_i, and the curve is generated by a point that is at a distance of d_i away from the center of the rolling circle. The formation is $3d_i$ away from the origin and rotated by α_i.

is used, with

$$r_i = \frac{1}{2}\sqrt{\left(y_{\text{off}} - \frac{3}{2}ntx_{\text{off}}\right)^2 + x_{\text{off}}^2} \tag{7.24a}$$

$$\phi_i = \arctan\left(\frac{y_{\text{off}} - \frac{3}{2}ntx_{\text{off}}}{-x_{\text{off}}}\right) \tag{7.24b}$$

$$d_i = \frac{1}{2}A_0 \tag{7.24c}$$

$$\alpha_i = -\alpha \tag{7.24d}$$

$$B_i = B_0 \tag{7.24e}$$

$$\beta_i = -\beta \tag{7.24f}$$

Ignoring the constant offset of $3d_i$ as well as the phase angles ϕ_i and α_i, the equations for X_p and Y_p are equivalent to the parametric equations of an epitrochoid.[1] An epitrochoid is the curve traced by a point attached to a circle rolling around the outside of a fixed circle without slip. In the case of Eq. (7.22), the radius of both circles is equal to r_i, and the distance between the generating point and the center of the rolling circle is equal to the arm length d_i. The fixed circle is offset by $3d_i$ away from the frame origin (the chief). The phase angle α_i rotates the epitrochoid

[1] see https://en.wikipedia.org/wiki/Epitrochoid. The equations only differ by a phase offset $\theta = \pi/2 - nt$ and are mirrored with $x = -X_p$. (Consulted on: 05/23/2025).

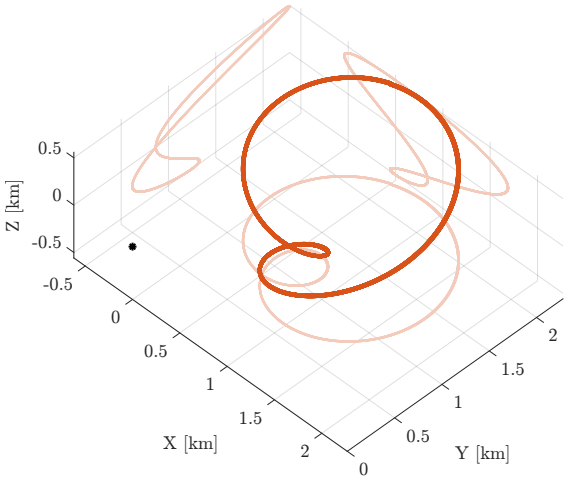

(a) Motion 1: $A_0 = 1$ km, $\alpha = -60$ deg, $x_{\text{off}} = 0$ km, $y_{\text{off}} = 0.5$ km, $B_0 = 0.5$ km, $\beta = 0$ deg

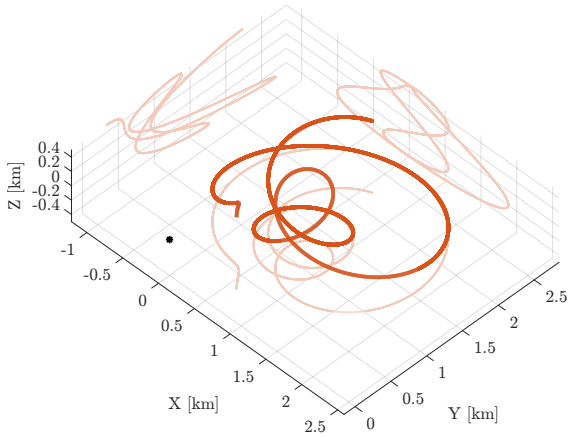

(b) Motion 2: $A_0 = 1$ km, $\alpha = -60$ deg, $x_{\text{off}} = 0.1$ km, $y_{\text{off}} = 0.5$ km, $B_0 = 0.5$ km, $\beta = 0$ deg

Figure 7.5: Relative motion in Inertial frame: The in-plane motion corresponds to an epitrochoid curve. The projections of the relative orbit on the three planes are shown in lighter color.

curve around the $\hat{\boldsymbol{p}}_3$ axis, and ϕ_i is a phase offset of the rolling circle. The phase offset ϕ_i is equal to $\phi_i = \frac{\pi}{2}$ unless $x_{\text{off}} \neq 0$. Drift motion through an orbit-radial offset x_{off} changes the radius r_i of the circles and the phase offset ϕ_i over time. That is, only r_i and ϕ_i are time-varying if the orbit-radial offset x_{off} is non-zero. The Z_p motion corresponds to a simple unforced oscillator with amplitude B_i and phase angle β_i, as is the case for the CWH equations (7.10) in the Hill frame.

Similar to the elliptic relative orbit shape in the Hill frame, the epitrochoid-based formulation provides an intuitive description of the relative motion in the perifocal frame and consequently the inertial frame, as shown in Fig. 7.4. The six inertial frame relative orbit elements (IROEs) in Eq. (7.24) are

- Circle radius r_i
- Phase offset of rolling circle ϕ_i
- Arm length d_i
- In-plane rotation α_i
- Out-of-plane sinusoidal amplitude B_i
- Out-of-plane phase angle β_i

The inverse mapping of Eq. (7.24) is derived in Appendix A.2 and is given by

$$A_0 = 2d_i \tag{7.25a}$$

$$\alpha = -\alpha_i \tag{7.25b}$$

$$x_{\text{off}} = -2r_i \cos\phi_i \tag{7.25c}$$

$$y_{\text{off}} = 2r_i \left(\sin\phi_i - \frac{3}{2} nt \cos\phi_i \right) \tag{7.25d}$$

$$B_0 = B_i \tag{7.25e}$$

$$\beta = -\beta \tag{7.25f}$$

To obtain the velocity states, the time derivatives of r_i and ϕ_i are derived first. Because x_{off} and y_{off} are constants, the time derivatives of Eqs. (7.25c) and (7.25d) are equal to

$$0 = -\dot{r}_i \cos\phi_i + r_i \sin\phi_i \dot{\phi}_i \tag{7.26}$$

and

$$0 = -\dot{r}_i \left(\sin\phi_i - \frac{3}{2} nt \cos\phi_i \right) + r_i \left(\cos\phi_i \dot{\phi}_i - \frac{3}{2} n \cos\phi_i + \frac{3}{2} nt \sin\phi_i \dot{\phi}_i \right) \tag{7.27}$$

Solving these two equations for $\dot{r}_i$ and $\dot{\phi}_i$ yields

$$\dot{r}_i = \frac{3}{2} r_i n \cos\phi_i \sin\phi_i = \frac{3}{4} r_i n \sin(2\phi_i) \tag{7.28}$$

and

$$\dot{\phi}_i = \frac{3}{2} n \cos^2\phi \tag{7.29}$$

Taking the time derivative of Eq. (7.22) and substituting Eqs. (7.28) and (7.29) gives the velocity states in the perifocal frame in terms of the IROEs:

$$\dot{X}_p(t) = 2d_i n \sin(2nt - \alpha_i) + \frac{1}{2} r_i n \big(\sin(nt - \phi_i) - 3\sin(nt + \phi_i) \big) \tag{7.30a}$$

$$\dot{Y}_p(t) = -2d_i n \cos(2nt - \alpha_i) - \frac{1}{2} r_i n \big(\cos(nt - \phi_i) - 3\cos(nt + \phi_i) \big) \tag{7.30b}$$

$$\dot{Z}_p(t) = -B_i n \sin(nt - \beta_i) \tag{7.30c}$$

The same relative orbits as in Fig. 7.3 are shown in Fig. 7.5 in the inertial frame.

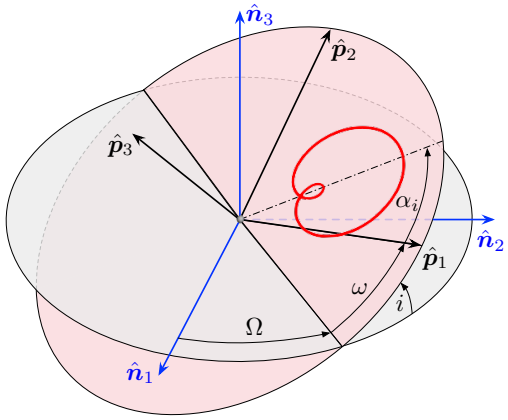

Figure 7.6: Effect of chief orbit orientation (Ω, i, ω) on inertial frame relative motion: the relative motion may be conveniently described in the perifocal frame, as the mapping from perifocal frame to inertial frame is a pure rotation.

7.2.2 General chief orbit orientation

In Eq. (7.22), the relative motion is described in the perifocal frame, which corresponds to the inertial frame only if $\Omega = i = \omega = 0$. However, the derived inertial relative orbit elements are considered to be the relevant parameters for the inertial frame relative motion, because for general chief orbit elements only the orientation of the relative orbit changes, but not the shape. Unlike the transition from the Hill frame $\mathcal{H}$ to the perifocal frame $\mathcal{P}$, which results in a general change of the relative orbit shape, the mapping from the perifocal frame $\mathcal{P}$ to the inertial frame $\mathcal{N}$ is straightforward as it is a pure rotation. The effect of the chief orbit orientation due to (Ω, i, ω) on the orientation of the inertial frame relative orbit is illustrated in Fig. 7.6.

7.2.3 Invariants of motion

The inertial frame relative orbit elements provide an intuitive way of describing the relative motion in the inertial frame. However, two of the elements, r_i and ϕ_i, are time-varying if the orbit-radial offset x_{off} is non-zero. To obtain the invariants of motion in the inertial frame that are constant in time, r_i and ϕ_i are evaluated at epoch $t = 0$. This yields

$$r_{i,0} = \frac{1}{2}\sqrt{y_{\text{off}}^2 + x_{\text{off}}^2} \tag{7.31}$$

and

$$\phi_{i,0} = \arctan\left(\frac{y_{\text{off}}}{-x_{\text{off}}}\right) \tag{7.32}$$

to make up the time-invariant inertial relative state vector

$$\delta\boldsymbol{\alpha e}_{i,0} = \begin{bmatrix} r_{i,0} & \phi_{i,0} & d_i & \alpha_i & B_i & \beta_i \end{bmatrix}^T \tag{7.33}$$

To relate the general elements r_i and ϕ_i to the inertial frame invariants $r_{i,0}$ and $\phi_{i,0}$, Eqs. (7.25c) and (7.25d) are also evaluated at $t = 0$

$$x_{\text{off}} = -2r_{i,0}\cos\phi_{i,0} \tag{7.34a}$$

$$y_{\text{off}} = 2r_{i,0}\sin\phi_{i,0} \tag{7.34b}$$

$$\tag{7.34c}$$

and substituted into Eqs. (7.24a) and (7.24b) to give

$$r_i = r_{i,0}\sqrt{1 + 3nt\cos\phi_{i,0}\left(\sin\phi_{i,0} + \frac{3}{4}nt\cos\phi_{i,0}\right)} \tag{7.35}$$

and

$$\phi_i = \arctan\left(\tan\phi_{i,0} + \frac{3}{2}nt\right) \tag{7.36}$$

This allows to directly propagate r_i and ϕ_i in time given an initial radius $r_{i,0}$ and phase offset $\phi_{i,0}$. If $\phi_{i,0} = \frac{\pi}{2}$, then r_i and ϕ_i are constant in time and no drift motion occurs. Substituting Eqs. (7.35) and (7.36) into Eqs. (7.22) and (7.30) yields the position

$$X_p(t) = 3d_i\cos\alpha_i - d_i\cos(2nt - \alpha_i) - 2r_{i,0}\left(\cos(nt - \phi_{i,0}) + \frac{3}{2}nt\sin(nt)\cos\phi_{i,0}\right) \tag{7.37a}$$

$$Y_p(t) = 3d_i\sin\alpha_i - d_i\sin(2nt - \alpha_i) - 2r_{i,0}\left(\sin(nt - \phi_{i,0}) - \frac{3}{2}nt\cos(nt)\cos\phi_{i,0}\right) \tag{7.37b}$$

$$Z_p(t) = B_i\cos(nt - \beta_i) \tag{7.37c}$$

and velocity

$$\dot{X}_p(t) = 2d_i n \sin(2nt - \alpha_i) + \frac{1}{2} r_{i,0} n \big(\sin(nt - \phi_{i,0}) - 3\sin(nt + \phi_{i,0}) - 6nt \cos(nt) \cos\phi_{i,0} \big) \tag{7.38a}$$

$$\dot{Y}_p(t) = -2d_i n \cos(2nt - \alpha_i) - \frac{1}{2} r_{i,0} n \big(\cos(nt - \phi_{i,0}) - 3\cos(nt + \phi_{i,0}) + 6nt \sin(nt) \cos\phi_{i,0} \big) \tag{7.38b}$$

$$\dot{Z}_p(t) = -B_i n \sin(nt - \beta_i) \tag{7.38c}$$

in the inertial frame in terms of the time-invariant IROEs.

7.2.4 Closed relative orbits

For a closed relative orbit (no drift motion), the orbit-radial offset in the CW equations must be zero, i.e. $x_{\text{off}} = 0$. This results in $\phi_i = \phi_{i,0} = \frac{\pi}{2}$ and $r_i = r_{i,0}$. The shape and size of the inertial frame relative orbit are determined by r_i and d_i. Figure 7.7 shows inertial frame relative orbits for several different values of r_i and d_i, with all remaining IROEs equal to zero. If $r_i = 0$, the relative orbit shape is circular. The target completes two revolutions of this circle during one orbital period. This is more clear when r_i is slightly increased from 0 to 0.1, where an inner loop becomes visible. Increasing r_i causes the relative orbit size to grow, while the inner loop becomes smaller. The inner loop disappears when $r_i = d_i$. Increasing r_i even more makes the relative orbit shape more circular. If $d_i = 0$, the relative orbit is circular and centered at the chief, with one revolution per orbital period.

As mentioned in Sec. 7.2.1, the relative orbit is offset from the chief by a distance of $3d_i$. Increasing r_i increases the relative orbit size due to the greater size of the circles that generate the epitrochoid curve. The ratio of r_i and d_i determines the shape of the relative orbit. If $r_i < d_i$, the generating point is outside the rolling circle, creating an inner loop. If $r_i = d_i$, the generating point is on the surface of the rolling circle, creating a cusp. Finally, if $r_i > d_i$, the generating point is inside the rolling circle, creating a curve that becomes circular as $d_i \to 0$. If $r_i > 2d_i$, the deputy circumnavigates the chief, and if $r_i < 2d_i$, the deputy remains on one inertial side of the chief.

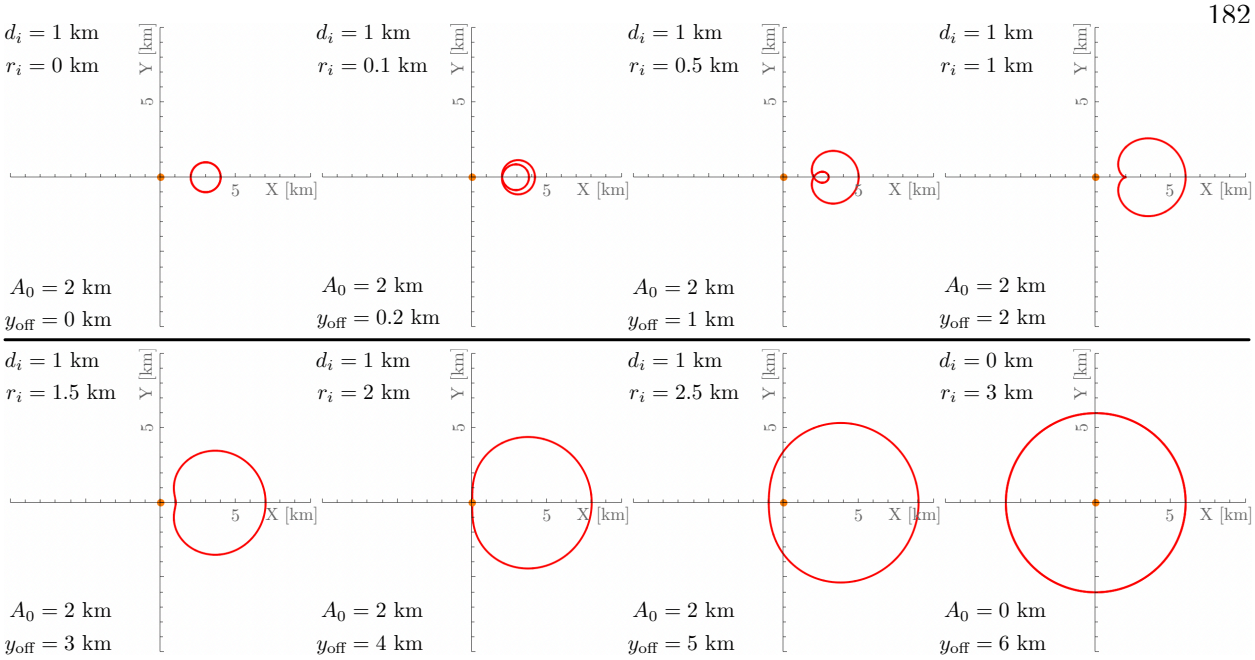

Figure 7.7: Inertial frame relative orbits for circular chief orbits: The size of the relative orbit changes with r_i, while the shape changes with the ratio of r_i and d_i.

7.2.5 Drift Motion

An orbit-radial offset x_{off}, resulting in $\phi_{i,0} \neq \frac{\pi}{2}$, causes drift of the deputy with respect to the chief due to the difference in semi-major axis of the two spacecraft that leads to different orbital periods. In the Hill frame, the drift motion occurs in the x-direction. In the inertial frame, the drift motion results in a change of the circle radius r_i and the in-plane phase offset ϕ_i over time. Such inertial frame drift motion is shown in Fig. 7.8. Because r_i changes while d_i remains constant, the shape (inner loop, cusp, no loop) of the epitrochoid changes over time as well.

7.3 Elliptic chief orbits

The Clohessy-Wilsthire equations assume a circular chief orbit and are not applicable to general chief orbit eccentricities. For elliptic chief orbits, the orbit element difference description is more appropriate. Using Eqs. (7.16) and (7.19) results after several simplification steps in the

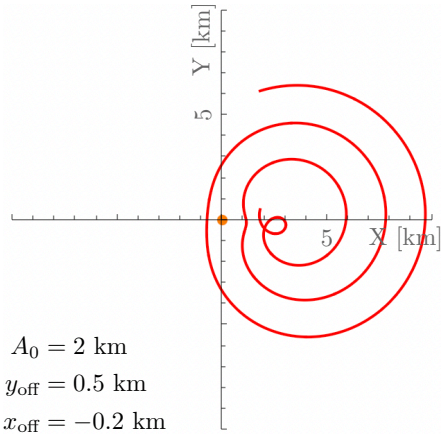

Figure 7.8: Drift motion in the inertial frame: An offset x_{off} causes the radius r_i to change over time.

analytical expression

$$
{}^{\mathcal{P}}\begin{bmatrix} X_p(f) \\ Y_p(f) \\ Z_p(f) \end{bmatrix} = {}^{\mathcal{P}}\begin{bmatrix} r\left(\frac{\delta a \cos f}{a} - \frac{\delta e(2e\cos f - \cos(2f)+3)}{2\eta^2} - \frac{\delta M(\sin f + e\sin f\cos f)}{\eta^3} - \delta\omega\sin f - \delta\Omega\cos i\sin f\right) \\ r\left(\frac{\delta a \sin f}{a} + \frac{\delta e\sin(2f)}{2\eta^2} + \delta M\frac{2(1+e^2)\cos f + e\cos(2f)+3e}{2\eta^3} + \delta\omega\cos f + \delta\Omega\cos i\cos f\right) \\ r\left(\delta i\sin\theta - \delta\Omega\sin i\cos\theta\right) \end{bmatrix} \tag{7.39}
$$

Similar to the inertial frame transformation for circular chief orbits, Eq. (7.21) is used to rewrite and simplify Eq. (7.39):

$$X_p(f) = \frac{\eta^2}{1+e\cos f}\left((3+2e\cos f)d_i\cos\alpha_i - d_i\cos(2f-\alpha_i) - 2r_i\cos(f-\phi_i)\right) \tag{7.40a}$$

$$Y_p(f) = \frac{\eta^2}{1+e\cos f}\left((3+2e\cos f)d_i\sin\alpha_i - d_i\sin(2f-\alpha_i) - 2r_i\sin(f-\phi_i)\right) \tag{7.40b}$$

$$Z_p(f) = \frac{\eta^2}{1+e\cos f}B_i\cos(\omega+f-\beta_i) \tag{7.40c}$$

Aside from the $2e\cos f$ term and the formulation as function of true anomaly f instead of time t, the form of these equations is the same as in Eq. (7.22). All components are multiplied by the chief orbit radius r, which is a function of f. For elliptic chief orbits and the differential orbit elements

description, the inertial frame relative orbit elements are determined by

$$r_i = \frac{a}{2}\sqrt{\left(\frac{1}{\eta^3}\delta M + \cos i\delta\Omega + \delta\omega\right)^2 + \left(\frac{\delta a}{a}\right)^2} \tag{7.41a}$$

$$\phi_i = \arctan\left(\frac{\frac{1}{\eta^3}\delta M + \cos i\delta\Omega + \delta\omega}{-\frac{\delta a}{a}}\right) \tag{7.41b}$$

$$d_i = \frac{a}{2\eta^3}\sqrt{(\eta\delta e)^2 + (e\delta M)^2} \tag{7.41c}$$

$$\alpha_i = \arctan\left(\frac{e\delta M}{-\eta\delta e}\right) \tag{7.41d}$$

$$B_i = a\sqrt{\delta i^2 + (\sin i\delta\Omega)^2} \tag{7.41e}$$

$$\beta_i = \arctan\left(\frac{\delta i}{-\sin i\delta\Omega}\right) \tag{7.41f}$$

Note that several of these IROEs are a function of the same differential orbital elements. However, if one wants to specify d_i and α_i, for example, and determine the values for δe and δM that result in these specified parameters, it is rather straightforward to substitute one equation into the other and solve for δe and δM. The inverse mapping for Eq. 7.41 is provided in Eq. A.14 in Appendix A.3. For $e = 0$, this differential orbit element description may be used for the circular chief orbit relative motion.

Figure 7.9 shows various closed inertial frame relative orbits for an elliptic chief orbit with eccentricity of $e = 0.5$ and semi-major axis of $a = 10000$ km. For the DOE description, δe is similar to the in-plane amplitude A_0 for the circular chief orbit, while $\delta\omega$ is similar to the along-track offset y_{off}. An eccentric orbit essentially stretches part of the 2-by-1 relative orbit ellipse in the Hill frame in the y-direction. This is due to the dependence of the relative motion on the chief orbit radius r, which is the greatest at apoapsis. The part of the Hill frame relative orbit ellipse that is stretched the most in the y-direction corresponds to the part that is traversed while the spacecraft are on the apoapsis side of the orbit. This is visible for the inertial frame relative orbits in Fig. 7.9 as well. For $\delta e = -0.00015$, the inertial frame relative orbit is stretched equally in the $-Y_p$ and $+Y_p$ direction. For a positive $\delta\omega$ the relative orbit stretches more in the $-Y_p$ direction. This is because the $\delta\omega$ offset shifts the relative orbit in the $+y$ direction of the Hill frame and stretches the orbit more in the $+y$ direction than the $-y$ direction. This stretched part of the relative orbit is traversed when

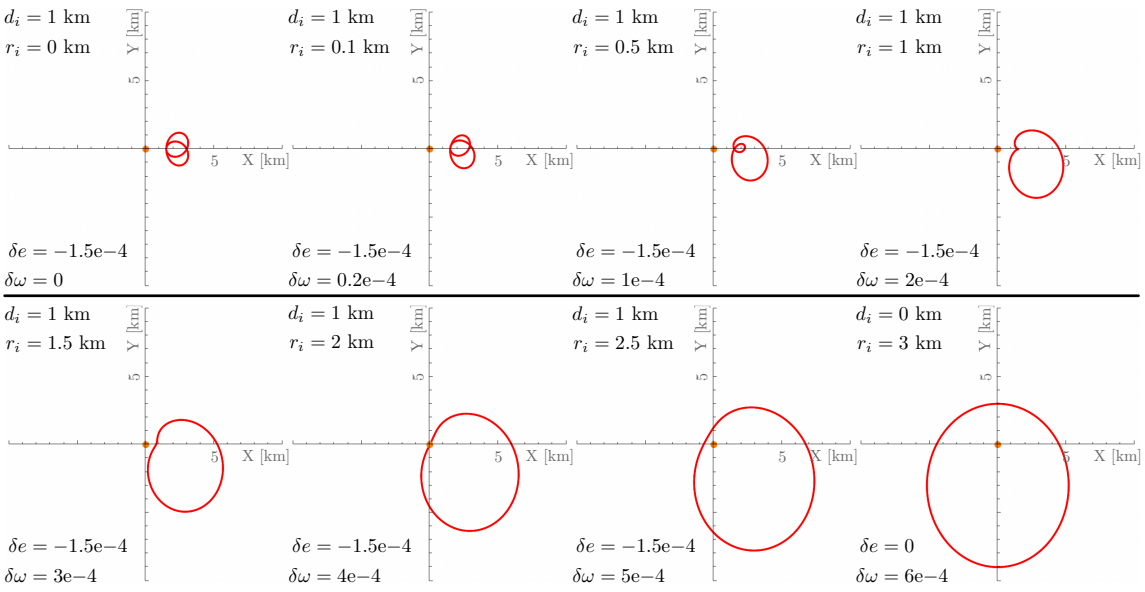

Figure 7.9: Inertial frame relative orbits for elliptic chief orbits: The relative orbit is stretched for elliptic chief orbits.

the $+y$ direction of the Hill frame is pointing in the $-Y_p$ direction of the perifocal frame, resulting in a larger relative orbit part in $-Y_p$. Similar to the circular chief orbit case, increasing r_i while d_i remains the same causes the inner loop to disappear and turn into a cusp when $r_i = d_i$. Increasing r_i further such that $r_i > d_i$ makes the inertial frame relative orbit more and more elliptic. If $d_i = 0$, the relative orbit is elliptic in the inertial frame.

An example for the inertial frame orbit rotation for an elliptic chief orbit is shown in Fig. 7.10. To induce a rotation of α_i, the ratio of $(e\delta M)/(-\eta\delta e)$ must be changed. To maintain the same d_i, $e\delta M$ and $-\eta\delta e$ cannot be arbitrarily changed, however, and $\delta\omega$ must be adjusted as well such that r_i remains the same. Thus, the relative orbit shape changes when a rotation of α_i is applied.

The effect of the chief orbit orientation (Ω, i, ω) on the relative orbit shape in the perifocal frame is already considered in Eq. (7.40). The remaining rotation of the relative orbit through (Ω, i, ω) is the same for the elliptic orbit as for the circular orbit, as illustrated in Fig. 7.6.

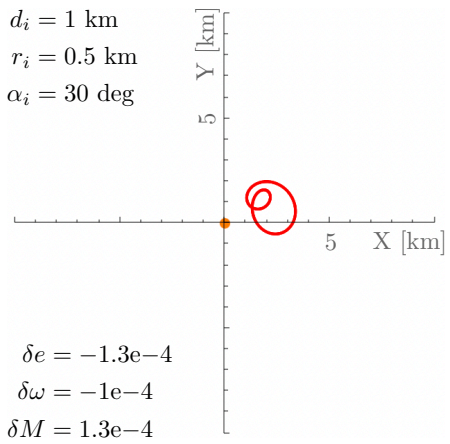

Figure 7.10: Rotation of inertial frame relative orbit for elliptic chief orbits: a rotation by α_i also changes the relative orbit shape.

7.4 Control development

The relative orbits discussed in the previous sections assume no perturbations. A continuous-time feedback control law based on the inertial frame relative orbit elements is developed to maintain a certain inertial relative orbit despite perturbations, and to allow for re-configurations from one formation to another.

7.4.1 Variational equations

The Lagrangian-bracket methodology is applied here to derive the variational equations, which show how the invariants of the unperturbed motion change in time due to perturbing accelerations. To aid readability, the δ notation to indicate a relative orbit element set is dropped, i.e. $\boldsymbol{oe}_i$ is used instead of $\delta\boldsymbol{oe}_i$. Moreover, all quantities are expressed in the perifocal frame $\mathcal{P}$, so $\boldsymbol{\rho}$ is written instead of ${}^{\mathcal{P}}\boldsymbol{\rho}$, for example. The time-invariant IROE set

$$\boldsymbol{oe}_{i,0} = \begin{bmatrix} r_{i,0} & \phi_{i,0} & d_i & \alpha_i & B_i & \beta_i \end{bmatrix}^T \tag{7.42}$$

changes in time according to [136, Chapter 12]

$$\dot{\boldsymbol{oe}}_{i,0} = [L]^{-1} \left[\frac{\partial \boldsymbol{\rho}}{\partial \boldsymbol{oe}_{i,0}} \right]^T \boldsymbol{a}_p \tag{7.43}$$

where $[L]$ is the Lagrangian-bracket matrix, $\boldsymbol{\rho}$ is the relative position vector, and $\boldsymbol{a}_p$ is the perturbing acceleration. Using the matrix

$$[J] = \begin{bmatrix} 0_{3\times3} & I_{3\times3} \\ -I_{3\times3} & 0_{3\times3} \end{bmatrix} \tag{7.44}$$

and the cartesian state in the perifocal frame

$$\boldsymbol{s}_p(t, \boldsymbol{oe}_{i,0}) = \begin{bmatrix} X_p & Y_p & Z_p & \dot{X}_p & \dot{Y}_p & \dot{Z}_p \end{bmatrix}^T \tag{7.45}$$

the Lagrangian-bracket matrix is computed by

$$[L] = \frac{\partial \boldsymbol{s}_p}{\partial \boldsymbol{oe}_{i,0}}^T [J] \frac{\partial \boldsymbol{s}_p}{\partial \boldsymbol{oe}_{i,0}} \tag{7.46}$$

or element-wise via

$$L_{ij} = [oe_i, oe_j] = \left(\frac{\partial \boldsymbol{\rho}}{\partial oe_i}\right)^T \frac{\partial \dot{\boldsymbol{\rho}}}{\partial oe_j} - \left(\frac{\partial \dot{\boldsymbol{\rho}}}{\partial oe_i}\right)^T \frac{\partial \boldsymbol{\rho}}{\partial oe_j} \tag{7.47}$$

where $\dot{\boldsymbol{\rho}}$ is the relative velocity vector and oe_i and oe_j are the i-th and j-th element of the relative orbit element set $\boldsymbol{oe}_{i,0}$, respectively. The partials are obtained by taking the derivative of Eqs. (7.37) and (7.38) with respect to the relative orbit elements $\boldsymbol{oe}_{i,0}$. By defining

$$[B] = [L]^{-1} \left[\frac{\partial \boldsymbol{\rho}}{\partial \boldsymbol{oe}_{i,0}}\right]^T \tag{7.48}$$

the equations of motion of the IROE set $\boldsymbol{oe}_{i,0}$ are compactly written as

$$\dot{\boldsymbol{oe}}_{i,0} = [B]\boldsymbol{a}_p \tag{7.49}$$

These linearized relative motion variational equations describe how a perturbing acceleration changes the osculating inertial frame relative orbit elements over time. Taking the partials of $\boldsymbol{\rho}$ in Eq. (7.37) and $\dot{\boldsymbol{\rho}}$ in Eq. (7.38) with respect to the IROE set $\boldsymbol{oe}_{i,0}$, yields the corresponding Lagrangian-bracket

matrix

$$[L]_{i,0} = \begin{bmatrix} 0 & 2r_{i,0}n & 0 & 0 & 0 & 0 \\ -2r_{i,0}n & 0 & 0 & 0 & 0 & 0 \\ 0 & 0 & 0 & 4d_i n & 0 & 0 \\ 0 & 0 & -4d_i n & 0 & 0 & 0 \\ 0 & 0 & 0 & 0 & 0 & B_i n \\ 0 & 0 & 0 & 0 & -B_i n & 0 \end{bmatrix} \tag{7.50}$$

Taking the inverse of Eq. (7.50) and multiplying with the partial of the relative position $\boldsymbol{\rho}$ w.r.t. the relative orbit element set $\boldsymbol{oe}_{i,0}$ gives

$$[B]_{i,0} = \begin{bmatrix} -\frac{-2\sin(nt-\phi_{i,0})+3nt\sin(\phi_{i,0})\sin(nt)}{2n} & \frac{-2\cos(nt-\phi_{i,0})+3nt\sin(\phi_{i,0})\cos(nt)}{2n} & 0 \\ -\frac{2\cos(nt-\phi_{i,0})+3nt\cos(\phi_{i,0})\sin(nt)}{2nr_{i,0}} & \frac{-2\sin(nt-\phi_{i,0})+3nt\cos(\phi_{i,0})\cos(nt)}{2nr_{i,0}} & 0 \\ \frac{\sin(2nt-\alpha_i)+3\sin(\alpha_i)}{4n} & -\frac{\cos(2nt-\alpha_i)+3\cos(\alpha_i)}{4n} & 0 \\ \frac{-\cos(2nt-\alpha_i)+3\cos(\alpha_i)}{4d_i n} & \frac{-\sin(2nt-\alpha_i)+3\sin(\alpha_i)}{4d_i n} & 0 \\ 0 & 0 & \frac{-\sin(nt-\beta_i)}{n} \\ 0 & 0 & \frac{\cos(nt-\beta_i)}{B_i n} \end{bmatrix} \tag{7.51}$$

This matrix may be used to directly relate the variation of the inertial frame relative orbit elements to perturbations in the perifocal frame. Note that the rows corresponding to $\dot{\phi}_{i,0}$, $\dot{\alpha}_i$ and $\dot{\beta}_i$ are singular if $r_{i,0}$, d_i or B_i are zero, respectively. Thus, while the IROE set derived in Sec. 7.2.1 is illustrative, it is not necessarily the best for control purposes. Instead, an alternative non-singular IROE set is introduced

$$\boldsymbol{oe}_{i,0,ns} = \begin{bmatrix} R_{1,0} & R_{2,0} & D_1 & D_2 & B_1 & B_2 \end{bmatrix}^T \tag{7.52}$$

where the relative orbit elements are similar to the LROE set proposed in Ref. [77]:

$$R_{1,0} = r_{i,0} \cos \phi_{i,0} \tag{7.53a}$$

$$R_{2,0} = r_{i,0} \sin \phi_{i,0} \tag{7.53b}$$

$$D_1 = d_i \cos \alpha_i \tag{7.53c}$$

$$D_2 = d_i \sin \alpha_i \tag{7.53d}$$

$$B_1 = B_i \cos \beta_i \tag{7.53e}$$

$$B_2 = B_i \sin \beta_i \tag{7.53f}$$

For this $\boldsymbol{\alpha e}_{i,0,ns}$ set, the Lagrangian-bracket matrix $[L]$ is equal to

$$[L]_{i,0,ns} = \begin{bmatrix} 0 & 2n & 0 & 0 & 0 & 0 \\ -2n & 0 & 0 & 0 & 0 & 0 \\ 0 & 0 & 0 & 4n & 0 & 0 \\ 0 & 0 & -4n & 0 & 0 & 0 \\ 0 & 0 & 0 & 0 & 0 & n \\ 0 & 0 & 0 & 0 & -n & 0 \end{bmatrix} \tag{7.54}$$

and the non-singular IROE variational equation $[B]$ matrix is equal to

$$[B]_{i,0,ns} = \begin{bmatrix} \frac{\sin(nt)}{n} & -\frac{\cos(nt)}{n} & 0 \\ -\frac{\cos(nt)+\frac{3}{2}nt\sin(nt)}{n} & \frac{-\sin(nt)+\frac{3}{2}nt\cos(nt)}{n} & 0 \\ \frac{\sin(2nt)}{4n} & -\frac{\cos(2nt)+3}{4n} & 0 \\ \frac{-\cos(2nt)+3}{4n} & -\frac{\sin(2nt)}{4n} & 0 \\ 0 & 0 & -\frac{\sin(nt)}{n} \\ 0 & 0 & \frac{\cos(nt)}{n} \end{bmatrix} \tag{7.55}$$

In this case, the denominators do not go to zero for any relative orbit elements, yielding non-singular variational equations. Moreover, note that in contrast to Eq. (7.51), this $[B]$ matrix does not depend on the IROEs, but only on the mean motion n and time t.

7.4.2 Continuous feedback control

A Lyapunov-based continuous feedback control law is developed to allow for station-keeping around a desired reference inertial frame orbit as well as reconfigurations from one formation to another. The deputy spacecraft (servicer) is assumed to be controlled, essentially replacing the perturbing acceleration $\boldsymbol{a}_p$ in Eq. (7.49) with the control acceleration $\boldsymbol{u}$. The difference between the osculating inertial frame relative orbit elements and the desired reference orbit elements corresponds to the IROE tracking error

$$\Delta\boldsymbol{oe}_i = \boldsymbol{oe}_i - \boldsymbol{oe}_{i,r} \tag{7.56}$$

where $\boldsymbol{oe}_i$ is used as a placeholder for either time-invariant IROE set described in Sec. 7.4.1, and $\boldsymbol{oe}_{i,r}$ is the corresponding reference IROE state. Taking the time-derivative and substituting Eq. (7.49) with the corresponding control vectors gives

$$\Delta\dot{\boldsymbol{oe}}_i = \dot{\boldsymbol{oe}}_i - \dot{\boldsymbol{oe}}_{i,r} = [B](\boldsymbol{u} - \boldsymbol{u}_r) \tag{7.57}$$

where $\boldsymbol{u}_r$ is a reference control vector allowing for a time-varying reference IROE state $\boldsymbol{oe}_{i,r} = \boldsymbol{oe}_{i,r}(t)$ [77]. Similar to the Lyapunov-based control development for mean orbit element differences [78] and the Hill frame non-singular orbit elements [77], the positive definite Lyapunov candidate function

$$V(\Delta\boldsymbol{oe}_i) = \frac{1}{2}\Delta\boldsymbol{oe}_i^T[K]\Delta\boldsymbol{oe}_i \tag{7.58}$$

is used, where $[K]$ is a 6×6 symmetric positive definite gain matrix. Taking the time derivative of the Lyapunov candidate function and substituting Eq. (7.57) yields

$$\dot{V}(\Delta\boldsymbol{oe}_i) = \Delta\boldsymbol{oe}_i^T[K][B](\boldsymbol{u} - \boldsymbol{u}_r) \tag{7.59}$$

Setting the Lyapunov rate $\dot{V}$ equal to the negative definite function

$$\dot{V}(\Delta\boldsymbol{oe}_i) = -\Delta\boldsymbol{oe}_i^T[K][K]\Delta\boldsymbol{oe}_i \tag{7.60}$$

gives

$$[B](\boldsymbol{u} - \boldsymbol{u}_r) = -[K]\Delta\boldsymbol{oe}_i \tag{7.61}$$

Table 7.1: Initial and desired inertial frame relative orbit elements

	$r_{i,0}$ [m]	$\phi_{i,0}$ [deg]	d_i [m]	α_i [deg]	B_i [m]	β_i [deg]
Initial	304.138	99.462	300	0	10	-5.730
Desired	850	90	650	90	100	45

Taking the least-squares inverse of $[B]$ yields the control law

$$\boldsymbol{u} = \boldsymbol{u}_r - ([B]^T[B])^{-1}[B]^T[K]\Delta\boldsymbol{oe}_i \tag{7.62}$$

and the resulting Lyapunov rate

$$\dot{V}(\Delta\boldsymbol{oe}_i) = -\Delta\boldsymbol{oe}_i^T[K][B]([B]^T[B])^{-1}[B]^T[K]\Delta\boldsymbol{oe}_i = -\boldsymbol{y}^T([B]^T[B])^{-1}\boldsymbol{y} \tag{7.63}$$

with $\boldsymbol{y} = [B]^T[K]\Delta\boldsymbol{oe}_i$. To guarantee Lyapunov stability, the Lyapunov rate must be negative semi-definite, and for asymptotic stability it must be negative definite. For the $\boldsymbol{oe}_{i,0,ns}$ set, the matrix $([B]^T[B])^{-1}$ is symmetric and has only positive eigenvalues, so it is positive definite. Thus, the Lyapunov rate is semi-definite and the control is stabilizing. For asymptotic stability, the Lyapunov rate, and thus $\boldsymbol{y}$, must only be zero if the IROE tracking error $\Delta\boldsymbol{oe}_i$ is zero. Because the $[B]$ matrix changes with time, there may be instances when $\boldsymbol{y}$ becomes zero while $\Delta\boldsymbol{oe}_i$ is non-zero. However, this occurs only for an instant, as the $[B]$ matrix keeps changing as the two spacecraft orbit the central body. The largest invariant set in which $\boldsymbol{y}$ remains zero for all time corresponds to $\Delta\boldsymbol{oe}_i = 0$. Consequently, the control is asymptotically stabilizing according to LaSalle's invariance principle.

7.4.3 Control application

The control law developed in Sec. 7.4.2 is tested here using the initial and desired inertial relative orbit elements shown in Tab. 7.1. First, the time-invariant IROE set from Eq. (7.42) with corresponding $[B]$ matrix from Eq. (7.51) is used with the gain matrix

$$[K]_{i,0} = \text{diag}([n, 10, 0.1n, 0.1, 0.1n, 0.1]) \tag{7.64}$$

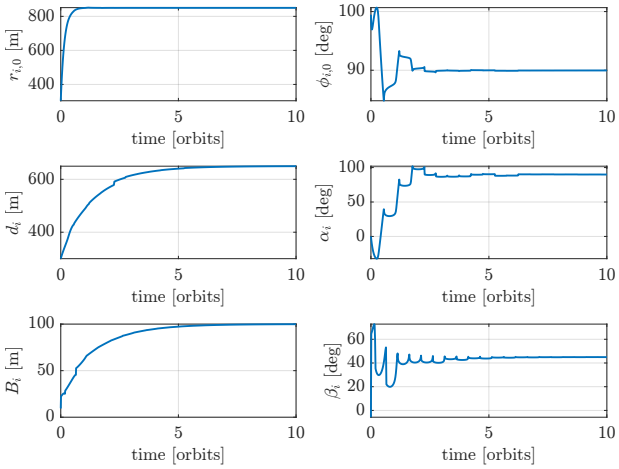

(a) Inertial frame relative orbit elements

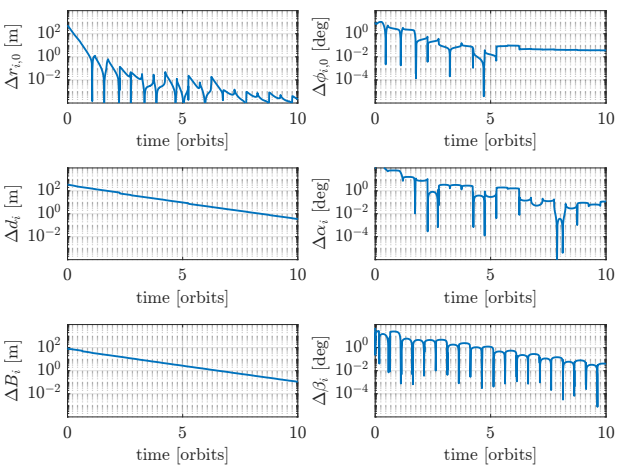

(b) Inertial frame relative orbit element errors

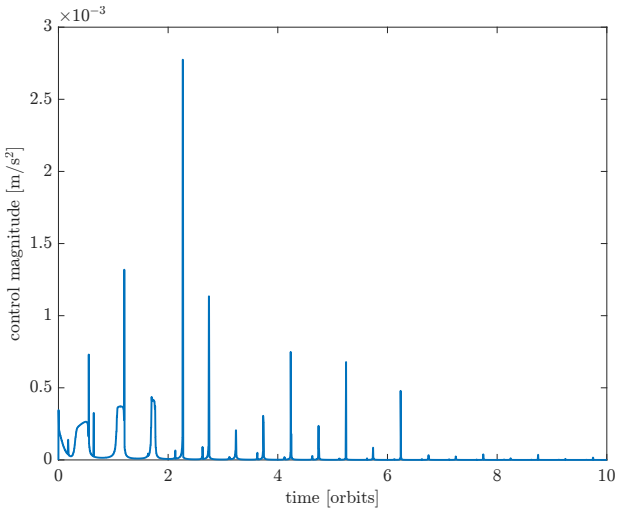

(c) Control magnitude

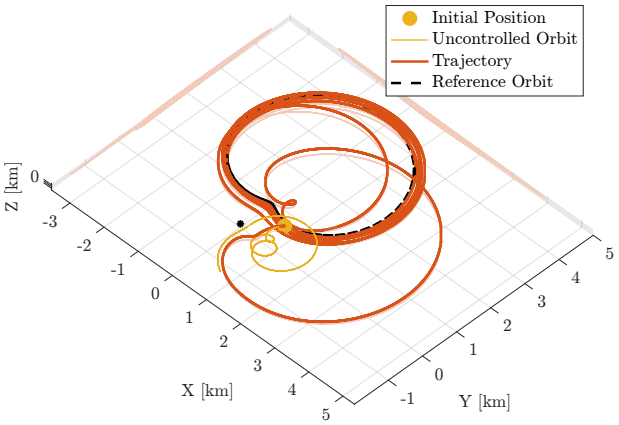

(d) Inertial frame relative orbit

Figure 7.11: Control of inertial frame relative orbit element set $\boldsymbol{oe}_{i,0}$

A relatively high feedback gain is chosen for the $\phi_{i,0}$ tracking error that is responsible for drift motion. Given the cartesian relative state, the IROE state is computed with Eq. A.15 in the control algorithm. The results are shown in Fig. 7.11. While the relative orbit successfully converges to the desired relative orbit (Figs. 7.11a and 7.11b), the control response is somewhat abrupt as visible in Fig. 7.11c. The various relative orbit elements are only controllable at certain times due to the control mapping matrix $[B]_{i,0}$, at which times the control magnitude increases significantly. During the times in between, barely any control is requested. This leads to a somewhat slow convergence of the relative orbit, especially of the angle states $\phi_{i,0}, \alpha_i, \beta_i$, as seen in Fig. 7.11d. The total Delta-V needed for this reconfiguration is $\Delta V = 2.7$ m/s.

In contrast, the non-singular time-invariant IROE set from Eq. (7.52) with corresponding $[B]$ matrix from Eq. (7.55) and gain matrix

$$[K]_{i,0,ns} = n \cdot \text{diag}([30, 1, 0.5, 0.5, 1, 1]) \tag{7.65}$$

yields a much smoother response, as shown in Fig. 7.12. Because all elements of the $\boldsymbol{oe}_{i,0,ns}$ set have the same unit, the feedback gain matrix is much easier to tune. Again, a higher feedback gain is chosen for the element corresponding to drift motion. Because the $[B]$ matrix is non-singular, this control description is also suitable for relative orbits with $r_{i,0}$, d_i or B_i equal to zero. The total Delta-V with this IROE set is $\Delta V = 2.0$ m/s.

7.5 Application to on-orbit servicing

The inertial frame relative orbit element description is used to design a relative orbit that satisfies inertially fixed keep-out constraints imposed by a cislunar plasma-wake. This plasma wake is modeled as a keep-out cylinder that extends in the $\hat{\boldsymbol{n}}_1$ direction with a radius of $r_c = 10$ m, and the chief orbit elements are equal to $[a,\ e,\ i,\ \Omega,\ \omega,\ M_0]^T = [10000 \text{ km},\ 0,\ 0\ 0\ 0\ 0]^T$. To remain outside the plasma wake keep-out zone, the servicer must maintain a minimum distance of $r_c = 10$ m from the cylinder axis. As can be seen in Fig. 7.4, this requires a rotation by α_i, as the relative orbit intersects the $\hat{\boldsymbol{n}}_1$ axis multiple times for $\alpha_i = 0$. To achieve the minimal distance, r_i

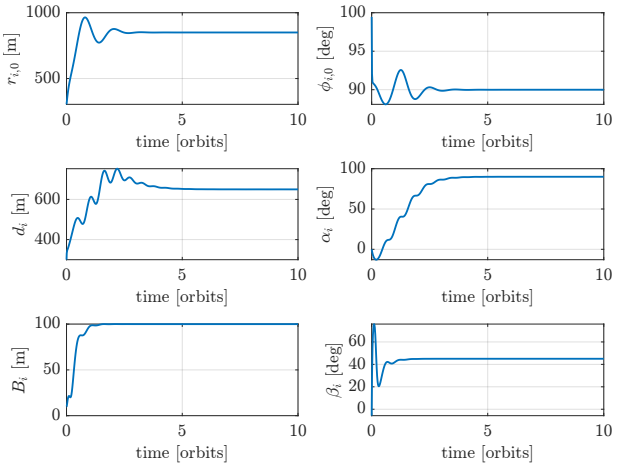

(a) Inertial frame relative orbit elements

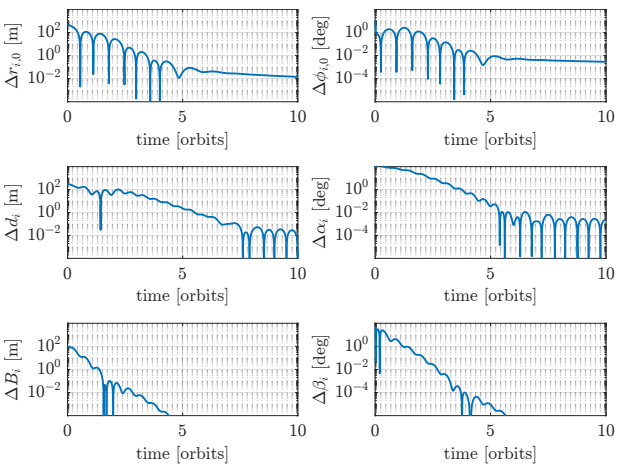

(b) Inertial frame relative orbit element errors

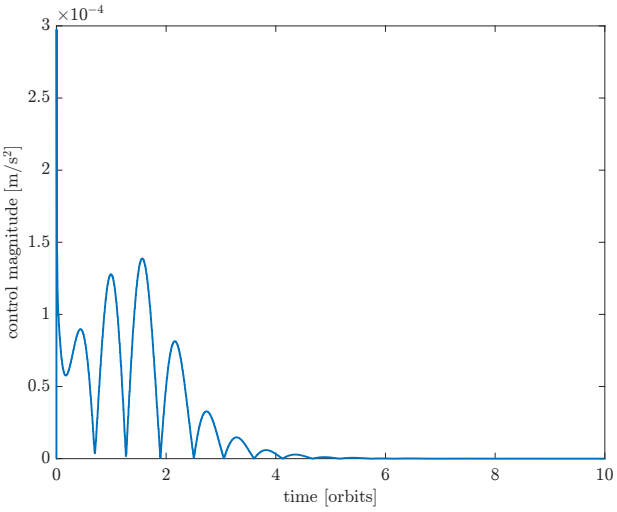

(c) Control magnitude

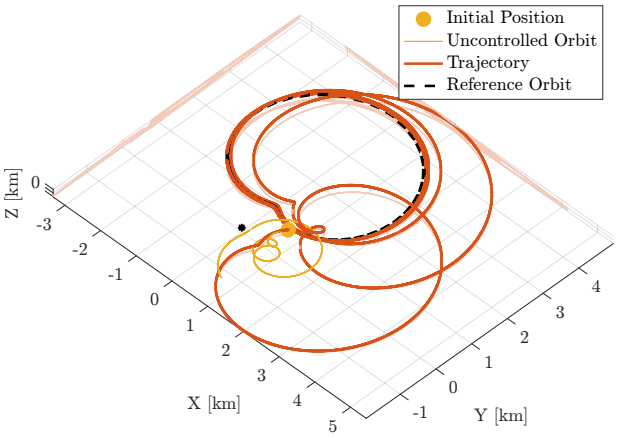

(d) Inertial frame relative orbit

Figure 7.12: Control of non-singular inertial frame relative orbit element set $\boldsymbol{oe}_{i,0,ns}$

and d_i must then be chosen accordingly.

The epitrochoid frame $\mathcal{E} : \{\hat{\boldsymbol{e}}_1, \hat{\boldsymbol{e}}_2, \hat{\boldsymbol{e}}_3\}$ is defined as the frame in which the orientation of the epitrochoid-shaped relative orbit is constant, with $[EP(\alpha_i)] = [M_3(\alpha_i)]$. That is, for $\alpha_i = 0$, the epitrochoid frame $\mathcal{E}$ corresponds to the perifocal frame $\mathcal{P}$, and otherwise it is obtained by rotating the frame $\mathcal{P}$ by α_i around the $\hat{\boldsymbol{p}}_3$ axis. The solution in the epitrochoid frame is obtained by setting $\alpha_i = 0$ in Eq. (7.22). For a closed orbit ($\phi_i = 0$), this gives

$$X_e(t) = 3d_i - d_i \cos(2nt) - 2r_i \cos(nt) \tag{7.66}$$

To determine the minimum distance in the $\hat{\boldsymbol{e}}_1$ direction, the derivative is taken

$$\dot{X}_e(t) = 2d_i n \sin(2nt) - 2r_i n \cos(nt) \tag{7.67}$$

and set equal to zero, using the trigonometric identity $\sin(2nt) = 2\sin(nt)\cos(nt)$:

$$0 = 2\cos(nt)\big(2d_i \sin(nt) - r_i\big) = 2\cos(f)\big(2d_i \sin(f) - r_i\big) \tag{7.68}$$

For $0 \leq f \leq 2\pi$, the roots of this equation are $\pm\frac{\pi}{2}$ and $f = \arcsin\left(\frac{r_i}{2d_i}\right)$. For non-negative r_i and d_i, this results in the minimum distance

$$X_{e,\min}(r_i, d_i) = \begin{cases} 2d_i\left(1 - \left(\dfrac{r_i}{2d_i}\right)^2\right) & \text{at} \quad f = \arcsin\left(\dfrac{r_i}{2d_i}\right) \quad \text{if} \quad 0 \leq \dfrac{r_i}{2d_i} < 1 \\ 4d_i\left(1 - \dfrac{r_i}{2d_i}\right) & \text{at} \quad f = \dfrac{\pi}{2} \qquad\qquad\quad \text{if} \quad \dfrac{r_i}{2d_i} \geq 1 \end{cases} \tag{7.69}$$

To avoid circumnavigation of the servicer around the target and for the minimum X_e distance to lie on the positive side, $\frac{r_i}{2d_i} < 1$. Thus, for a given $d_i = 10$ m, the required r_i to remain outside the wake is obtained by $r_{i,\text{req}} = \sqrt{2d_i(2d_i - X_{e,\min})}$. This yields $r_i = 14.142$ m for $X_{e,\min} = r_c = 10$ m. Finally, a rotation angle of $\alpha_i = 90$ deg is used to move the relative orbit outside of the wake. The corresponding inertial frame relative orbit and keep-out zone are shown in Fig. 7.13a.

Alternatively, a relative orbit with out-of plane motion may be chosen, as shown in Fig. 7.13b. In this case, the in-plane rotation α_i can remain zero, but an out-of-plane rotation $\beta_i = 90$ deg must be introduced to satisfy the keep-out constraint. Figure 7.14 shows the YZ-plane projection of the relative motion for the same relative orbits as in Fig. 7.13 to clearly show the satisfaction of the keep-out constraint.

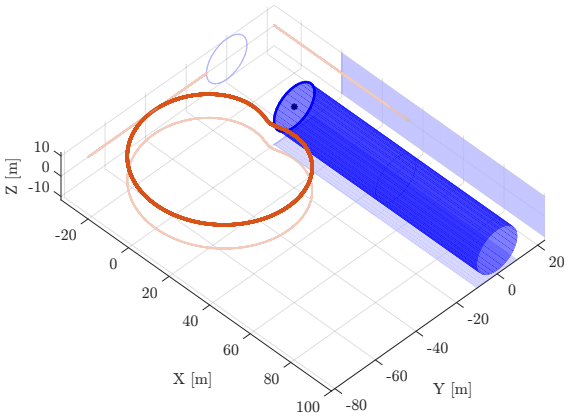

(a) Motion 1: $r_{i,0} = 14.142$ m, $\phi_{i,0} = 90$ deg, $d_i = 10$ m, $\alpha_i = 90$ deg, $B_i = 0$ m, $\beta_i = 0$ deg

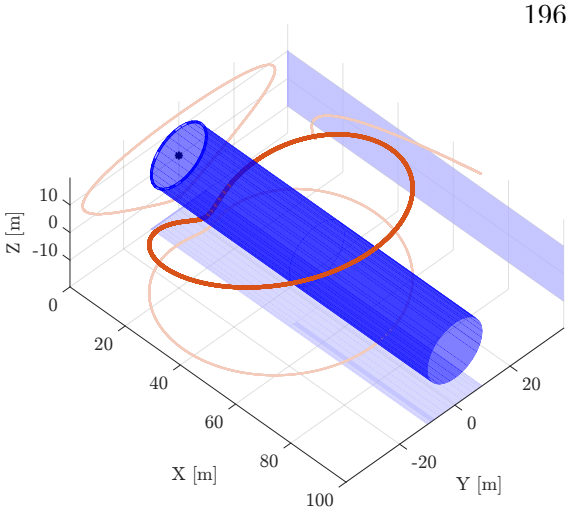

(b) Motion 2: $r_{i,0} = 15$ m, $\phi_{i,0} = 90$ deg, $d_i = 10$ m, $\alpha_i = 0$ deg, $B_i = 15$ m, $\beta_i = 90$ deg

Figure 7.13: Relative motion in Inertial frame subject to cylindrical keep-out zone

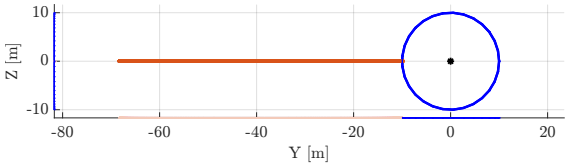

(a) Motion 1: $r_{i,0} = 14.142$ m, $\phi_{i,0} = 90$ deg, $d_i = 10$ m, $\alpha_i = 90$ deg, $B_i = 0$ m, $\beta_i = 0$ deg

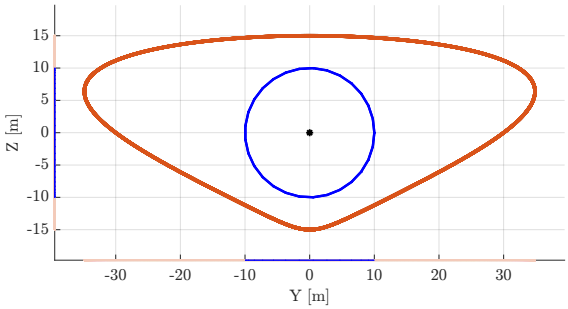

(b) Motion 2: $r_{i,0} = 15$ m, $\phi_{i,0} = 90$ deg, $d_i = 10$ m, $\alpha_i = 0$ deg, $B_i = 15$ m, $\beta_i = 90$ deg

Figure 7.14: Relative motion in Inertial frame subject to cylindrical keep-out zone, YZ-plane projection

7.6 Conclusions

The relative motion of two spacecraft is investigated as seen from a frame that is centered at the chief spacecraft and with axes that are aligned with an inertial frame. Such an inertial frame description is beneficial compared to the conventional rotating Hill frame when the relative motion is subject to inertially fixed constraints. Examples for such missions include inertial targets for distributed space telescopes and coronagraphs, spacecraft formations and servicing operations with

constraints imposed by the Sun (lighting conditions, eclipses, space plasma conditions, etc.), as well as rendezvous with a non-rotating target. The last example is relevant because the body frame of a non-rotating body remains aligned with the inertial frame, and body frames are frequently used for servicing and docking operations.

It is found that the inertial frame relative motion for a circular chief orbit is equivalent to the epitrochoid curve, in which a circle rolls without slip on a fixed circle, and the curve is generated by a point that is at a certain distance away from the center of the rolling circle. Thus, inertial frame relative orbit elements (IROEs) are defined that are based on the parameters of an epitrochoid curve and correspond to the invariants of relative motion in the inertial frame. This allows for an intuitive description of the inertial frame relative motion. For elliptic chief orbits, the inertial frame relative orbits are stretched and distorted compared to the epitrochoid curve for circular chief orbits, but similar IROEs are defined as well. An asymptotically stabilizing continuous feedback control law based on IROEs is derived using an alternative non-singular set of IROEs, showing asymptotic stability. Finally, the IROE description is applied to an on-orbit servicing example, illustrating the intuitive relative orbit design process with inertial frame relative orbit elements.

Chapter 8

Conclusions and future work

On-orbit servicing and active space debris removal are two key technologies to make the space environment safer by extending the life of old satellites or relocating retired satellites to avoid collisions. The electrostatic forces and torques due to charged spacecraft in close proximity may significantly impact the spacecraft relative motion during on-orbit servicing operations, but can also be utilized to reorbit or detumble space debris. This dissertation explores the coupled interactions between two charged spacecraft during servicing as well as debris removal operations in terms of electric potential sensing, spacecraft charging, and relative motion.

8.1 Contributions of this work

In Chapter 2, it is found that differential charging of a spacecraft significantly affects the inter-craft electrostatic forces and torques, including a possible change in polarity of some force and torque components. The electrostatic torque, which has a greater impact on servicing operations than the force, may even be enhanced due to differential charging. Consequently, the focus of Chapter 3 is to identify and sense differential charging of a nearby complex-shaped spacecraft using x-rays excited by an electron beam. The orientation of the complex-shaped target object determines the landing spot of the electron beam and consequently the component of which the potential is measured. Experiments show that it is possible to simultaneously measure multiple electric potentials of a differentially charged target object using theoretical x-ray models and the principle of superposition. Such simultaneous measurements are possible when the target object rotates,

for example, causing the beam to impact on different components during the sensing time frame. However, it is found that the estimation of more than two different potentials is rather inaccurate and that the presence of characteristic x-ray peaks introduces challenges to the estimation process. A theoretical study of the required sensing time shows that minimum sensing times in the order of a few seconds or even less than a second are possible with the beam currents used for the Electrostatic Tractor debris removal method. However, for on-orbit servicing, where very low beam currents may be required to avoid changing the potential of the target, sensing times in the order of 10s to 100s of seconds are required to produce a sufficient x-ray signal.

The existence of multiple equilibria of the target and servicer potential in a single-maxwellian plasma is discovered in Chapter 4 for a continuous electron beam. Whether or not multiple equilibria are possible depends on the magnitude of the electron beam current relative to the currents caused by the space environment, as well as the surface material properties of the target spacecraft. A switch from one type of equilibrium to another is possible due to a fast decrease in beam energy or increase in servicer potential; or due to current fluctuations caused by a rotating spacecraft, changes in beam current or the plasma environment. An open-loop charging control strategy is proposed that takes advantage of the stability of the most negative equilibrium potential of the target. The effect of the electron beam current on the target potential is also studied for sensing purposes, where it is found that very low beam currents may be required if it is not desired to change the potential of the target while sensing. Using a pulsed beam instead of a continuous beam is proposed in Chapter 5 to aid electric potential sensing and charging control processes. Pulsing between two electron beam energies creates sensing conditions that are beneficial for both the x-ray sensing method as well as another sensing method based on electrons. Finally, a pulsed beam may be used to improve the open-loop charging control strategy proposed for the continuous beam by providing a signal that can be used to confirm that the beam is actually hitting the target.

Finally, the relative motion is studied in Chapters 6 and 7. The effect of electric potential estimation errors and debris attitude on the Electrostatic tractor relative motion control for active debris removal is investigated in Chapter 6. It is found that the sensitivity to electric potential

estimation errors depends on the debris attitude. The control is most sensitive when protruding structures of the debris such as solar panels are pointing toward the servicer. Thus, it is recommended to tune the relative motion control feedback gains based on the worst case orientation of the debris. Because such an orientation increases the electrostatic force and consequently reduces the reorbit time, it is advantageous to maintain a fixed orientation of the debris while reorbiting using electrostatic torque actuation, as opposed to tugging a tumbling debris. Additionally, it is found that the debris orientation with respect to the Sun significantly affects the electric potential and electrostatic force due to the photoelectric current. In Chapter 7, inertial frame relative orbits are explored to satisfy constraints fixed in the inertial frame, such as avoiding plasma wakes in cislunar space during on-orbit servicing operations. It is found that the relative motion of two spacecraft for a circular chief orbit, described in inertial frame components, is equivalent to the motion of an epitrochoid. An intuitive relative motion description is developed for the inertial frame with relative orbit elements that are based on the parameters of the epitrochoid curve. Finally, an asymptotically stabilizing continuous feedback control law based on inertial frame relative orbit elements is derived and applied.

8.2 Directions for future work

As with most research, some assumptions had to be made at the current state of this work that should be relaxed in the future to allow for a more accurate investigation. Additionally, as often the case, answering some questions opened up many other questions, leading to several directions for future work.

While two key assumptions of prior work were relaxed in this dissertation by considering differential charging as well as non-spherical spacecraft objects for both charging and force modeling, several other assumptions were made for the charging model that should be reconsidered in future work. The perturbation of the plasma distribution due to a highly charged nearby spacecraft, the attraction of photoelectrons and secondary electrons to the servicer that were emitted from target, and the enhanced ion collection in the mesothermal case may all affect the equilibrium

potentials of the target and servicer, but are not considered in this work. Especially the attraction of photoelectrons and secondary electrons to the servicer is expected to have a significant effect.

Future work may look into the dynamic effects of the jump between equilibria on electric potential sensing and control methods, and how this affects the reorbit process with the Electrostatic Tractor. Multiple equilibria also exist in double-maxwellian plasma, motivating a potential study about the similarities between electron beam induced and plasma induced multiple equilibria. A focus of experiments may be the validation of the open-loop charging control strategy, multiple equilibria, as well as other pulsed beam control approaches.

A more detailed study is recommended to determine whether a tumbling or detumbled retired satellite is beneficial for the reorbit process with the Electrostatic Tractor. Maintaining a constant debris orientation requires advanced electrostatic torque actuation methods that allow for the attitude control of a nearby spacecraft. Such methods could be explored in greater detail for spacecraft with complex shapes and possibly for differentially charged targets. If the orientation of the debris with respect to the servicer remains constant while reorbiting, the inertial attitude and consequently the sun-facing area, the electric potential, and the electrostatic force do change. This should be considered for the Electrostatic Tractor charging control. Finally, a relative motion control strategy that adjusts the separation distance based on the debris orientation or the time-varying electrostatic force may also be considered to allow for a more constant reorbit rate.

Finally, the development and analysis of the inertial frame relative motion description in this work focused primarily on circular chief orbits. This should be extended in more detail to elliptic chief orbits, including the derivation of invariants of motion and the development of control laws. Additionally, impulsive control laws may be considered for inertial frame relative orbit formations. For a non-rotating target spacecraft, the relative motion as seen from the body frame of the target corresponds to the relative motion as seen from the inertial frame. A similar approach to the one in this work for inertial frame relative motion may be used to establish a description of the body frame relative motion for various body frame rotations.

Bibliography

[1] Kessler, D. J., and Cour-Palais, B. G., "Collision frequency of artificial satellites: The creation of a debris belt," Journal of Geophysical Research, Vol. 83, No. A6, 1978, p. 2637. https://doi.org/10.1029/JA083iA06p02637.

[2] Inter-Agency Space Debris Coordination Committee, "IADC Space Debris Mitigation Guidelines, Revision 4," Tech. rep., Inter-Agency Space Debris Coordination Committee, Vienna, Austria, 2025. URL https://www.unoosa.org/res/oosadoc/data/documents/2025/aac_105c_12025crp/aac_105c_12025crp_9_0_html/AC105_C1_2025_CRP09E.pdf.

[3] European Space Agency, "ESA's Annual Space Environment Report, Revision 9.0," Tech. rep., ESA Space Debris Office, Darmstadt, Germany, 2025. URL https://www.sdo.esoc.esa.int/environment_report/Space_Environment_Report_latest.pdf.

[4] Shan, M., Guo, J., and Gill, E., "Review and comparison of active space debris capturing and removal methods," Progress in Aerospace Sciences, Vol. 80, 2016, pp. 18–32. https://doi.org/10.1016/j.paerosci.2015.11.001.

[5] Mark, C. P., and Kamath, S., "Review of Active Space Debris Removal Methods," Space Policy, Vol. 47, 2019, pp. 194–206. https://doi.org/10.1016/j.spacepol.2018.12.005.

[6] Shan, M., Guo, J., and Gill, E., "Deployment dynamics of tethered-net for space debris removal," Acta Astronautica, Vol. 132, No. October 2016, 2017, pp. 293–302. https://doi.org/10.1016/j.actaastro.2017.01.001.

[7] Dudziak, R., Tuttle, S., and Barraclough, S., "Harpoon technology development for the active removal of space debris," Advances in Space Research, Vol. 56, No. 3, 2015, pp. 509–527. https://doi.org/10.1016/j.asr.2015.04.012.

[8] Nishida, S.-I., Kawamoto, S., Okawa, Y., Terui, F., and Kitamura, S., "Space debris removal system using a small satellite," Acta Astronautica, Vol. 65, No. 1-2, 2009, pp. 95–102. https://doi.org/10.1016/j.actaastro.2009.01.041.

[9] Bombardelli, C., and Pelaez, J., "Ion Beam Shepherd for Contactless Space Debris Removal," Journal of Guidance, Control, and Dynamics, Vol. 34, No. 3, 2011, pp. 916–920. https://doi.org/10.2514/1.51832.

[10] Cartmell, M., and McKenzie, D., "A review of space tether research," Progress in Aerospace Sciences, Vol. 44, No. 1, 2008, pp. 1–21. https://doi.org/https://doi.org/10.1016/j.paerosci.2007.08.002.

[11] Šilha, J., Pittet, J.-N., Hamara, M., and Schildknecht, T., "Apparent rotation properties of space debris extracted from photometric measurements," Advances in Space Research, Vol. 61, No. 3, 2018, pp. 844–861. https://doi.org/10.1016/j.asr.2017.10.048.

[12] Papushev, P., Karavaev, Y., and Mishina, M., "Investigations of the evolution of optical characteristics and dynamics of proper rotation of uncontrolled geostationary artificial satellites," Advances in Space Research, Vol. 43, No. 9, 2009, pp. 1416–1422. https://doi.org/10.1016/j.asr.2009.02.007.

[13] Nishida, S.-I., and Kawamoto, S., "Strategy for capturing of a tumbling space debris," Acta Astronautica, Vol. 68, No. 1-2, 2011, pp. 113–120. https://doi.org/10.1016/j.actaastro.2010.06.045.

[14] Li, W.-J., Cheng, D.-Y., Liu, X.-G., Wang, Y.-B., Shi, W.-H., Tang, Z.-X., Gao, F., Zeng, F.-M., Chai, H.-Y., Luo, W.-B., et al., "On-orbit service (OOS) of spacecraft: A review of engineering developments," Progress in Aerospace Sciences, Vol. 108, 2019, pp. 32–120.

[15] Hastings, D. E., and Joppin, C., "On-orbit upgrade and repair: The hubble space telescope example," Journal of spacecraft and rockets, Vol. 43, No. 3, 2006, pp. 614–625.

[16] Redd, N. T., "Bringing satellites back from the dead: Mission extension vehicles give defunct spacecraft a new lease on life-[News]," IEEE Spectrum, Vol. 57, No. 8, 2020, pp. 6–7.

[17] Shoemaker, M. A., Vavrina, M., Gaylor, D. E., Mcintosh, R., Volle, M., and Jacobsohn, J., "OSAM-1 decommissioning orbit design," AAS/AIAA Astrodynamics Specialis t Conference, 2020, pp. 1–15.

[18] Lai, S. T., Fundamentals of Spacecraft Charging, Princeton University Press, 2011. https://doi.org/10.2307/j.ctvcm4j2n.

[19] Olsen, R. C., "Record charging events from Applied Technology Satellite 6," Journal of Spacecraft and Rockets, Vol. 24, No. 4, 1987, pp. 362–366. https://doi.org/10.2514/3.25925.

[20] Minow, J. I., Space, M., Parker, L. N., Blackwell, W. C., and Engineering, J., "Extreme Space Weather Events and Charging Hazard Assessments in Lunar Environments," 37th COSPAR Scientific Assembly, Montreal, Canada, 2008, pp. 1–24.

[21] Garrett, H. B., and Whittlesey, A. C., Guide to Mitigating Spacecraft Charging Effects, John Wiley & Sons, Inc., Hoboken, NJ, USA, 2012. https://doi.org/10.1002/9781118241400.

[22] Katz, I., Davis, V., and Snyder, D., "Mechanism for spacecraft charging initiated destruction of solar arrays in GEO," 36th AIAA Aerospace Sciences Meeting and Exhibit, AIAA Paper 1998-1002, 1998, pp. 1–5. https://doi.org/10.2514/6.1998-1002.

[23] Brandhorst, H., and Rodiek, J., "Improving Space Utilization by Increasing Solar Array Reliability," AIAA SPACE 2007 Conference and Exposition, AIAA Paper 2007-6024, 2007, pp. 1–5. https://doi.org/10.2514/6.2007-6024.

[24] Newman, C. P., Davis, D. C., Whitley, R. J., Guinn, J. R., and Ryne, M. S., "Stationkeeping, orbit determination, and attitude control for spacecraft in near rectilinear halo orbits," Proceedings of the AAS/AIAA Astrodynamics Specialist Conference 2018, AAS Paper 18-388, 2018, pp. 1–20. URL https://ntrs.nasa.gov/citations/20180006800.

[25] Wilson, K., and Schaub, H., "Impact of Electrostatic Perturbations on Proximity Operations in High Earth Orbits," Journal of Spacecraft and Rockets, Vol. 58, No. 5, 2021, pp. 1293–1302. https://doi.org/10.2514/1.A35039.

[26] Hammerl, J., and Schaub, H., "Debris Attitude Effects on Electrostatic Tractor Relative Motion Control Performance," Proceedings of the AAS/AIAA Astrodynamics Specialist Conference, AAS Paper 21-548, 2021, pp. 1–13. URL http://hanspeterschaub.info/Papers/Hammerl2021a.pdf.

[27] Wilson, K., and Schaub, H., "Constrained guidance for spacecraft proximity operations under electrostatic perturbations," IEEE Aerospace Engineering Conference, Big Sky, MT, 2021, pp. 1–11.

[28] Murdoch, N., Izzo, D., Bombardelli, C., Carnelli, I., Hilgers, A., and Rodgers, D., "Electrostatic tractor for near earth object deflection," 59th International Astronautical Congress, Vol. 29, 2008, pp. 1–11.

[29] Schaub, H., and Moorer, D. F., "Geosynchronous Large Debris Reorbiter: Challenges and Prospects," The Journal of the Astronautical Sciences, Vol. 59, No. 1-2, 2012, pp. 161–176. https://doi.org/10.1007/s40295-013-0011-8.

[30] Bengtson, M., Wilson, K., Hughes, J., and Schaub, H., "Survey of the electrostatic tractor research for reorbiting passive GEO space objects," Astrodynamics, Vol. 2, No. 4, 2018, pp. 291–305. https://doi.org/10.1007/s42064-018-0030-0.

[31] Schaub, H., and Stevenson, D., "Prospects of Relative Attitude Control Using Coulomb Actuation," The Journal of the Astronautical Sciences, Vol. 60, No. 3-4, 2013, pp. 258–277. https://doi.org/10.1007/s40295-015-0048-y.

[32] Bennett, T., and Schaub, H., "Touchless Electrostatic Three-dimensional Detumbling of Large Axi-symmetric Debris," The Journal of the Astronautical Sciences, Vol. 62, No. 3, 2015, pp. 233–253. https://doi.org/10.1007/s40295-015-0075-8.

[33] Hammerl, J., and Schaub, H., "Effects of Electric Potential Uncertainty on Electrostatic Tractor Relative Motion Control Equilibria," Journal of Spacecraft and Rockets, Vol. 59, No. 2, 2022, pp. 552–562. https://doi.org/10.2514/1.A35165.

[34] Wilson, K., Romero-Calvo, Á., and Schaub, H., "Constrained Guidance for Spacecraft Proximity Operations Under Electrostatic Perturbations," Journal of Spacecraft and Rockets, 2022, pp. 1–13. https://doi.org/10.2514/1.A35162, in press.

[35] Bengtson, M., Hughes, J., and Schaub, H., "Prospects and Challenges for Touchless Sensing of Spacecraft Electrostatic Potential Using Electrons," IEEE Transactions on Plasma Science, Vol. 47, No. 8, 2019, pp. 3673–3681. https://doi.org/10.1109/TPS.2019.2912057.

[36] Wilson, K., and Schaub, H., "X-Ray Spectroscopy for Electrostatic Potential and Material Determination of Space Objects," IEEE Transactions on Plasma Science, Vol. 47, No. 8, 2019, pp. 3858–3866. https://doi.org/10.1109/TPS.2019.2910576.

[37] Mott-Smith, H. M., and Langmuir, I., "The Theory of Collectors in Gaseous Discharges," Phys. Rev., Vol. 28, 1926, pp. 727–763. https://doi.org/10.1103/PhysRev.28.727.

[38] Brace, L. H., "Langmuir probe measurements in the ionosphere," Geophysical Monograph-American Geophysical Union, Vol. 102, 1998, pp. 23–36. https://doi.org/10.1029/GM102p0023.

[39] Lai, S. T., and Miller, C., "Retarding potential analyzer: Principles, designs, and space applications," AIP Advances, Vol. 10, No. 9, 2020, p. 095324. https://doi.org/10.1063/5.0014266.

[40] Ferguson, D. C., Murray-Krezan, J., Barton, D. A., Dennison, J. R., and Gregory, S. A., "Feasibility of detecting spacecraft charging and arcing by remote sensing," Journal of Spacecraft and Rockets, Vol. 51, No. 6, 2014, pp. 1907–1913. https://doi.org/10.2514/1.A32958.

[41] Bennett, T. J., "On-Orbit 3-Dimensional Electrostatic Detumble for Generic Spacecraft Geometries," Doctoral thesis, University of Colorado Boulder, 2017. URL http://hanspeterschaub.info/Papers/grads/TrevorBennett.pdf.

[42] Engwerda, H. J. A., "Remote Sensing for Spatial Electrostatic Characterization using the Multi-Sphere Method," Master's thesis, Delft University of Technology, 2017. URL http://hanspeterschaub.info/Papers/grads/HeikoEngwerda.pdf.

[43] Fahleson, U., "Theory of electric field measurements conducted in the magnetosphere with electric probes," Space Science Reviews, Vol. 7, No. 2-3, 1967, pp. 238–262. https://doi.org/10.1007/BF00215600.

[44] Bengtson, M. T., Wilson, K. T., and Schaub, H., "Experimental Results of Electron Method for Remote Spacecraft Charge Sensing," Space Weather, Vol. 18, No. 3, 2020, pp. 1–12. https://doi.org/10.1029/2019SW002341.

[45] Wilson, K. T., Bengtson, M. T., and Schaub, H., "X-ray Spectroscopic Determination of Electrostatic Potential and Material Composition for Spacecraft: Experimental Results," Space Weather, Vol. 18, No. 4, 2020, pp. 1–10. https://doi.org/10.1029/2019SW002342.

[46] Wilson, K., Romero-Calvo, Á., Bengtson, M., Hammerl, J., Maxwell, J., and Schaub, H., "Development and characterization of the ECLIPS space environments simulation facility," Acta Astronautica, Vol. 194, No. July 2021, 2022, pp. 48–58. https://doi.org/10.1016/j.actaastro.2021.12.037.

[47] Wilson, K. T. H., "Remote Electrostatic Potential Determination for Spacecraft Relative Motion Control," Doctoral thesis, University of Colorado Boulder, 2021. URL http://hanspeterschaub.info/Papers/grads/KieranWilson.pdf.

[48] Wilson, K., Hammerl, J., and Schaub, H., "Using Plasma-Induced X-Ray Emission to Estimate Electrostatic Potentials on Nearby Space Objects," Journal of Spacecraft and Rockets, Vol. 59, No. 4, 2022, pp. 1402–1405. https://doi.org/10.2514/1.A35161.

[49] Bengtson, M. T., Wilson, K., and Schaub, H., "Broad-Spectrum Electron Gun for Laboratory Simulation of Orbital Environments," Proceedings of the AIAA SciTech 2021 Forum and Exposition, AIAA Paper 2021-1539, 2021, pp. 1–10. https://doi.org/10.2514/6.2021-1539.

[50] Mandell, M., Davis, V., Cooke, D., Wheelock, A., and Roth, C., "Nascap-2k Spacecraft Charging Code Overview," IEEE Transactions on Plasma Science, Vol. 34, No. 5, 2006, pp. 2084–2093. https://doi.org/10.1109/TPS.2006.881934.

[51] Lundgreen, P., and Dennison, J. R., "Strategies for Determining Electron Yield Material Parameters for Spacecraft Charge Modeling," Space Weather, Vol. 18, No. 4, 2020, pp. 1–13. https://doi.org/10.1029/2019SW002346.

[52] Hastings, D. E., "A review of plasma interactions with spacecraft in low Earth orbit," Journal of Geophysical Research: Space Physics, Vol. 100, No. A8, 1995, pp. 14457–14483. https://doi.org/https://doi.org/10.1029/94JA03358.

[53] Matéo-Vélez, J.-C., Theillaumas, B., Sévoz, M., Andersson, B., Nilsson, T., Sarrailh, P., Thiébault, B., Jeanty-Ruard, B., Rodgers, D., Balcon, N., and Payan, D., "Simulation and Analysis of Spacecraft Charging Using SPIS and NASCAP/GEO," IEEE Transactions on Plasma Science, Vol. 43, No. 9, 2015, pp. 2808–2816. https://doi.org/10.1109/TPS.2015.2447523.

[54] Parker, L. N., Minow, J., and Blackwell Jr., W., "Analysis of Lunar Surface Charging for a Candidate Spacecraft Using NASCAP-2K," 10th Spacecraft Charging Technology Conference, 2007, pp. 1–11.

[55] Schaub, H., and Sternovsky, Z., "Active space debris charging for contactless electrostatic disposal maneuvers," Advances in Space Research, Vol. 53, No. 1, 2014, pp. 110–118. https://doi.org/10.1016/j.asr.2013.10.003.

[56] Hogan, E. A., and Schaub, H., "Impacts of tug and debris sizes on electrostatic tractor charging performance," Advances in Space Research, Vol. 55, No. 2, 2015, pp. 630–638. https://doi.org/https://doi.org/10.1016/j.asr.2014.10.023.

[57] Hogan, E. A., and Schaub, H., "Impacts of Hot Space Plasma and Ion Beam Emission on Electrostatic Tractor Performance," IEEE Transactions on Plasma Science, Vol. 43, No. 9, 2015, pp. 3115–3129. https://doi.org/10.1109/TPS.2015.2451001.

[58] Hughes, J. A., and Schaub, H., "Electrostatic Tractor Analysis Using a Measured Flux Model," Journal of Spacecraft and Rockets, Vol. 57, No. 2, 2020, pp. 207–216. https://doi.org/10.2514/1.A34359.

[59] Romero-Calvo, A., Hammerl, J., and Schaub, H., "Touchless Potential Sensing of Differentially Charged Spacecraft Using Secondary Electrons," Journal of Spacecraft and Rockets, Vol. 59, No. 5, 2022, pp. 1623–1633. https://doi.org/10.2514/1.A35355.

[60] Stevenson, D., and Schaub, H., "Electrostatic spacecraft rate and attitude control—Experimental results and performance considerations," Acta Astronautica, Vol. 119, 2016, pp. 22–33. https://doi.org/10.1016/j.actaastro.2015.10.023.

[61] Aslanov, V., and Schaub, H., "Detumbling Attitude Control Analysis Considering an Electrostatic Pusher Configuration," Journal of Guidance, Control, and Dynamics, Vol. 42, No. 4, 2019, pp. 900–909. https://doi.org/10.2514/1.G003966.

[62] Casale, F., Schaub, H., and Douglas Biggs, J., "Lyapunov Optimal Touchless Electrostatic Detumbling of Space Debris in GEO Using a Surface Multisphere Model," Journal of Spacecraft and Rockets, Vol. 58, No. 3, 2021, pp. 764–778. https://doi.org/10.2514/1.A34787.

[63] Hogan, E., and Schaub, H., "Space Weather Influence on Relative Motion Control using the Touchless Electrostatic Tractor," Journal of Astronautical Sciences, Vol. 63, No. 3, 2016, pp. 237–262. https://doi.org/10.1007/s40295-016-0090-4.

[64] Hughes, J., and Schaub, H., "Prospects of using a pulsed electrostatic tractor with nominal geosynchronous conditions," IEEE Transactions on Plasma Science, Vol. 45, No. 8, 2017, pp. 1887–1897.

[65] Hogan, E. A., and Schaub, H., "Relative Motion Control For Two-Spacecraft Electrostatic Orbit Corrections," Journal of Guidance, Control, and Dynamics, Vol. 36, No. 1, 2013, pp. 240–249. https://doi.org/10.2514/1.56118, URL https://arc.aiaa.org/doi/10.2514/1.56118.

[66] Hughes, J., and Schaub, H., "Space Weather Influence on Electromagnetic Geosynchronous Debris Perturbations Using Statistical Fluxes," Space Weather, Vol. 16, No. 4, 2018, pp. 391–405. https://doi.org/https://doi.org/10.1002/2017SW001768.

[67] Wang, J., and Hastings, D., "Ionospheric plasma flow over large high-voltage space platforms. II: The formation and structure of plasma wake," Physics of Fluids B: Plasma Physics, Vol. 4, No. 6, 1992, pp. 1615–1629.

[68] Seubert, C. R., Stiles, L. A., and Schaub, H., "Effective Coulomb force modeling for spacecraft in Earth orbit plasmas," Advances in Space Research, Vol. 54, No. 2, 2014, pp. 209–220. https://doi.org/10.1016/j.asr.2014.04.005.

[69] Hastings, D. E., "A review of plasma interactions with spacecraft in low Earth orbit," Journal of Geophysical Research: Space Physics, Vol. 100, No. A8, 1995, pp. 14457–14483. https://doi.org/https://doi.org/10.1029/94JA03358.

[70] Ergun, R. E., Malaspina, D. M., Bale, S. D., McFadden, J. P., Larson, D. E., Mozer, F. S., Meyer-Vernet, N., Maksimovic, M., Kellogg, P. J., and Wygant, J. R., "Spacecraft charging and ion wake formation in the near-Sun environment," Physics of Plasmas, Vol. 17, No. 7, 2010, p. 072903. https://doi.org/10.1063/1.3457484.

[71] Sullivan, J., Grimberg, S., and D'Amico, S., "Comprehensive Survey and Assessment of Spacecraft Relative Motion Dynamics Models," Journal of Guidance, Control, and Dynamics, Vol. 40, No. 8, 2017, pp. 1837–1859. https://doi.org/10.2514/1.G002309.

[72] Alfriend, K., Vadali, S. R., Gurfil, P., How, J., and Breger, L., Spacecraft Formation Flying: Dynamics, control and navigation, Vol. 2, Butterworth-Heinemann, Burlington, MA, 2009.

[73] Tschauner, J., and Hempel, P., "Rendezvous zu einem in elliptischer Bahn umlaufenden Ziel," Astronautica Acta, Vol. 11, No. 2, 1965, pp. 104–109.

[74] Clohessy, W. H., and Wiltshire, R. S., "Terminal Guidance System for Satellite Rendezvous," Journal of the Aerospace Sciences, Vol. 27, No. 9, 1960, pp. 653–658. https://doi.org/10.2514/8.8704.

[75] Broucke, R. A., "Solution of the Elliptic Rendezvous Problem with the Time as Independent Variable," Journal of Guidance, Control, and Dynamics, Vol. 26, No. 4, 2003, pp. 615–621. https://doi.org/10.2514/2.5089.

[76] Newman, B. A., Sinclair, A. J., Lovell, A., and Perez, A., "Comparison of Nonlinear Analytical Solutions for Relative Orbital Motion," AIAA/AAS Astrodynamics Specialist Conference, 2014, pp. 1–29. https://doi.org/10.2514/6.2014-4163.

[77] Bennett, T., and Schaub, H., "Continuous-Time Modeling and Control Using Nonsingular Linearized Relative-Orbit Elements," Journal of Guidance, Control, and Dynamics, Vol. 39, No. 12, 2016, pp. 2605–2614. https://doi.org/10.2514/1.G000366.

[78] Schaub, H., Vadali, S. R., Junkins, J. L., and Alfriend, K. T., "Spacecraft formation flying control using mean orbit elements," The Journal of the Astronautical Sciences, Vol. 48, 2000, pp. 69–87. https://doi.org/10.1007/BF03546219.

[79] Schaub, H., and Alfriend, K. T., "J_2 invariant relative orbits for spacecraft formations," Celestial Mechanics and Dynamical Astronomy, Vol. 79, 2001, pp. 77–95.

[80] Schaub, H., "Relative Orbit Geometry Through Classical Orbit Element Differences," Journal of Guidance, Control, and Dynamics, Vol. 27, No. 5, 2004, pp. 839–848. https://doi.org/10.2514/1.12595.

[81] Koenig, A. W., Guffanti, T., and D'Amico, S., "New State Transition Matrices for Spacecraft Relative Motion in Perturbed Orbits," Journal of Guidance, Control, and Dynamics, Vol. 40, No. 7, 2017, pp. 1749–1768. https://doi.org/10.2514/1.G002409.

[82] Gim, D.-W., and Alfriend, K. T., "Satellite relative motion using differential equinoctial elements," Celestial Mechanics and Dynamical Astronomy, Vol. 92, 2005, pp. 295–336.

[83] Alfriend, K., "Nonlinear Considerations In Satellite Formation Flying," AIAA/AAS Astrodynamics Specialist Conference and Exhibit, 2002, pp. 1–8. https://doi.org/10.2514/6.2002-4741.

[84] Montenbruck, O., Kirschner, M., D'Amico, S., and Bettadpur, S., "E/I-vector separation for safe switching of the GRACE formation," Aerospace Science and Technology, Vol. 10, No. 7, 2006, pp. 628–635. https://doi.org/10.1016/j.ast.2006.04.001.

[85] D'Amico, S., and Montenbruck, O., "Proximity Operations of Formation-Flying Spacecraft Using an Eccentricity/Inclination Vector Separation," Journal of Guidance, Control, and Dynamics, Vol. 29, No. 3, 2006, pp. 554–563. https://doi.org/10.2514/1.15114.

[86] Albert, S. W., and Schaub, H., "Relative Motion in the Velocity Frame for Atmospheric Entry Trajectories," Journal of Spacecraft and Rockets, Vol. 60, No. 5, 2023, pp. 1614–1624. https://doi.org/10.2514/1.A35753.

[87] Roger, A. B., and McInnes, C. R., "Safety Constrained Free-Flyer Path Planning at the International Space Station," Journal of Guidance, Control, and Dynamics, Vol. 23, No. 6, 2000, pp. 971–979. https://doi.org/10.2514/2.4656.

[88] Dong, H., Hu, Q., and Akella, M. R., "Safety Control for Spacecraft Autonomous Rendezvous and Docking Under Motion Constraints," Journal of Guidance, Control, and Dynamics, Vol. 40, No. 7, 2017, pp. 1680–1692. https://doi.org/10.2514/1.G002322.

[89] Naasz, B., "Safety ellipse motion with coarse sun angle optimization," 595 Flight Mechanics Symposium, 2005, pp. 1–13.

[90] Yao, Y., Xie, R., and He, F., "Flyaround Orbit Design for Autonomous Rendezvous Based on Relative Orbit Elements," Journal of Guidance, Control, and Dynamics, Vol. 33, No. 5, 2010, pp. 1687–1692. https://doi.org/10.2514/1.48494.

[91] Harrington, R. F., Field Computation by Moment Methods, Wiley-IEEE Press, 1993.

[92] Mehta, P. D., and Chakrabarty, S. B., "Capacitance of Dielectric-Coated Metallic Bodies Isolated in Free Space," Electromagnetics, Vol. 31, No. 4, 2011, pp. 294–314. https://doi.org/10.1080/02726343.2011.568923.

[93] Alad, R. H., and Chakrabarty, S., "Electrostatic Analysis of an Artificial Orbiting Satellite for Absolute Charging," IEEE Transactions on Plasma Science, Vol. 43, No. 9, 2015, pp. 2887–2893. https://doi.org/10.1109/TPS.2015.2454054.

[94] Stevenson, D., and Schaub, H., "Multi-Sphere Method for modeling spacecraft electrostatic forces and torques," Advances in Space Research, Vol. 51, No. 1, 2013, pp. 10–20. https://doi.org/10.1016/j.asr.2012.08.014.

[95] Ingram, G., Hughes, J., Bennett, T., Reilly, C., and Schaub, H., "Volume multi-sphere-model development using electric field matching," The Journal of the Astronautical Sciences, Vol. 65, 2018, pp. 377–399.

[96] Hughes, J. A., and Schaub, H., "Heterogeneous Surface Multisphere Models Using Method of Moments Foundations," Journal of Spacecraft and Rockets, Vol. 56, No. 4, 2019, pp. 1259–1266. https://doi.org/10.2514/1.A34434.

[97] Hammerl, J., and Schaub, H., "Coupled Spacecraft Charging Due to Continuous Electron Beam Emission and Impact," Journal of Spacecraft and Rockets, Vol. 61, No. 5, 2024, pp. 1258–1271. https://doi.org/10.2514/1.A36010.

[98] Hammerl, J., and Schaub, H., "Reduced Order Spacecraft Charging Models for Electrostatic Proximity Operations," IEEE Transactions on Plasma Science, Vol. 52, No. 11, 2024, pp. 5402–5413. https://doi.org/10.1109/TPS.2024.3503356.

[99] Davis, V. A., and Mandell, M. J., "NASCAP-2K Version 4.3 Scientific Documentation," Tech. rep., Air Force Research Laboratory, 2016.

[100] Hippler, R., Pfau, S., Schmidt, M., and Schoenbach, K. H., Low Temperature Plasma Physics: Fundamental Aspects and Applications, 1st ed., Wiley, 2001.

[101] Jahn, J. M., Goldstein, J., Reeves, G. D., Fernandes, P. A., Skoug, R. M., Larsen, B. A., and Spence, H. E., "The Warm Plasma Composition in the Inner Magnetosphere During 2012–2015," Journal of Geophysical Research: Space Physics, Vol. 122, No. 11, 2017, pp. 11,018–11,043. https://doi.org/10.1002/2017JA024183.

[102] Pisacane, V. L., The Space Environment and its Effects on Space Systems, American Institute of Aeronautics and Astronautics, 2008. https://doi.org/10.2514/4.862533.

[103] Draine, B. T., and Salpeter, E. E., "On the physics of dust grains in hot gas," The Astrophysical Journal, Vol. 231, 1979, pp. 77–94. https://doi.org/10.1086/157165.

[104] Sternovsky, Z., Chamberlin, P., Horanyi, M., Robertson, S., and Wang, X., "Variability of the lunar photoelectron sheath and dust mobility due to solar activity," Journal of Geophysical Research: Space Physics, Vol. 113, No. 10, 2008, pp. 18–21. https://doi.org/10.1029/2008JA013487.

[105] Romero-Calvo, Á., Cano-Gómez, G., and Schaub, H., "Simulation and Uncertainty Quantification of Electron Beams in Active Spacecraft Charging Scenarios," Journal of Spacecraft and Rockets, Vol. 59, No. 3, 2022, pp. 739–750. https://doi.org/10.2514/1.A35190.

[106] Jasper, L. E. Z., and Schaub, H., "Effective Sphere Modeling for Electrostatic Forces on Three-Dimensional Spacecraft Shapes," AAS/AIAA Spaceflight Mechanics Meeting, Girdwood, Alaska, 2011, pp. 1–19.

[107] Maxwell, J., Wilson, K., Hughes, J., and Schaub, H., "Multisphere Method for Flexible Conducting Space Objects: Modeling and Experiments," Journal of Spacecraft and Rockets, Vol. 57, No. 2, 2020, pp. 225–234. https://doi.org/10.2514/1.A34560.

[108] Seubert, C. R., Stiles, L. A., and Schaub, H., "Effective Coulomb force modeling for spacecraft in Earth orbit plasmas," Advances in Space Research, Vol. 54, No. 2, 2014, pp. 209–220. https://doi.org/https://doi.org/10.1016/j.asr.2014.04.005.

[109] Roberts, B. C., "SLS-SPEC-159: Cross-Program Design Specification for Natural Environments (DSNE)," Tech. rep., National Aeronautics and Space Administration, Marshall Space Flight Center, 2019. URL https://ntrs.nasa.gov/citations/20200000867.

[110] Halekas, J. S., Bale, S. D., Mitchell, D. L., and Lin, R. P., "Electrons and magnetic fields in the lunar plasma wake," Journal of Geophysical Research: Space Physics, Vol. 110, No. A7, 2005. https://doi.org/10.1029/2004JA010991.

[111] Ness, N. F., "Interaction of the Solar Wind with the Moon," Solar-Terrestrial Physics/1970: Part II, Springer, Dordrecht, 1972, pp. 159–205. https://doi.org/10.1007/978-94-009-3693-5_21.

[112] Schubert, G., and Lichtenstein, B. R., "Observations of Moon-plasma interactions by orbital and surface experiments," Reviews of Geophysics, Vol. 12, No. 4, 1974, p. 592. https://doi.org/10.1029/RG012i004p00592.

[113] Prokopenko, S., and Laframboise, J., "High-voltage differential charging of geostationary spacecraft," Journal of Geophysical Research: Space Physics, Vol. 85, No. A8, 1980, pp. 4125–4131. https://doi.org/https://doi.org/10.1029/JA085iA08p04125.

[114] Lai, S., and Tautz, M., "Aspects of Spacecraft Charging in Sunlight," IEEE Transactions on Plasma Science, Vol. 34, No. 5, 2006, pp. 2053–2061. https://doi.org/10.1109/TPS.2006.883362.

[115] Hammerl, J., López, A., Romero-Calvo, A., and Schaub, H., "Touchless Potential Sensing of Differentially Charged Spacecraft Using X-Rays," Journal of Spacecraft and Rockets, Vol. 60, No. 2, 2023, pp. 648–658. https://doi.org/10.2514/1.A35492.

[116] Reimer, L., Scanning Electron Microscopy, 2nd ed., Springer Series in Optical Sciences, Springer, Berlin, Heidelberg, 1998. https://doi.org/10.1007/978-3-540-38967-5.

[117] Duane, W., and Hunt, F. L., "On X-Ray Wave-Lengths," Phys. Rev., Vol. 6, No. 2, 1915, pp. 166–172. https://doi.org/10.1103/PhysRev.6.166.

[118] Berger, M. J., and Seltzer, S. M., "Stopping powers and ranges of electrons and positrons," Tech. rep., National Bureau of Standards, Washington DC, 1982. URL https://ui.adsabs.harvard.edu/abs/1982spre.reptR....B.

[119] Berger, M., Coursey, J., Zucker, M., and Chang, J., "Stopping-Power & Range Tables for Electrons, Protons, and Helium Ions," , 2017. URL https://dx.doi.org/10.18434/T4NC7P.

[120] McCall, G. H., "Calculation of X-ray bremsstrahlung and characteristic line emission produced by a Maxwellian electron distribution," Journal of Physics D: Applied Physics, Vol. 15, No. 5, 1982, pp. 823–831. https://doi.org/10.1088/0022-3727/15/5/012.

[121] Trincavelli, J., and Castellano, G., "The prediction of thick target electron bremsstrahlung spectra in the 0.25–50 keV energy range," Spectrochimica Acta Part B: Atomic Spectroscopy, Vol. 63, No. 1, 2008, pp. 1–8. https://doi.org/10.1016/j.sab.2007.11.009.

[122] Castellano, G., Osán, J., and Trincavelli, J., "Analytical model for the bremsstrahlung spectrum in the 0.25-20 keV photon energy range," Spectrochimica Acta - Part B Atomic Spectroscopy, Vol. 59, No. 3, 2004, pp. 313–319. https://doi.org/10.1016/j.sab.2003.11.008.

[123] An, Z., Tian, L., Zhu, J., and Liu, M., "Bremsstrahlung spectrum data for thick Al, Ti, Zr, Mo, and W targets by keV electron impact," Data in Brief, Vol. 17, 2018, pp. 744–746. https://doi.org/10.1016/j.dib.2018.01.111.

[124] Kissel, L., Quarles, C., and Pratt, R., "Shape functions for atomic-field bremsstrahlung from electrons of kinetic energy 1–500 keV on selected neutral atoms $1 \leq Z \leq 92$," Atomic Data and Nuclear Data Tables, Vol. 28, No. 3, 1983, pp. 381–460. https://doi.org/10.1016/0092-640X(83)90001-3.

[125] Chervenak, J. G., and Liuzzi, A., "Experimental thick-target bremsstrahlung spectra from electrons in the range 10 to 30 keV," Phys. Rev. A, Vol. 12, 1975, pp. 26–33. https://doi.org/10.1103/PhysRevA.12.26.

[126] Gonzales, D., Cavness, B., and Williams, S., "Angular distribution of thick-target bremsstrahlung produced by electrons with initial energies ranging from 10 to 20 keV incident on Ag," Phys. Rev. A, Vol. 84, 2011, pp. 1–5. https://doi.org/10.1103/PhysRevA.84.052726.

[127] Romero-Calvo, A., Champion, K., and Schaub, H., "Enabling Ultraviolet Lasers for Touchless Spacecraft Potential Sensing," IEEE Transactions on Plasma Science, Vol. 51, No. 9, 2023, pp. 2468–2481. https://doi.org/10.1109/TPS.2023.3264914.

[128] Maxwell, J. H., "Development of Electrostatic Actuation Techniques for Close-Proximity Formation Flying in Low Earth Orbit Plasma Wakes," Doctoral thesis, University of Colorado Boulder, 2020.

[129] Champion, K., and Schaub, H., "Electrostatic Lenses for Laboratory Spacecraft Wake Generation," IEEE Transactions on Plasma Science, Vol. 53, No. 4, 2025, pp. 649–660. https://doi.org/10.1109/TPS.2025.3547749.

[130] Walker, J., and Schaub, H., "Development of Experimental Methods for Active Charge Control using Remote Sensing Methods," Spacecraft Charging and Technology Conference, Avignon, France, 2024, pp. 1–8.

[131] Lamoureux, M., and Charles, P., "General deconvolution of thin-target and thick-target Bremsstrahlung spectra to determine electron energy distributions," Radiation Physics and Chemistry, Vol. 75, No. 10, 2006, pp. 1220–1231. https://doi.org/10.1016/j.radphyschem.2006.06.006.

[132] Wilson, K., Bengtson, M., and Schaub, H., "Remote Electrostatic Potential Sensing for Proximity Operations: Comparison and Fusion of Methods," Journal of Spacecraft and Rockets, Vol. 59, No. 5, 2022, pp. 1425–1436. https://doi.org/10.2514/1.A35071.

[133] Deslattes, R., Kessler Jr., E., Indelicato, P., de Billy, L., Lindroth, E., Anton, J., Coursey, J., Schwab, D., Chang, C., Sukumar, R., Olsen, K., and Dragoset, R., "X-ray Transition Energies," , 2005. URL https://dx.doi.org/10.18434/T4859Z.

[134] Denton, M. H., Thomsen, M. F., Korth, H., Lynch, S., Zhang, J. C., and Liemohn, M. W., "Bulk plasma properties at geosynchronous orbit," Journal of Geophysical Research: Space Physics, Vol. 110, No. A7, 2005. https://doi.org/https://doi.org/10.1029/2004JA010861.

[135] Ozkul, A., Lopatin, A., Shipp, A., Pitchford, D., Mazur, J., Roeder, J., Koons, H., Bogorad, A., and Herschitz, R., "Initial correlation results of charge sensor data from six INTELSAT VIII class satellites with other space and ground based measurements," Spacecraft Charging Technology Conference, Vol. 476, European Space Agency, 2001, pp. 293–298.

[136] Schaub, H., and Junkins, J. L., Analytical Mechanics of Space Systems, 4th ed., AIAA Education Series, Reston, VA, 2018. https://doi.org/10.2514/4.105210.

[137] Dettleff, G., "Plume flow and plume impingement in space technology," Progress in Aerospace Sciences, Vol. 28, No. 1, 1991, pp. 1–71. https://doi.org/10.1016/0376-0421(91)90008-R.

[138] Teil, T., and Schaub, H., "Force and torque disturbance modeling due to general thruster plume impingements," International Astronautical Congress, Vol. 10, Adelaide, Australia, 2017, pp. 6797–6808.

[139] Schaub, H., and Jasper, L. E., "Orbit boosting maneuvers for two-craft coulomb formations," Journal of Guidance, Control, and Dynamics, Vol. 36, No. 1, 2013, pp. 74–82. https://doi.org/10.2514/1.57479.

[140] Kenneally, P. W., Piggott, S., and Schaub, H., "Basilisk: A flexible, scalable and modular astrodynamics simulation framework," Journal of Aerospace Information Systems, Vol. 17, No. 9, 2020, pp. 496–507. https://doi.org/10.2514/1.I010762.

[141] Bennett, T., and Schaub, H., "Contactless electrostatic detumbling of axi-symmetric GEO objects with nominal pushing or pulling," Advances in Space Research, Vol. 62, No. 11, 2018, pp. 2977–2987. https://doi.org/10.1016/j.asr.2018.07.021.

[142] Champion, K., and Schaub, H., "Cislunar Touchless Potential Sensing Through Barriers," Applied Space Environments Conference, Kauai, Hawaii, 2025, pp. 1–24.

[143] Koenig, A. W., D'Amico, S., Macintosh, B., and Titus, C. J., "Optimal Formation Design of a Miniaturized Distributed Occulter/Telescope in Earth Orbit," 2015 AAS/AIAA Astrodynamics Specialist Conference, 2015, pp. 1–29.

[144] Kolmas, J., Banazadeh, P., Koenig, A. W., Macintosh, B., and D'Amico, S., "System design of a miniaturized distributed occulter/telescope for direct imaging of star vicinity," 2016 IEEE Aerospace Conference, 2016, pp. 1–11. https://doi.org/10.1109/AERO.2016.7500783.

[145] Koenig, A., D'Amico, S., and Lightsey, E. G., "Formation flying orbit and control concept for the VISORS mission," AIAA Scitech 2021 Forum, 2021, pp. 1–22.

[146] Cash, W., Oakley, P., Turnbull, M., Glassman, T., Lo, A., Polidan, R., Kilston, S., and Noecker, C., "The New Worlds Observer: scientific and technical advantages of external occulters," Space Telescopes and Instrumentation 2008: Optical, Infrared, and Millimeter, Vol. 7010, edited by J. M. O. Jr., M. W. M. de Graauw, and H. A. MacEwen, International Society for Optics and Photonics, SPIE, 2008, p. 70101Q. https://doi.org/10.1117/12.789717.

[147] Glassman, T., Lo, A. S., Arenberg, J., Cash, W., and Noecker, C., "Starshade scaling relations," Techniques and Instrumentation for Detection of Exoplanets IV, Vol. 7440, edited by S. B. Shaklan, International Society for Optics and Photonics, SPIE, 2009, p. 744013. https://doi.org/10.1117/12.825033.

[148] Aung, M., Ahmed, A., Wette, M., Scharf, D., Tien, J., Purcell, G., Regehr, M., and Landin, B., "An overview of formation flying technology development for the Terrestrial Planet Finder mission," 2004 IEEE Aerospace Conference Proceedings (IEEE Cat. No.04TH8720), Vol. 4, 2004, pp. 2667–2679 Vol.4. https://doi.org/10.1109/AERO.2004.1368062.

[149] Quanz, S. P., Ottiger, M., Fontanet, E., Kammerer, J., Menti, F., Dannert, F., Gheorghe, A., Absil, O., Airapetian, V. S., Alei, E., Allart, R., Angerhausen, D., Blumenthal, S., Buchhave, L. A., Cabrera, J., Carrión-González, Ó., Chauvin, G., Danchi, W. C., Dandumont, C., Defrére, D., Dorn, C., Ehrenreich, D., Ertel, S., Fridlund, M., García Muñoz, A., Gascón, C., Girard, J. H., Glauser, A., Grenfell, J. L., Guidi, G., Hagelberg, J., Helled, R., Ireland, M. J., Janson, M., Kopparapu, R. K., Korth, J., Kozakis, T., Kraus, S., Léger, A., Leedjärv, L., Lichtenberg, T., Lillo-Box, J., Linz, H., Liseau, R., Loicq, J., Mahendra, V., Malbet, F., Mathew, J., Mennesson, B., Meyer, M. R., Mishra, L., Molaverdikhani, K., Noack, L., Oza, A. V., Pallé, E., Parviainen, H., Quirrenbach, A., Rauer, H., Ribas, I., Rice, M., Romagnolo, A., Rugheimer, S., Schwieterman, E. W., Serabyn, E., Sharma, S., Stassun, K. G., Szulágyi, J., Wang, H. S., Wunderlich, F., Wyatt, M. C., and the LIFE Collaboration, "Large Interferometer For Exoplanets (LIFE) - I. Improved exoplanet detection yield estimates for a large mid-infrared space-interferometer mission," Astronomy & Astrophysics, Vol. 664, 2022, p. A21. https://doi.org/10.1051/0004-6361/202140366.

[150] Scheeres, D., and Vinh, N., "Dynamics and control of relative motion in an unstable orbit," Astrodynamics Specialist Conference, 2000, p. 4135.

[151] Bucci, L., Colagrossi, A., and Lavagna, M., "Rendezvous in lunar near rectilinear halo orbits," Advances in Astronautics Science and Technology, Vol. 1, 2018, pp. 39–43.

[152] Franzini, G., and Innocenti, M., "Relative Motion Dynamics in the Restricted Three-Body Problem," Journal of Spacecraft and Rockets, Vol. 56, No. 5, 2019, pp. 1322–1337. https://doi.org/10.2514/1.A34390.

[153] Khoury, F., and Howell, K. C., "Orbital Rendezvous and Spacecraft Loitering in the Earth-moon System," AAS/AIAA Astrodynamics Specialist Conference, Lake Tahoe, California, USA, 2020, pp. 1–20.

[154] Llorente, J., Agenjo, A., Carrascosa, C., de Negueruela, C., Mestreau-Garreau, A., Cropp, A., and Santovincenzo, A., "PROBA-3: Precise formation flying demonstration mission," Acta Astronautica, Vol. 82, No. 1, 2013, pp. 38–46. https://doi.org/https://doi.org/10.1016/j.actaastro.2012.05.029, 6th International Workshop on Satellite Constellation and Formation Flying.

[155] Hill, G. W., "Researches in the Lunar Theory," American Journal of Mathematics, Vol. 1, No. 1, 1878, pp. 5–26. https://doi.org/10.2307/2369430.

[156] Lovell, T. A., and Tragesser, S., "Guidance for Relative Motion of Low Earth Orbit Spacecraft Based on Relative Orbit Elements," AIAA/AAS Astrodynamics Specialist Conference and Exhibit, 2004, p. 1. https://doi.org/10.2514/6.2004-4988.

Appendix A

Mappings between relative orbit element sets

A.1 Cartesian Hill state to linearized relative orbit elements

The inverse mapping between the cartesian state in the Hill frame $\boldsymbol{s} = [x, y, z, \dot{x}, \dot{y}, \dot{z}]^T$ and the linearized relative orbit elements (LROEs) $\delta\boldsymbol{oe}_{CW} = [A_0, \alpha, x_{\text{off}}, y_{\text{off}}, B_0, \beta]^T$ used in Eq. (7.10) is obtained by solving Eq. (7.10) and Eq. (7.11) for the LROEs and is equal to [77]

$$A_0 = \frac{\sqrt{9n^2x^2 + \dot{x}^2 + 12nx\dot{y} + 4\dot{y}^2}}{n} \tag{A.1a}$$

$$\alpha = \arctan\left(\frac{-\dot{x}}{-3nx - 2\dot{y}}\right) - nt \tag{A.1b}$$

$$x_{\text{off}} = 4x + 2\frac{\dot{y}}{n} \tag{A.1c}$$

$$y_{\text{off}} = -2\frac{\dot{x}}{n} + y + (6nx + 3\dot{y})t \tag{A.1d}$$

$$B_0 = \frac{\sqrt{n^2z^2 + \dot{z}^2}}{n} \tag{A.1e}$$

$$\beta = \arctan\left(\frac{-\dot{z}}{zn}\right) - nt \tag{A.1f}$$

A.2 Inertial frame relative orbit elements to linearized relative orbit elements

The inverse mapping between the inertial frame relative orbit elements (IROEs) $\delta\boldsymbol{oe}_i = [r_i, \phi_i, d_i, \alpha_i, B_i, \beta_i]^T$ used in Eq. (7.24) and the linearized relative orbit elements (LROEs) $\delta\boldsymbol{oe}_{CW} = [A_0, \alpha, x_{\text{off}}, y_{\text{off}}, B_0, \beta]^T$ used in Eq. (7.10) is obtained by solving the relations in Eq. (7.24) for the

LROEs. Four of those relations are trivially solved:

$$A_0 = 2d_i \tag{A.2}$$

$$\alpha = -\alpha_i \tag{A.3}$$

$$B_0 = B_i \tag{A.4}$$

$$\beta = -\beta \tag{A.5}$$

Using the relation for ϕ_i in Eq. (7.24)

$$\phi_i = \arctan\left(\frac{y_{\text{off}} - \frac{3}{2}ntx_{\text{off}}}{-x_{\text{off}}}\right) \tag{A.6}$$

and substituting into the relation for r_i in Eq. (7.24)

$$r_i = \frac{1}{2}\sqrt{\left(y_{\text{off}} - \frac{3}{2}ntx_{\text{off}}\right)^2 + x_{\text{off}}^2} \tag{A.7}$$

gives

$$\begin{aligned}(2r_i)^2 &= \left(y_{\text{off}} - \frac{3}{2}ntx_{\text{off}}\right)^2 + x_{\text{off}}^2 \\ (2r_i)^2 &= x_{\text{off}}^2 \tan^2\phi_i + x_{\text{off}}^2 = x_{\text{off}}^2(\tan^2\phi_i + 1) \\ (2r_i)^2 &= \left(\frac{x_{\text{off}}}{\cos\phi_i}\right)^2\end{aligned} \tag{A.8}$$

Solving for x_{off}, one obtains

$$x_{\text{off}} = \pm 2r_i \cos\phi_i \tag{A.9}$$

Looking at Eq. (A.6), one finds that if $x_{\text{off}} > 0$ then $\frac{\pi}{2} < \phi_i < \frac{3\pi}{2}$ and consequently $\cos\phi_i < 0$. Thus, because $r_i > 0$, the minus sign in the above equation applies, leading to

$$x_{\text{off}} = -2r_i \cos\phi_i \tag{A.10}$$

In a similar fashion, using Eqs. (A.7) and (A.10) give

$$y_{\text{off}} = 2r_i(\pm\sin\phi_i - \frac{3}{2}nt\cos\phi_i) \tag{A.11}$$

Looking at Eq. (A.6), one finds that if $y_{\text{off}} - \frac{3}{2}ntx_{\text{off}} > 0$ then $0 < \phi_i < \pi$ and consequently $\sin\phi_i > 0$. Thus, because $r_i > 0$, the plus sign in the above equation applies, leading to

$$y_{\text{off}} = 2r_i(\sin\phi_i - \frac{3}{2}nt\cos\phi_i) \tag{A.12}$$

This yields the mapping from IROEs to LROEs:

$$A_0 = 2d_i \tag{A.13a}$$

$$\alpha = -\alpha_i \tag{A.13b}$$

$$x_{\text{off}} = -2r_i\cos\phi_i \tag{A.13c}$$

$$y_{\text{off}} = 2r_i\left(\sin\phi_i - \frac{3}{2}nt\cos\phi_i\right) \tag{A.13d}$$

$$B_0 = B_i \tag{A.13e}$$

$$\beta = -\beta \tag{A.13f}$$

A.3 Inertial frame relative orbit elements to differential orbit elements

The inverse mapping between the inertial frame relative orbit elements (IROEs) $\delta\boldsymbol{oe}_i = [r_i, \phi_i, d_i, \alpha_i, B_i, \beta_i]^T$ used in Eq. (7.24) and the differential orbit elements (DOEs) $\delta\boldsymbol{oe} = [\delta a, \delta e, \delta i, \delta\Omega, \delta\omega, \delta M]^T$ used in Eq. (7.16) is obtained by solving the relations in Eq. (7.24) for the DOEs. Using a similar approach to the one in Appendix A.2 and the relation $\eta = \sqrt{1-e^2}$ yields the mapping from IROEs to DOEs:

$$\delta a = -2r_i\cos\phi_i \tag{A.14a}$$

$$\delta e = -2\frac{d_i}{a}\eta^2\cos\alpha_i \tag{A.14b}$$

$$\delta i = \frac{B_i}{a}\sin\beta_i \tag{A.14c}$$

$$\delta\Omega = -\frac{B_i}{a}\frac{\cos\beta_i}{\sin i} \tag{A.14d}$$

$$\delta\omega = 2\frac{r_i}{a}\sin\phi_i - 2\frac{d_i}{ae}\sin\alpha_i + \frac{B_i}{a}\frac{\cos\beta_i}{\tan i} \tag{A.14e}$$

$$\delta M = 2\frac{d_i}{ae}\eta^3\sin\alpha_i \tag{A.14f}$$

A.4 Cartesian perifocal state to inertial frame relative orbit elements

The inverse mapping between the cartesian state in the perifocal frame $\boldsymbol{s}_p = [X_p, Y_p, Z_p, \dot{X}_p, \dot{Y}_p, \dot{Z}_p]^T$ and the time-invariant inertial frame relative orbit elements (IROEs) $\delta\boldsymbol{\alpha e}_{i,0} = [r_{i,0}, \phi_{i,0}, d_i, \alpha_i, B_i, \beta_i]^T$ used in Eq. (7.37) is obtained by solving Eq. (7.37) and Eq. (7.38) for the time-invariant IROEs and is equal to

$$r_{i,0} = \frac{1}{2n}\sqrt{\begin{aligned}&\Big((X_p n - 2\dot{Y}_p)\sin(nt) - (Y_p n + 2\dot{X}_p)\cos(nt)\\&\quad - 3nt\big((\dot{X}_p - Y_p n)\sin(nt) - (X_p n + \dot{Y}_p)\cos(nt)\big)\Big)^2\\&+ \Big(2\big((\dot{X}_p - Y_p n)\sin(nt) - (X_p n + \dot{Y}_p)\cos(nt)\big)\Big)^2\end{aligned}} \tag{A.15a}$$

$$\phi_{i,0} = \arctan\left(\frac{(X_p n - 2\dot{Y}_p)\sin(nt) - (Y_p n + 2\dot{X}_p)\cos(nt)}{2\big((\dot{X}_p - Y_p n)\sin(nt) - (X_p n + \dot{Y}_p)\cos(nt)\big)} - \frac{3}{2}nt\right) \tag{A.15b}$$

$$d_i = \frac{1}{2n}\sqrt{\begin{aligned}&\Big((X_p n - \dot{Y}_p)\sin(nt) - (Y_p n + \dot{X}_p)\cos(nt)\Big)^2\\&+ \Big((2\dot{X}_p - Y_p n)\sin(nt) - (X_p n + 2\dot{Y}_p)\cos(nt)\Big)^2\end{aligned}} \tag{A.15c}$$

$$\alpha_i = nt - \arctan\left(\frac{(X_p n - \dot{Y}_p)\sin(nt) - (Y_p n + \dot{X}_p)\cos(nt)}{(2\dot{X}_p - Y_p n)\sin(nt) - (X_p n + 2\dot{Y}_p)\cos(nt)}\right) \tag{A.15d}$$

$$B_i = \frac{\sqrt{Z_p^2 n^2 + \dot{Z}_p^2}}{n} \tag{A.15e}$$

$$\beta_i = nt - \arctan\left(\frac{-\dot{Z}_p}{Z_p n}\right) \tag{A.15f}$$

Subsequently using Eqs. (7.35) and (7.36), the inverse mapping between the cartesian state in the perifocal frame $\boldsymbol{s}_p = [X_p, Y_p, Z_p, \dot{X}_p, \dot{Y}_p, \dot{Z}_p]^T$ and the general inertial frame relative orbit elements (IROEs) $\delta\boldsymbol{\alpha e}_i = [r_i, \phi_i, d_i, \alpha_i, B_i, \beta_i]^T$ used in Eq. (7.22) is obtained:

$$r_i = \frac{1}{2n}\sqrt{\begin{aligned}&\Big((X_p n - 2\dot{Y}_p)\sin(nt) - (Y_p n + 2\dot{X}_p)\cos(nt)\\&+ \Big(2\big((\dot{X}_p - Y_p n)\sin(nt) - (X_p n + \dot{Y}_p)\cos(nt)\big)\Big)^2\end{aligned}} \tag{A.16a}$$

$$\phi_i = \arctan\left(\frac{(X_p n - 2\dot{Y}_p)\sin(nt) - (Y_p n + 2\dot{X}_p)\cos(nt)}{2\big((\dot{X}_p - Y_p n)\sin(nt) - (X_p n + \dot{Y}_p)\cos(nt)\big)}\right) \tag{A.16b}$$

$$d_i = \frac{1}{2n}\sqrt{\begin{array}{l}\Big((X_p n - \dot{Y}_p)\sin(nt) - (Y_p n + \dot{X}_p)\cos(nt)\Big)^2 \\ + \Big((2\dot{X}_p - Y_p n)\sin(nt) - (X_p n + 2\dot{Y}_p)\cos(nt)\Big)^2\end{array}} \tag{A.16c}$$

$$\alpha_i = nt - \arctan\left(\frac{(X_p n - \dot{Y}_p)\sin(nt) - (Y_p n + \dot{X}_p)\cos(nt)}{(2\dot{X}_p - Y_p n)\sin(nt) - (X_p n + 2\dot{Y}_p)\cos(nt)}\right) \tag{A.16d}$$

$$B_i = \frac{\sqrt{Z_p^2 n^2 + \dot{Z}_p^2}}{n} \tag{A.16e}$$

$$\beta_i = nt - \arctan\left(\frac{-\dot{Z}_p}{Z_p n}\right) \tag{A.16f}$$